Numerical Modeling of Tsunamis with Applications to the Sea of Japan and the Pacific Northwest

Edward Payson Myers III

B.Sc., Washington University, 1992

A thesis submitted to the faculty of the
Oregon Graduate Institute of Science & Technology
in partial fulfillment of the
requirements for the degree of
Master of Science
in
Environmental Science and Engineering

October 1994

The thesis "Numerical Modeling of Tsunamis with Applications to the Sea of Japan and the Pacific Northwest" by Edward P. Myers has been examined and approved by the following Examination Committee:

ANTÓNIO M. BAPTISTA, PhD.
Associate Professor
Thesis Advisor

WILLIAM FISH, PhD.
Associate Professor

CURT D. PETERSON, PhD.
Portland State University

GEORGE R. PRIEST, PhD.
Department of Geology and Mineral Industries

To my parents, Edward Jr. and Shirley,
my sister, Brynn,
and to family members,
Bobbie, G.P.,
Evelyn, Clifford,
Helen, Fred, Gene,
Edward, and Petriva

ACKNOWLEDGEMENTS

I would like to thank my advisor, Dr. António M. Baptista, for his advice and encouragement in preparing this thesis. His experience, dedication, and acumen have made the graduate level experience all the more rewarding. I would also like to express my gratitude to my other thesis committee members Dr. William Fish, Dr. Curt Peterson, and Dr. George Priest for their review of this thesis and valuable suggestions.

I would also like to express my gratitude to those that have provided invaluable field work. Dr. Curt Peterson has pioneered the way in collecting field evidence supporting past subduction earthquakes along the Oregon and Washington coastlines. Dr. António Baptista and Dr. George Priest have investigated the effects of the September 1, 1992 Nicaragua tsunami and the July 12, 1993 Hokkaido Nansei-oki tsunami. They also led us along the Oregon and Washington coastline to view the evidence of past subduction earthquakes found by Dr. Peterson. All of these field contributions are vital and can be integrated with computer models to provide an in-depth understanding of the processes involved in these events.

The communication of ideas among members of a scientific community is crucial in the advancement of science. I would like to thank Dr. Tad Murty for coming to our school to teach a special topics course on tsunamis. His experience and ideas were invaluable to my learning experience, and it was an honor to have him here. Thanks also to Dr. Kenji Satake from the University of Michigan for his visit and seminar presentation. His tsunami research and seismology background were a critical link in the development of this thesis. Thanks to Dr. Frank Gonzalez from the Pacific Marine Environmental Laboratories in Seattle, Washington for his seminar presentation and exchange of ideas. Thanks as well to J.J. Westerink and R.A. Luettich for providing the base code for the finite element model ADCIRC.

I would also like to express my appreciation to Paul Turner, Brad Beck, André Fortunato, Anabela Oliveira, and Yongyan Wang for their advice and suggestions throughout the development of my work. Paul's computer programs and visualization tools play a major role in the investigation and presentation of numerical modeling results in our research group.

Research was partially sponsored by Oregon Sea Grant and by DOD/AASERT Contract DAALO3-92-G-0065.

TABLE OF CONTENTS

LIST OF TABLES

LIST OF FIGURES

ABSTRACT

Numerical Modeling of Tsunamis with Applications to the Sea of Japan and the Pacific Northwest

Edward Payson Myers III

Oregon Graduate Institute of Science & Technology, 1994

Supervising Professor: António M. Baptista

Recent evidence along the Oregon and Washington coastlines suggests that the Pacific Northwest experiences great subduction earthquakes every 200 to 600 years. Such events appear to occur as the Juan de Fuca tectonic plate subducts beneath the North American plate in what is termed the Cascadia Subduction Zone. These earthquakes are estimated to range between 8 and 9 on the magnitude scale and cause sufficient displacement in the sea floor to generate large tsunamis.

This evidence provides the incentive for numerical modeling of tsunamis. Two test cases are used as the framework for evaluating the ability of a numerical model to represent tsunami wave activity. A finite element approach is used which shows that a wave continuity formulation is capable of handling such tsunami simulations. Details of initial and boundary conditions are provided, taking into account a moving sea floor and allowing waves to travel undisturbed through transmissive boundaries.

Principles of mass conservation and energy conservation are used as benchmarks for how well the physics is represented in the systems. Such results have historically not

been presented in numerical studies of tsunamis. A detailed evaluation of them here shows that mass is generally well conserved while energy is not. Some of the energy loss can be taken into account by energy leaving the domain through transmissive boundaries, yet problems still occur during the early time steps when initial conditions have been imposed and when the waves interact with land boundaries. My interpretation is that both of these situations are ones in which vertical accelerations are important. However, the shallow water equations assume a hydrostatic approximation which neglects pressure gradients due to vertical accelerations. It is therefore possible that the shallow water equations do not inherently conserve energy.

The July 7, 1993 Hokkaido Nansei-Oki tsunami is used to test the ability of the model to reproduce observed waveforms at tidal gauge stations. This involves calibration with respect to seismic source scenarios, friction, and diffusion. Waveforms are reasonably reproduced at near-field stations, yet far-field stations show differences in amplitude and wavelength. If the width and length of the fault plane are correctly specified, the numerical results at near-field stations suggest that fault plane models are able to generate initial conditions quite well.

Two seismic source scenarios are then considered for the Pacific Northwest. Waveforms are computed for various coastal locations, and patterns of energy distribution are displayed. Such information should be useful for coastal communities in terms of what types of waves would be arriving near their portion of the coastline and what regions may be more susceptible to energy focusing. Uncertainty remains, in particular regarding the source mechanism, because computed subsidence from fault plane models for both scenarios is less than what field evidence from past subduction events suggests.

CHAPTER 1
Introduction

Context

Tsunamis (from the Japanese, 'tsu'=harbor, 'nami'=wave) are seismically generated ocean waves which result from motion disturbances on the sea floor. Such disturbances result from either deformations arising from subduction of one plate underneath another (Figure 1.1), landslides generated by submarine volcanoes [*Smith and Shepherd, Heinrich*, 1991], or from landslides generated by the shaking of an earthquake. Subduction generated tsunamis are common around the Pacific rim, but have also occurred in other regions such as the Mediterranean Sea and parts of the Atlantic Ocean. Similar wave phenomena may be generated due to underwater chemical explosions such as the one which occurred in Halifax, Nova Scotia in 1917 [*Greenberg et. al.*,1993].

The tsunami may only have one associated wave, but in most circumstances their will be a series of waves generated by the motion disturbance. Any one of this set of waves may have the largest amplitude. The periods of the waves are typically very long and may range anywhere between several minutes to several hours. Since their wavelengths are large relative to the depth of the water, tsunami waves can be approximated using the shallow water equations. Thus, the waves travel at a speed approximately equal to the square root of the depth times the gravitational constant. In the deep parts of the ocean, this can be several hundreds of kilometers per second.

Recent tsunamis such as those which occurred in Nicaragua (September, 1992), Indonesia (December, 1992), and Hokkaido (July, 1993) have generated significant interest from the numerical modeling community. Data from these events have been collected

thoroughly and with the best available measuring devices [*Baptista et.al.*, 1993, *Bernard and Gonzalez*, 1993, *Satake et. al.*, 1992]. Despite the fact that these tsunamis have been investigated thoroughly, the numerical modeler is still faced with many tasks.

Why is numerical modelling of tsunamis important after these events already have occurred? Numerical modelling provides an understanding of the processes involved from the moment the earthquake occurs until any point in time afterwards. Physical models of tsunamis have been employed to study important generation and propagation effects [*Goring and Raichlen*, 1980]. However, such models face problems of dimensional scaling and cannot easily be applied to actual tsunami events. The understanding of processes involved with particular tsunami events is therefore primarily obtained by comparing numerical model results with available data from tsunamis which have already occurred. What the modeler learns from numerical analysis may then be applied to regions which are known to have a high probability of earthquake/tsunami occurrence. This modelling of potential tsunamis may in turn be used to educate communities that are not well prepared for such an event. One of the purposes of this thesis is to gather an understanding of modeling the July,12 1993 Hokkaido Nansei-oki tsunami and then to apply this knowledge to modeling of potential Pacific Northwest tsunamis.

Three key components are involved in tsunami modeling: the generation, propagation, and inundation of the tsunami waves. Understanding the generation of a tsunami relies heavily on available seismological information for a particular event. Unfortunately, as will be exemplified later, information relating to seismological parameters is not always well determined. These parameters are necessary as input to fault plane models which compute the amount that the sea floor deforms (bottom deformation) during the event. Such fault plane models assume a simple seismic source (rectangular source in a isotropic homogeneous half-space) in part due to the lack of data on bottom deformation to compare results from more elaborate source models [*Okada*,1985]. As Okada points out, though, such models based on simple source configurations are inherently nonunique and are useful only as a first approximation. The region within which most of the deformation

occurs from a fault plane model should work out to be approximately the same as the area which encompasses the distribution of aftershocks from the earthquake. Once this bottom deformation is computed for a particular earthquake, it may be used as input to a hydrodynamic model. The initial conditions in the hydrodynamic model may be assigned such that the initial free surface water elevation is equal to the bottom deformation (an assumption of approximately instantaneous motion) or the continuity equation may be altered to take into account a moving sea bottom.

The second component of tsunami modeling is the propagation of the waves away from the generation source. The Ursell parameter U is useful for testing which equations are more suitable for the simulation of tsunamis:

$$U = \frac{\varepsilon}{\mu} = \frac{\zeta\lambda^2}{D^3} \qquad \text{(EQ 1.1)}$$

where: $\varepsilon = \frac{\zeta}{D}$

$\mu = \frac{D^2}{\lambda^2}$

$\zeta =$ free surface water elevation

$D =$ water depth

$\lambda =$ wave length

ε here is a measure of the amplitude dispersion and μ is a measure of the phase dispersion. Therefore, the Ursell parameter measures the relative importance of the two types of dispersion occurring in the tsunami wave. If the Ursell parameter is approximately equal to one, then both types of dispersion are important and the Boussinesq equations should be used [*Murty*, 1977]. Antunes do Carmo et. al. [1993] have demonstrated a finite element scheme for solving the Boussinesq equations which incorporate a moving bottom. For any

case in which $\frac{H}{\lambda}$ is much less than one, the shallow water equations are appropriate. The Boussinesq equations assume shallow water theory, but also make the assumption that:

$$\frac{\zeta}{H} \approx \left(\frac{H}{\lambda}\right)^2 \qquad \text{(EQ 1.2)}$$

For the purposes in this thesis, the shallow water equations are appropriate. The shallow water equations consist of the depth-integrated horizontal momentum equations and the depth-integrated continuity equation. These three equations are needed to solve for the two depth-averaged horizontal velocities u and v and the free surface elevation ζ.

Numerical simulation of tsunamis through the use of the shallow water equations may be accomplished with either finite difference or finite element schemes. Finite difference schemes have been widely used to simulate tsunamis in the past [*Kowalik and Murty*, 1993, *Imamura and Goto*, 1988, *Chubarov et. al.*, 1984, *Dunbar et. al.*, 1991, *Nagano et. al.*, 1991]. However, finite element schemes allow better discretization of coastlines and smoother gradients of spatial discretization (such as from small elements in shallow regions to larger elements in deeper waters). Depending on the formulation of the weighted residual statement used in a particular model, boundary conditions can be included naturally rather than explicitly. Early finite element solutions of the primitive shallow water equations were plagued with spurious oscillations. As will be shown in Chapter 2, these problems have been resolved through the use of a wave continuity equation approach.

The third component of tsunami modeling is the aspect of flooding, or inundation. There are analytical models which determine the run-up of certain waveforms onto sloping beaches, namely that of Carrier and Greenspan [1958]. However, actual tsunami waves will have different forms and will progress onto beaches of varying slopes (not necessary constant). Therefore, numerical techniques are needed to solve such run-up calculations. Various finite element and finite difference schemes have been introduced to simulate inundation conditions [*Mader*, 1988, *Okamoto* et. al., 1992]. However, such con-

ventional schemes have only been able to simulate inundation at the expense of not obeying at least one fundamental equation. Numerical schemes are currently being developed to handle inundation while at the same time obeying all of the appropriate equations. Therefore, this thesis does not consider inundation and only focuses on the generation and propagation properties of the tsunami.

An Introduction to the Test Cases

As mentioned, two geographic regions are considered here for the application of a numerical model to represent the effects of local tsunamis. These two regions, the Sea of Japan and the Pacific Northwest, have been hypothesized to be similar in terms of their subduction regions [*Heaton and Hartzell*, 1986]. Both appear to have subduction regions in which strain accumulates over many years and at some time is released in a subduction earthquake which generates tsunamis. Furthermore, this sequence seems to be repeated. The strain accumulation stage will commence after one earthquake and will continue until the next earthquake. The period of time between subduction earthquakes will vary, but on average it is estimated that Pacific Northwest earthquakes occur on the order of several centuries, while those in the Sea of Japan occur at a much smaller interval.

The Japanese islands have not only experienced frequent earthquake events accompanied by subsequent tsunamis, but have also been literally geographically encompassed by such events. On the southeastern edge of the islands, the Philippine Sea plate is subducting beneath the Eurasian plate in a zone termed the Nankai trough. Large subduction earthquakes have occurred along the Nankai trough at intervals on the order of one hundred years [*Satake*, 1993]. Subduction zone earthquake also occur to the east of the islands of Honshu and Hokkaido, where they are bounded by the Japan trench and the Kurile trench. The area of interest for this thesis is however located in the Sea of Japan where subduction has been observed at the border of the Eurasian plate and the North American plate. Two major events have occurred in recent history in this area, the first in 1983 off the coast of northwestern Honshu and the second in 1993 off the western coasts

of Okushiri and Hokkaido. The earthquake which occurred on July 12, 1993 is the one which is focused upon here.

Several aspects of the Hokkaido Nansei-Oki event make it a good test for numerical models of tsunami generation and propagation. First, available field data are relatively abundant including a reasonably detailed bathymetry, observations of coastal subsidence/uplift along the coast of Okushiri, combined records of tides and tsunami waveforms at several tidal gauges throughout the Sea of Japan, and observations of tsunami run-up at a large number of locations along the coasts of Okushiri and Hokkaido, and, to a lesser extent, along the coasts of Korea and Russia. Second, the source mechanism is relatively well constrained, and geodetic data on coastal uplift/subsidence on Okushiri permit comparisons with results of bottom deformation models.

Seismic reports of the July 12, 1993 event have varied not only in the values of many of the parameters (as will be shown in Chapter 2), but also in the number of seismic sources. Some reports point to only one seismic source while others indicate two seismic sources. The location of the source in the one-source scenarios coincides with the location of the northern source in the two-source scenarios. The ambiguity among various reports of the seismic processes involved with this event is investigated later through the use of a numerical model.

The Pacific Northwest appears to experience subduction processes similar to those in the vicinity of Japan. The Cascadia Subduction Zone is a subduction zone off the northwest coast which stretches from the northern tip of California to regions off of British Columbia. The Juan de Fuca plate meets the North American plate at a convergent boundary at which point the former subducts beneath the latter (Figure 1.2). Researchers are not sure whether or not the entire locked portion of the subduction zone (which stretches approximately 1500 km in length) will rupture as one segment or a number of smaller segments. The width of the locked zone is another dimension which needs to be determined. Based upon evidence presented by Peterson et. al. [1991], the rupture zone of the fault

appears to be approximately 100 km wide, from the landward edge of the locked zone to the trench.

A number of geological and geophysical findings over the last six years argue for large subduction earthquakes and tsunamis in this region [*Atwater*, 1987, *Grant and McLaren*, 1987, *Darienzo*, 1991, *Darienzo and Peterson*, 1990, *Peterson and Darienzo*, 1991]. Such evidence points to the existence of buried marshes along the coasts of Oregon and Washington. As strain accumulates in the locked portion of the fault, the North American plate buckles into a sinusoidal shape, buckling down at the leading edge of the plate boundary. During this buckling process, areas which were once low-lying areas such as intertidal flats may be uplifted enough such that the ecosystem changes significantly. For example, such a process may cause an intertidal flat to evolve into a marsh which may even further evolve into a forest ecosystem. However, once the strain is released during a great subduction earthquake, the plate will "rebound" to a shape which no longer has a buckled shape. Thus, such areas which were able to evolve into marshes or even forests due to the increase in land elevation will fall back into a low-lying position after such a strain release. These regions will then be covered by the mud of flats and/or bays over a number of years until again the strain increase will elevate them enough for ecosystem change. The evidence therefore lies in these buried marshes which appear as fossilized peat separated by years of accumulated intertidal mud. In many instances, small layers of sand have been noticed directly above the buried peat layers, possibly indicating sand which has been deposited by a tsunami which arrived after the fault rupture occurred (Figure 1.3).

Turbidite layers off the coasts of Oregon and Washington also indicate that great earthquakes have occurred. Sediments deposited into coastal waters by rivers such as the Columbia River tend to accumulate into thick layers. Once these accumulated layers become so thick that they are unstable, a submarine landslide is formed by which the sediments will be deposited into deeper parts of the ocean. These submarine landslides are termed turbidity currents because they travel great distances as dense slurries, depositing

layers of sediments called turbidites. Such turbidite layers may be counted for various channels along the coasts to discern how many and at what times the layers were formed [*Griggs and Kulm*, 1970]. Turbidite layers appear to have been formed at the same times even at different locations along the coast [*Adams*, 1990]. This may indicate that the submarine landslides were initiated by the same event, namely a large earthquake in that region. Perhaps most compelling is the observation that turbidites are found above the Mazama ash marker horizon in submarine canyons and channels tributary to these canyons [*Adams*, 1990]. If turbidites were not triggered by earthquakes, more layers should be in the canyons.

Geodetic data may also provide useful information as to what land regions are currently experiencing in terms of uplift or subsidence from the strain accumulation within the locked zone. Geodetic data has been able to show that uplift rates many times higher than can be sustained without release of the strain by earthquakes is occurring in some coastal land areas. This supports the notion that the subduction in the Cascadia Subduction Zone is coseismic rather than aseismic. Indian legends of tsunami-like events [*Heaton and Snavely*, 1985] and archaeological sites apparently flooded by coseismic subsidence [*Woodward et. al.*, 1990] are additional evidence that large subduction zone earthquakes have occurred.

Dendrochronological data appears to indicate that the last Cascadia subduction earthquake occurred about 300 years ago. However, the recurrence interval is approximately the same order of magnitude, thus making it difficult to determine when the next event may occur. The evidence mentioned above provides certain clues and constraints as to how the subduction will occur. A variety of these clues will be used as the numerical model is applied to Pacific Northwest tsunamis.

Methodology

The available data for the two test cases will provide constraints as well as a means to verify the results obtained through numerical modeling. For the Sea of Japan, such data will include bathymetry, coastline representations, tidal gauge waveforms, geodetic data, seismic reports, and measurements of wave run-up onto the land. The database for the Pacific Northwest is a bit more limited due to the fact that the tsunamis which have impacted this region occurred hundreds of years ago. However, there is still data in the form of bathymetry, coastline representations, geodetic data, and prehistoric evidence of buried peat layers and sands probably deposited by the associated tsunami as a result of subduction earthquakes.

In order to represent the physics of the two regions correctly, the numerical soundness of the simulations must be maintained. Ensuring this soundness begins with the construction of the finite element grids which will be used for the simulations. The grids need to be built in a way that best represents dimensionless numbers such as the Courant number and the dimensionless wavelength. Such dimensionless numbers are developed through formal analyses and may be shown to indicate stability requirements. For example, the Courant number β may be shown to be constrained as,

$$\beta = \frac{u\Delta t}{\Delta x} \leq 1 \qquad \text{(EQ 1.3)}$$

where u is the velocity, Δt is the time step, and Δx is the spatial discretization. Likewise, the dimensionless wavelength $\frac{L_m}{\Delta x}$ is generally recommended to be greater than 40. Once the simulations have been run, stability needs to be checked to make sure it was maintained. Similarly, conservation of mass and energy need to be optimized.

Some of the input parameters to the equations which are used to represent the physical processes can be removed or varied depending on a particular simulation. For example, nonlinearities such as friction, advection, and finite amplitude terms may or may not be included. In some instances, inclusion of non-linear terms may lead to numerical

instabilities. Whenever possible, though, such terms should be included since they are certainly occurring in the physical systems. The amounts of friction and diffusion may likewise be varied. For a test case such as the 1993 Hokkaido tsunami where tidal gauge data is available, various values for the friction and diffusion may be introduced independently. A root mean square error may then be evaluated for each of the terms by comparing model results with tidal gauge data, and then determining the best value of each.

Once these issues have been resolved, the numerical modeling of the tsunamis needs to be used to determine the likelihood of the various seismic source scenarios. The scenarios which are looked at for both the Hokkaido tsunami and a Pacific Northwest tsunami are those which have been proposed from a logical viewpoint. In this manner, the numerical modeling not only allows an understanding of the hydrodynamic processes occurring, but it also provides insight as to the seismic processes involved. Results from the hydrodynamic model will primarily be verified by comparing waveforms with the tidal gauge time records for the Sea of Japan and by comparing coastal wave heights with the distribution of buried peat layers for the Pacific Northwest.

References

Adams, J., Paleoseismicity of the Cascadia Subduction Zone: Evidence from Turbidites off the Oregon-Washington margin, *Tectonics*, 9, pp. 569-583, 1990.

Antunes do Carmo, J.S. Seabra Santos, J., and Barthelemy, E., Surface Waves Propagation in Shallow Water: A Finite Element Model, *International Journal for Numerical Methods in Fluids*, 16, pp. 447-459, 1993.

Atwater, B.F., Evidence for Great Holocene Earthquakes Along the Outer Coast of Washington State, *Science*, 236, pp. 942-944, 1987.

Baptista, A.M., Priest, G.R., and Murty, T.S., Field Survey of the 1992 Nicaragua Tsunami, *Marine Geodesy*, 16, pp. 169-203, 1993.

Bernard, E. and Gonzalez, F.I., Tsunami Devastates Japanese Coastal Region, *EOS Transactions*, 74(37), p. 417, 1993.

Carrier, G.F. and Greenspan, H.P., Water Waves of Finite Amplitude on a Sloping Beach, *Journal of Fluid Mechanics*, 4, pp. 97-109, 1958.

Chubarov, L.B., Shokin, Y.I., and Gusiakov, V.K., Numerical Simulation of the 1973 Shikotan (Nemuro-Oki) Tsunami, *Computers and Fluids*, 12(2), pp.123-132, 1984.

Darienzo, M.E., 1991, Late Holocene Paleoseismicity Along the Northern Oregon Coast, *Doctor of Philosophy Dissertation*, Portland State University, 1991.

Darienzo, M.E. and Peterson, C.D., Episodic Tectonic Subsidence of Late Holocene Salt Marshes, Northern Oregon, Central Cascadia Margin, *Tectonics*, 9, pp. 1-22, 1990.

Dunbar, D., LeBlond, P., and Murty, T.S., Evaluation of Tsunami Amplitudes for the Pacific Coast of Canada, *Progress in Oceanography*, 26, pp. 115-177, 1991.

Goring, D. and Raichlen, F., The Generation of Long Waves in the Laboratory, *Coastal Engineering*, pp. 763-783, 1980.

Grant, W.C. and McLaren, D.D., Evidence for Holocene Subduction Earthquakes Along the Northern Oregon Coast, *EOS*, 68, p. 1469, 1987.

Greenberg, D.A., Murty, T.S., and Ruffman, A., A Numerical Model for the Tsunami in Halifax Harbor due to the Explosion in 1917, *Marine Geodesy*, 16, n. 2, p.153, 1993.

Griggs, G.B. and Kulm, L.D., Sedimentation on the Cascadia Deep-Sea Channel, *Geological Society of America Bulletin*, 81, pp. 1361-1384, 1970

Heaton, T.H. and Hartzell, S.H., Source Characteristics of Hypothetical Subduction Earthquakes in the Northwestern United States, *Bulletin of the Seismological Society of America*, 76, pp. 675-708, 1986.

Heaton, T.H. and Snavely, P.D., Possible Tsunami Along the Northwestern Coast of the United States Inferred from Indian Traditions, *Bulletin of the Seismological Society of America*, 75, pp. 1455-1460.

Heinrich, P., Non-linear numerical Model of Landslide-generated Water Waves, *International Journal of Engineering Fluid Mechanics*, 4(4), pp. 403-416, 1991.

Hyndman, R.D. and Wang, K., Thermal Constraints on the Zone of Major Thrust Earthquake Failure: The Cascadia Subduction Zone, *Journal of Geophysical Research*, 98(B2), pp. 2039-2060, 1993.

Kowalik, Z. and Murty, T.S., Numerical Simulation of Two-Dimensional Tsunami Run-up, *Marine Geodesy*, 16(2), p. 87, 1993.

Imamura, F. and Goto, C., Truncation Error in numerical Tsunami Simulation by the Finite Difference Method, *Coastal Engineering in Japan*, 31(2), pp. 246-263, 1988.

Mader, C.L., Numerical Modeling of Water Waves, *Los Alamos Series in Basic and Applied Sciences*, 1988.

Madin, I., Seismic Hazards on the Oregon Coast, *Coastal Natural Hazards*, Oregon Sea Grant ORESU-B-92-001, pp. 3-27, 1992.

Murty, T.S. *Seismic Sea Waves; Tsunamis*, Department of Fisheries and the Environment, Ottawa, 1977.

Nagano, O., Imamura, F., Shuto, N., A Numerical Model for Far-Field Tsunamis and Its Application to Predict Damage Done to Aquaculture, *Natural Hazards*, 4(2/3), p.235, 1991.

Okada, Y., Surface Deformation due to Shear and Tensile Faults in a Half-Space, *Bulletin of the Seismological Society of America*, 75, pp. 1135-1154, 1985.

Peterson, C.D. and Darienzo, M.E., Discrimination of Climatic, Oceanic and Tectonic Mechanisms of Cyclic Marsh Burial from Alsea Bay, Oregon, *USGS*, 1991.

Peterson, C.D., Darienzo, M.E., and Clough, C., Recurrence Intervals of Coseismic Subsidence Events in Northern Oregon bays of the Cascadia Margin, *Final Technical Report to the Oregon Department of Geology and Mineral Industries*, 1991.

Satake, K., Depth Distribution of Coseismic Slip Along the Nankai Trough, Japan, From Joint Inversion of Geodetic and Tsunami Data, *Journal of Geophysical Research*, 98, pp. 4553-4565, 1993.

Satake, K., Bourgeois, J., Abe, Kuniaki, Abe, Katsuyuki, Tsuji, Y., Imamura, F., Iio, Y., Katao, H., Noguera, E., and Estrada, F., Tsunami Field Survey of the 1992 Nicaragua Earthquake, *EOS Transactions*, p. 8, 1992.

Woodward, J., White, J., and Cummings, R., Paleoseismicity and the Archaeological Record: Areas of Investigation on the Northern Oregon Coast, *Oregon Geology*, 52, pp. 57-65, 1990.

FIGURE 1.1 Subduction Process (Extracted from Hyndman and Wang, 1993)

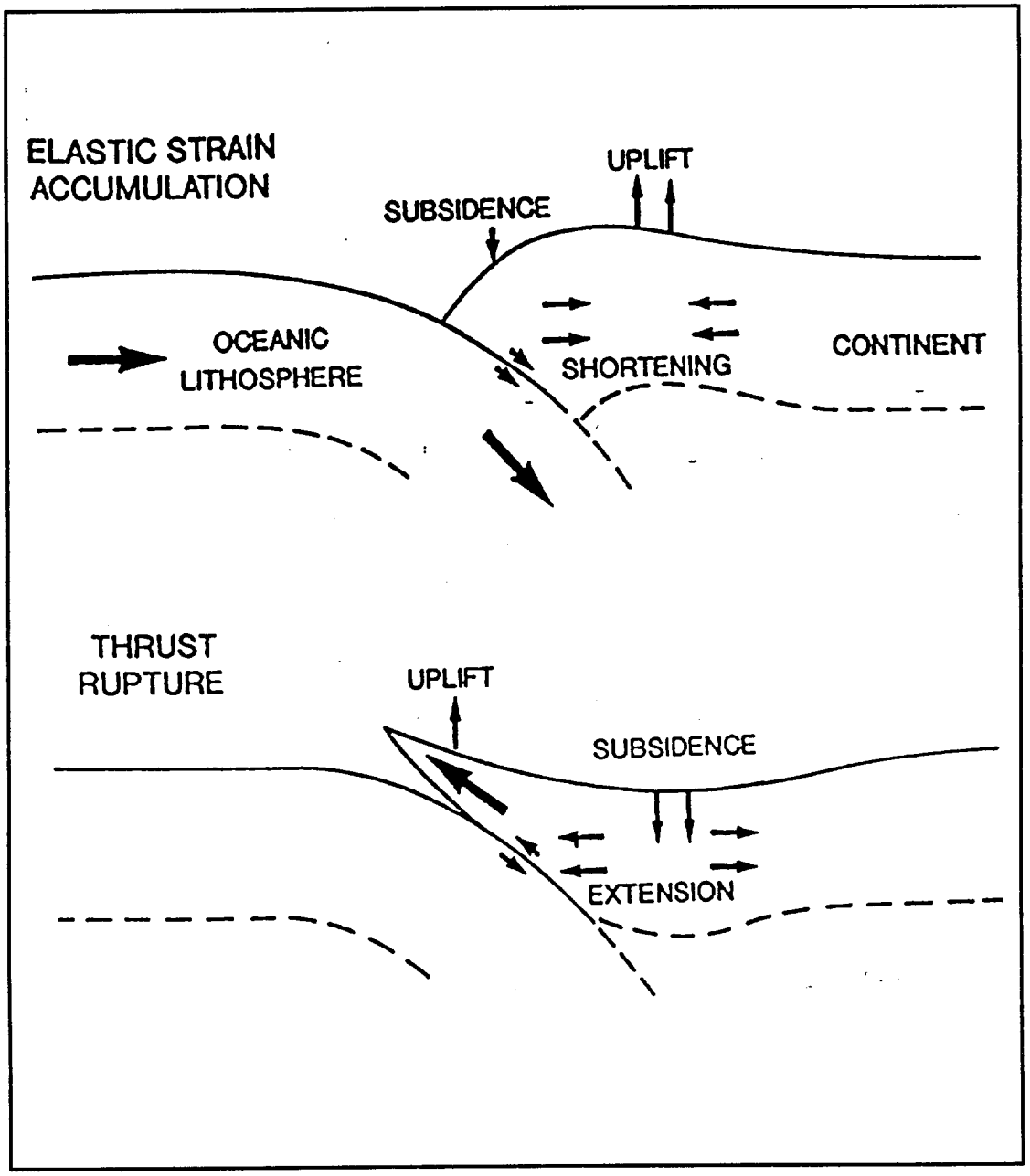

FIGURE 1.2 Northwest Plate Tectonics (Extracted from Darienzo, 1991)

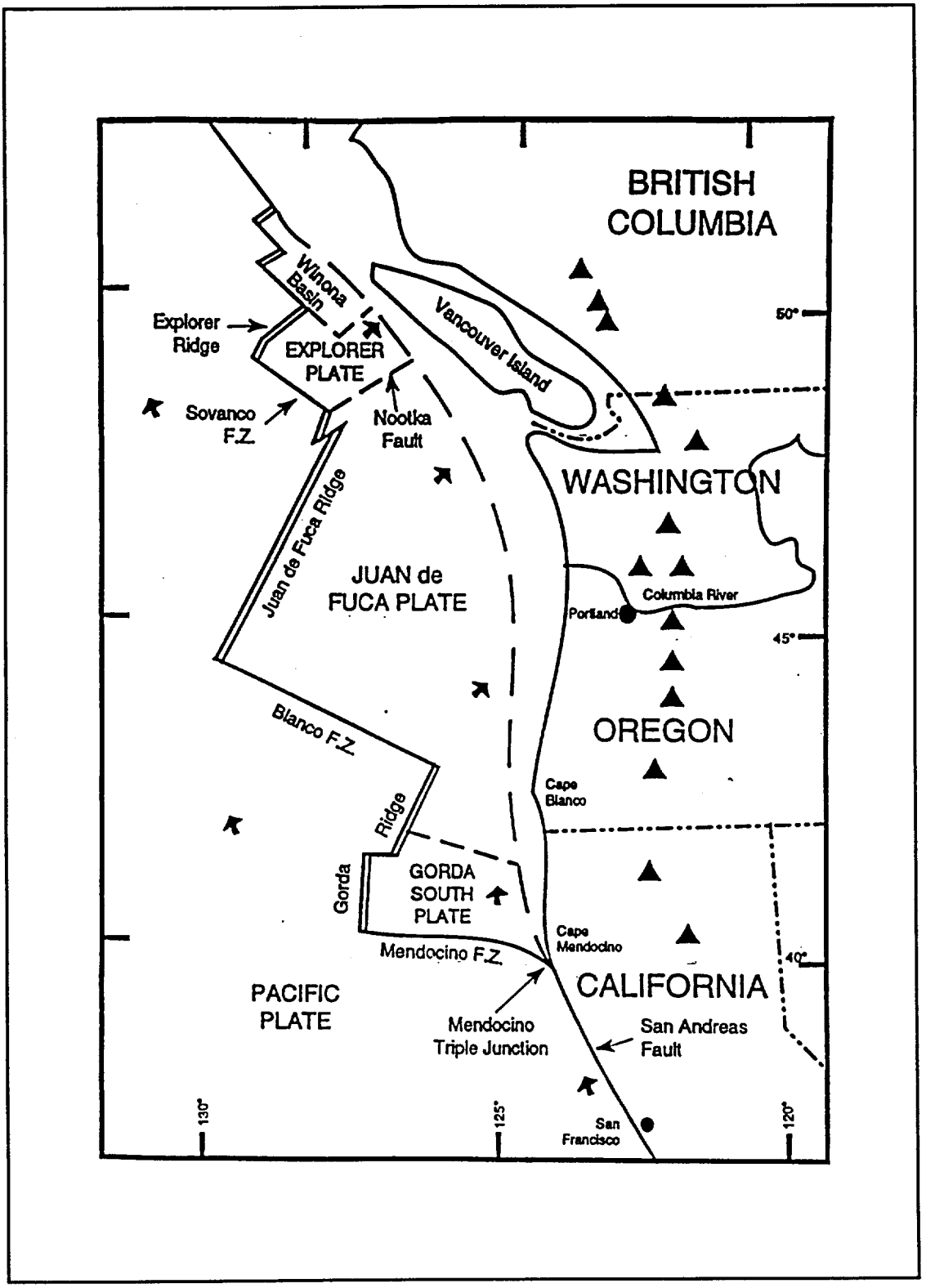

FIGURE 1.3 Buried Peat from Willapa Bay, WA (Extracted from Madin, 1992)

CHAPTER 2

Numerical Modeling of Tsunamis

Seismic Parameters Used in Initial Conditions

The movement of the sea floor, or bottom deformation, is used as an initial condition to tsunami propagation models. This bottom deformation is dependent upon a number of seismic parameters, including the distribution of aftershocks, fault length, fault width, dip angle, slip rake angle, strike direction, depth of the fault plane, and the total slip (dislocation) within the fault plane. Figure 2.1 shows some of these parameters in a simple fault model.

The length and width of the fault define the area of bottom deformation. These may be determined based upon the energy released by the earthquake. The energy released as seismic waves for a particular event may be related to the moment magnitude as shown below:

$$M_w = \frac{2}{3}(\log E_s - 11.8) \qquad \text{(EQ 2.1)}$$

where: M_w = moment magnitude

E_s = energy released as seismic waves

The seismic moment, M_0, may then be calculated as

$$M_0 = 10^{(\frac{3}{2}M_w + 16.1)} \qquad \text{(EQ 2.2)}$$

and, finally, the area of the fault may be computed as

$$A = \frac{M_0}{(\mu)\ (u)} \qquad \text{(EQ 2.3)}$$

where: μ = rigidity (generally assumed as $3 - 7 \times 10^{11} \frac{dyne}{cm^2}$)

A = area of the fault

The length and width are often determined based upon the locations of the aftershocks which follow the main earthquake shock. The ratio between the length and width, or the aspect ratio, may then be related to the area as computed above. Often this ratio appears to be approximately 1/2 (width/length), although it really depends upon the particular earthquake as well as the moment magnitude.

The dip angle is that angle at which the subducting plate dips below the continental plate. The slip rake angle prescribes the angle at which the dislocation occurs along the plane of the fault. It is measured in the plane of the fault counterclockwise from a horizontal line which points in the direction of the strike. The slip (dislocation) is the distance a point on the fault plane moves (at the slip rake angle) between the time the subduction begins and ends. The slip may be purely dip-slip (U_{dip} is the only component of $\vec{U}$), purely strike-slip (U_{strike} is the only component of $\vec{U}$), purely tensile ($U_{tensile}$ is the only component of $\vec{U}$), or a combination of the various components (most likely). The strike direction is the angle measured counterclockwise from north to the main axis of the fault (the main axis lies in the direction of the length of the fault). The depth of the fault plane is that depth (measured from the sea floor) at which the main earthquake shock occurs.

The depth of the earthquake can provide the necessary information as to the type of earthquake. For example, if the earthquake occurs within the continental plate (in which case the depth will be fairly shallow), a crustal earthquake has most likely occurred. If the earthquake occurs at a depth which is within the subducting plate, it is probably an intraplate earthquake. Subduction earthquakes are believed to occur at a depth which lies

directly on the interface between the subducting and continental plates [*Madin*, 1992]. Figure 2.2 shows these three types of scenarios.

Thermal models of heat flow in subduction zones can provide useful seismological information such as the width and depth of the locked portion of the fault, accumulated strain in the fault, and vertical/horizontal deformation associated with the fault zone [*Hyndman and Wang*, 1993]. Such models allow identification of the seismogenic, transition, and plastic regions of the fault.

Current Bottom Deformation Models

Okada [1985] developed a set of analytical expressions for surface displacements, strains, and tilts associated with shear and tensile faults in a half-space. The derived expressions assume a simple source configuration and an isotropic homogeneous half-space. The closed analytical expressions allow one to devise an algorithm for computing the bottom deformation associated with a particular earthquake, and Okada provides some test cases and a numerical checklist for various seismic source scenarios.

Assumptions such as those used in Okada's expressions are needed at this time, since more elaborate source models face many barriers such as the poor availability of actual data on bottom deformation. Efforts have been undertaken to describe the effects of more elaborate sources [i.e., *Mansinha and Smylie*, 1971] which take into account such features as the effect of earth curvature, surface topography, crustal layering, lateral inhomogeneity, and obliquely layered mediums. However, these models are mostly theoretical and it is more appropriate to use a simpler deformation model when dealing with actual observations.

The calculation of displacements through the use of the closed analytical expressions requires input of various seismological parameters such as those mentioned in the previous section. These parameters are obtained from centroid moment tensor solutions such as those from Harvard, NEIC, or the USGS. As will be shown in the next section, the

various solutions (and thus the reported seismic parameters) are often ambiguous for particular earthquake events. Furthermore, as each of these solutions may be different, the tsunamis which are numerically generated using the various solutions will likewise be ambiguous.

Ambiguity of Reported Seismic Parameters

After an earthquake, different agencies report the seismic parameters based upon each of their individual centroid moment tensor solutions. The July 12, 1993 Hokkaido Nansei-oki earthquake is a prime example of the ambiguity which may exist among the various agencies for the same earthquake event. The differences in the reported seismic parameters are displayed in Table 2.1.

The two Tohoku scenarios include two seismic faults, whereas all of the other scenarios only report one seismic fault. The fault that these one-source scenarios are referring to is the northern one (north of the island of Okushiri). EQ 2.3 may be used to compute the area based upon certain values of the moment magnitude (M_0) and the slip (u). The rigidity μ is assumed to be approximately 4×10^{11} dyne/cm^2. In order to calculate a length and width for each source scenario, a ratio between the two must be assumed. The aspect ratio W/L will usually be close to 1/2 but can vary depending on the particular earthquake. For the Hokkaido event, 1/2 should be close to the true aspect ratio. Using the values shown in Table 2.1, the areas can be computed, thus providing the length and width of each fault plane (assuming W/L $\approx$ 1/2. These computations are shown in Table 2.2.

Using the closed analytical expressions provided by Okada [1985], the deformation to the sea floor may be computed for different centroid moment tensor solutions derived from the same earthquake event. This bottom deformation is used as input to a hydrodynamic numerical model. A description of the hydrodynamic model used for the simulations of the July 12, 1993 Hokkaido tsunami and potential Pacific Northwest tsunamis now ensues.

Application of ADCIRC to Tsunamis - Initial Conditions

The two-dimensional finite element model ADCIRC-2DDI is used to study the propagation of tsunamis. Initial conditions for ADCIRC-2DDI may be imposed in one of two ways. First, the initial water surface elevation may be assumed to be equivalent to the deformation to the sea floor. Second, the continuity equation may be altered to take into account a time and spatially dependent bottom deformation. The second option is accomplished, rather conventionally, by incorporating a time and spatially dependent bottom deformation into the kinematic boundary conditions. The depth integrated continuity equation can be shown to be derived as:

$$\frac{\partial \zeta}{\partial t} - \frac{\partial \beta}{\partial t} + \frac{\partial}{\partial x} UH + \frac{\partial}{\partial y} VH = 0 \qquad \text{(EQ 2.4)}$$

where β is the bottom deformation (+ for uplift and - for subsidence), ζ is the free surface elevation, U and V are the depth-integrated velocities, and H is the depth plus free surface elevation.

In order to determine the differences between the two treatments of initial conditions, a test case was set up for the Sea of Japan. Using one of the seismic source scenarios mentioned later in Chapter 3, ADCIRC-2DDI was run for the two treatments. The elevation time histories for four of the stations located near the centers of the seismic sources were computed to check for differences between the waveforms. The waveforms generated by the two treatments of initial conditions appeared to be practically the same. Thus the two treatments are fairly equivalent.

Incorporating the bottom deformation into the continuity equation is the more appropriate option, since the other option of assuming a surface elevation equal to the deformation is only an assumption. Using a revised continuity equation, the time interval over which the bottom deformation is imposed should be consistent with the rise time of the earthquake. The rise time τ_s is defined as the amount of dislocation divided by the dislocation velocity, and is therefore the time over which the dislocation occurs. Geller

[1976] noted that the average dislocation velocity is proportional to the initial effective stress. Approximating this initial effective stress by the mean stress drop which occurs during the earthquake, the rise time is theoretically defined as:

$$\ddot{\tau}_s = \frac{\mu \bar{D}}{\beta \Delta\sigma} \qquad \text{(EQ 2.5)}$$

where: $\ddot{\tau}_s$ = theoretical rise time

μ = rigidity

$\bar{D}$ = average dislocation

β = shear wave velocity

$\Delta\sigma$ = mean stress drop

The time step selected for the hydrodynamic model needs to be consistent with the rise time of the earthquake when the modified continuity equation is employed.

Application of ADCIRC to Tsunamis - Model Equations

The finite element model used in this study belongs to a class of models which use a wave continuity formulation. Developed by Luettich et. al. [1991], ADCIRC-2DDI solves the generalized wave continuity equation (GWCE) for elevations and the non-conservative form of the momentum equations for depth-integrated velocities throughout the domain of interest. Lynch and Gray [1979] proposed using a wave continuity equation instead of the primitive continuity equation in order to eliminate the $2\Delta x$ oscillations often associated with such early finite element solutions of coastal flow simulations.

Let L represent the primitive continuity equation shown in EQ 2.6:

$$L \equiv \frac{\partial \zeta}{\partial t} - \frac{\partial \beta}{\partial t} + \frac{\partial}{\partial x} UH + \frac{\partial}{\partial y} VH = 0 \qquad \text{(EQ 2.6)}$$

Now let M represent the non-conservative form of the momentum equations subject to the Boussinesq, hydrostatic, and incompressibility assumptions:

$$M \equiv \frac{\partial \vec{v}}{\partial t} + \vec{v} \bullet \nabla \vec{v} + f \times \vec{v} + \tau \vec{v} + \nabla \left[\frac{p_s}{\rho_0} + g(\zeta - \alpha\eta) \right] + \frac{E_h^2}{H} \left[\frac{\partial^2}{\partial x^2} \vec{v} H + \frac{\partial^2}{\partial y^2} \vec{v} H \right] + \frac{\tau_{s\vec{x}}}{\rho_0 H} = 0 \qquad \text{(EQ 2.7)}$$

The conservative form of the momentum equations M^c is therefore equal to:

$$M^c = (H)\ (M) + (\vec{v})\ (L) \qquad \text{(EQ 2.8)}$$

The wave continuity equation W may now be constructed as:

$$W \equiv \frac{\partial L}{\partial t} + \tau L - \nabla \bullet M^c = 0 \qquad \text{(EQ 2.9)}$$

where τ is the same as the friction factor used in the momentum equations. The GWCE is an extension of EQ 2.9 whereby τ is replaced by a weighting factor (which does not necessarily have to equal τ) called G. Thus the GWCE takes the form:

$$W^G \equiv \frac{\partial L}{\partial t} + GL - \nabla \bullet M^c = 0 \qquad \text{(EQ 2.10)}$$

The full GWCE is displayed in EQ 2.11. The advective terms in EQ 2.11 have been formulated into non-conservative form in order to be consistent with the non-conservative advective terms in EQ 2.7 [*Kolar et. al.*, 1993]. The larger the value that G is specified, the more primitive the GWCE will be. Thus, if G is too large, spurious oscillations may arise. However, if G is too small on the other hand, the solutions will most likely be plagued with mass balance errors. A balance must therefore be achieved such that G is neither too large or too small. Kolar et. al. [1993] note that the optimum value for τ is generally between 1 to $10\tau_{max}$, where τ_{max} is the maximum nonlinear bottom friction factor.

Kolar et. al. [1993] also provide an algorithm for checking mass conservation in a numerical simulation.

$$
\begin{aligned}
W^G \equiv & \frac{\partial^2}{\partial t^2}(\zeta) + G\frac{\partial \zeta}{\partial t} - \frac{\partial^2 \beta}{\partial t^2} - G\frac{\partial \beta}{\partial t} + \\
& \frac{\partial}{\partial x}\{U\frac{\partial \zeta}{\partial t} - UH\frac{\partial U}{\partial x} - VH\frac{\partial U}{\partial y} + fVH - H\frac{\partial}{\partial x}\left[\frac{p_s}{\rho_0} + g(\zeta - \alpha\eta)\right]\} + \\
& \frac{\partial}{\partial x}\{-E_{h_2}\frac{\partial^2 \zeta}{\partial x \partial t} + \frac{\tau_{sx}}{\rho_0} - (\tau - G)UH\} + \\
& \frac{\partial}{\partial y}\{V\frac{\partial \zeta}{\partial t} - UH\frac{\partial V}{\partial x} - VH\frac{\partial V}{\partial y} - fUH - H\frac{\partial}{\partial y}\left[\frac{p_s}{\rho_0} + g(\zeta - \alpha\eta)\right]\} + \\
& \frac{\partial}{\partial y}\{-E_{h_2}\frac{\partial^2 \zeta}{\partial y \partial t} + \frac{\tau_{sy}}{\rho_0} - (\tau - G)VH\} = 0
\end{aligned}
\qquad \text{(EQ 2.11)}
$$

Care must be taken to ensure continuity is conserved in applying the initial conditions. If one modifies the continuity equation to handle the initial conditions, then the bottom deformation will be assumed to occur over a certain number of time steps and at varying amounts. Since the GWCE is formulated by combining the time derivative of the primitive continuity equation, the spatial derivatives of the conservation of momentum equations (in conservative form), and the continuity equation multiplied by the factor G, then the following terms appear in the GWCE which take into account the bottom deformation:

$$\frac{\partial^2 \beta}{\partial t^2}, \ \tau\frac{\partial \beta}{\partial t}, \text{ and spatial derivatives of } \beta \text{ such as } \frac{\partial \beta}{\partial x}$$

where:
$$\frac{\partial^2 \beta}{\partial t^2} \equiv \frac{\beta^{k+1} - 2\beta^k + \beta^{k-1}}{\Delta t^2}$$

$$\tau\frac{\partial \beta}{\partial t} \equiv \tau\left(\frac{\beta^{k+1} - \beta^{k-1}}{2\Delta t}\right)$$

$$\frac{\partial}{\partial x}(H-\beta) \equiv \sum_{i=1}^{3} (\beta_i)\frac{\partial \varphi_i}{\partial x} \qquad (\varphi_i \text{ is the weighting function})$$

Using this adaptation to account for the bottom deformation allows one to specify the total time over which the bottom deformation occurred as well as how it deformed during that time interval. For example, the deformation may have a linear or a non-linear time dependence.

If the initial conditions are imposed by assuming that the initial free surface elevation ζ is equal to the deformation to the sea floor β, then one must make sure that the values for the bottom deformation (and hence the free surface elevation) are equivalent for the first two specified time steps. If they are not equal, the following two events may occur. First, if the generalized wave-continuity equation (GWCE) weighting factor τ is specified as a large value, then the GWCE will become more similar to the primitive continuity equation. If it is assumed that the initial horizontal velocities are zero and that a centered scheme is used to handle time dependency, then

$$\frac{\zeta_{n+1} - \zeta_{n-1}}{2\Delta t} = 0 \qquad \text{(EQ 2.12)}$$

and $\zeta_{n+1} = \zeta_{n-1}$. However, the initial velocity conditions are improper in this case, and instability will result in the form of $2\Delta t$ oscillations. Problems may also arise if the GWCE weighting factor τ is specified too small. In this case, ζ_{n+1} will be computed to be different from ζ_{n-1} and (EQ 2.6) will not be satisfied. Mass will therefore be artificially introduced to the problem, and the result will be seen as a growing wave.

Application of ADCIRC to Tsunamis - Boundary Conditions

Boundaries for the finite element grid of interest may be either land (no flow) boundaries, amplitude/phase specified ocean boundaries, or open ocean transmissive boundaries. No flow boundaries are imposed by forcing the normal velocities at the land boundary to be zero. Open ocean transmissive boundaries are imposed by first backtracking from the boundary node in the direction of the incoming wave and then interpolating the elevation from the previous time step at that spatial location. The incident angle of the incoming wave is approximated as,

$$\theta = \text{atan}\left(\frac{V^n}{U^n}\right) \qquad \text{(EQ 2.13)}$$

The wave is backtracked a distance

$$S = \Delta t\sqrt{gH} \qquad \text{(EQ 2.14)}$$

in the direction prescribed by θ. This is shown schematically in Figure 2.3. Once the backtracked positions (X_{int}, Y_{int}) are known, the elevation from the previous time step may be interpolated from the appropriate element. The new elevation at the boundary node may then be set equal to this interpolated old elevation, thus allowing the wave to leave the domain of interest.

A couple of problems may arise from using the velocities to approximate the incident angle of the wave. First, if the velocities are very small (such as in the beginning of a simulation), the wave angle will not be computed very well. The interpolated point may be computed at strange angles to the boundary, or even outside the domain boundary. Such errors will most likely lead to instability. Second, even if the velocities are large enough, the interpolated point may still be computed to be outside the domain due to the errors associated with representing the incident wave angle based upon depth-integrated velocities. Again, this will lead to instability in the simulation. Therefore, the transmissive

boundary condition should only be imposed if $\hat{v} \bullet \hat{n} \geq 0$ and if the velocities are not relatively small compared to what is expected for a particular simulation.

Mass Balance Algorithm

Kolar et. al. (1993) present an algorithm to check whether or not mass is being added or lost from a system. The algorithm involves integrating the primitive continuity equation over time and space. Using the continuity equation which takes into account a time-dependent bottom deformation, this mass balance check becomes:

$$\int_{t_0}^{t}\iint_{\Omega}\left[\frac{\partial \zeta}{\partial t} - \frac{\partial \beta}{\partial t} + \nabla\bullet\left(\hat{v}H\right)\right] d\Omega dt = 0 \qquad \text{(EQ 2.15)}$$

The divergence theorem of Gauss states that for an arbitrary variable F,

$$\iint_{\Omega}\left(\nabla\bullet F\right) d\Omega = \int_{\partial\Omega}\left(F\bullet\hat{n}\right) d\left(\partial\Omega\right) \qquad \text{(EQ 2.16)}$$

Applying this theorem to the third term of EQ 2.15 and integrating over time the first two terms,

$$\int_{\Omega}\left(\zeta_t - \zeta_{t_0}\right) d\Omega - \int_{\Omega}\left(\beta_t - \beta_{t_0}\right) d\Omega + \int_{t_0}^{t}\left[\int_{\partial\Omega} H\hat{v}\bullet\hat{n} d\left(\partial\Omega\right)\right] dt = 0 \qquad \text{(EQ 2.17)}$$

The domain is spatially discretized with linear triangular elements which allows the first two terms to be evaluated exactly as:

$$\int_{\Omega}\left(\zeta_t - \zeta_{t_0}\right) d\Omega = \sum_{el}\left[\bar{\zeta}_t - \bar{\zeta}_{t_0}\right]_{el} A_{el} \qquad \text{(EQ 2.18)}$$

$$\int_{\Omega}\left(\beta_t - \beta_{t_0}\right) d\Omega = \sum_{el}\left[\bar{\beta}_t - \bar{\beta}_{t_0}\right]_{el} A_{el} \qquad \text{(EQ 2.19)}$$

Such spatial discretization also allows the integral over the boundary in EQ 2.17 to be evaluated exactly as:

$$Q^{net} \equiv \int_{\partial\Omega} H\vec{v} \bullet \vec{n} d(\partial\Omega) = \sum_{e_b} \frac{w_e}{6} [2H_1 v_{n1} + H_1 v_{n2} + H_2 v_{n1} + 2H_2 v_{n2}] \qquad \text{(EQ 2.20)}$$

for which w_e is the length of the boundary portion of element e_b, $v_n = \vec{v} \bullet \vec{n}$, and the indices [1,2] represent the beginning and ending nodes of each boundary segment. In order to satisfy the third term in EQ 2.17, Q^{net} needs to be integrated over time as follows (using an approximation for the integration):

$$\int_{t_0}^{t} \left[\int_{\partial\Omega} H\vec{v} \bullet \vec{n} d(\partial\Omega) \right] dt = \int_{t_0}^{t} Q^{net} dt \approx \sum_{Ntimesteps} \frac{1}{2} [Q_t^{net} + Q_{t+\Delta t}^{net}] \Delta t \qquad \text{(EQ 2.21)}$$

Summing the quantities provided by EQs 2.18, 2.19, and 2.21 will provide a measure as to how much mass is being added or lost from a particular system. Ideally, for no change in mass, this summation should be zero.

Conservation of Energy Algorithm

The potential energy E_p of the tsunami at a point in time can be described as:

$$E_p = \frac{1}{2} \rho g \int_{\Omega} \zeta^2 d\Omega \qquad \text{(EQ 2.22)}$$

For a finite element grid consisting of linear triangular elements, this can be evaluated as:

$$E_p = \sum_{el=1}^{N_{el}} \frac{1}{2} \rho g \int_{\Omega_{el}} \zeta_{el}^2 d\Omega_{el} \qquad \text{(EQ 2.23)}$$

$$= \sum_{el=1}^{N_{el}} \frac{1}{2}\rho g \int_{\Omega_{el}} \left[\sum_{i=1}^{3} (\zeta_i \varphi_i)^2 d\Omega \right] \quad \text{(EQ 2.24)}$$

$$= \frac{1}{2}\rho g \sum_{el=1}^{N_{el}} \sum_{i=1}^{3} \frac{A_{el}\zeta_i^2}{6} = \frac{\rho g}{12} \sum_{el=1}^{N_{el}} A_{el} \sum_{i=1}^{3} \zeta_i^2 \quad \text{(EQ 2.25)}$$

If the density of water ρ is specified as 1000 kg/m^3, g as 9.81 m/s^2, and the areas and elevations are specified with respect to meters, then the units of EQ 2.25 will be in Joules.

The kinetic energy E_k of the tsunami at a point in time can be evaluated as follows (again assuming linear triangular elements; also assuming that the vertical component of the velocity is negligible):

$$E_k = \frac{1}{2}\rho \int_{\Omega} \left[\int_{0}^{(h+\zeta)} (u^2 + v^2)\, dz \right] d\Omega \quad \text{(EQ 2.26)}$$

$$= \sum_{el=1}^{N_{el}} \frac{1}{2}\rho \int_{\Omega_{el}} \left[\int_{0}^{(h+\zeta)} (u^2 + v^2)\, dz \right] d\Omega_{el} \quad \text{(EQ 2.27)}$$

For the shallow water equations, this should lead to the following:

$$= \sum_{el=1}^{N_{el}} \frac{1}{2}\rho \int_{\Omega_{el}} (h+\zeta)\ (u^2 + v^2)\, d\Omega_{el} \quad \text{(EQ 2.28)}$$

$$= \sum_{el=1}^{N_{el}} \frac{1}{2}\rho \int_{\Omega_{el}} \left(\sum_{i=1}^{3} (h_i\varphi_i + \zeta_i\varphi_i)\ (u_i^2\varphi_i^2 + v_i^2\varphi_i^2) \right) d\Omega_{el} \quad \text{(EQ 2.29)}$$

$$= \sum_{el=1}^{N_{el}} \frac{1}{2}\rho \left[\sum_{i=1}^{3} (h+\zeta)_i (u_i^2 + v_i^2) \int_{\Omega_{el}} \varphi_i^3 d\Omega_{el} \right] \quad \text{(EQ 2.30)}$$

$$= \sum_{el=1}^{N_{el}} \frac{1}{2}\rho \left[\sum_{i=1}^{3} (h+\zeta)_i (u_i^2 + v_i^2) \left(\frac{12A_{el}}{120}\right) \right] \quad \text{(EQ 2.31)}$$

$$= \sum_{el=1}^{N_{el}} \frac{\rho A_{el}}{20} \sum_{i=1}^{3} (h+\zeta)_i (u_i^2 + v_i^2) \quad \text{(EQ 2.32)}$$

The units for E_k should again be in Joules. Thus, the total tsunami energy E_t at a point in time will be:

$$E_t = \frac{\rho g}{12} \sum_{el=1}^{N_{el}} A_{el} \sum_{i=1}^{3} \zeta_i^2 + \sum_{el=1}^{N_{el}} \frac{\rho A_{el}}{20} \sum_{i=1}^{3} (h+\zeta)_i (u_i^2 + v_i^2) \quad \text{(EQ 2.33)}$$

Kajiura (1981) developed a relationship between the seismic energy released during the earthquake E_s and the total tsunami energy E_t:

$$\log\left(\frac{E_t}{E_s}\right) = 0.5M_w - 7.26 \quad \text{(EQ 2.34)}$$

Since the information which is generally available is in the form of M_0, then we can compute M_w as:

$$M_w = \frac{2\,(\log M_0 - 16.1)}{3} \quad \text{(EQ 2.35)}$$

E_s may also be computed based upon M_0 as:

$$E_s = (5x10^{-5})\,M_0 \quad \text{(EQ 2.36)}$$

Therefore, the tsunami energy should be approximately equal to:

$$E_t = 10^{(0.5M_w - 7.26)} E_S \quad \text{(EQ 2.37)}$$

using EQ 2.35 and EQ 2.36 to substitute for M_w and E_s, respectively. The equation for the total tsunami energy E_t shown in EQ 2.33, however, fails to recognize an important energy loss term. The wave energy will be dissipated by friction in the system. To take into account this loss, Tolman [1992] suggested using the following expression which represents the energy loss per unit time and per unit bed area,

$$E_L = \langle \vec{\tau} \cdot \vec{v} \rangle \qquad \text{(EQ 2.38)}$$

$$\vec{\tau} = \frac{1}{2} \rho c_f \vec{v} |\vec{v}| \qquad \text{(EQ 2.39)}$$

Therefore, these relations may be checked in the finite element model using the following relation:

$$E_f = \rho \Delta t \sum_{i=1}^{N_{elem}} A_{el} c_f (u_i^3 + v_i^3) \qquad \text{(EQ 2.40)}$$

To check the validity of these energy relations, a one-dimensional test is utilized for which an analytical solution exists. The results from the analytical solution may be extended to two dimensions which will allow comparison with numerical results from ADCIRC-2DDI. The test case considered is a solitary wave traveling in a frictionless channel 100 meters long. It is the same case considered by Antunes do Carmo et. al. [1993]. The analytical solution is provided as follows:

$$h(x,t) = H + A \operatorname{sech}^2 \{ \sqrt{(\frac{3A}{4H^3})} \, (x - \sqrt{g(H+A)}\, t - x_0) \} \qquad \text{(EQ 2.41)}$$

where $h(x, t)$ is the depth plus the wave elevation, H is the water depth, x_0 is the initial position of the solitary wave, A is the amplitude of the solitary wave, and g is the acceleration due to gravity. The comparison of energy levels between the analytical solution and the numerical solution are displayed in Figures 2.4-2.5. These figures show that energy is

fairly well conserved (although it does not match exactly the analytical energy) for this channel case either with constant bathymetry or varying bathymetry.

References

Antunes do Carmo, J.S., Santos, F.J., and Barthelemy, E., Surface Waves Propagation in Shallow Water: A Finite Element Model, *International Journal for Numerical Methods in Fluids*, 16, pp. 447-459, 1993.

Geller, R.J., Scaling Relations for Earthquake Source Parameters and Magnitudes, *Bulletin of the Seismological society of America*, 66(5), pp. 1501-1523, 1976.

Hyndman, R.D. and Wang, K., Thermal Constraints on the Zone of Major Thrust Earthquake Failure: The Cascadia Subduction Zone, *Journal of Geophysical Research*, 98(B2), pp. 2039-2060, 1993.

Kajiura, K., Tsunami Energy in Relation to Parameters of the Earthquake Fault Model, *Bulletin of the Earthquake Research Institute*, 56, pp. 415-440, 1981.

Kolar, R.L., Westerink, J.J., Cantekin, M.E., Blain, C.A., Aspects of Nonlinear Simulations Using Shallow Water Models Based on the Wave Continuity Equation, *Computers and Fluids*, 23(3), p. 523, 1993.

Luettich, R.A., Westerink, J.J., and Scheffner, N.W., *ADCIRC: An Advanced Three-Dimensional Circulation Model for Shelves, Coasts, and Estuaries*, Dept. of the Army, U.S. Army Corps of Engineers, Washington, D.C., 1991.

Lynch, D.R. and Gray, W.G., A Wave Equation Model for Finite Element Tidal Computations, *Computers and Fluids*, 7(3), pp. 207-228, 1979.

Madin, I., Seismic Hazards on the Oregon Coast, *Coastal Natural Hazards*, Oregon Sea Grant ORESU-B-92-001, pp. 3-27, 1992.

Mansinha, L. and Smylie, D. E., The Displacement Fields of Inclined Faults, *Bulletin of the Seismological Society of America*, 61(5), pp. 1433-1440, 1971.

Okada, Y., Surface Deformation due to Shear and Tensile Faults in a Half-Space, *Bulletin of the Seismological Society of America*, 75(4), pp. 1135-1154, 1985.

Tolman, H.L., An Evaluation of expressions for wave energy dissipation due to bottom friction in the presence of currents, *Coastal Engineering*, 16, pp. 165-179, 1992.

Westerink, J.J., Luettich, R.A., Baptista, A.M., Scheffner, N.W., and Farrar, P., Tide and Storm Surge Predictions Using Finite Element Model, *Journal of Hydraulic Engineering*, 118(10), pp. 1373-1390, 1992.

FIGURE 2.1 Definition of Seismic Parameters

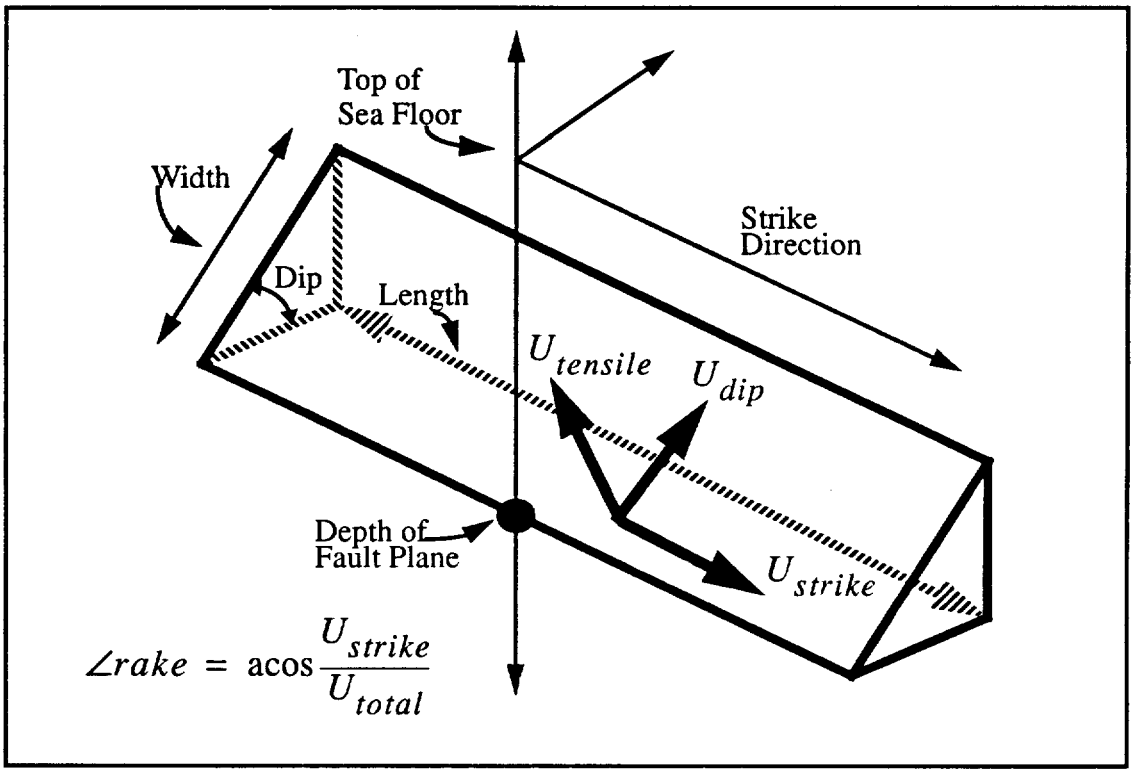

FIGURE 2.2 Depths Among Various Earthquakes (Madin, 1992)

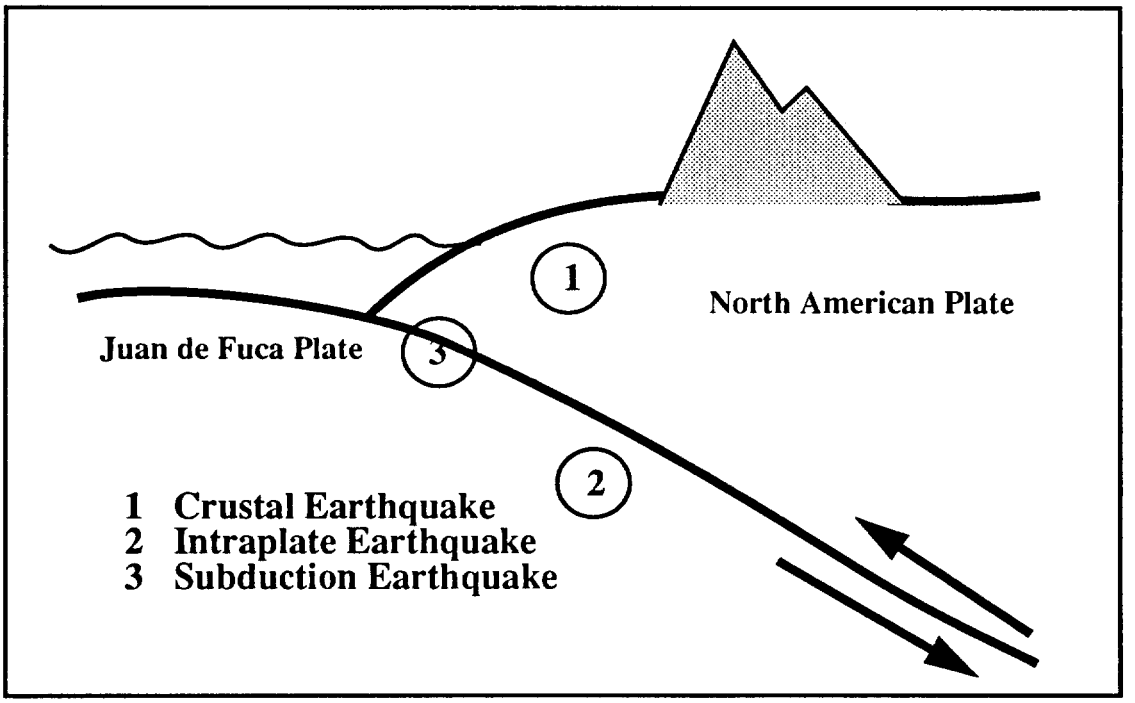

TABLE 2.1 Parameters for the July 12 1993 Hokkaido Nansei-oki Earthquake

Solution	$M_0(*10^{27})$	Depth(km)	Strike	Dip	Rake	Slip(m)
Harvard	5.7	15	1°	24°	84°	3.7
University of Tokyo	4.2	10	9°	35°	97°	2.8
DCRC-1	2.3 (N)	10	10°	60°	85°	3.8
Tohoku	3.4 (S)	5	320°	30°	120°	5.6
DCRC-2	2.3 (N)	10	190°	30°	80°	3.8
Tohoku	3.4 (S)	5	140°	60°	105°	5.6
JMA	6.3	37	3°	41°	72°	4.2
Hokkaido U.	6.3	30	12°	49°	102°	4.2
USGS	0.93	18	1°	60°	67°	0.6

TABLE 2.2 Areas, Lengths, and Widths as Computed Using EQ 2.3

Solution	Area (km^2)	Length(km)	Width(km)
Harvard	3851.35	87.77	43.88
University of Tokyo	3750.00	86.60	43.30
DCRC-1	1513.16	55.01	27.51
Tohoku	1517.86	55.10	27.55
DCRC-2	1513.16	55.01	27.51
Tohoku	1517.86	55.10	27.55
JMA	3750.00	86.60	43.30
Hokkaido U.	3750.00	86.60	43.30
USGS	3875.00	88.03	44.02

FIGURE 2.3 Method of Backtracking to Point of Interpolation

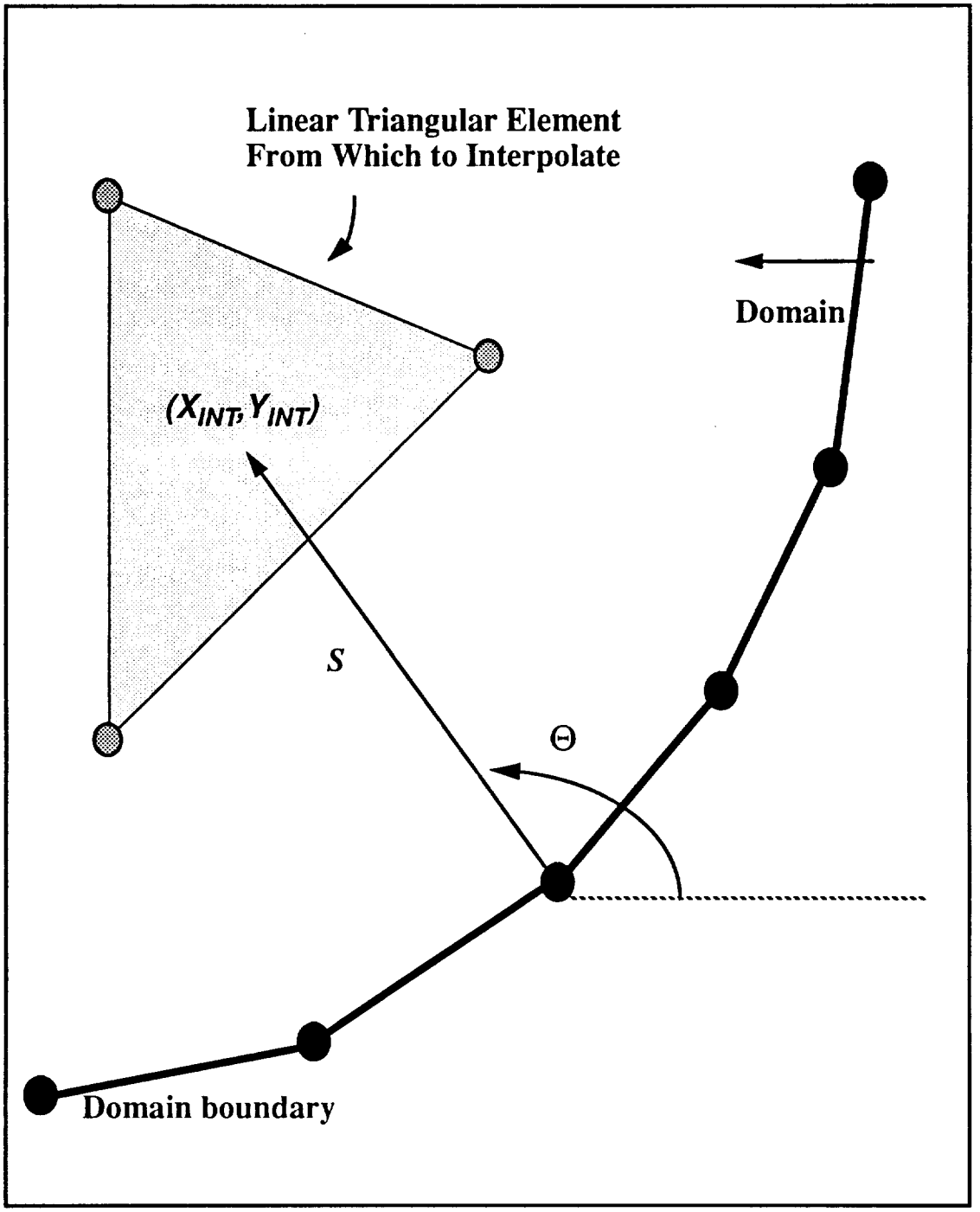

FIGURE 2.4 Conservation of Energy for Channel with Constant Bathymetry

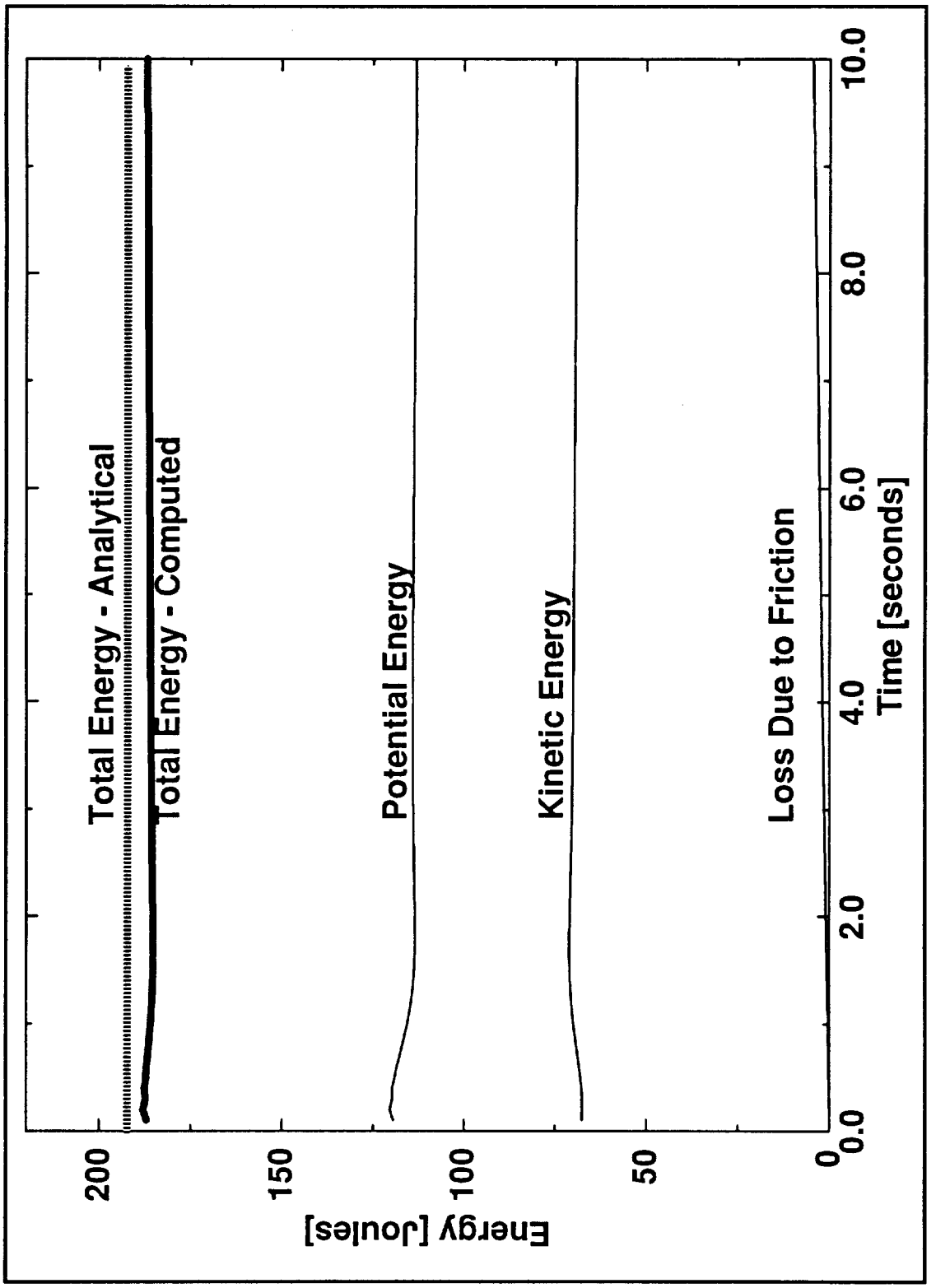

FIGURE 2.5 Conservation of Energy for Channel with Variable Bathymetry

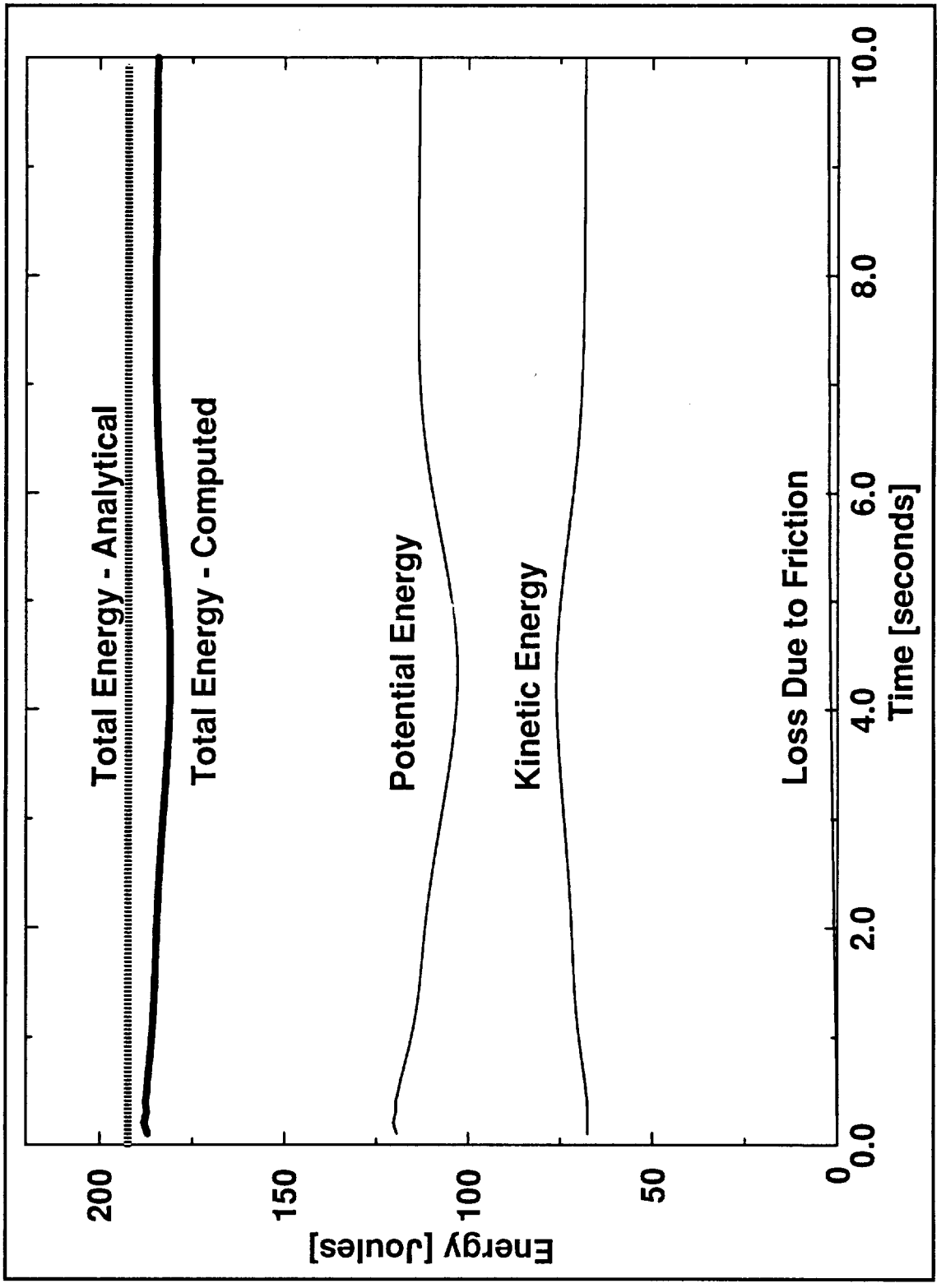

CHAPTER 3

Modeling the July 12, 1993 Hokkaido Nansei-oki Tsunami

Seismic Source Scenarios

The seven seismic source scenarios mentioned in Chapter 2 for the July 12, 1993 event were used independently to generate the initial conditions for numerical simulations with ADCIRC-2DDI. In this chapter four additional seismic sources [*Satake*, 1994] will be considered which have the characteristics shown in Table 3.1.

TABLE 3.1 Additional Seismic Sources Considered for Chapter 3

Scenario	Length (km)	Width (km)	Strike	Dip	Rake	Depth (km)	Slip (m)
EE	80.0 70.0	40.0 40.0	-20.0 20.0	30.0 60.0	90.0 90.0	0.0 0.0	3.0 3.0
EW	80.0 70.0	40.0 40.0	160.0 20.0	60.0 60.0	90.0 90.0	0.0 0.0	3.0 3.0
WW	80.0 70.0	40.0 40.0	160.0 200.0	60.0 30.0	90.0 90.0	0.0 0.0	3.0 3.0
WE	80.0 70.0	40.0 40.0	-20.0 200.0	30.0 30.0	90.0 90.0	0.0 0.0	3.0 3.0

Each scenario shown in the above Table consists of two seismic sources. Figures 3.1-3.11 show the sea floor deformations associated with each of the eleven source scenarios. Geodetic data gathered from this event appear to indicate that the majority of the island of Okushiri experienced subsidence. The northern tip of the island, however, seems to have been uplifted. The computed deformations were not able to reproduce the uplift on the northern tip of Okushiri. Comparisons between geodetic data and deformations as com-

puted with a fault plane model are shown in Figure 3.12. Most of the two-source scenarios show the entire island of Okushiri subsiding significantly, whereas the one-source scenarios show the island subsiding little, if any. The location of all sources was determined based upon available aftershock data.

Calibration

The first step in calibrating the numerical models for the Sea of Japan system is to ensure that the simulations conserve mass and remain numerically stable. The primary parameter which will influence these qualities is the generalized wave continuity equation (GWCE) weighting factor. In general, too small a value of the weighting factor will lead to mass balance errors, while too large a value will lead to numerical instability. Therefore, the model needs to be calibrated in such a way that neither too large nor too small a GWCE weighting factor is selected. To perform this calibration, the EE seismic source scenario shown in Table 3.1 was selected as a characteristic event to use as initial conditions for the numerical model. Various values of the GWCE weighting factor were then utilized in simulations for this initial condition. The grid used in all of the numerical simulations is displayed in Figures 3.13 and 3.14. As may be seen, smaller triangular elements are used in regions where the bathymetry is shallower and elevation gradients are larger. Smaller elements were also used in the region of the seismic sources in order to achieve better resolution of the initial conditions. The grid was generated using ACE/gredit, a flexible interactive grid generation tool developed by Turner and Baptista [1991]. Bathymetry used in the grid includes the ETOPO-5 database, local bathymetry around Okushiri, and 1' x 1' bathymetry for the Sea of Japan [*Okada*, 1994].

Figures 3.15 through 3.19 show the mass variation which resulted from the use of the different values of the GWCE weighting factor. The mass variation has units of volume, and the figures scale this error by the initial volume of deformation to the sea floor. It can be seen in the figures that the results from the use of lower values of the weighting factor have difficulties in conserving mass, and that those results from the use of larger values

show difficulties with numerical instability. In the middle of the spectrum of values considered, it was decided that a value of 0.3 did the best at conserving mass while remaining stable. Therefore, for all remaining simulations considered in this chapter, the value of 0.3 is used.

For the July 12, 1993 event, information from tidal gauges is available on the islands of Hokkaido and Honshu [*Satake*, 1994]. The locations of these stations is shown in Figure 3.20. The elevation time histories provided at these gauges were provided in a filtered form so as to remove the effects from tides. Using information from these tidal gauges, the model was then calibrated for the amount of friction introduced to the system. Manning coefficients of 0.0250, 0.0275, 0.0300, 0.0325 were tested as to their effect on the waveforms at the tidal gauge stations. Root mean square errors were used to evaluate the differences between the numerically generated waveforms and the observed waveforms at the tidal gauges. These errors are of the form

$$\left[\frac{1}{N} \sum_{k=1}^{N} \{ (\eta_k - \tilde{\eta}_k) - \frac{1}{N} \sum_{p=1}^{N} (\eta_p - \tilde{\eta}_p) \} \right]^{2}^{1/2} \qquad \text{(EQ 3.1)}$$

where η is the observed surface elevation, $\tilde{\eta}$ is the computed surface elevation from numerical simulations, and N is the number of equally spaced sampling points. The results from this analysis for individual stations are displayed in Figure 3.21. These results show that changing the Manning coefficient does not alter the errors between the numerically generated and true waveforms much. It should be noted that stations such as Esashi and Iwanai are located closer to the seismic sources and therefore recorded larger amplitude waves. Thus the errors for these two stations shown in Figure 3.21 are also a bit larger than those at other stations. Figure 3.22 shows the average of these root mean square errors for all of the stations. Although the error does not change much for different values of the Manning coefficient (less than 1 cm), the coefficient of 0.0275 was selected for the remainder of numerical simulations in this chapter since it did have the lowest

average root mean square error and appeared to reduce the error best for the near-source station Iwanai.

Another parameter which may be used to calibrate the numerical model is the amount of diffusion introduced into the system. Diffusion coefficients of 0.0, 1.0, 2.0, 3.0, 4.0, 5.0, and 10.0 m^2/sec were used in this calibration. The root mean square expression in EQ3.1 was again employed for these tests. Figure 3.23 shows the root mean square averaged over all of the tidal gauge stations. The simulation for 2.0 m^2/sec became unstable and therefore is not displayed. As may be seen, though, the error differences among different coefficients is small. Figures 3.24 and 3.25 reveal some more information about the use of various diffusion coefficients. These figures show the mass errors from the simulations for the diffusion calibration. They show that use of coefficients equal to 1.0, 2.0, 3.0, and 4.0 m^2/sec lead to mass balance errors, while coefficients of 0.0, 5.0, and 10.0 m^2/sec conserved mass fairly well. In order to avoid mass errors as well as the introduction of too much diffusion into the simulations, a coefficient of 0.0 m^2/sec was selected for the remainder of the simulations.

Unfortunately, not having inundation in the numerical model means not being able to use run-up measurements for verifying results or for calibration. Inundation will have a high dependence on local geometry and topography. For example, the highest run-up measurement for this event was on the order of 30 meters. However, this measurement was made in a narrow valley where local geometry could focus the tsunami energy.

Numerical Results

In order to look at possible propagation patterns due to the effect of bathymetry, raytracing was applied to the Sea of Japan. The following formulas were used to perform the raytracing [*Satake*, 1988]:

$$\frac{d\theta}{dt} = \frac{1}{nR}\cos\zeta \qquad \text{(EQ 3.2)}$$

$$\frac{d\phi}{dt} = \frac{1}{nR\sin\theta}\sin\zeta \qquad \text{(EQ 3.3)}$$

$$\frac{d\zeta}{dt} = -\frac{\sin\zeta}{n^2R}\frac{\partial n}{\partial\theta} + \frac{\cos\zeta}{n^2R\sin\theta}\frac{\partial n}{\partial\phi} - \frac{1}{nR}\sin\zeta\cot\theta \qquad \text{(EQ 3.4)}$$

EQ 3.2-3.4 are not valid near caustics, where the wavelength of a wave becomes so small that geometrical approximations of the wave theory are more appropriate. These formulas may be applied to single points located near the earthquake sources. Figure 3.26 shows the results from this analysis by looking at the propagation of the collection of rays radiating from two point sources placed approximately near the centers of the two seismic sources. The rays in the deeper regions of water are seen to travel much faster than those in shallower regions. In the deep ocean, the two seismic sources lead to two waves traveling with a small time lag. Honshu and southern Hokkaido appear to be first impacted by the wave generated from the southern source, while northern Hokkaido is first affected by the northern source.

Using the optimal values for the GWCE weighting factor, Manning coefficient, and diffusion coefficient mentioned in the previous section, numerical simulations were made for each of the eleven seismic source scenarios. The conservation of mass and energy for these simulations are displayed in Figures 3.27 through 3.37. The mass error appears to be sufficiently small through approximately 40 or 50 minutes for all cases. At this time, conservation of mass problems arise for the remainder of the simulations. Possible reasons for mass errors involve interaction of the waves with the boundaries and departure of mass through the transmissive boundaries. For the Sea of Japan, the waves are not likely to interact with transmissive boundaries until at least half an hour into the simulation.

Energy conservation appears to be a problem in all of the simulations. The initial energy achieved over the time steps of deformation appears to be just less than the theoretical energy of the tsunami. Using the theoretical relation between seismic energy and tsunami energy mentioned in Chapter 2, the theoretical tsunami energy is compared with the

numerically computed initial energy in Table 3.2. Only the numerical simulations for Hokkaido University and JMA overestimate the energy as derived theoretically. As soon as the energy reaches a peak at the end of the deformation in each case, it proceeds to decrease at a rapid pace. This sharp decrease in energy evolves into a gradual decrease over the remainder of all simulations. The reasons for the variation in energy are discussed in detail in Chapter 5. As will be mentioned, the sharp energy decline in the first few minutes is hypothesized to be a result of the inability of the shallow water equations to conserve energy since they neglect pressure gradients associated with vertical accelerations. As the waves interact with the land boundaries, energy would be lost for the same reason. Some energy will also be lost as the waves travel through the transmissive boundaries.

TABLE 3.2 Comparison of Theoretical and Computed Tsunami Energy

Scenario	Theoretical Energy [Joules]	Computed Initial Energy [Joules]
EE	1.119 e+13	0.957 e+13
EW	1.119 e+13	1.174 e+13
WE	1.119 e+13	0.764 e+13
WW	1.119 e+13	0.998 e+13
DCRC-1	1.203 e+13	0.874 e+13
DCRC-2	1.203 e+13	1.165 e+13
HARVARD	1.203 e+13	0.614 e+13
HOKKAIDO U.	6.379 e+11	1.275 e+13
JMA	6.379 e+11	0.977 e+13
USGS	1.072 e+12	0.258 e+12
UNIV. OF TOKYO	8.004 e+12	4.792 e+12

To examine the effects of the transmissive boundaries on both mass and energy variation, the WW scenario was simulated using a grid in which all of the boundaries were

land boundaries. Therefore, no transmissive condition is imposed at any of the boundaries. The results for this test are shown in Figure 3.38. As can be seen, mass is extremely well conserved when no transmissive boundaries are imposed. Therefore, the formulation of the transmissive boundary condition has mass conservation difficulties. One possible explanation is that the continuity equation is not obeyed when imposing either transmissive boundaries or amplitude/phase specified boundaries in the numerical model [Lynch, 1985]. For these boundary nodes, the elevation is simply specified as a certain value and the velocities are than solved for using the momentum equations. The difference between the two curves in the energy variation graph represents how much energy leaves the system as the wave departs through the transmissive boundaries.

In order to determine which source scenario appears to reproduce best the actual initial conditions, waveforms from three tidal gauges were compared with the actual observations at those stations. The tidal gauges selected for this purpose include two stations close to the seismic sources, Iwanai and Esashi, and another station located far away from the seismic sources, Awashima. These comparisons are shown in Figures 3.39 through 3.44. It should be noted that corrections for tidal gauge response to tsunamis are small at both Esashi and Iwanai [*Satake*, 1988]. Iwanai is likely to be affected first by the northern seismic source since it is located on the northern coast of Hokkaido. Therefore, the arrival time of the first wave at Iwanai should provide an indication of the correct orientation of the northern seismic source. Figures 3.39 and 3.40 show that the first waves resulting from the WE, WW, and DCRC2 sources arrive at the same time as the recorded waveform. Among these sources, the WE and WW do the best at reproducing the amplitude of the first wave. Since the nomenclature for the sources listed in Table 3.1 is [northern source][southern source], it is concluded that the northern seismic source is most likely a "W" orientation. Since Esashi is located further south on the island of Hokkaido and will first be impacted by the waves generated from the southern seismic source, Figures 3.41 and 3.42 may be used to determine the most likely orientation of the southern source. A close examination of these figures shows that EW and WW reproduce best the trough of the first incoming wave. The southern seismic source therefore most likely has a

"W" orientation. Figures 3.43 and 3.44 show that none of the scenarios reproduce well what is occurring at far-field stations such as Awashima. The reason for this is discussed further in the next paragraph. Based upon the above discussion, it appears that the WW scenario is the most likely source scenario from those considered.

All simulations were made using a minimum depth of five meters in order to avoid wetting and drying of elements. Representation of the coastal bathymetry may lead to coastal waveforms which have longer periods and smaller amplitudes, such as those in Figures 3.43 and 3.44. In order to check whether or not the coastal bathymetry was accurately depicted, additional simulations using the WW source were made in which (a) the grid was refined in coastal regions and (b) the minimum depth was lowered to three meters in those areas where the wave height was not expected to be greater than three meters. These results are displayed in Figures 3.45 through 3.47 for Iwanai, Esashi, and Awashima. It can be seen that the refinement and the change in minimum depth do not alter significantly the amplitudes of the tsunami waves. There are some additional oscillations which appear in the Iwanai waveform as a result of grid refinement. From these figures it can be concluded that the non-refined grid with a five meter minimum bathymetry is satisfactory, and that the dissipation of the computed waves at far-field stations is occurring for some other reason.

Figures 3.48 through 3.51 show comparisons between the waveforms generated by the WW source with the observed waveforms at 16 tidal gauges. All of the stations located far away from the seismic source appeared to dissipate the wave enough such that the amplitude was decreased and the wavelength was increased. This suggests that the model may not be representing correctly local dispersion or resonance effects. Computed amplitudes at near-field stations were the same order of magnitude as observed amplitudes, thus indicating that the fault plane model used to generate the initial conditions did a good job of representing the amount of sea floor deformation. Although amplitudes and arrival times of the tsunami at these near-field stations were reproduced satisfactorily, the wave periods were generally underestimated.

Propagation of energy throughout the domain can be seen in Figures 3.52 and 3.53. The darker shades in these figures correspond to higher energy values. Much of the energy is seen to dissipate once the waves have impacted land boundaries. This is particularly exemplified in Figure 3.53 which shows that as the larger values of energy (the darker regions) fade away, there is not a corresponding redistribution of the energy (i.e. to the lighter regions). Figure 3.54 shows the isolines of maximum energy throughout the entire simulation. Also displayed on this figure are run-up measurements made along the islands of Okushiri and Hokkaido. It can be seen that the larger run-up measurements correspond fairly well with the isolines of maximum energy. The island of Okushiri and the northwest coast of Hokkaido sustained the higher energy levels which is consistent with field survey reports as to where the larger run-up measurements were observed.

The computed maximum elevations along the Okushiri and Hokkaido coastlines are displayed in Figures 3.55 and 3.56. These figures show results from both a non-linear simulation and a linear simulation. Since the minimum depth can be lowered to zero for linear simulations, the maximum wave elevations are much larger than those generated by the non-linear simulation which requites a larger minimum depth to avoid instabilities. The distribution of computed maximum wave heights shows some similarities to the measured vertical run-ups shown in Figure 3.54.

References

Okada, M., Meteorological Research Institute, Japan.

Lynch, D.R., Mass Balance in Shallow Water Simulations, *Communications in Applied Numerical Methods*, 1, pp. 153-159, 1985.

Satake, K., Tide Gauge Response to tsunamis: Measurements at 40 Tide Gauge Stations in Japan, *Journal of Marine Research*, 46, pp. 557-571, 1988.

Satake, K., Effects of Bathymetry on Tsunami Propagation: Application of Ray Tracing to Tsunamis, *PAGEOPH*, 126, pp. 27-36, 1988.

Satake, K. *personal communication*, 1994.

Turner, P.J. and Baptista, A.M., ACE/Gredit Users Manual: Software for Semi-automatic Generation of Two-Dimensional Finite Element Grids, *CCALMR Software Report SDS2(91-2)*, Oregon Graduate Institute of Science & Technology, Portland, OR.

FIGURE 3.1 Bottom Deformation for EE Source

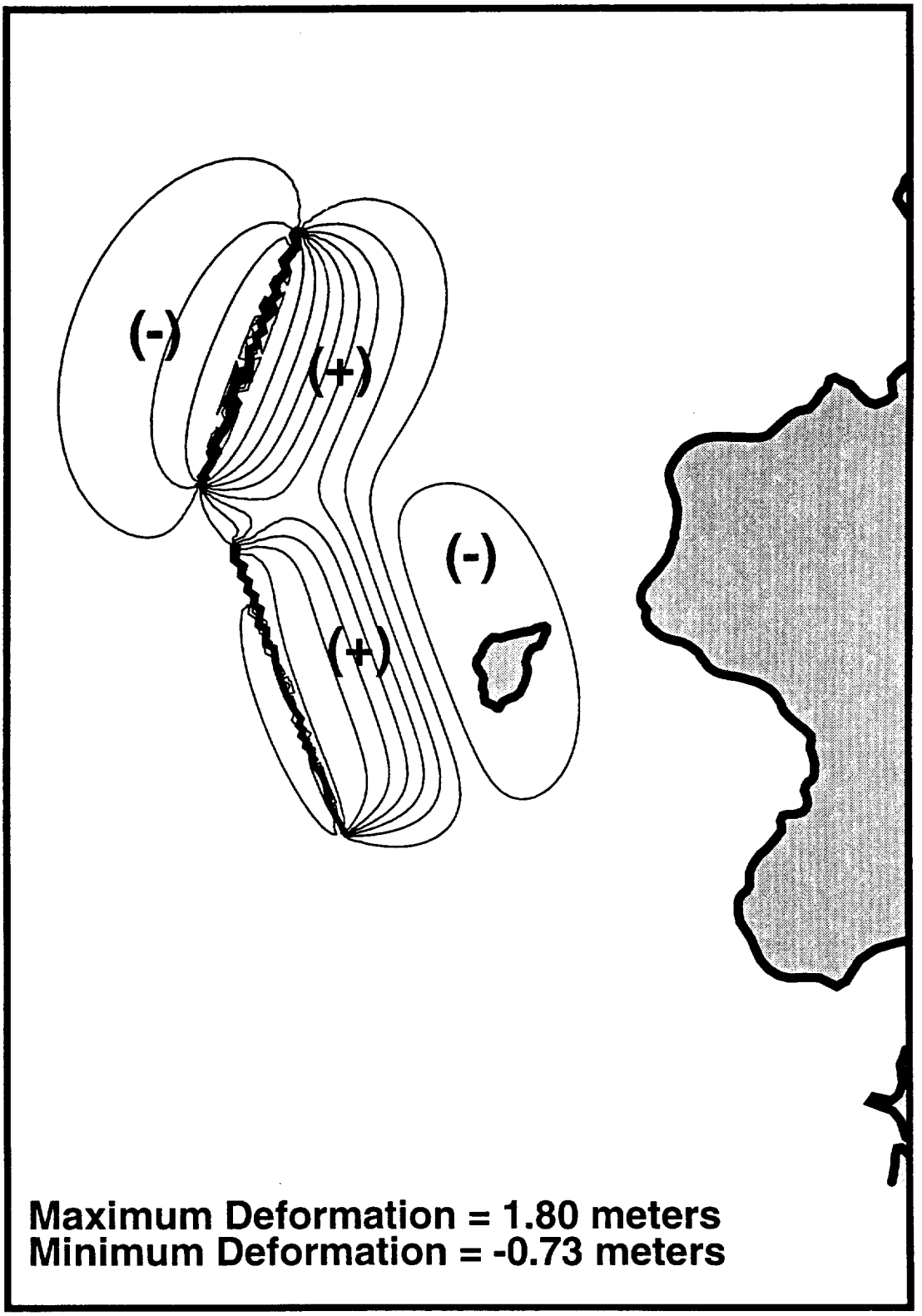

FIGURE 3.2 Bottom Deformation for WW Source

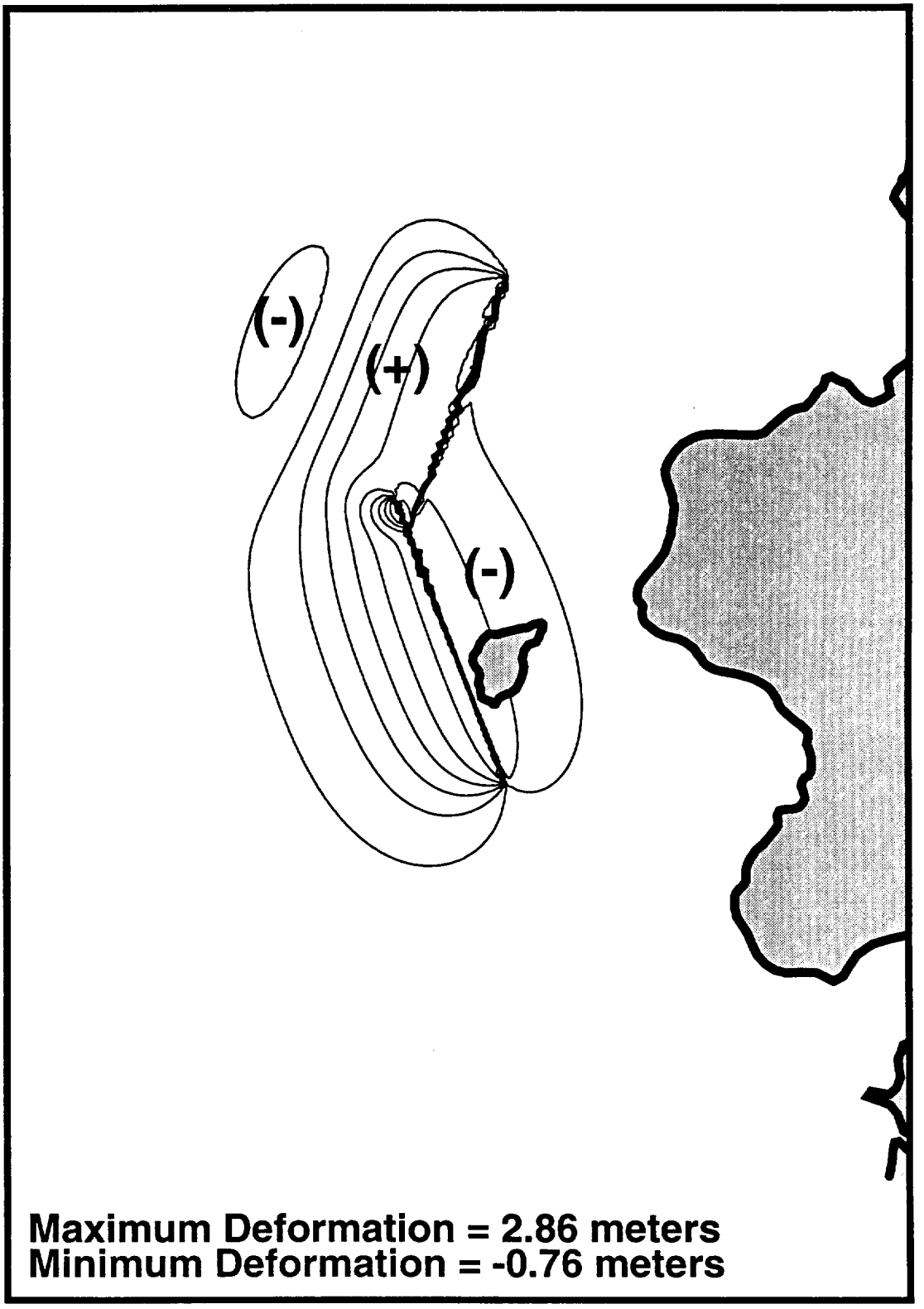

FIGURE 3.3 Bottom Deformation for EW Source

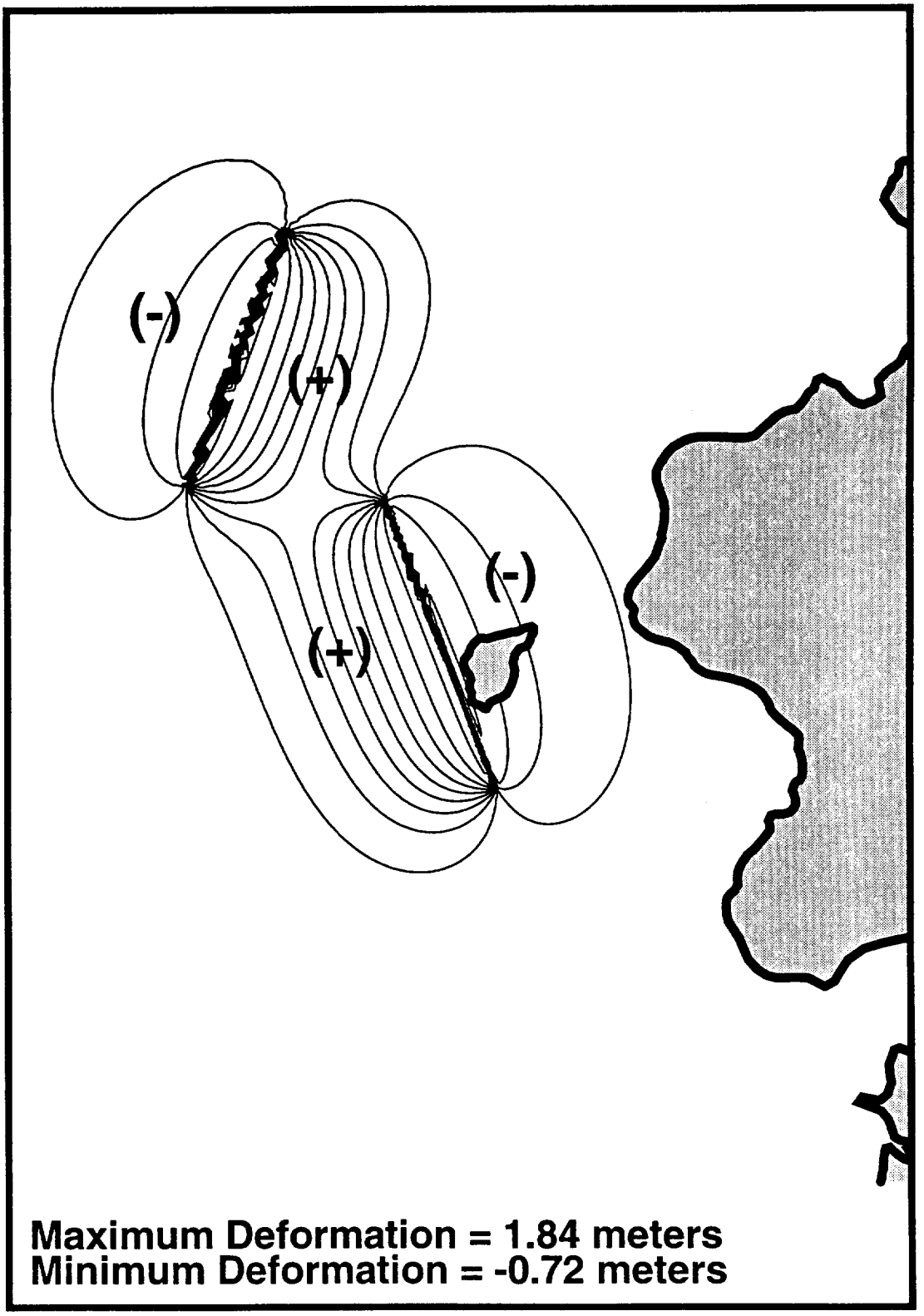

FIGURE 3.4 Bottom Deformation for WE Source

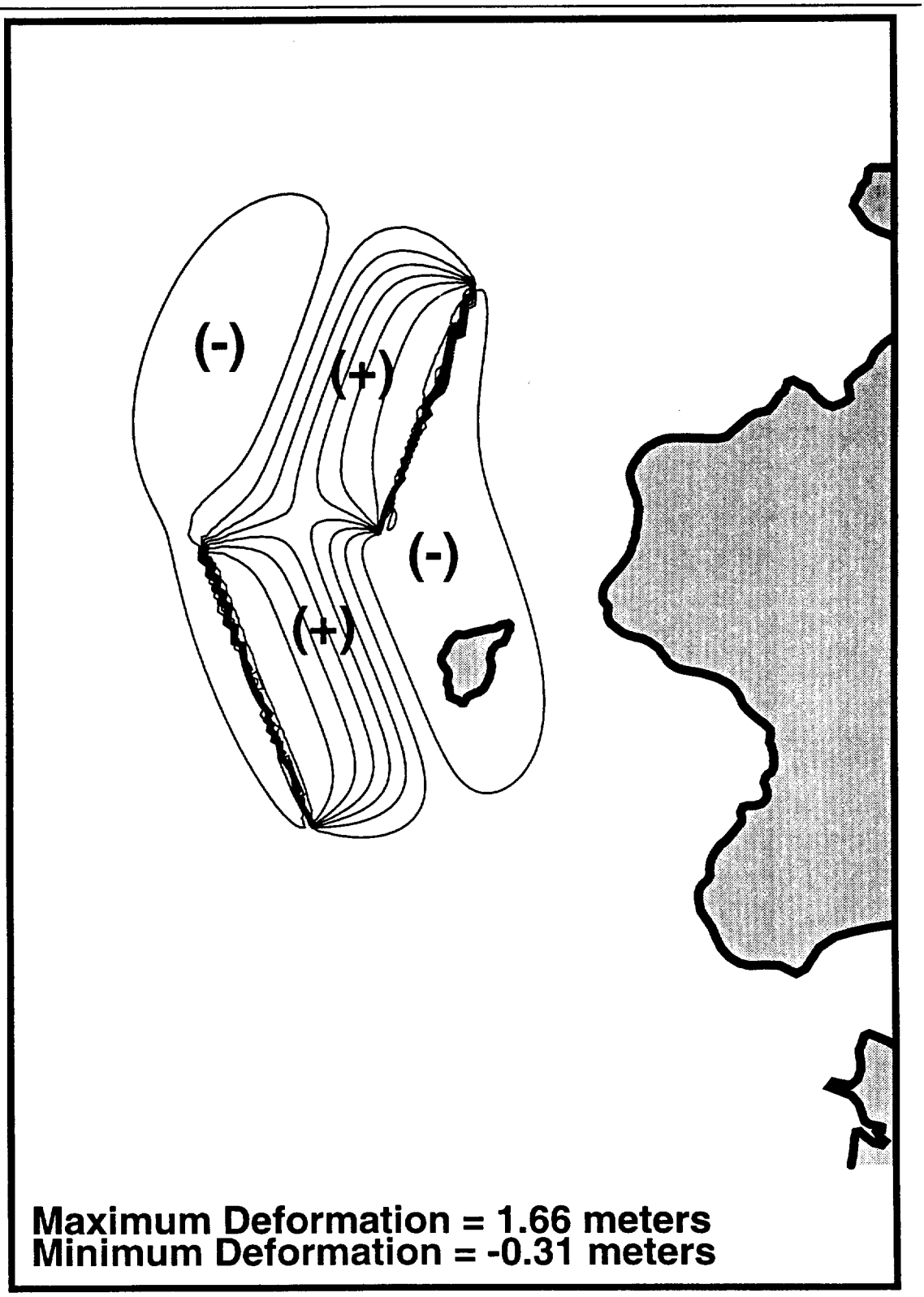

FIGURE 3.5 Bottom Deformation for DCRC-1 Source

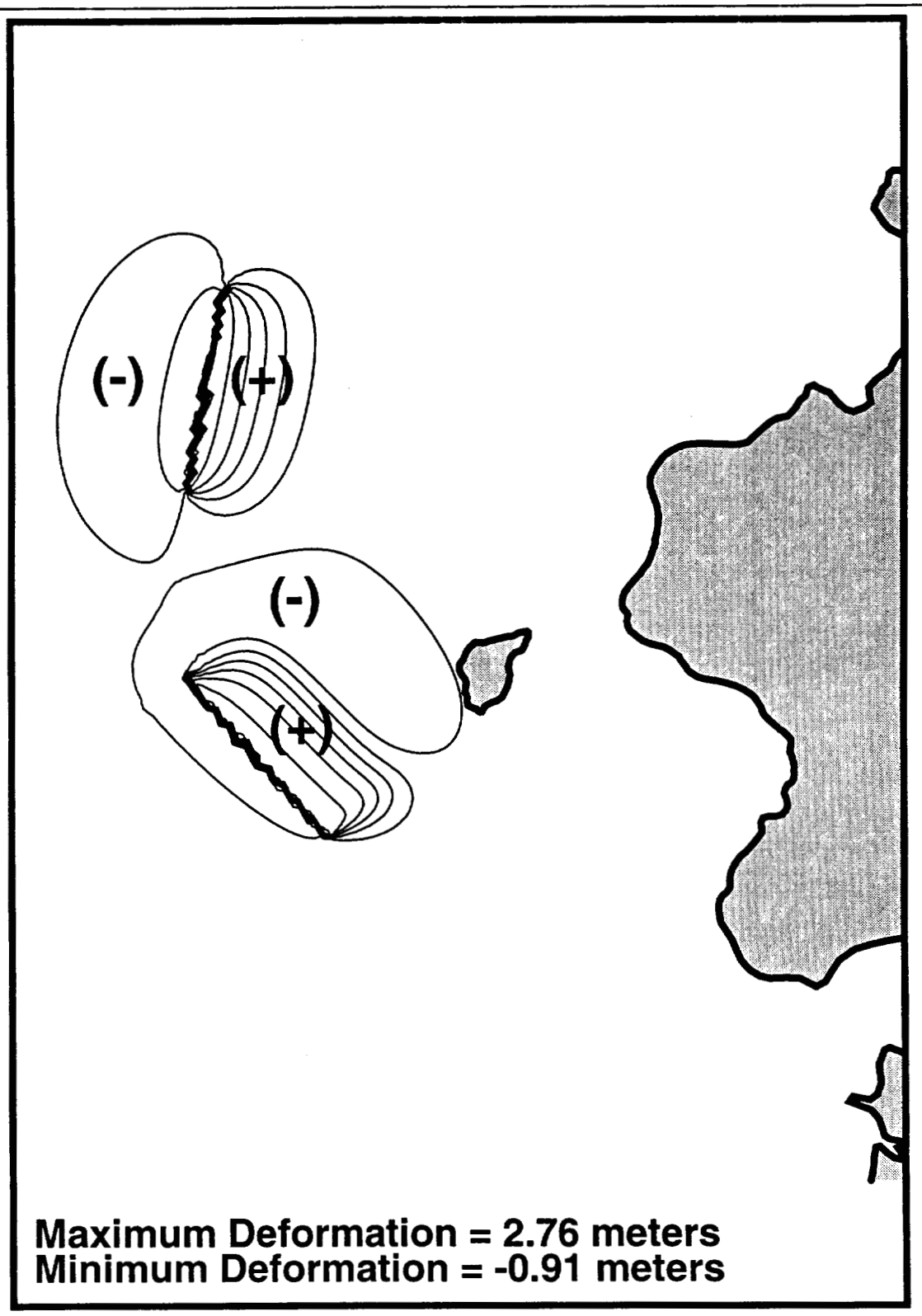

FIGURE 3.6 Bottom Deformation for DCRC-2 Source

FIGURE 3.7 Bottom Deformation for Harvard Source

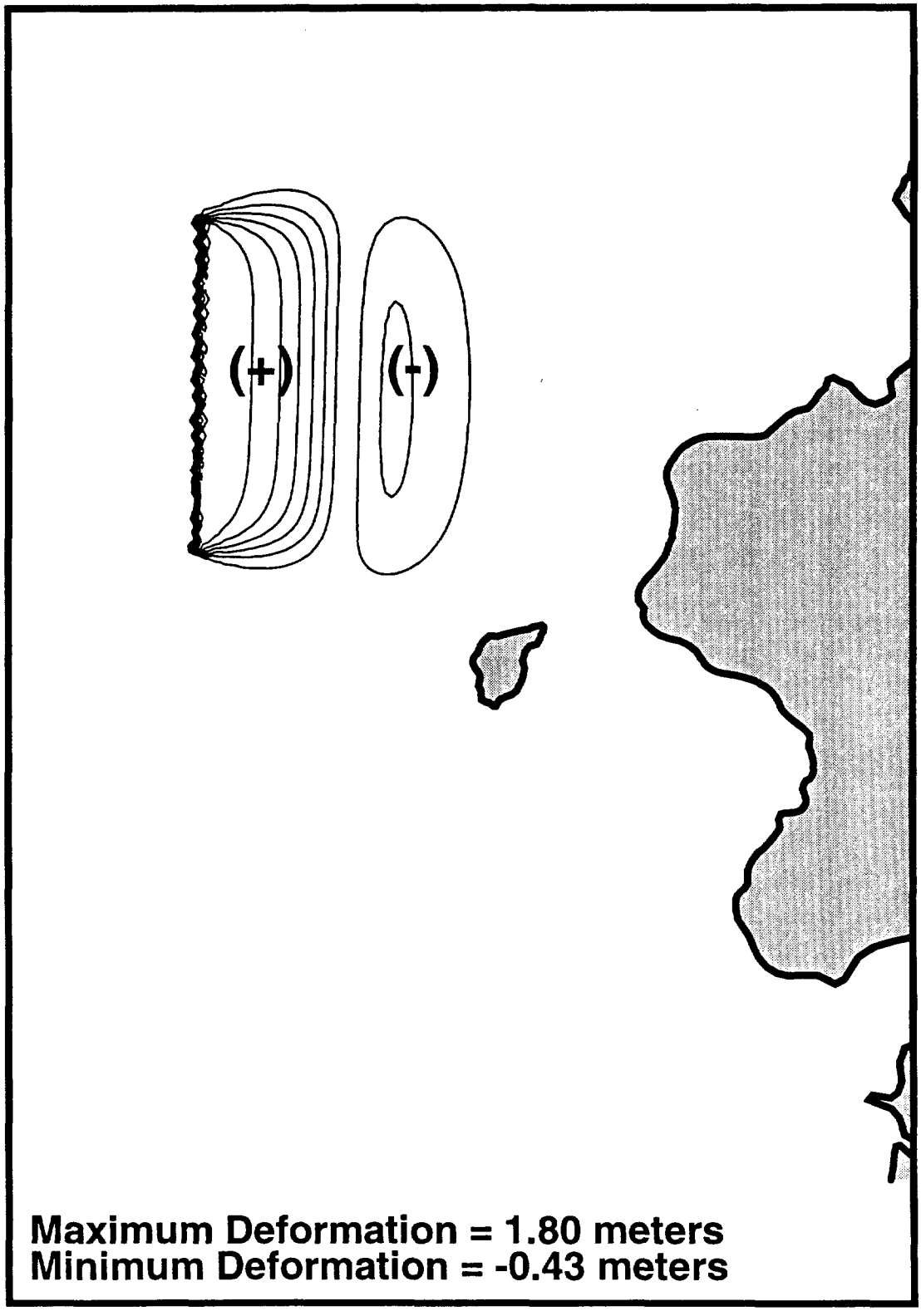

FIGURE 3.8 Bottom Deformation for Hokkaido University Source

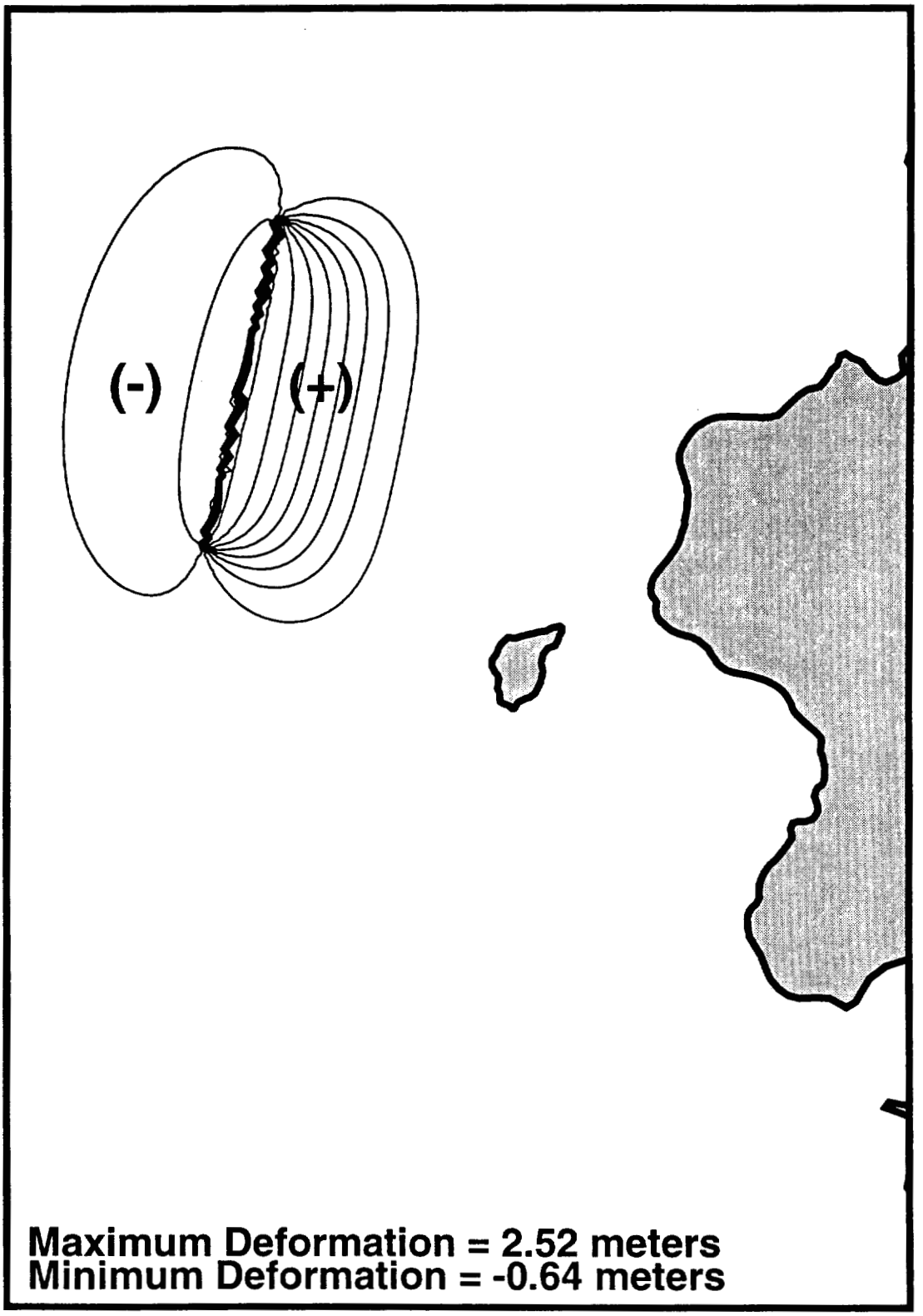

FIGURE 3.9 Bottom Deformation for JMA Source

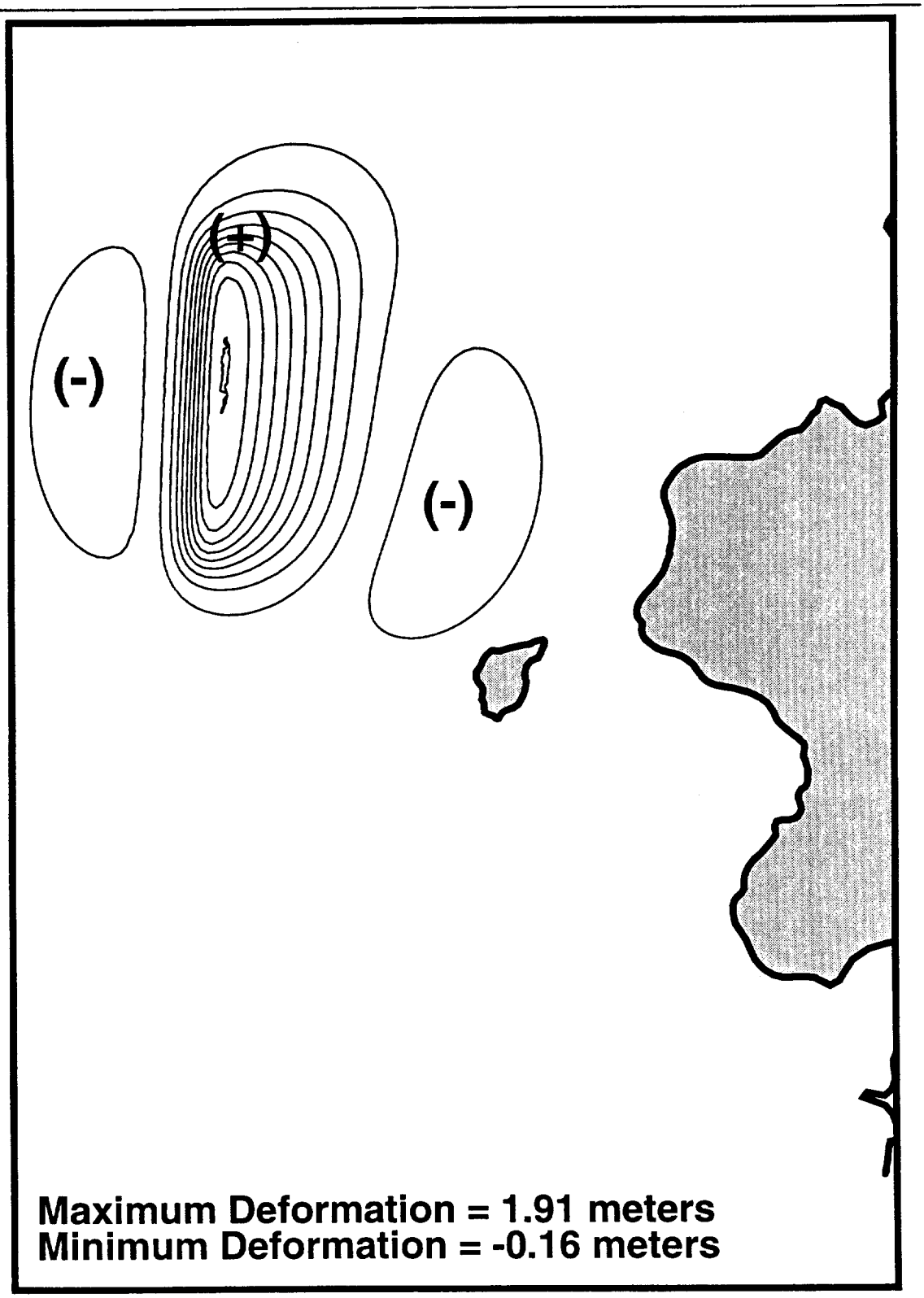

FIGURE 3.10 Bottom Deformation for USGS Source

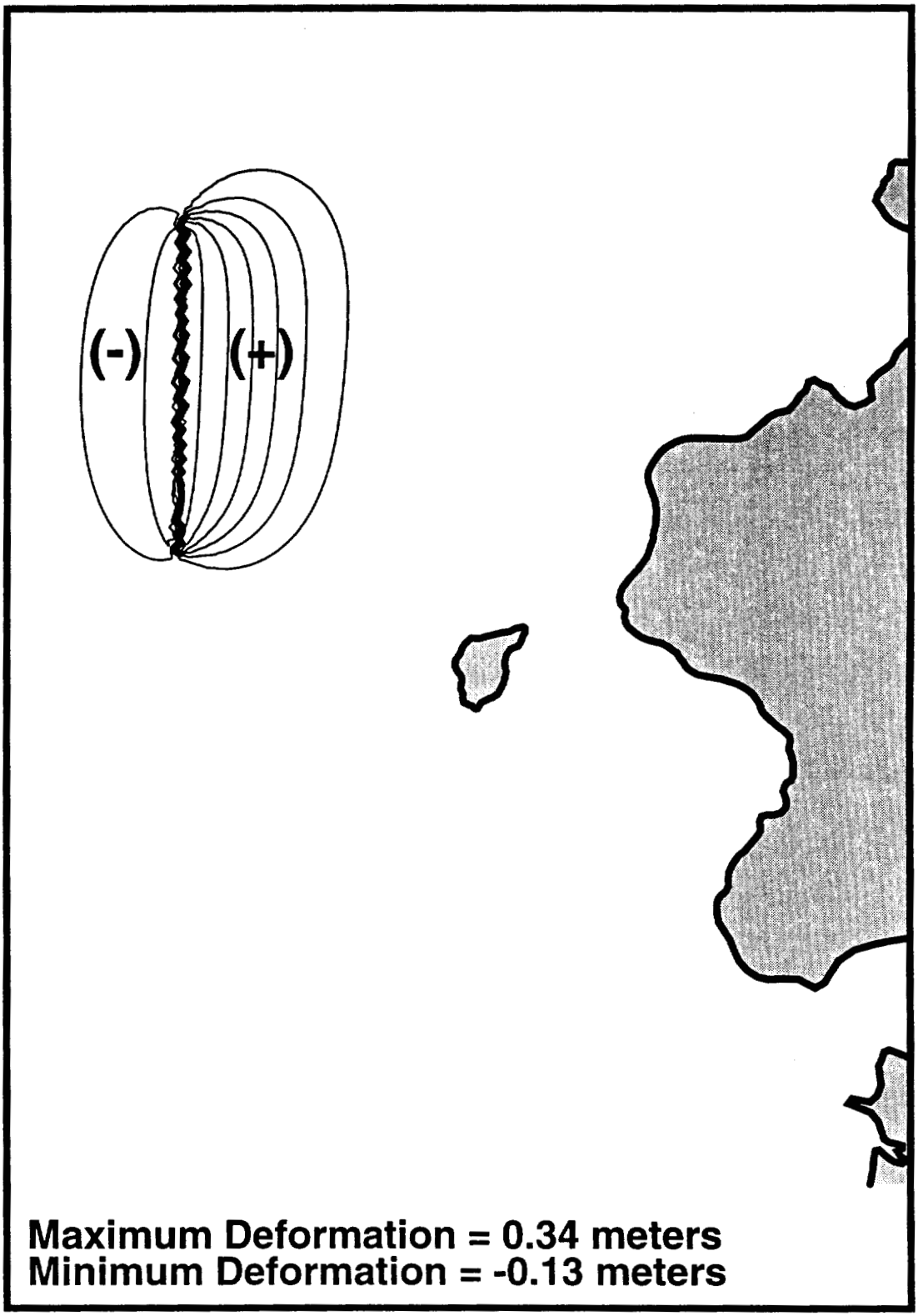

FIGURE 3.11 Bottom Deformation for University of Tokyo Source

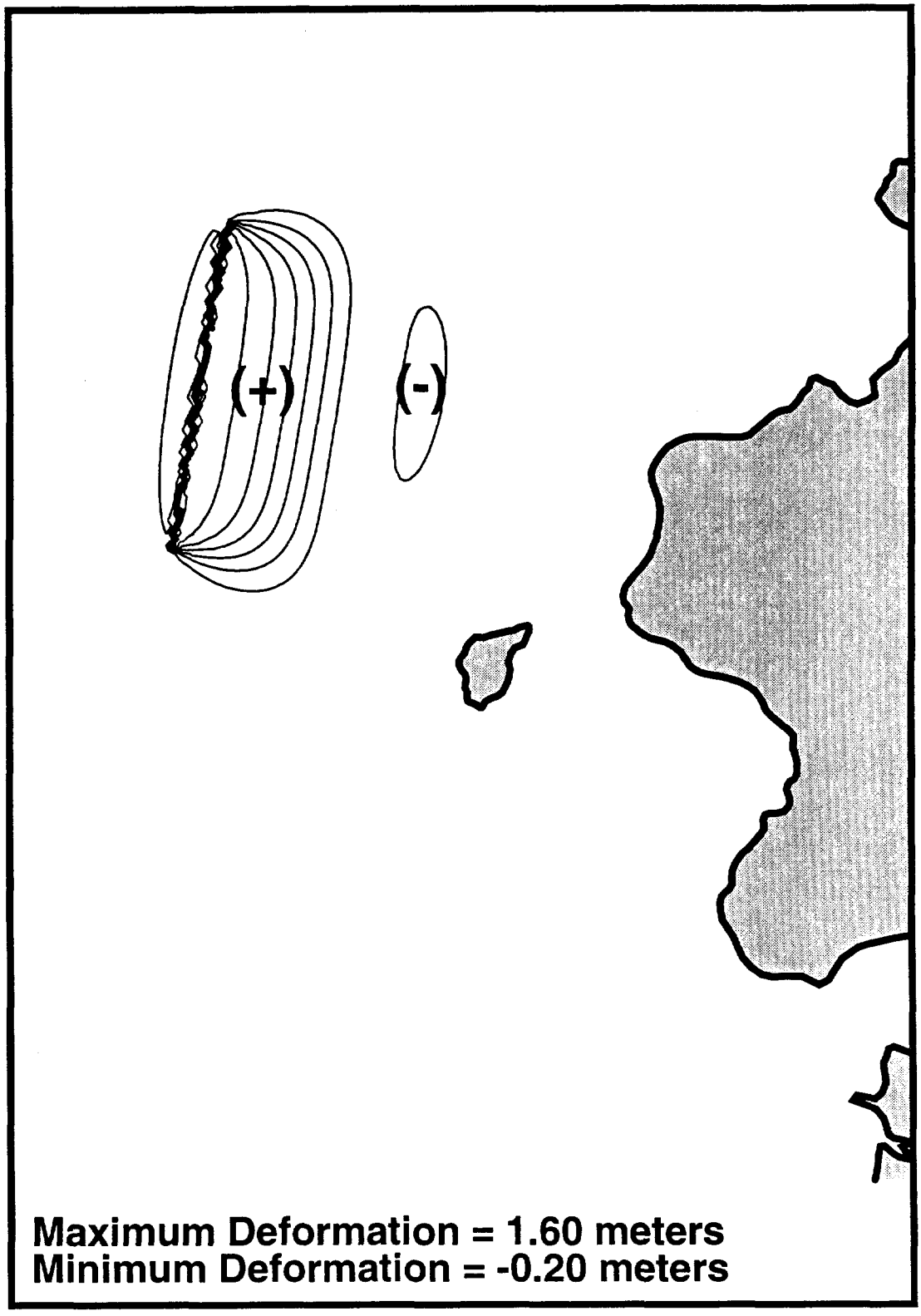

FIGURE 3.12 Subsidence/Uplift Measurements for Okushiri Island

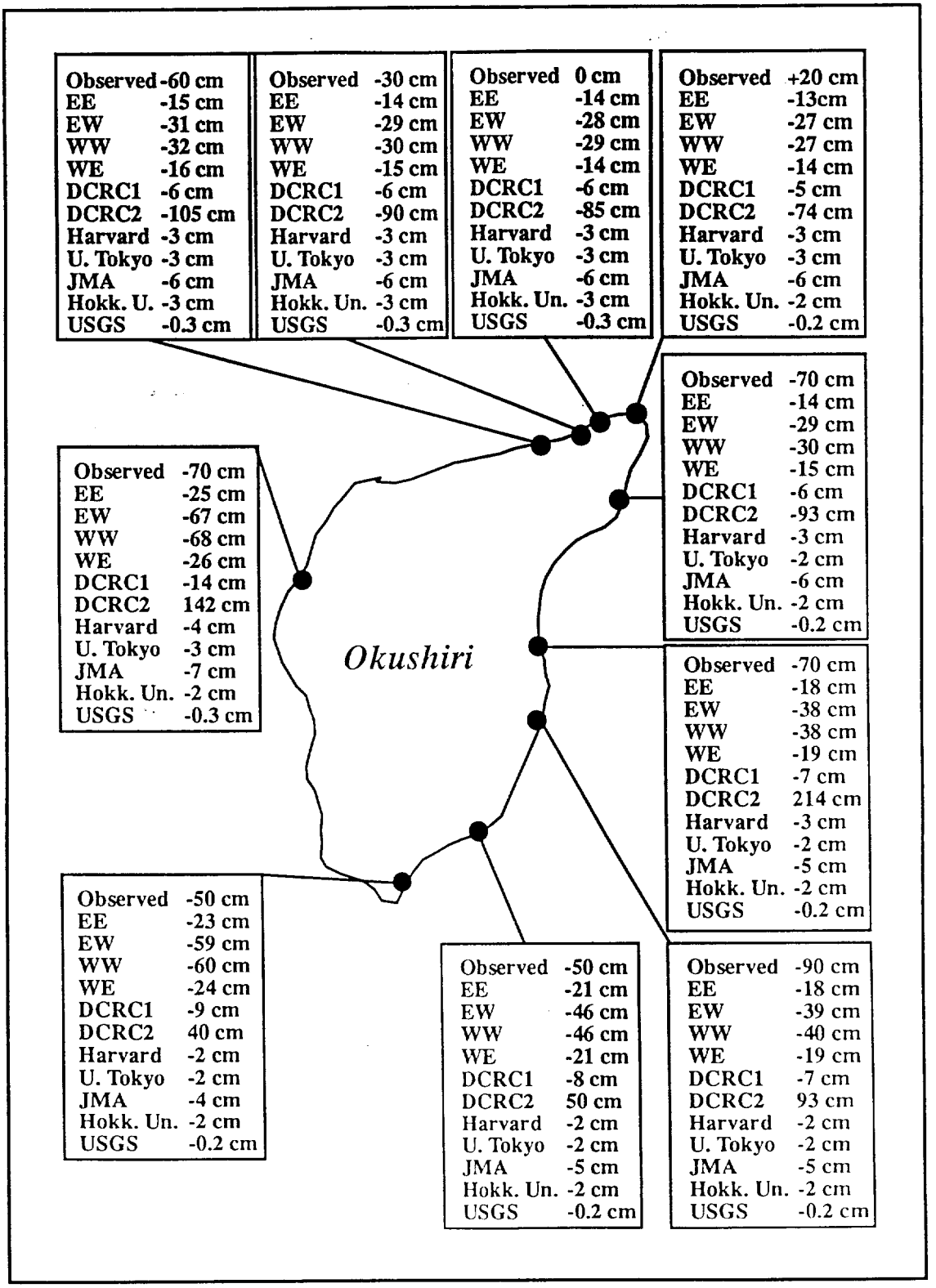

FIGURE 3.13 Finite Element Grid Used for Sea of Japan Simulations

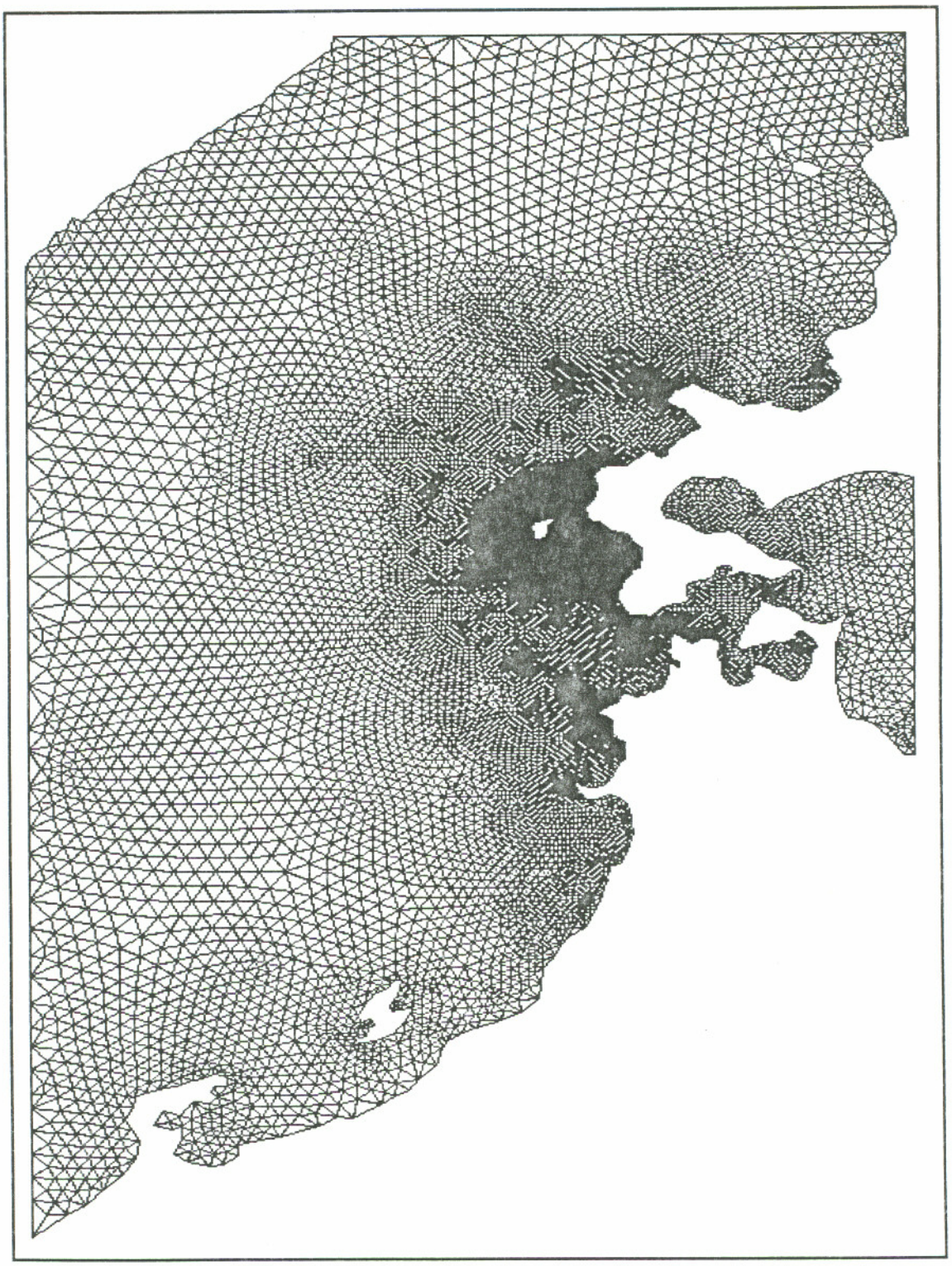

FIGURE 3.14 Close-up of Finite Element Grid Near the Island of Okushiri

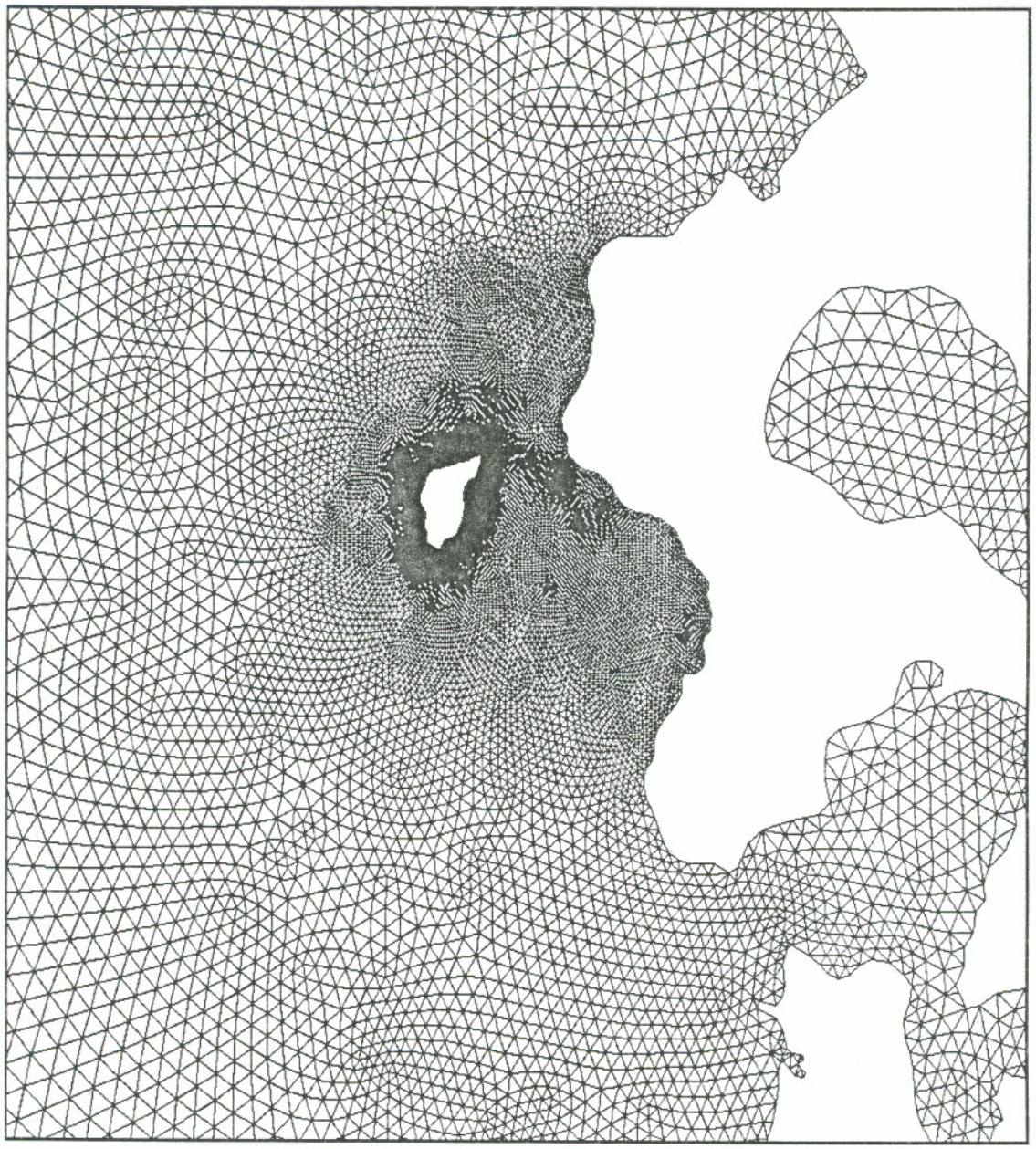

FIGURE 3.15 Mass (Scaled by Volume of Deformation) Conservation Over Time

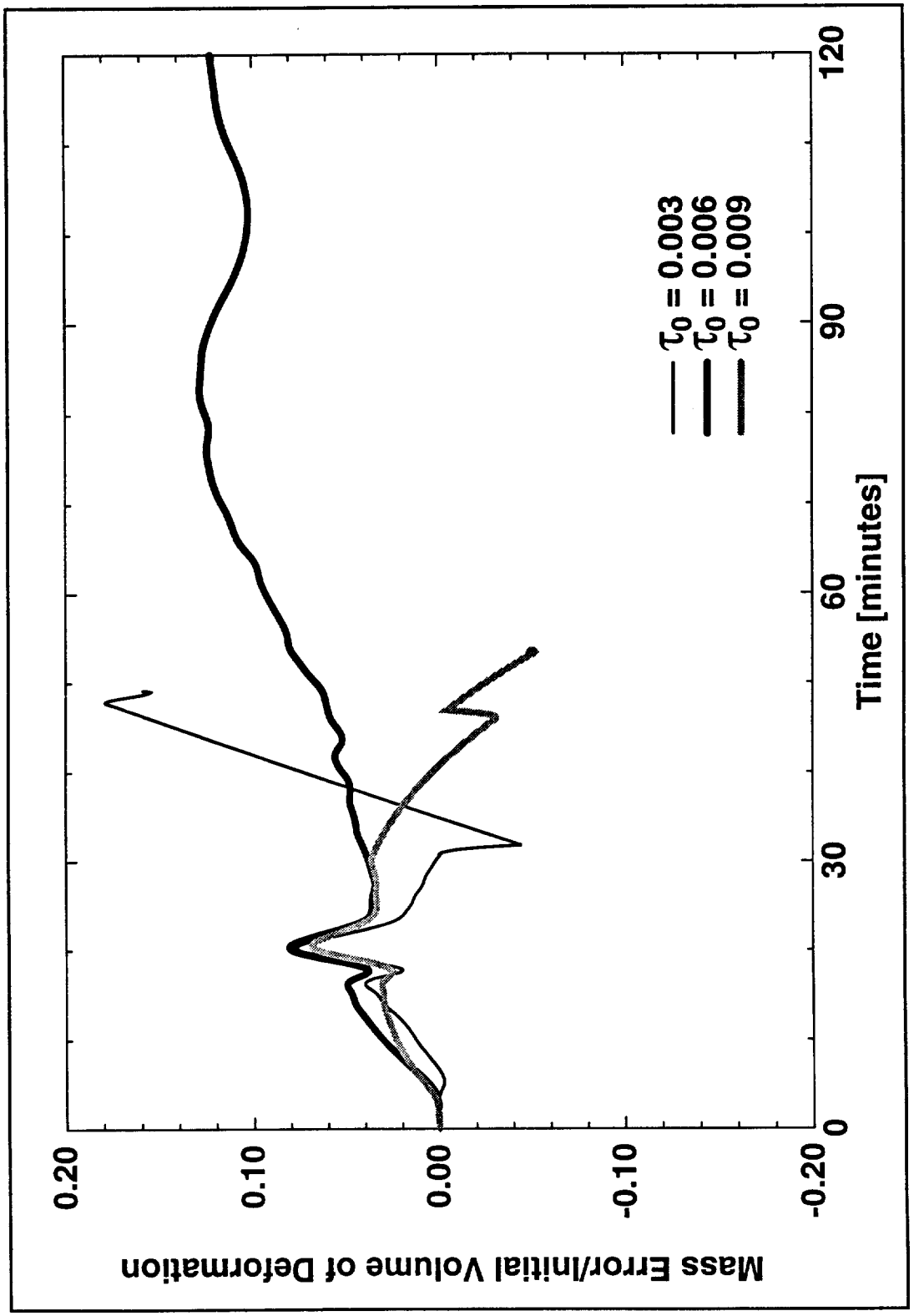

FIGURE 3.16 Mass (Scaled by Volume of Deformation) Conservation Over Time

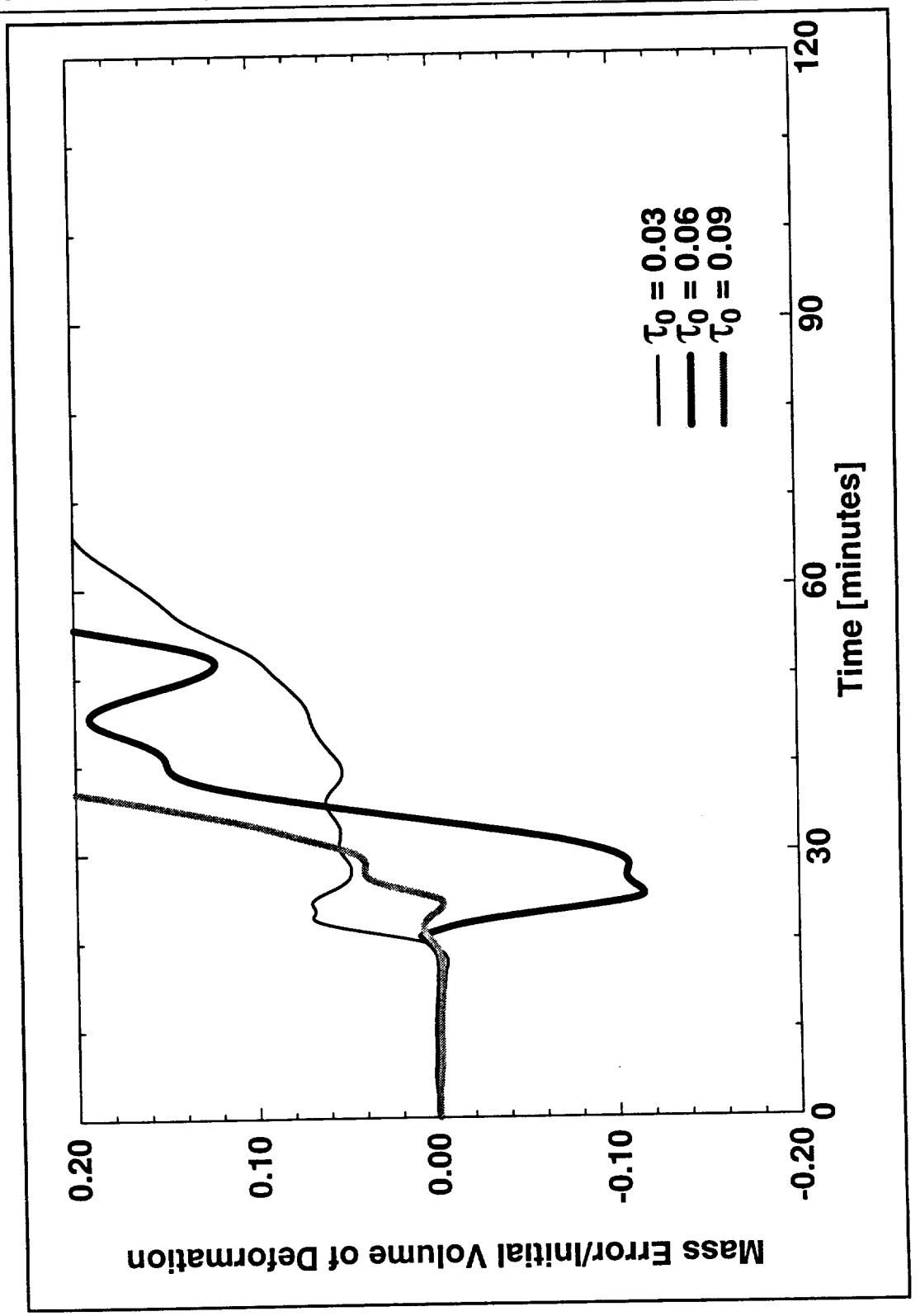

FIGURE 3.17 Mass (Scaled by Volume of Deformation) Conservation Over Time

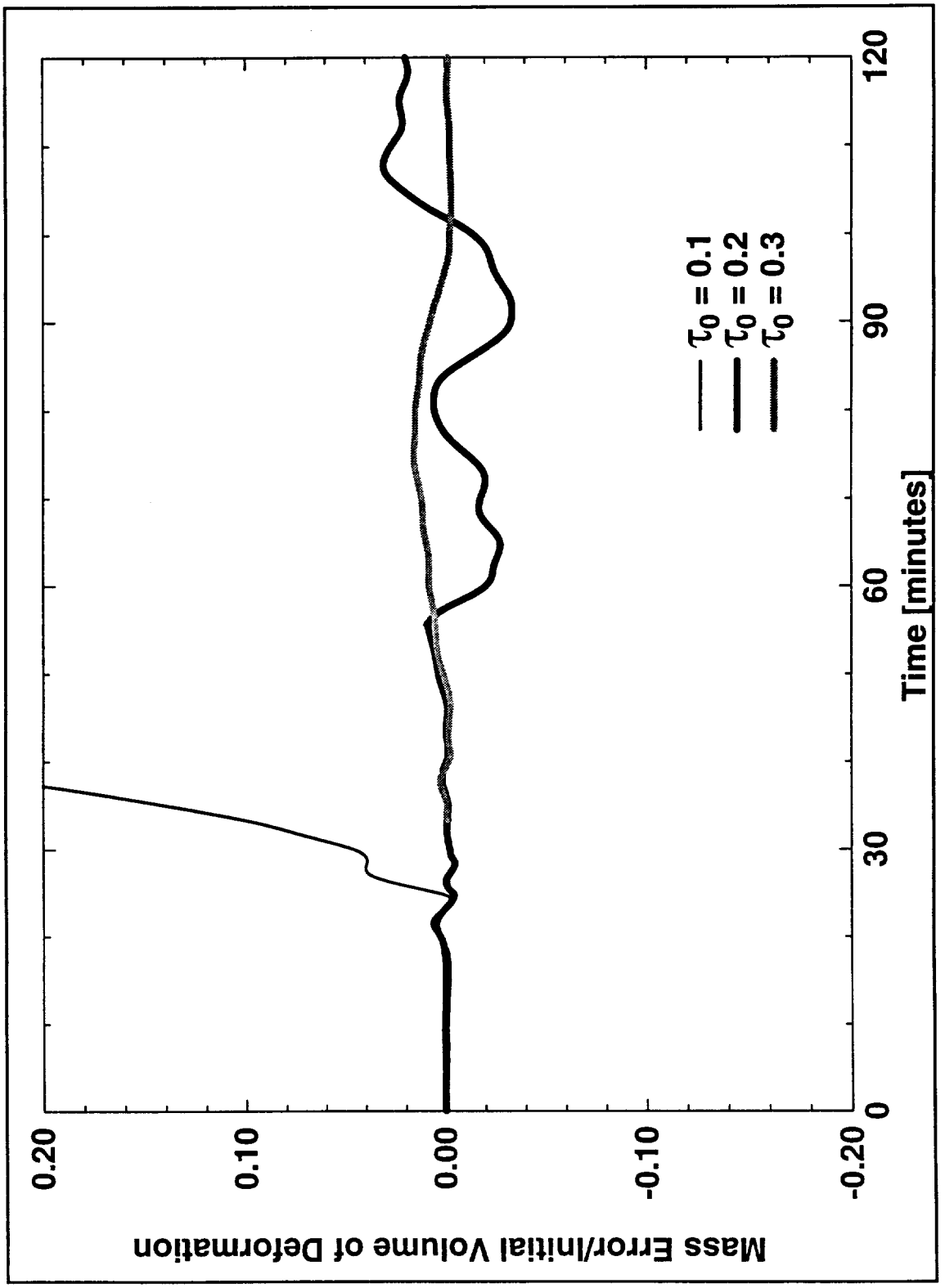

FIGURE 3.18 Mass (Scaled by Volume of Deformation) Conservation Over Time

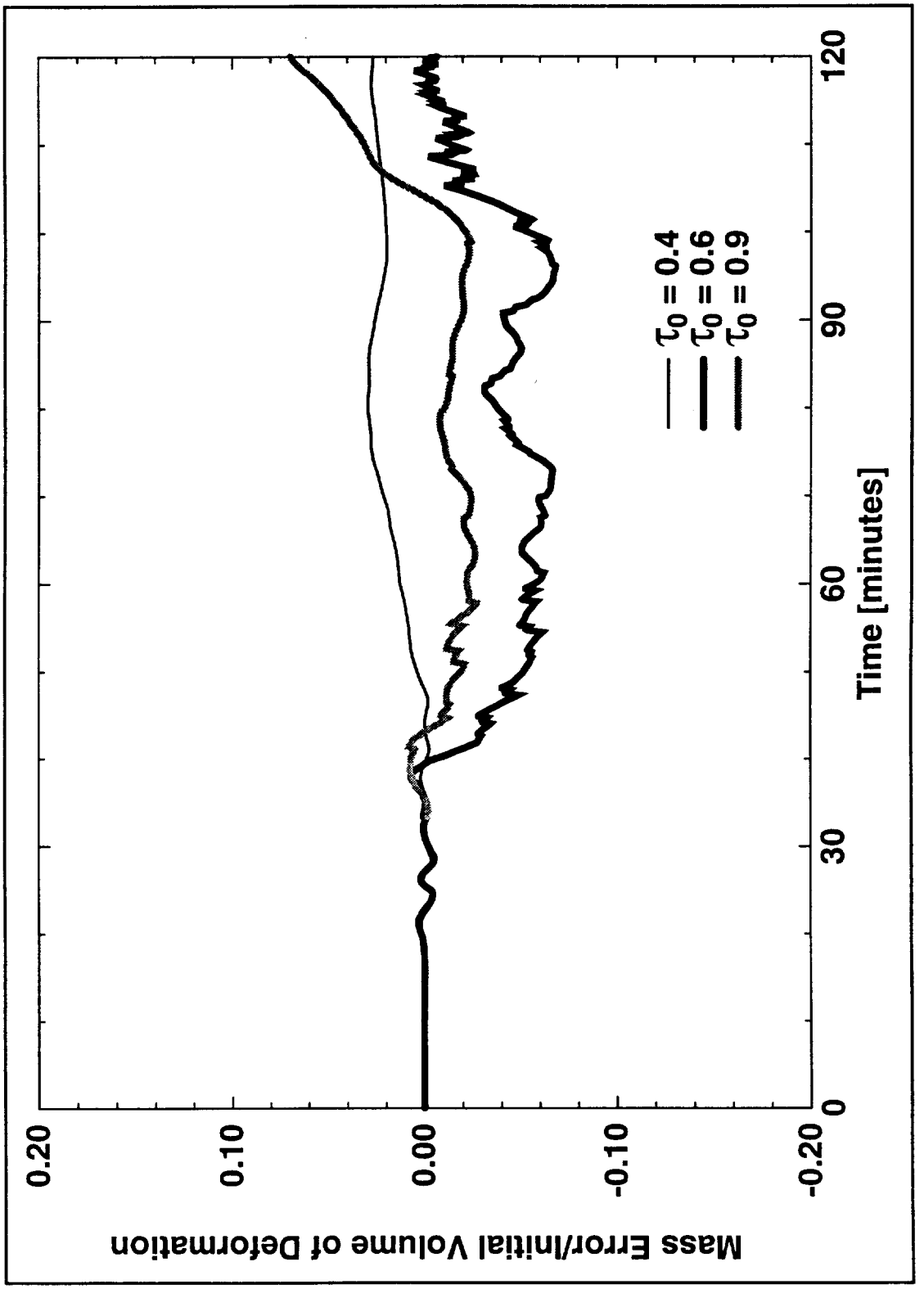

FIGURE 3.19 Mass (Scaled by Volume of Deformation) Conservation Over Time

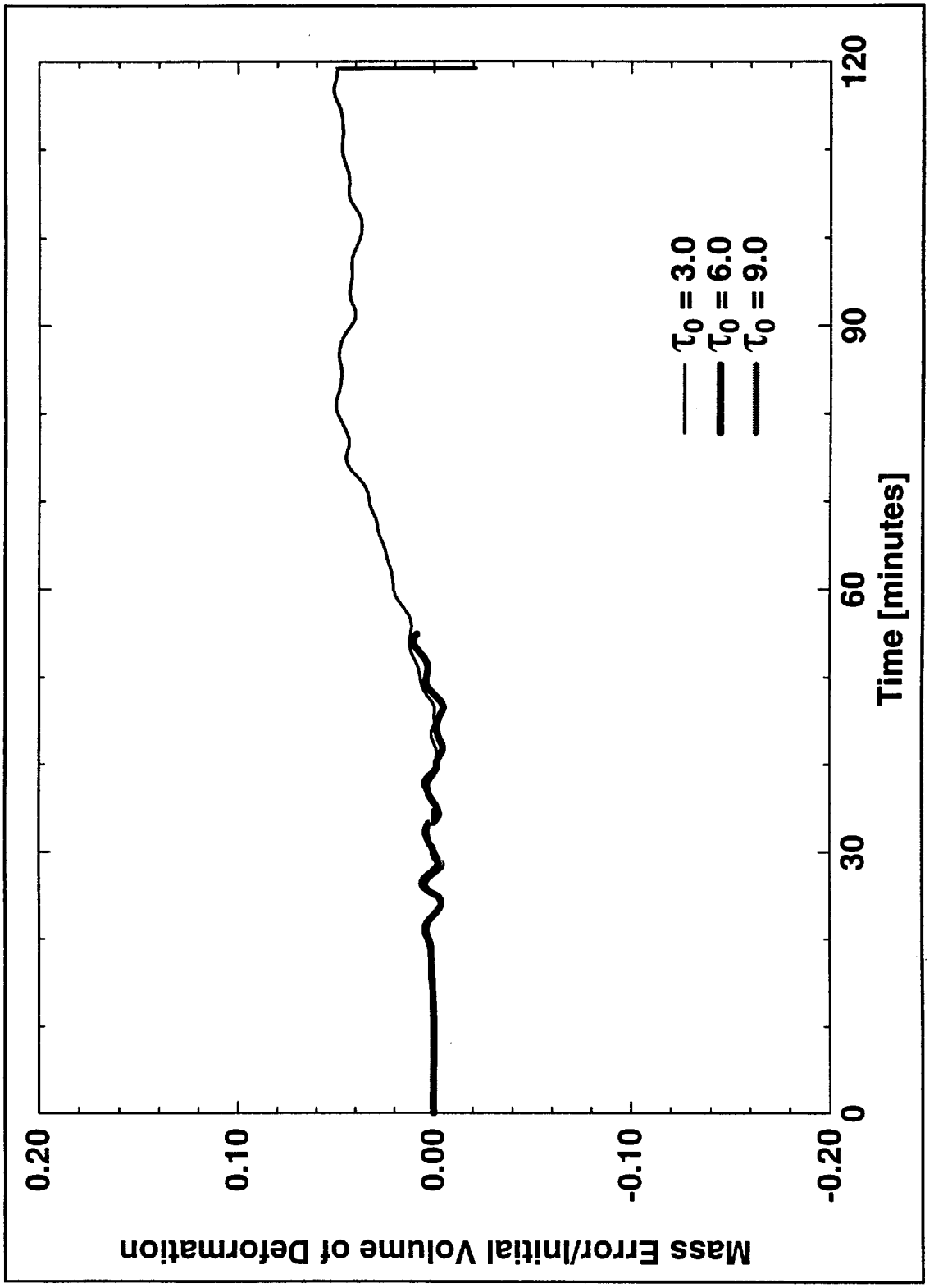

FIGURE 3.20 Locations of Tidal Gauge Stations

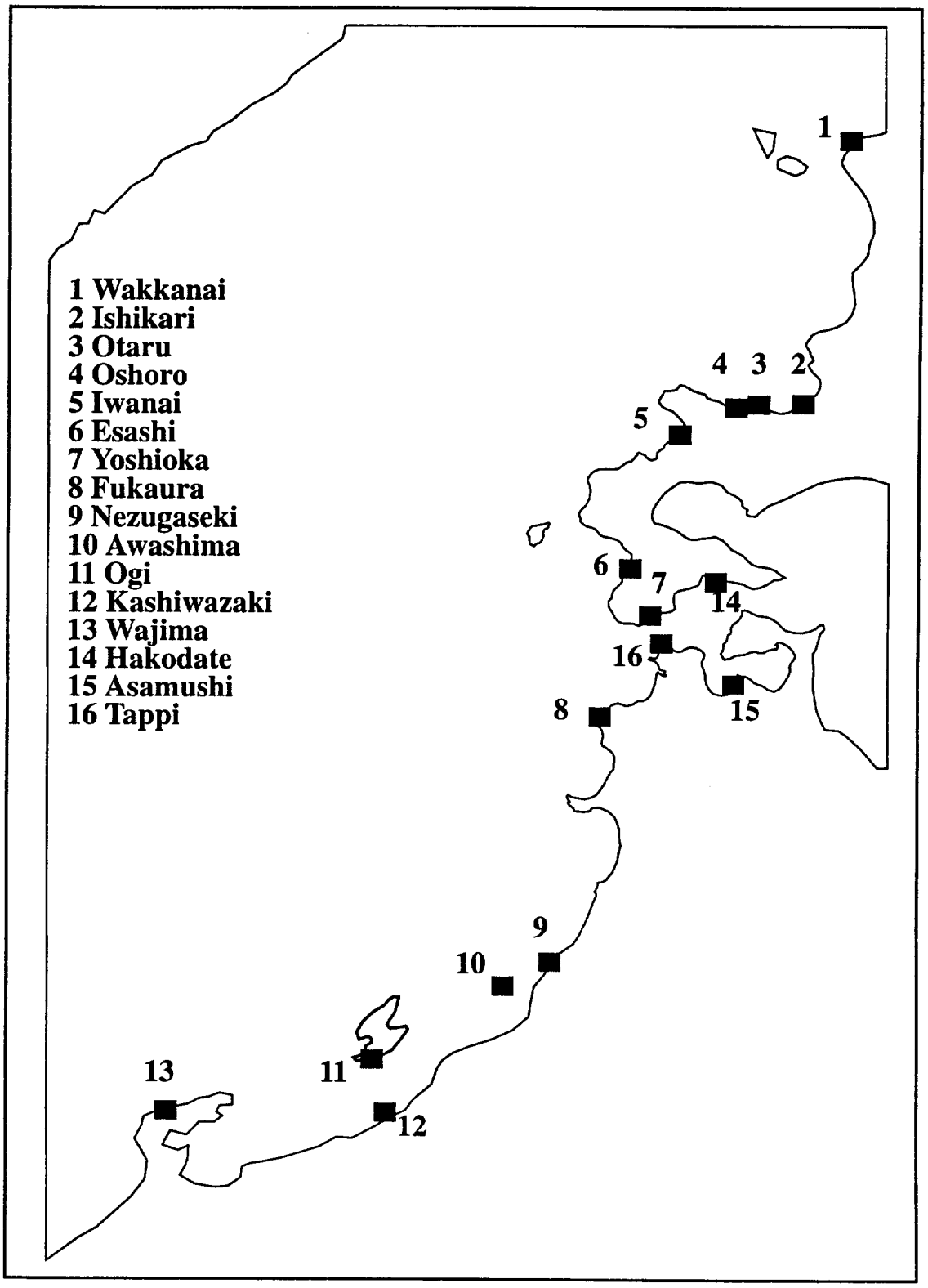

FIGURE 3.21 Root Mean Square Error for Different Manning Values

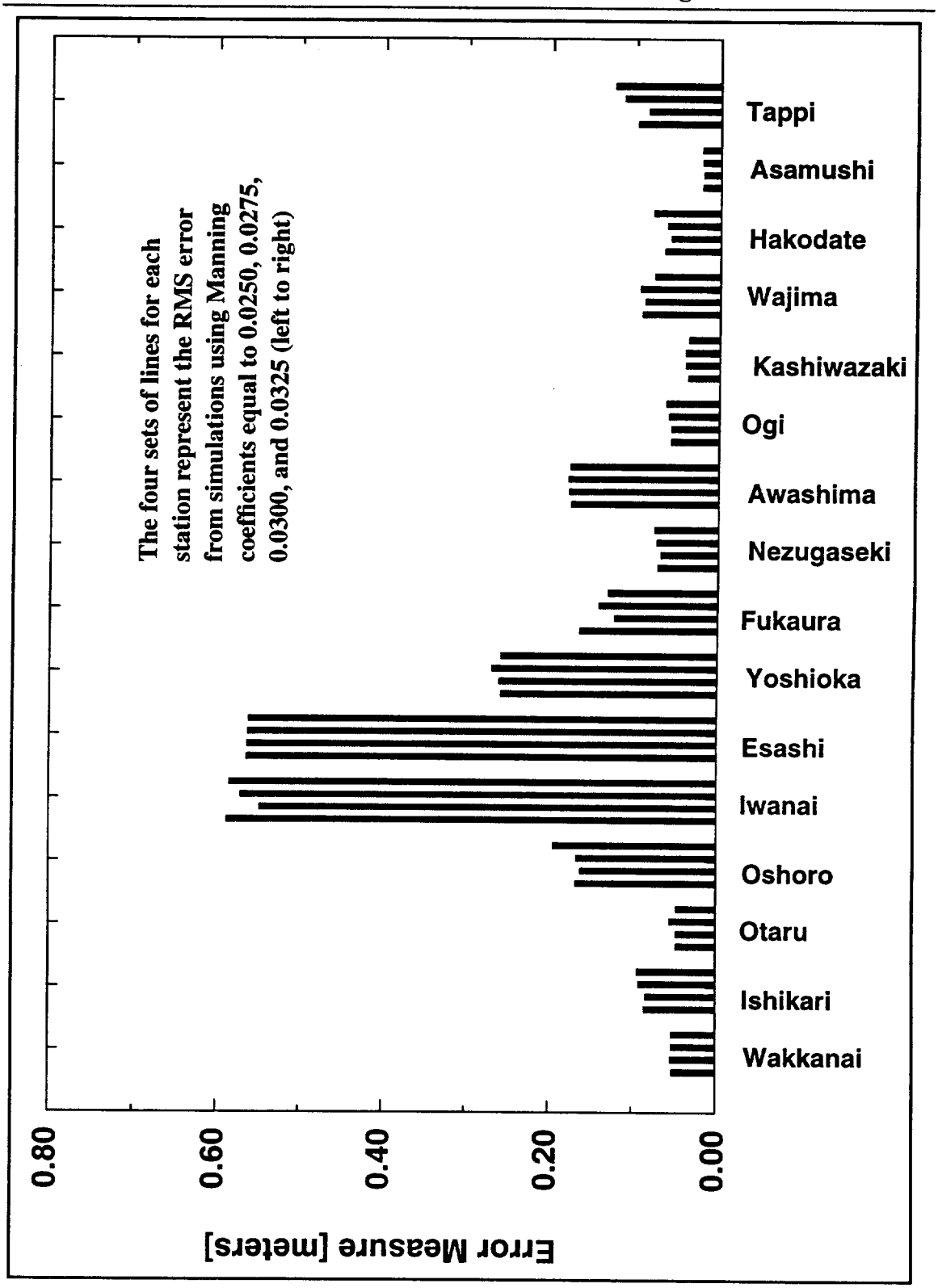

FIGURE 3.22 Root Mean Square Error - Friction

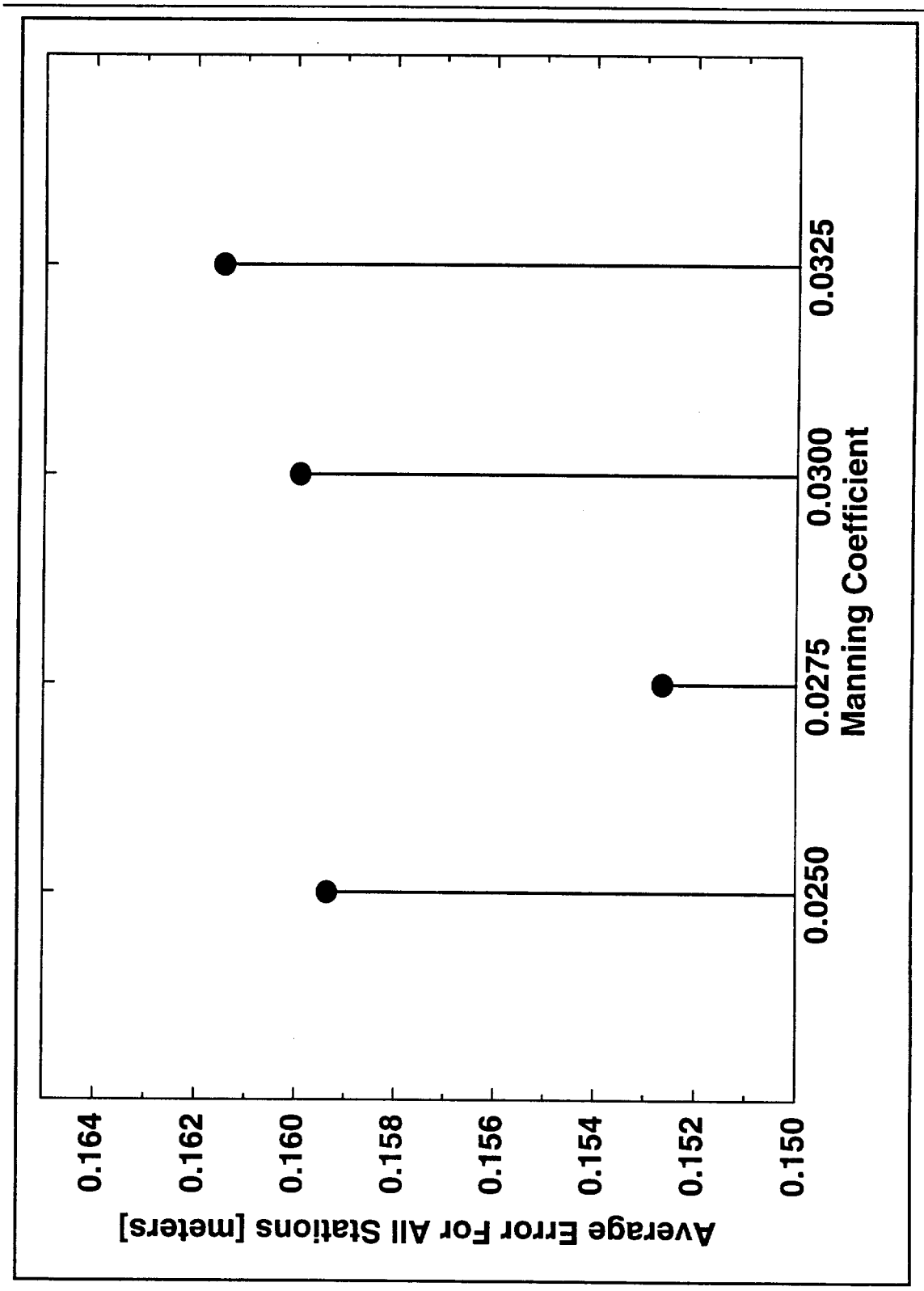

FIGURE 3.23 Root Mean Square Error - Diffusion

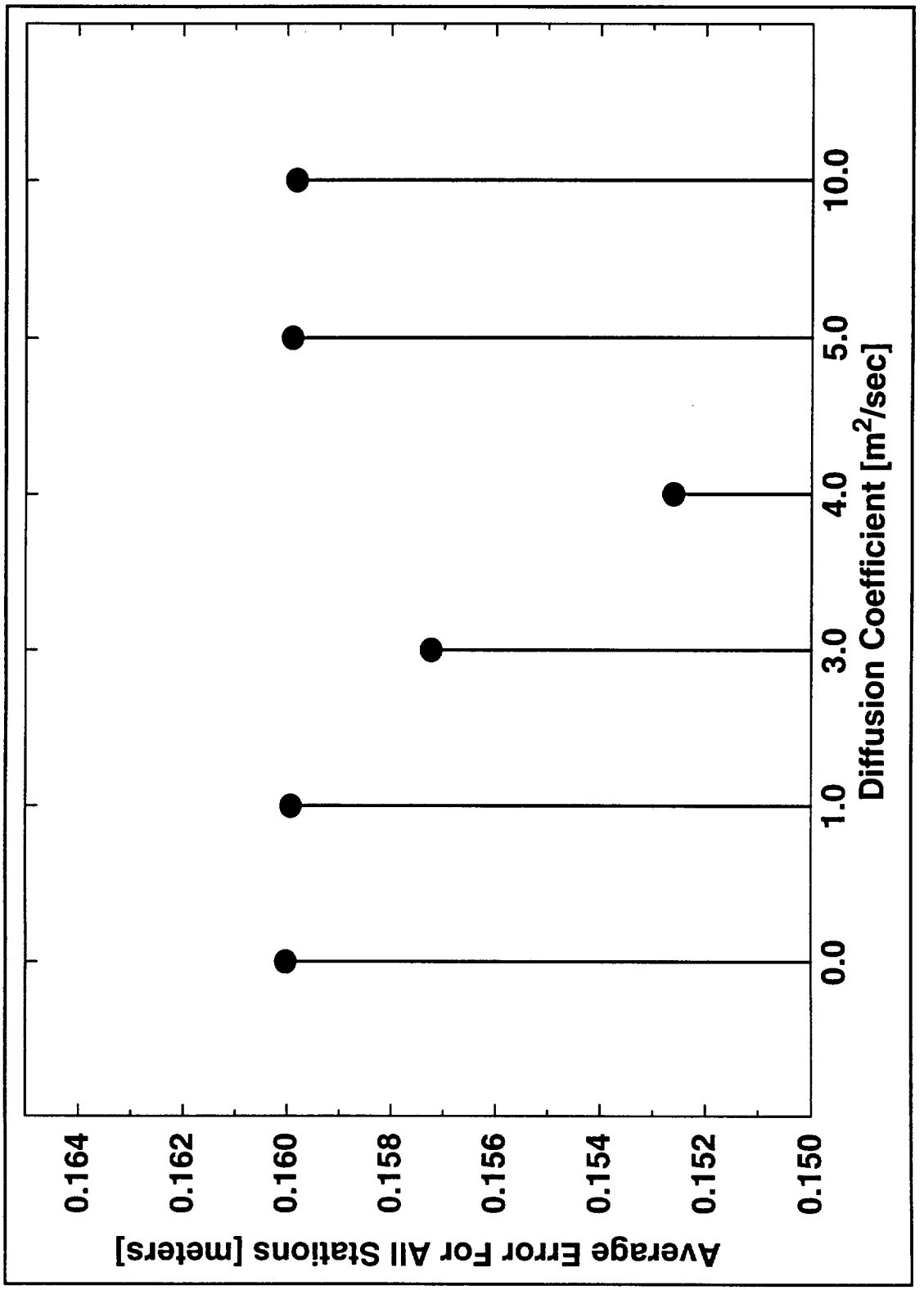

FIGURE 3.24 Mass Conservation Over Time for Diffusion Coefficients

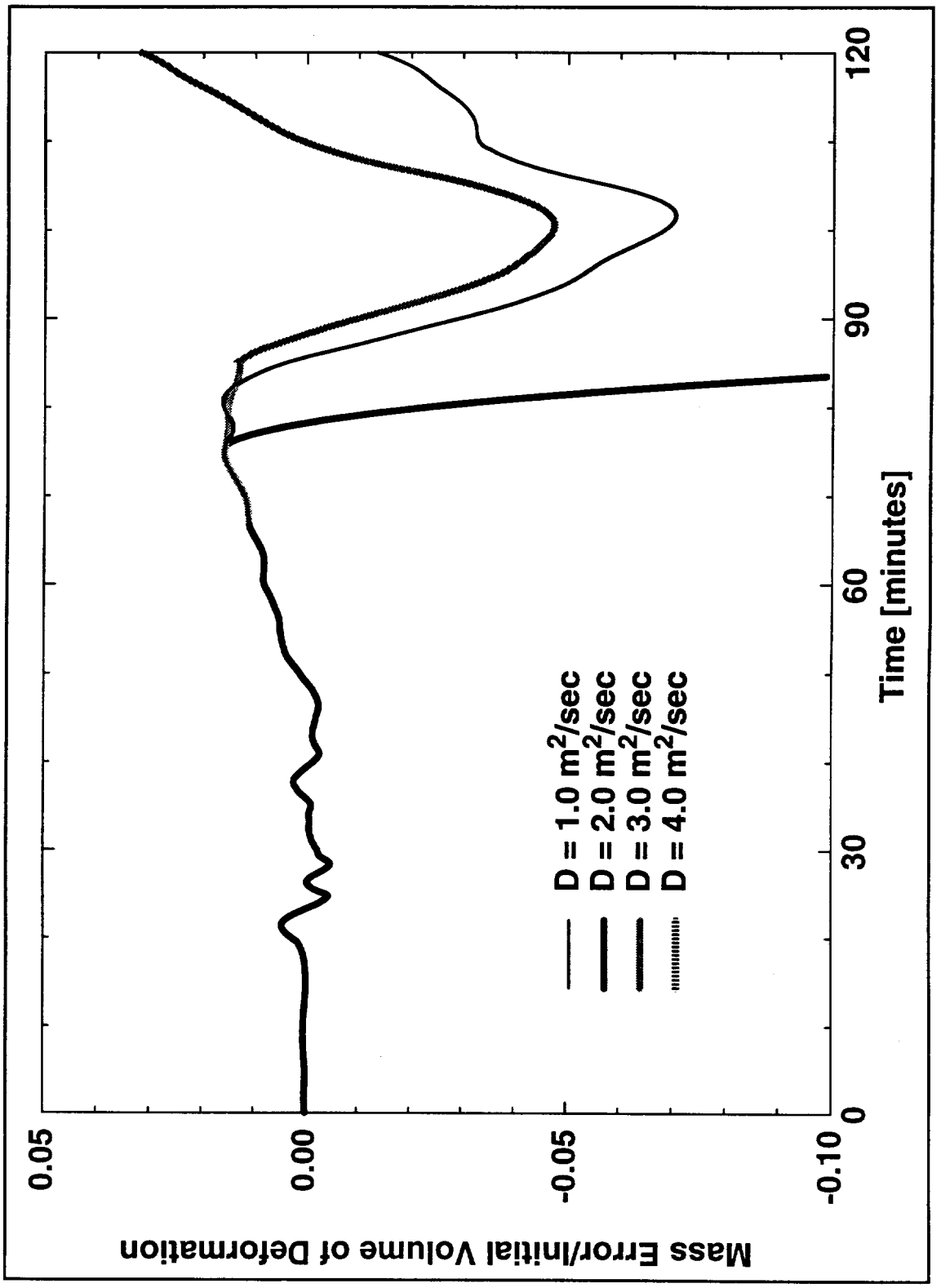

FIGURE 3.25 Mass Conservation Over Time for Diffusion Coefficients

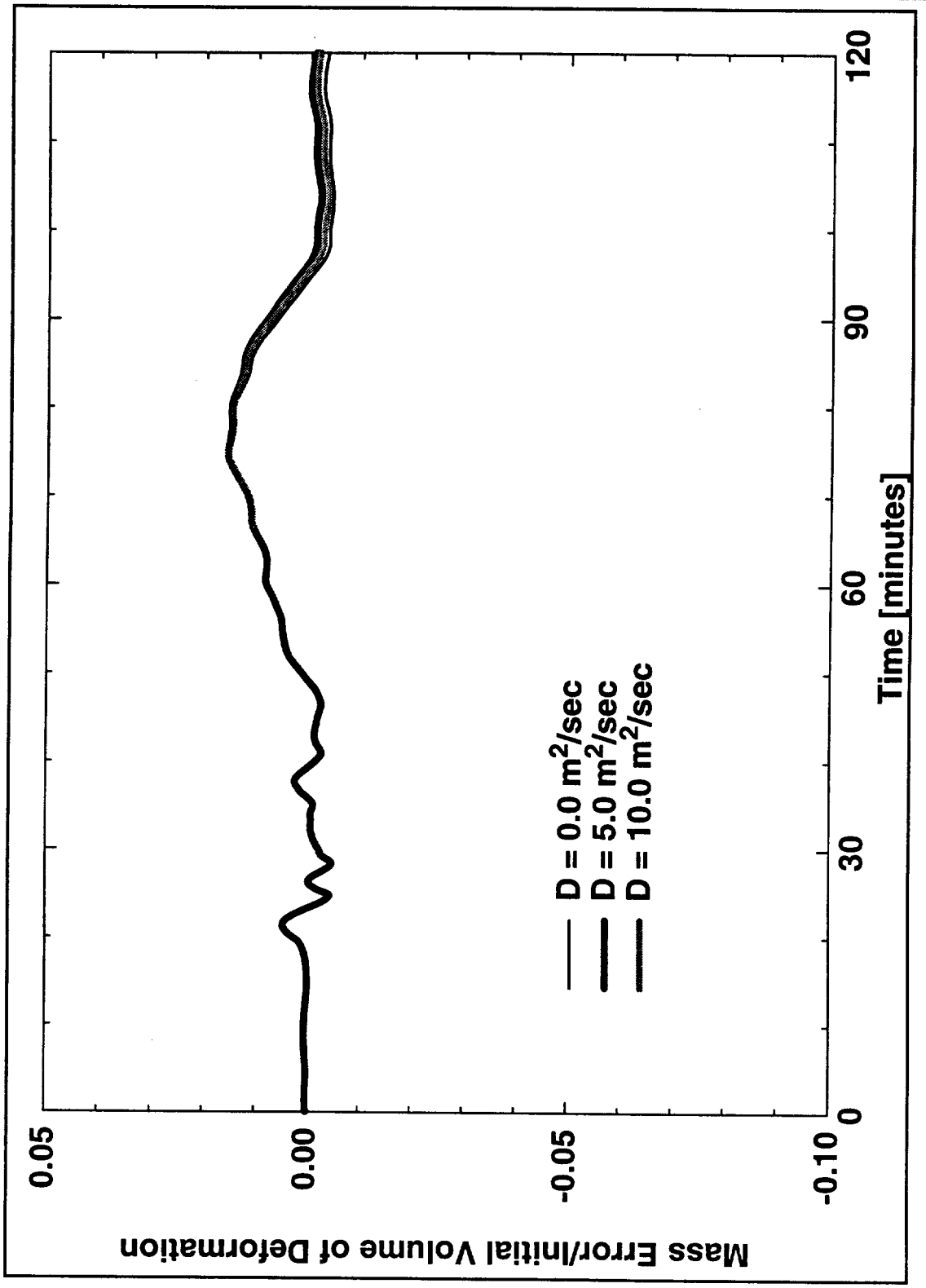

FIGURE 3.26 Results from Raytracing from Two Point Sources

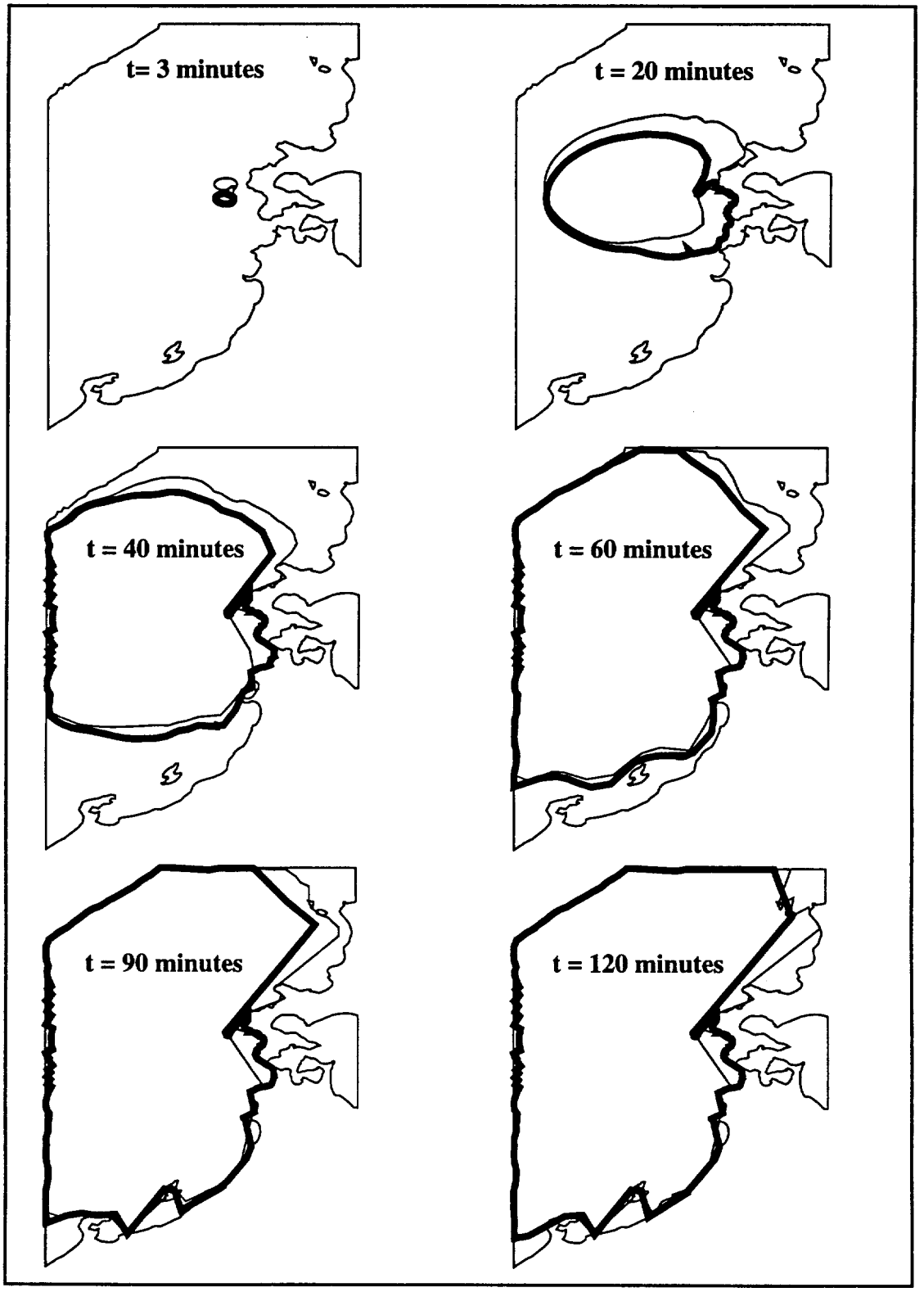

FIGURE 3.27 Coservation of Mass and Energy for EE Source

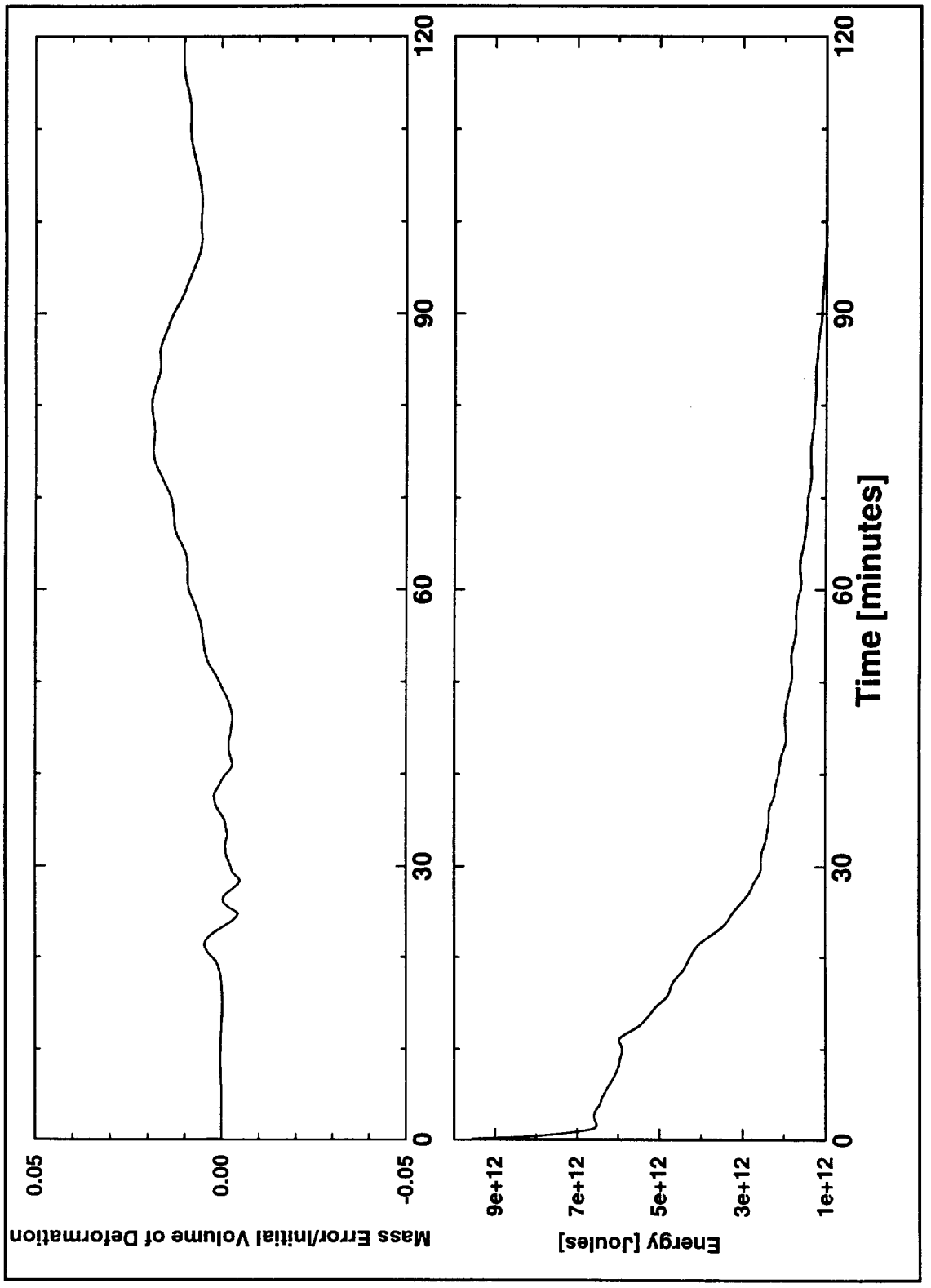

FIGURE 3.28 Conservation of Mass and Energy for EW Source

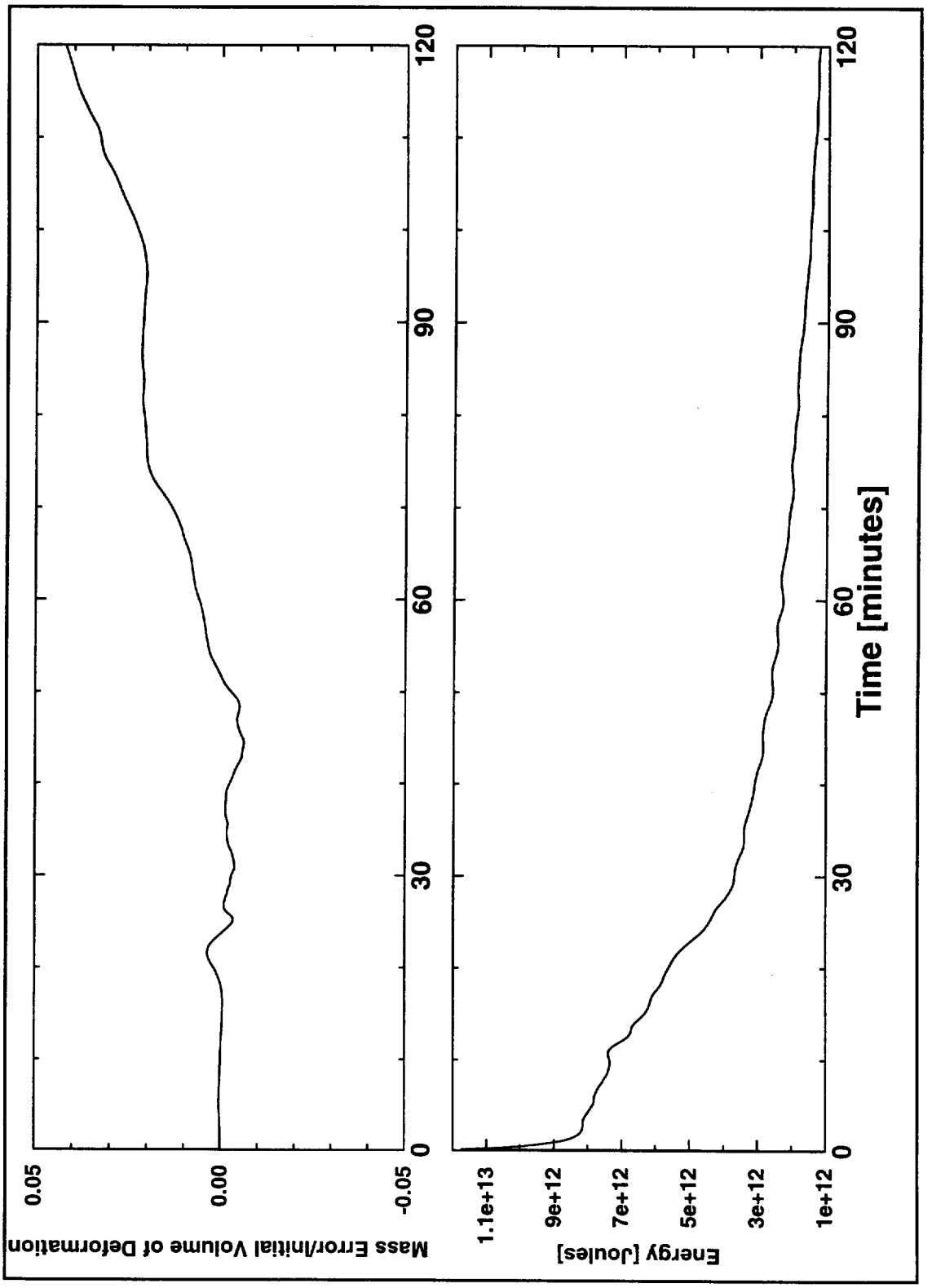

FIGURE 3.29 Conservation of Mass and Energy for WE Source

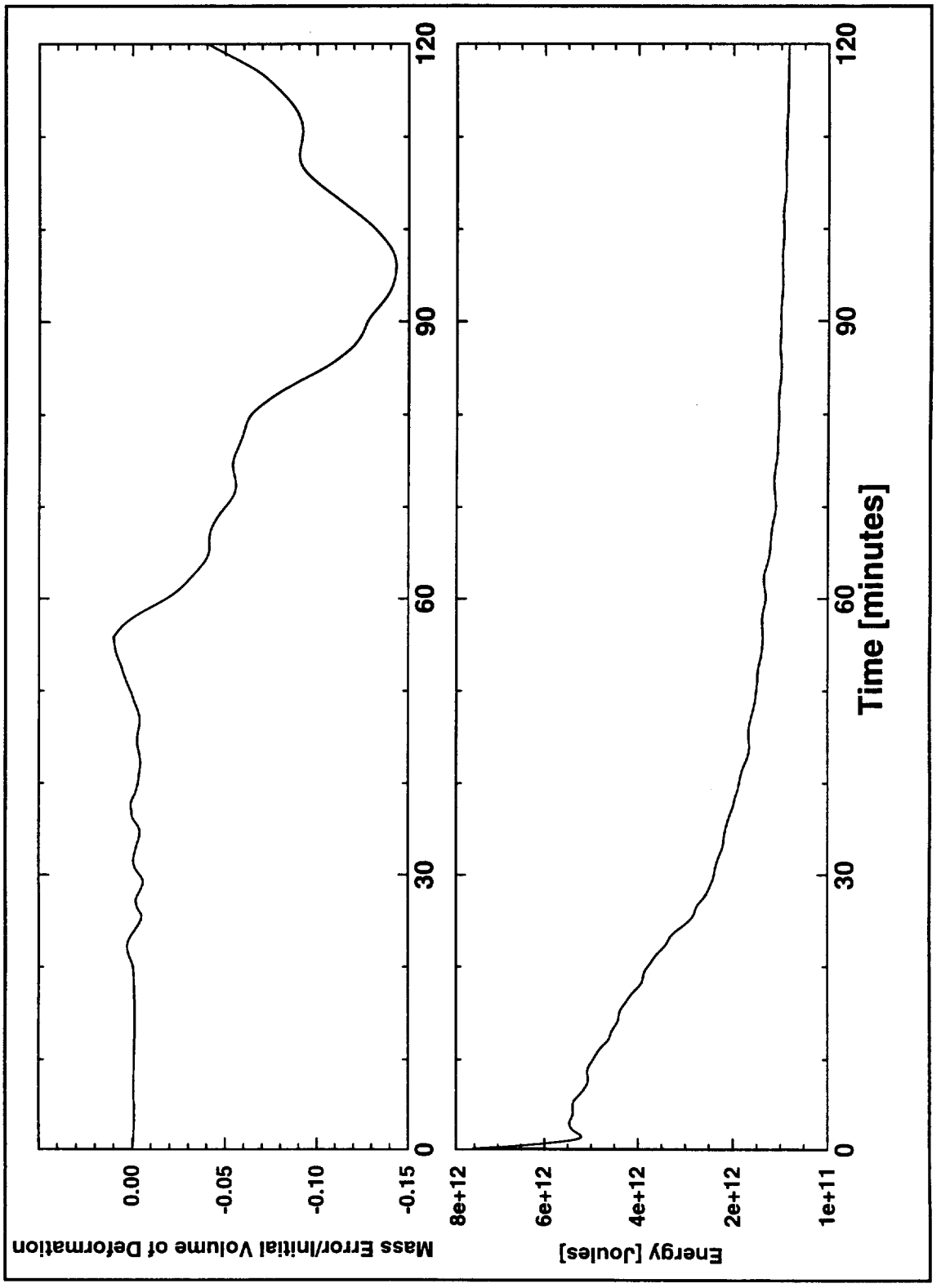

FIGURE 3.30 Conservation of Mass and Energy for WW Source

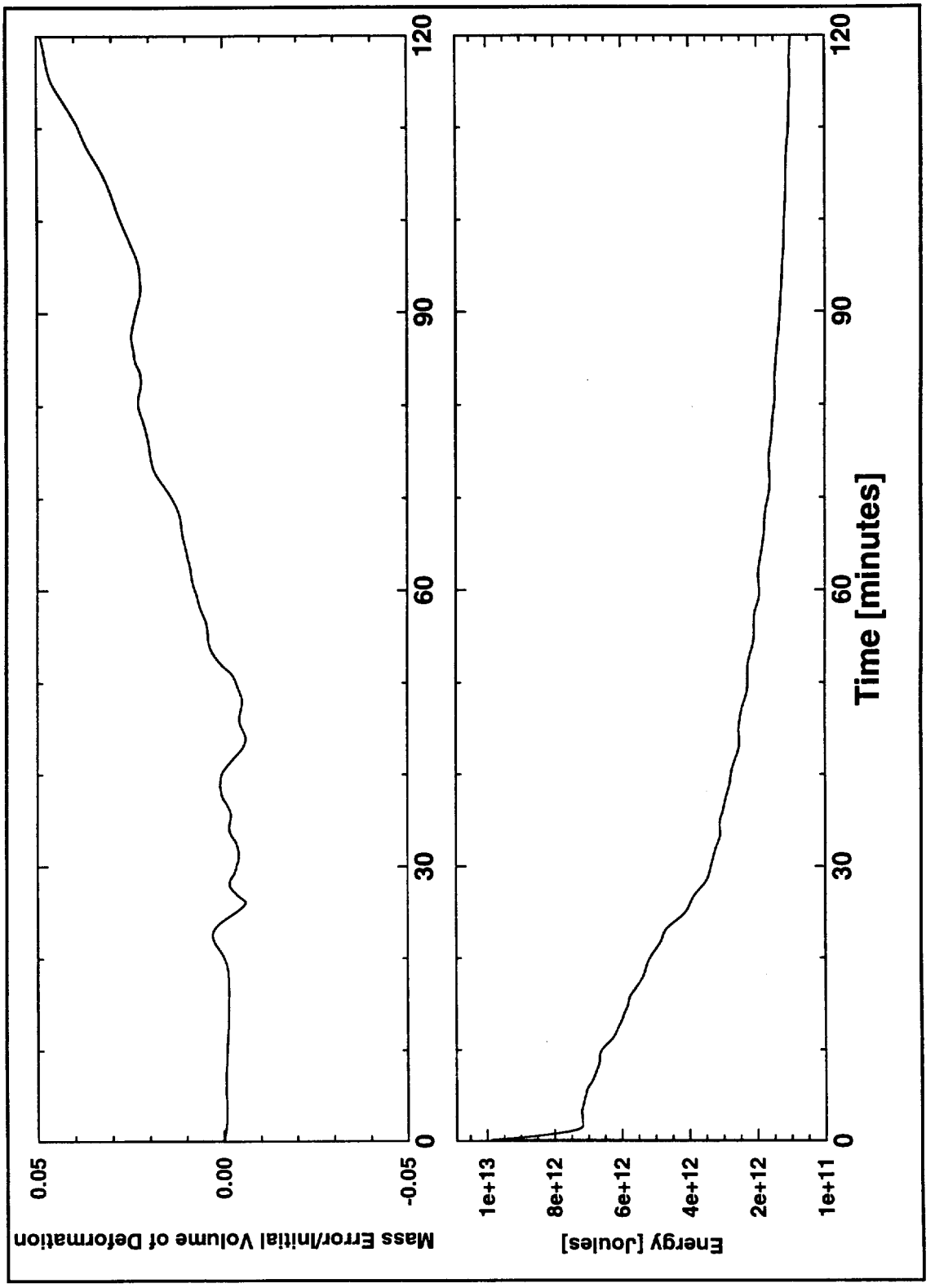

FIGURE 3.31 Conservation of Mass and Energy for DCRC1 Source

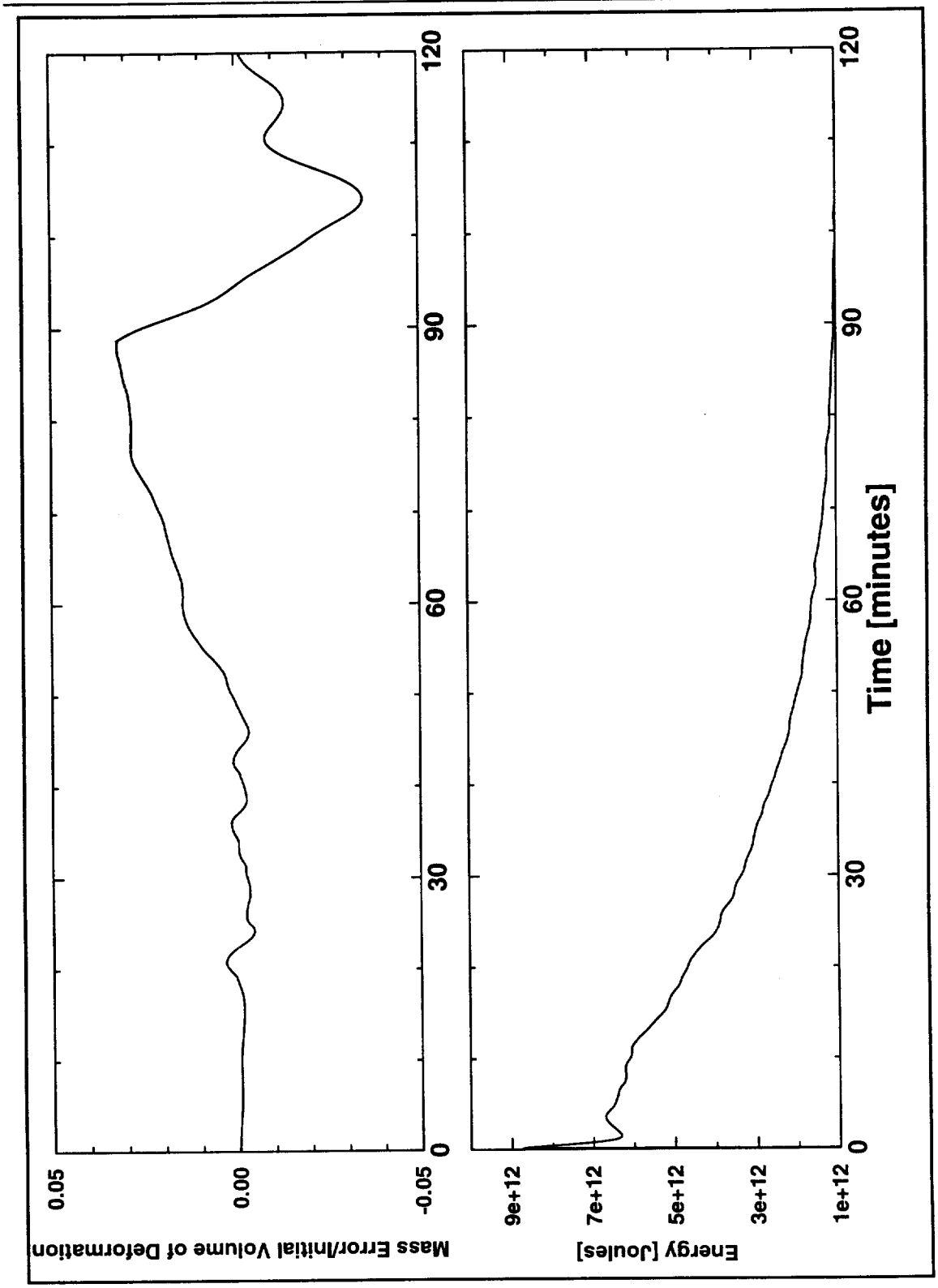

FIGURE 3.32 Conservation of Mass and Energy for DCRC2 Source

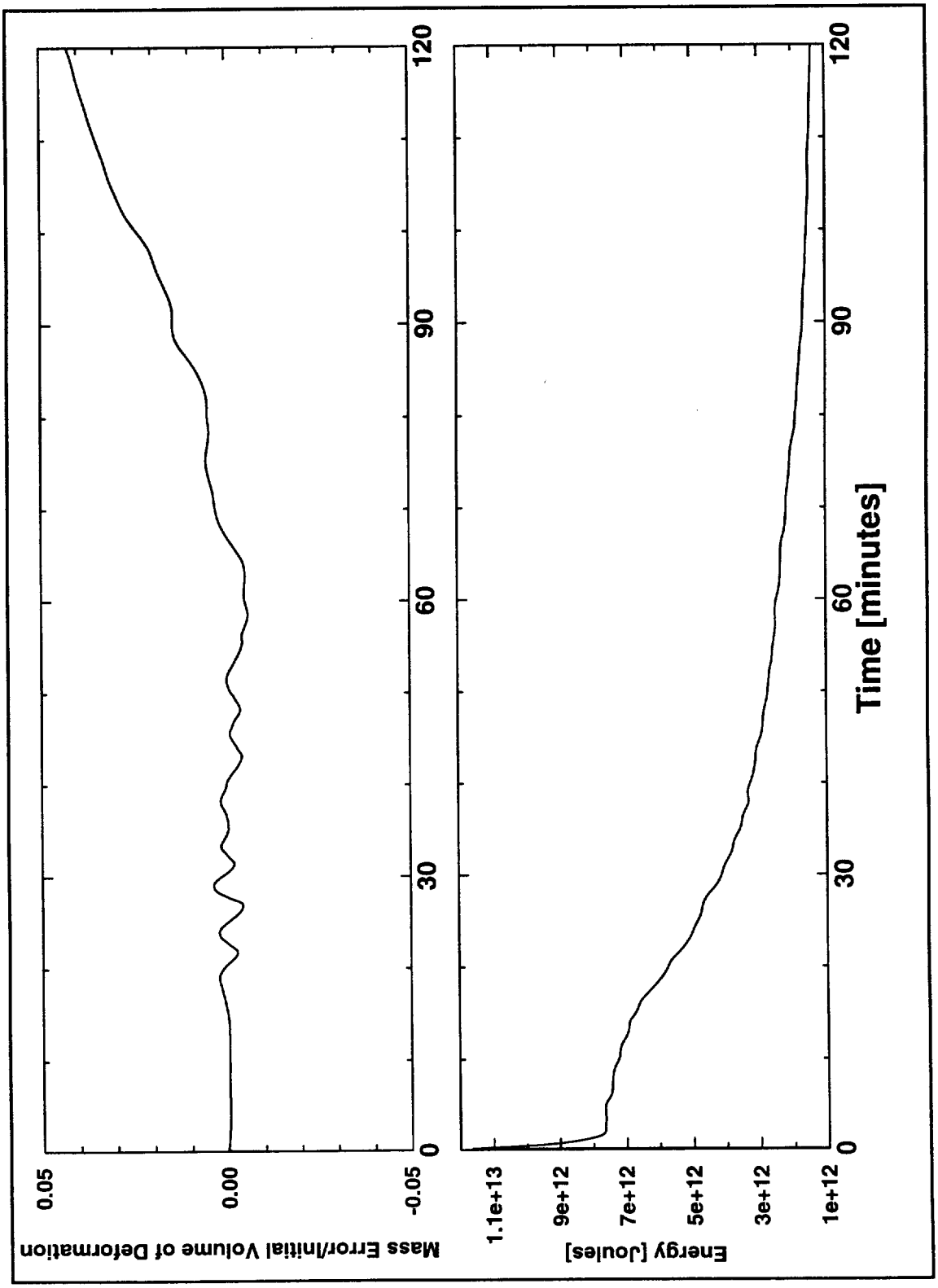

FIGURE 3.33 Conservation of Mass and Energy for Harvard Source

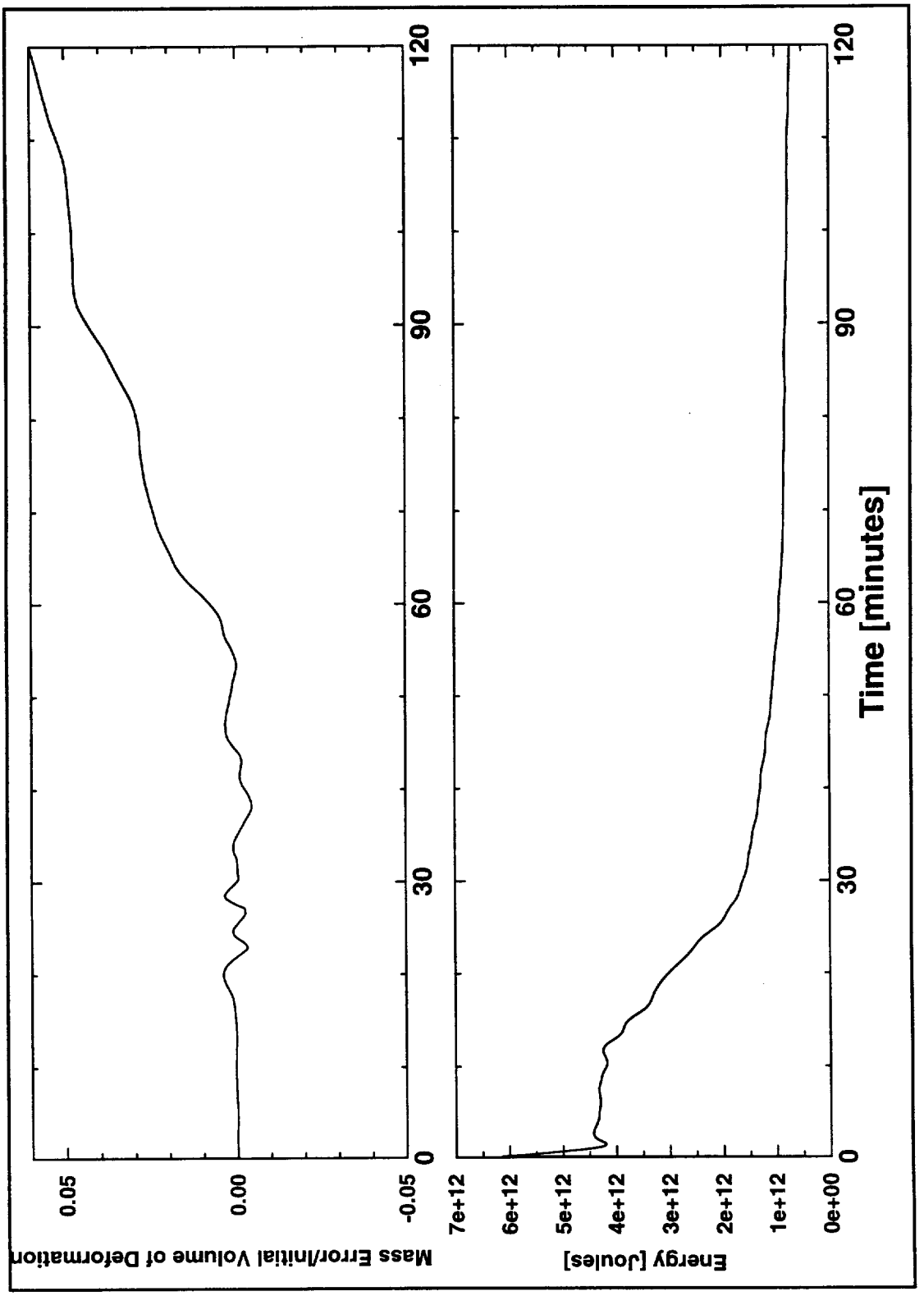

FIGURE 3.34 Conservation of Mass and Energy for Hokkaido University Source

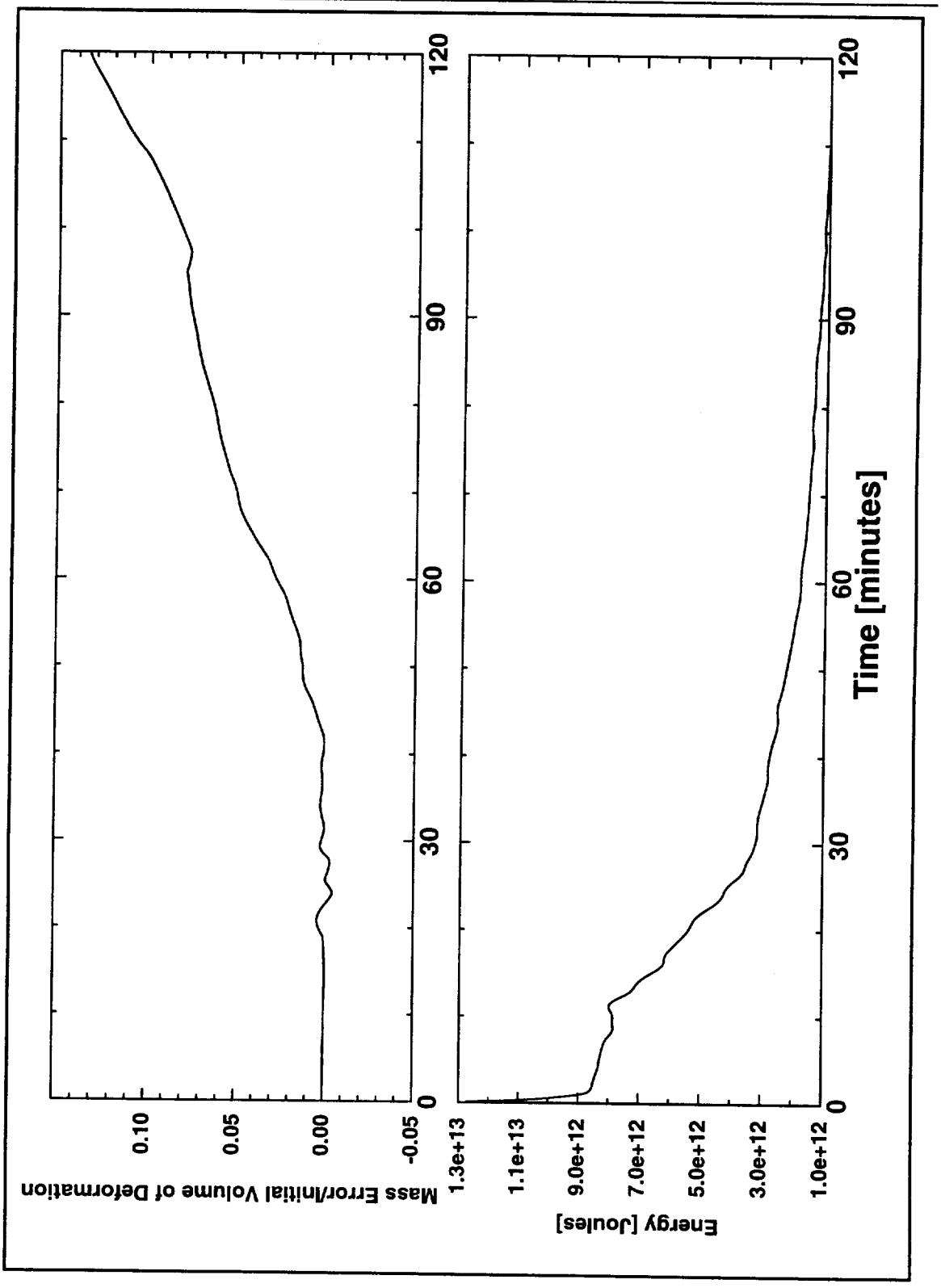

FIGURE 3.35 Conservation of Mass and Energy for JMA Source

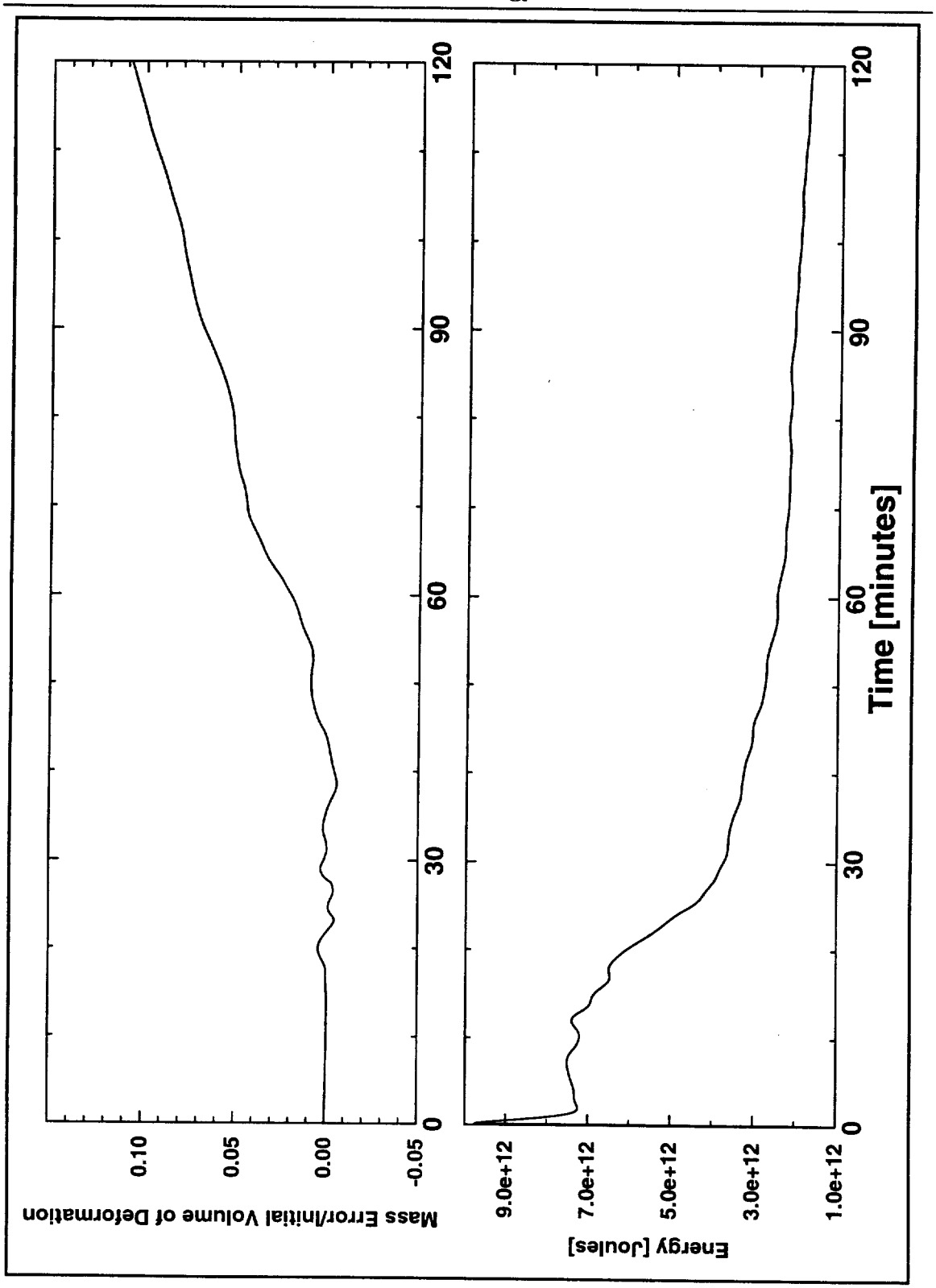

FIGURE 3.36 Conservation of Mass and Energy for USGS Source

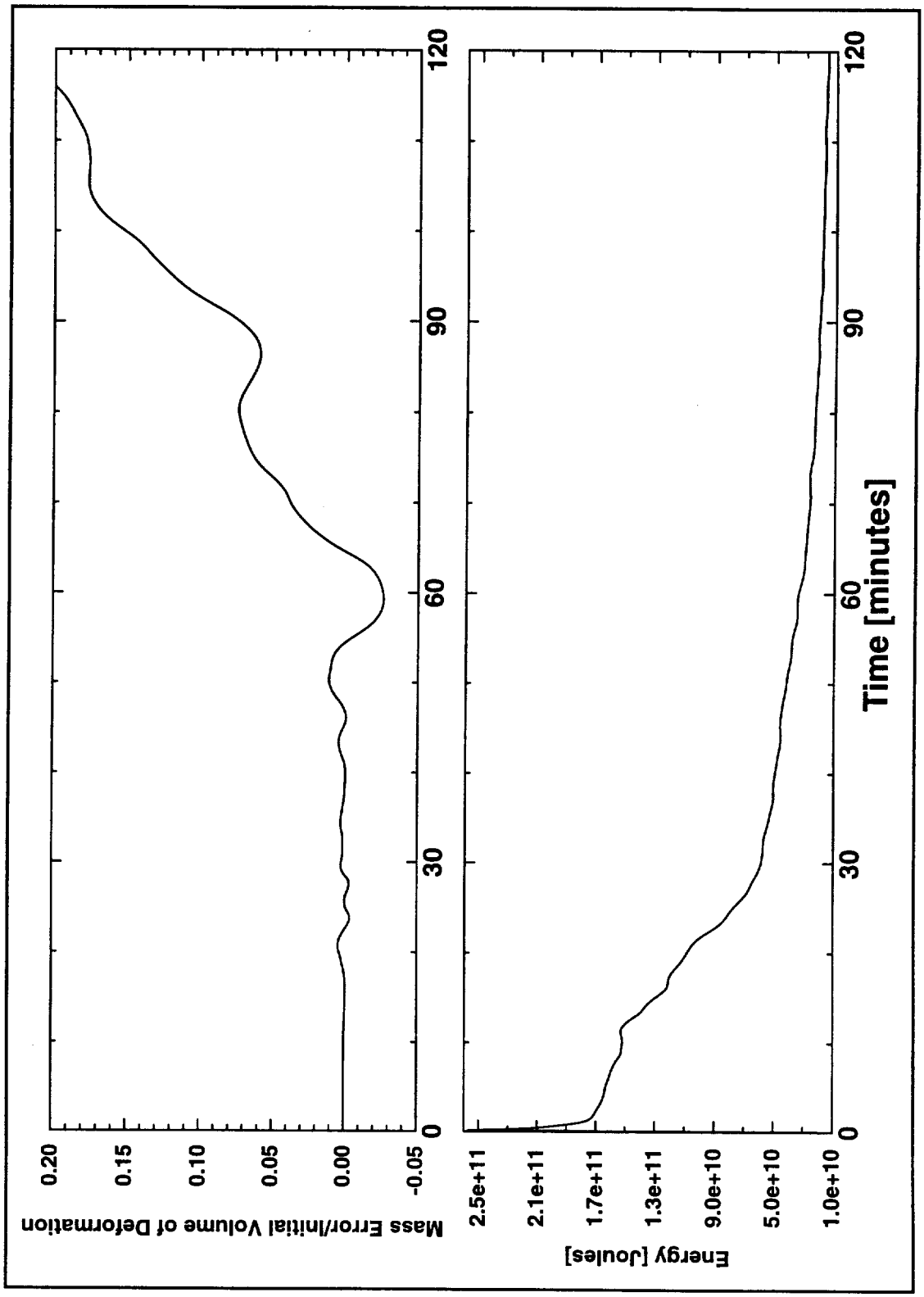

FIGURE 3.37 Conservation of Mass and Energy for University of Tokyo Source

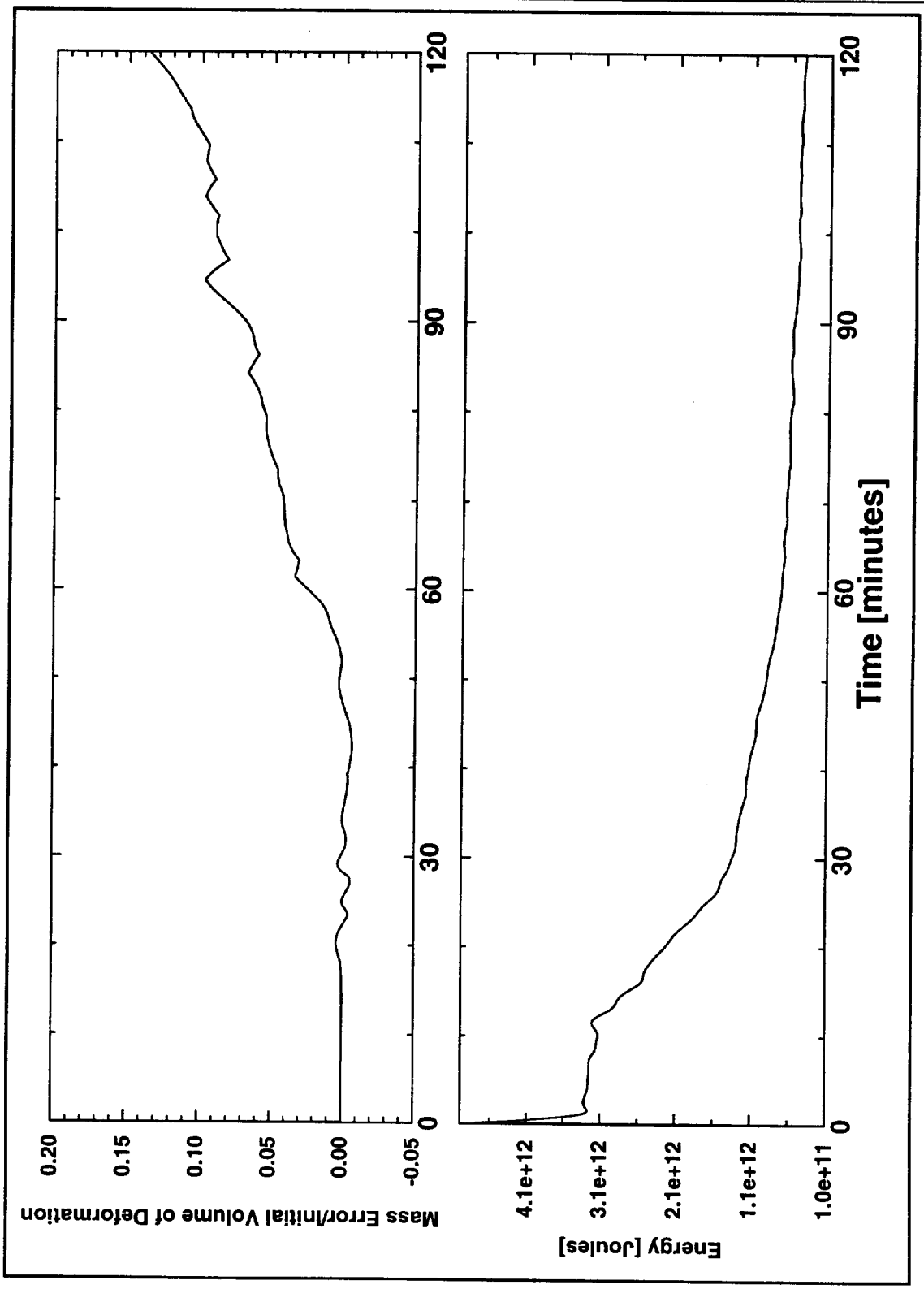

FIGURE 3.38 Effect of Transmissive Boundaries on Mass and Energy

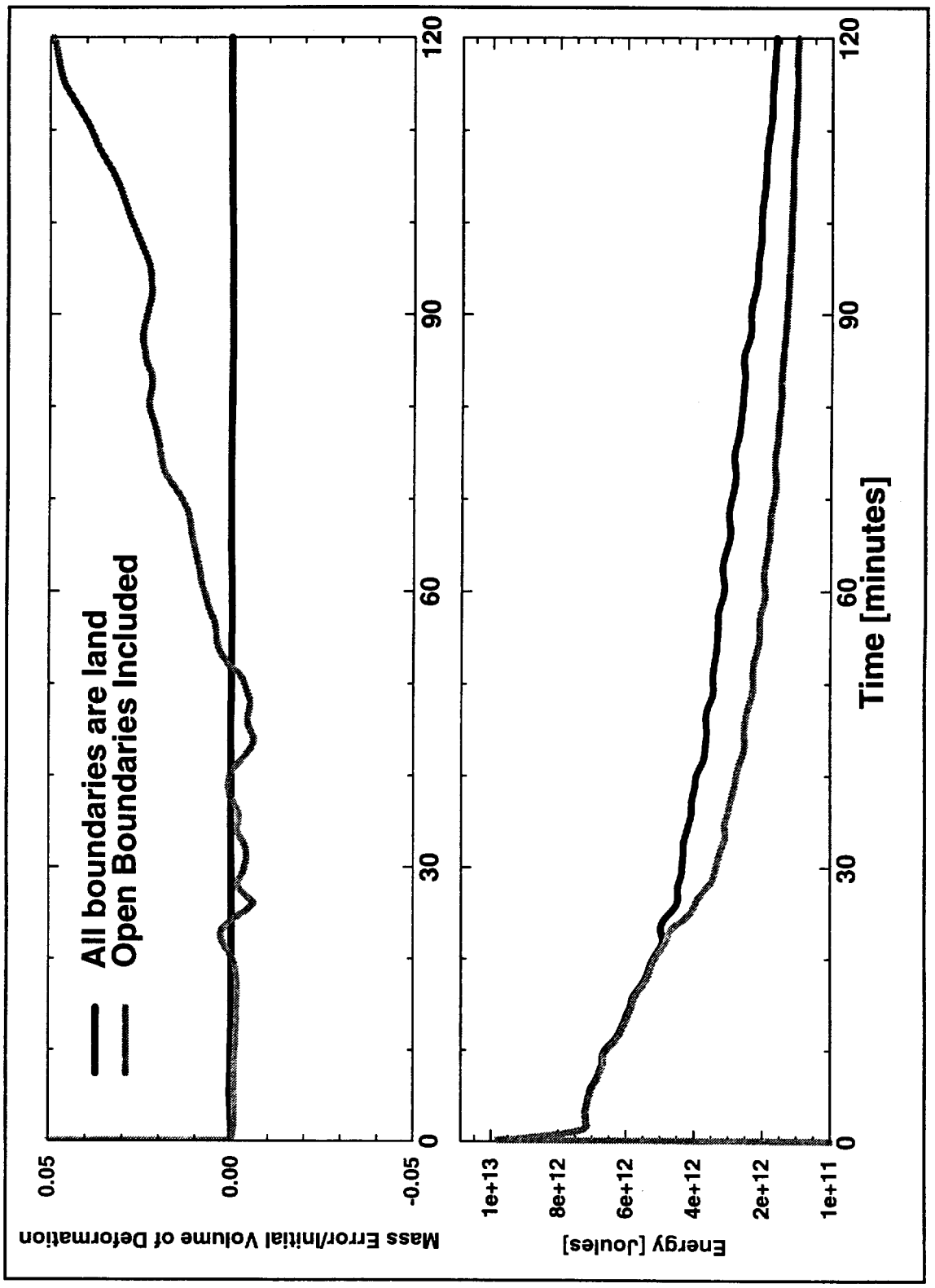

FIGURE 3.39 Numerical Results and Observed Waveforms at Iwanai

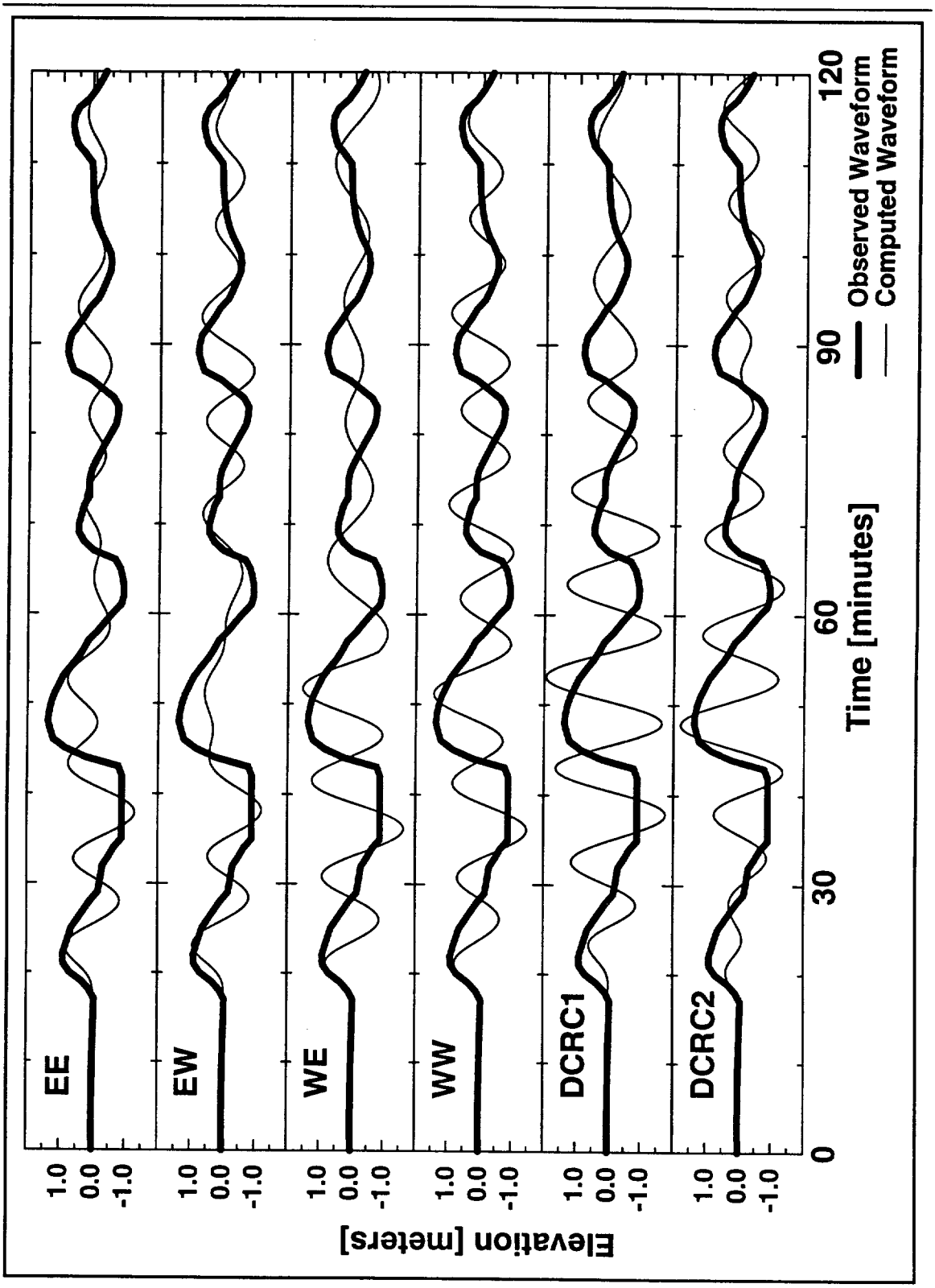

FIGURE 3.40 Numerical Results and Observed Waveforms at Iwanai

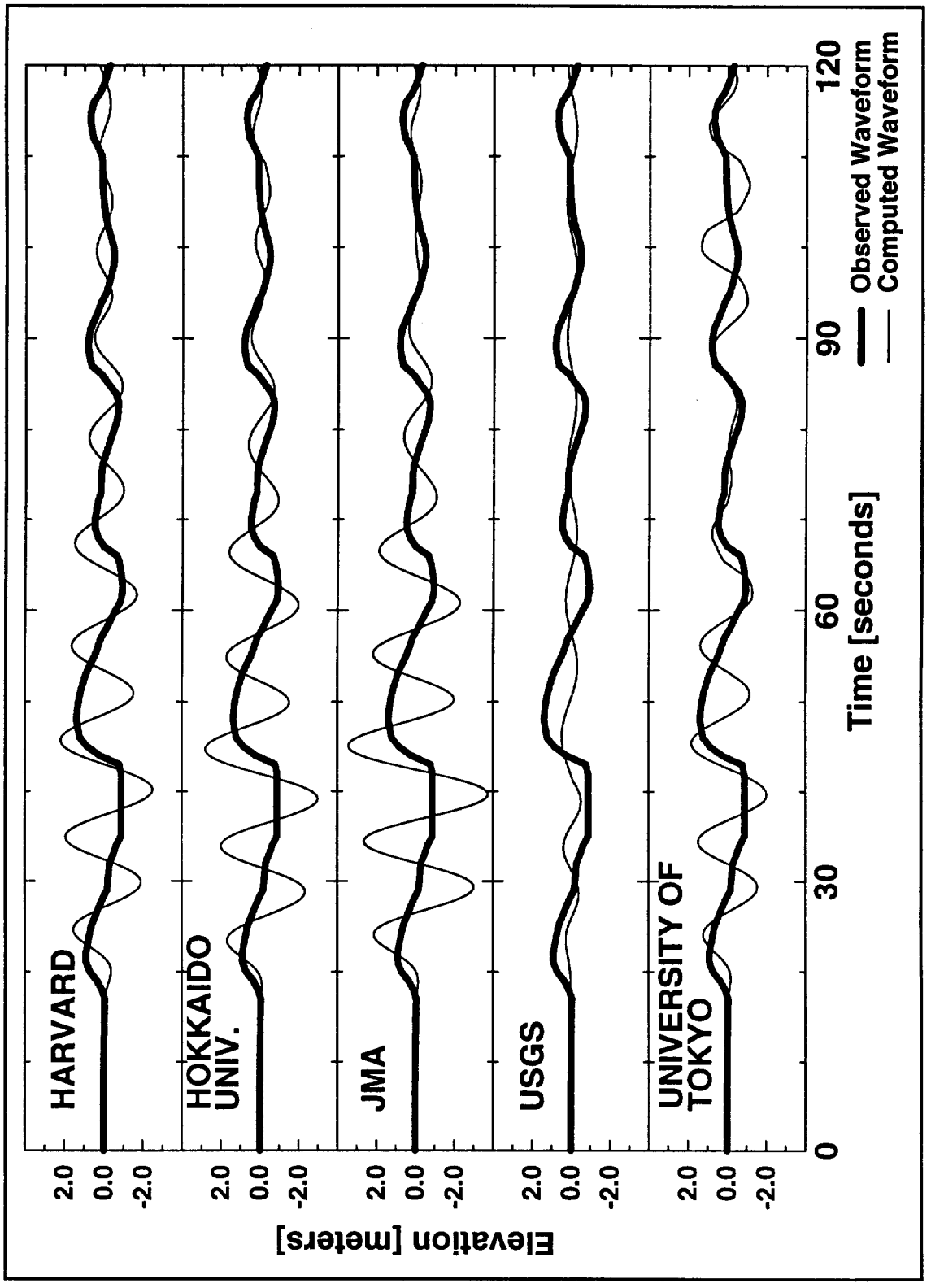

FIGURE 3.41 Numerical Results and Observed Waveforms at Esashi

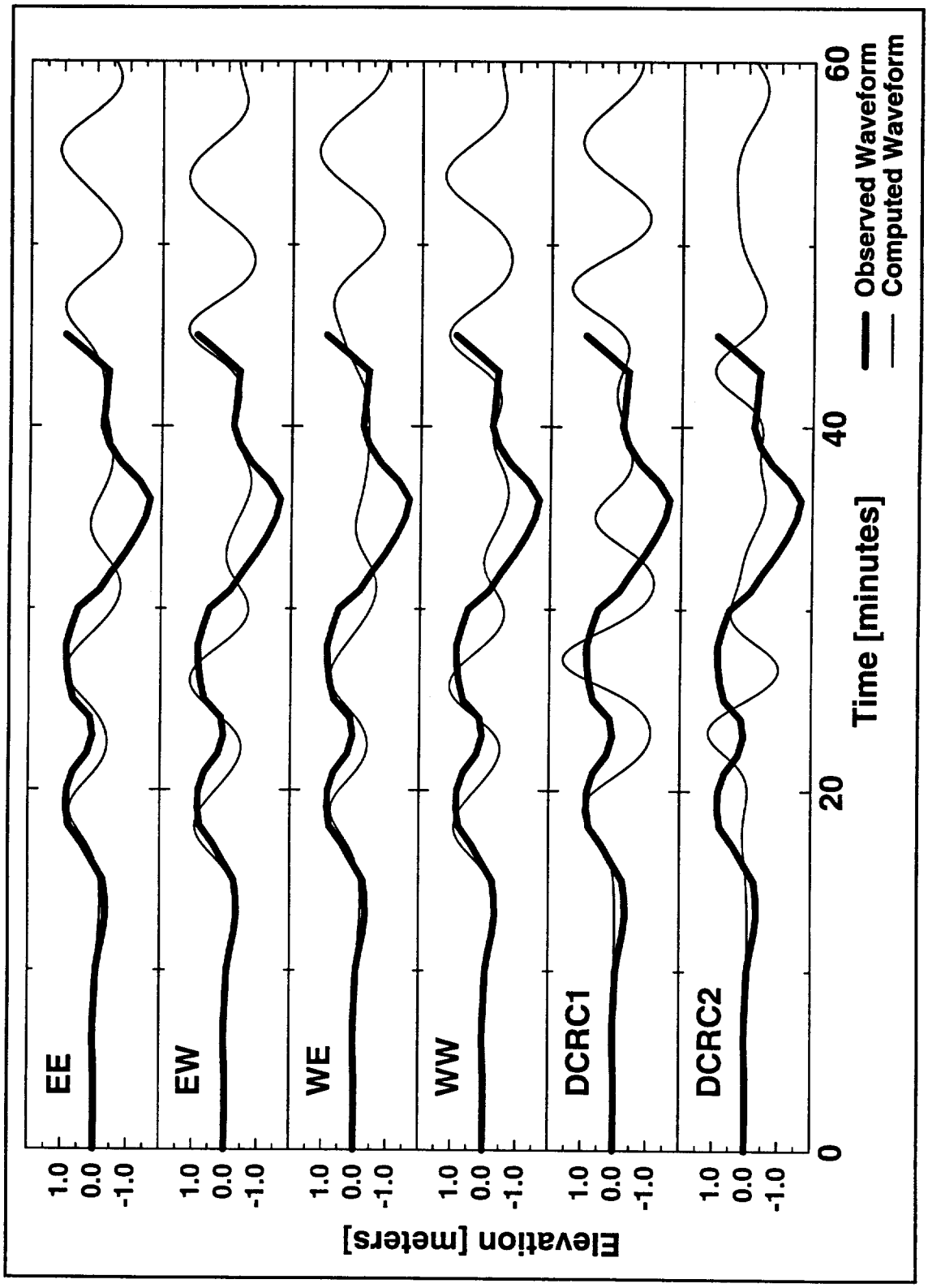

FIGURE 3.42 Numerical Results and Observed Waveforms at Esashi

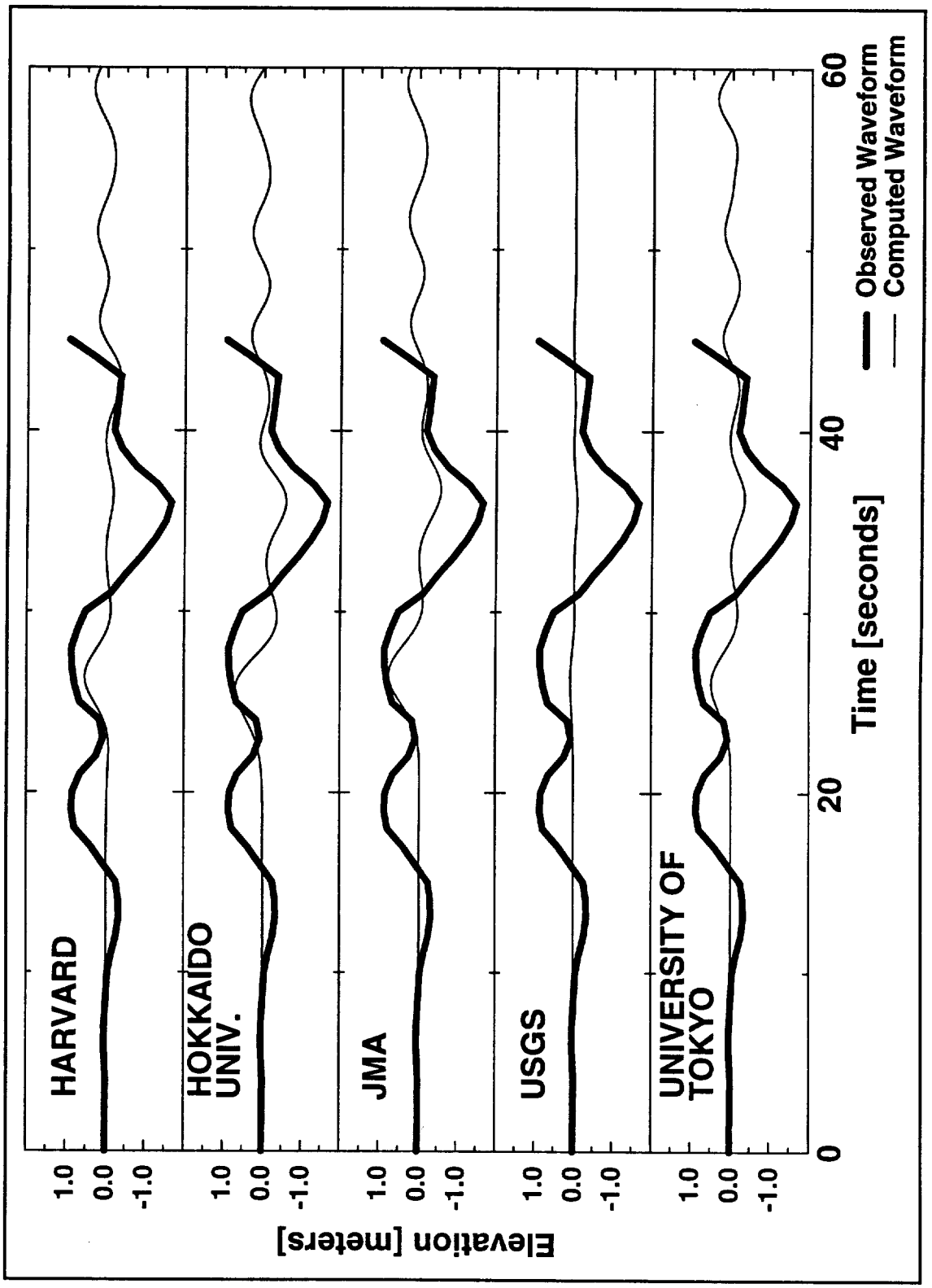

FIGURE 3.43 Numerical Results and Observed Waveforms at Awashima

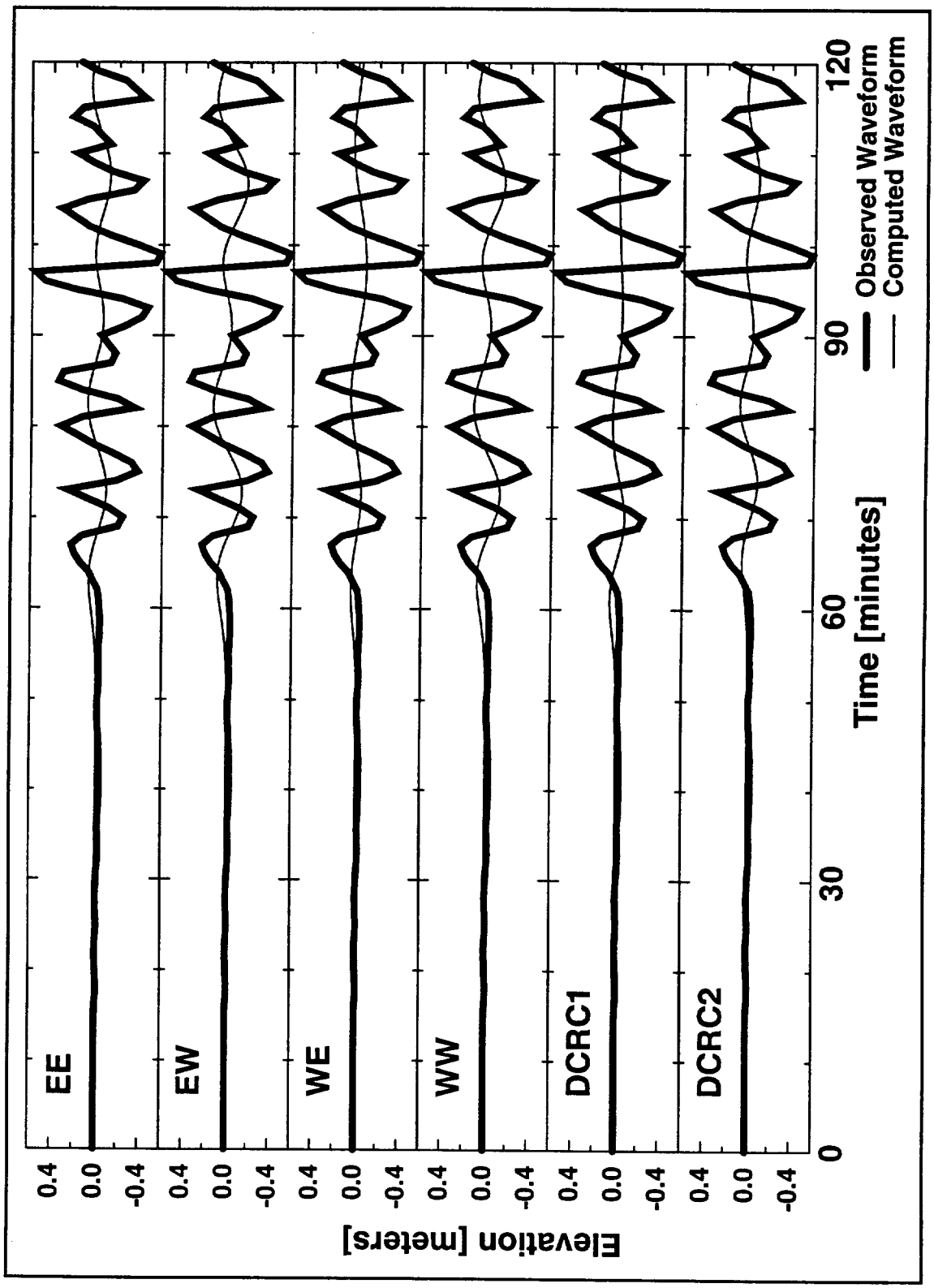

FIGURE 3.44 Numerical Results and Observed Waveforms at Awashima

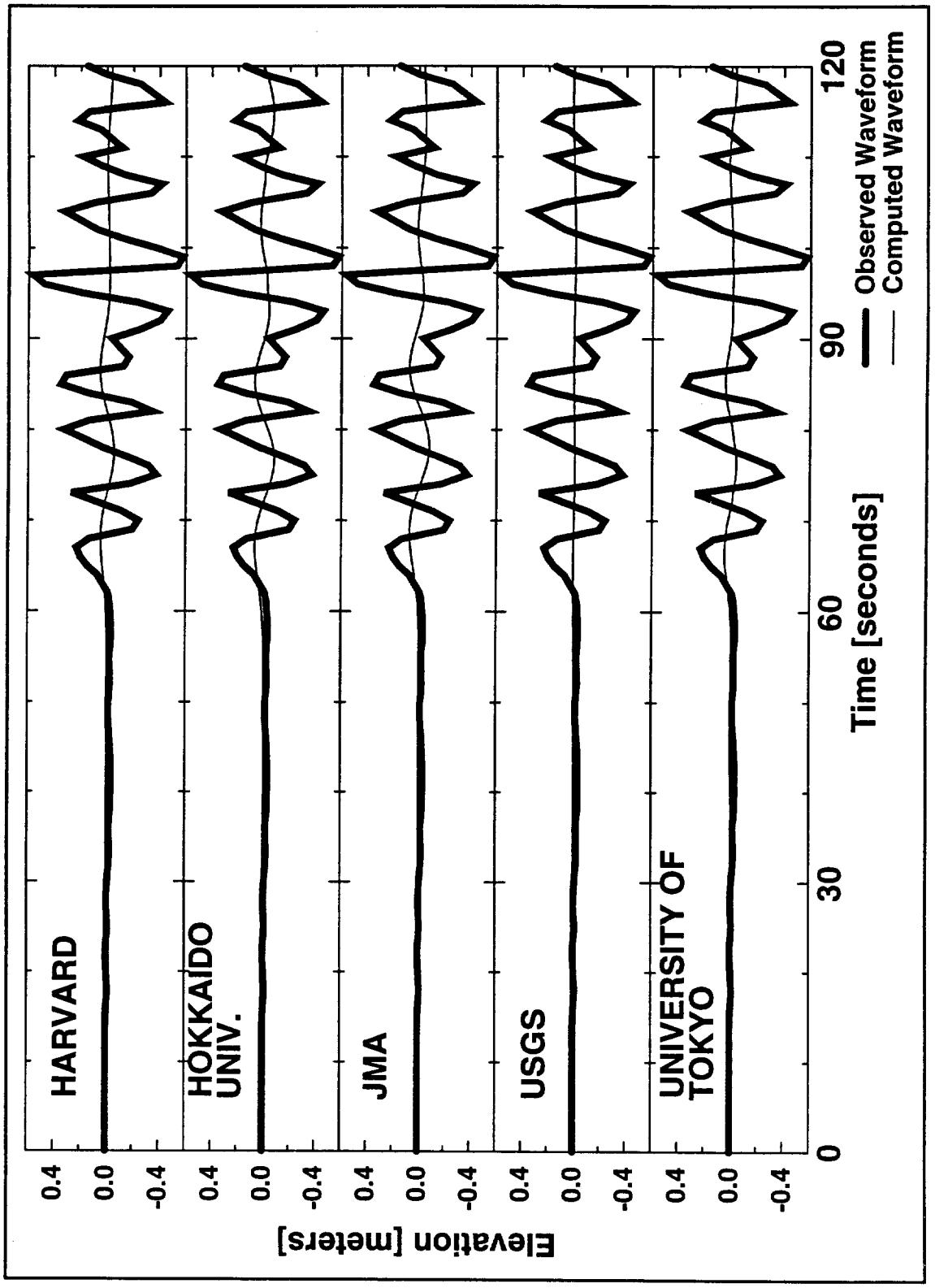

FIGURE 3.45 Minimum Bathymetry and Grid Refinement Results at Iwanai

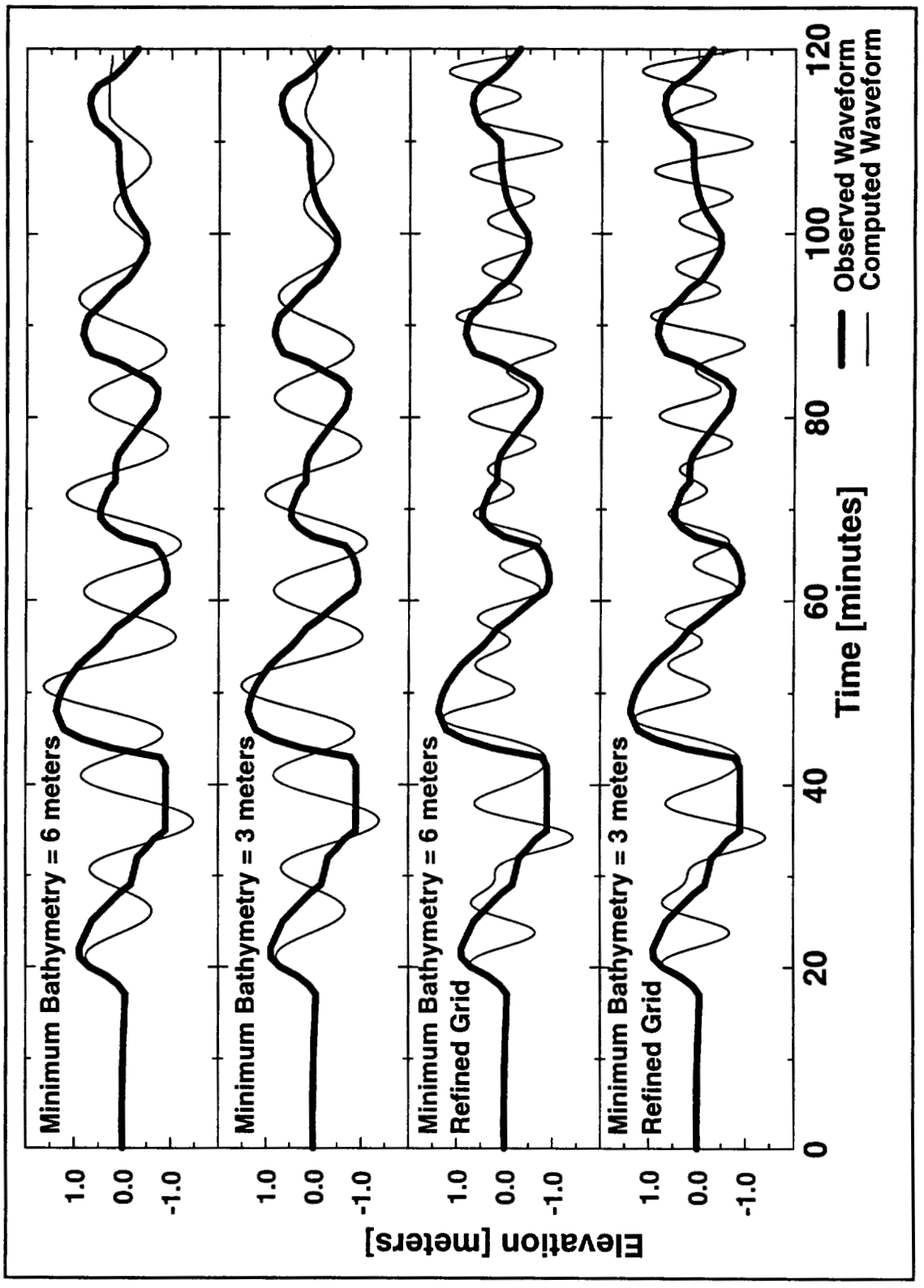

FIGURE 3.46 Minimum Bathymetry and Grid Refinement Results at Esashi

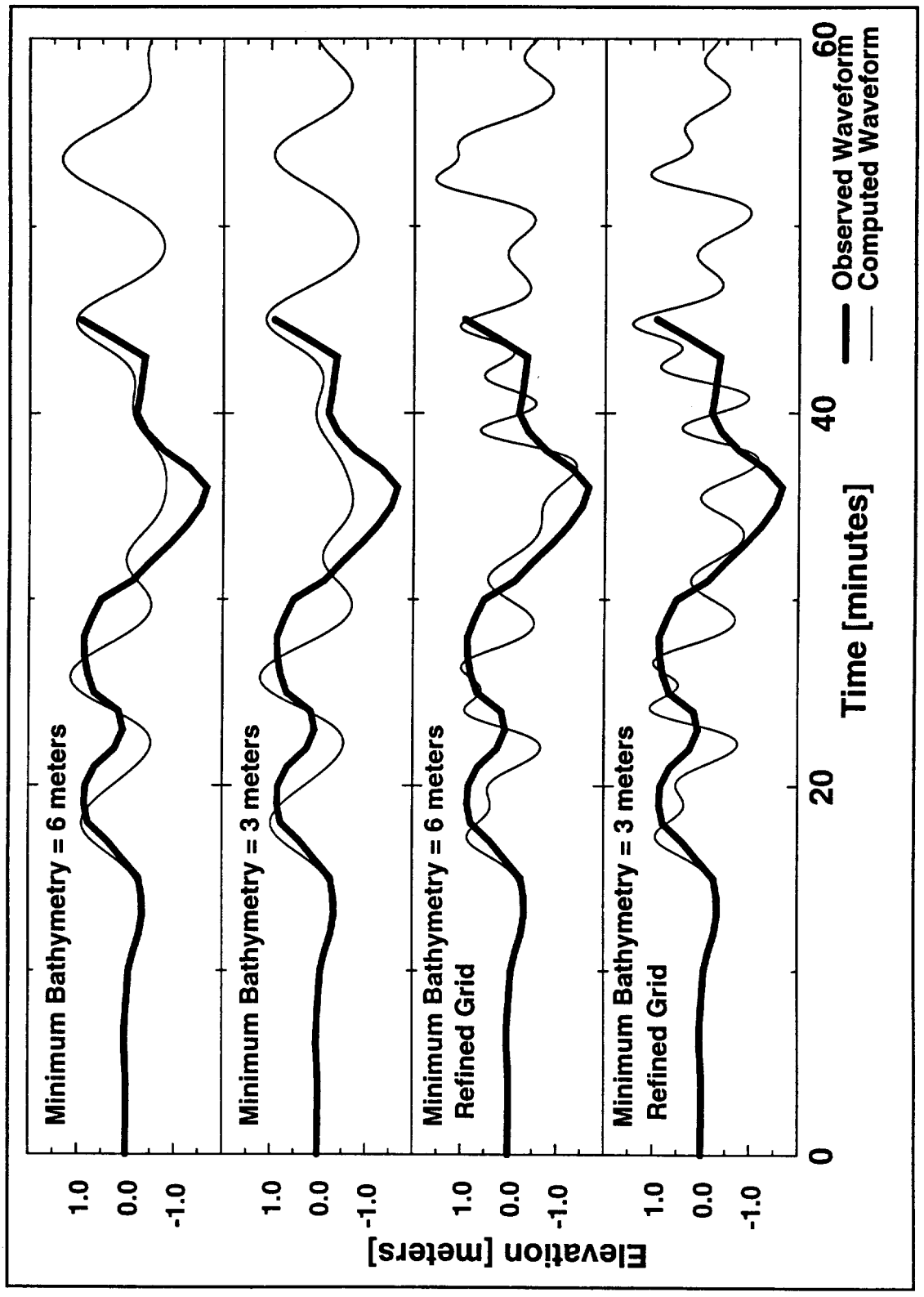

FIGURE 3.47 Minimum Bathymetry and Grid Refinement Results at Awashima

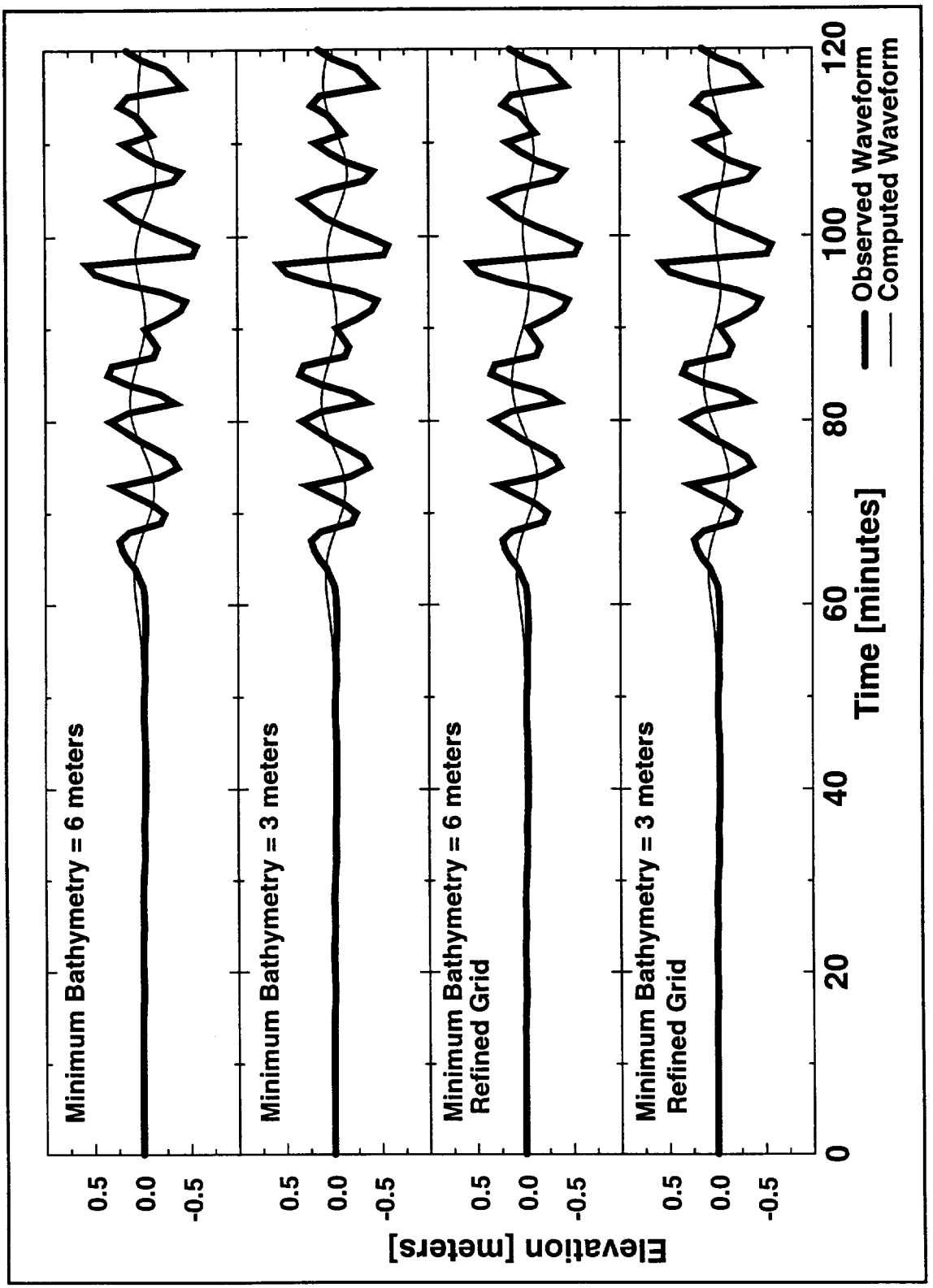

FIGURE 3.48 Comparisons of Source WW Results with Observed Waveforms

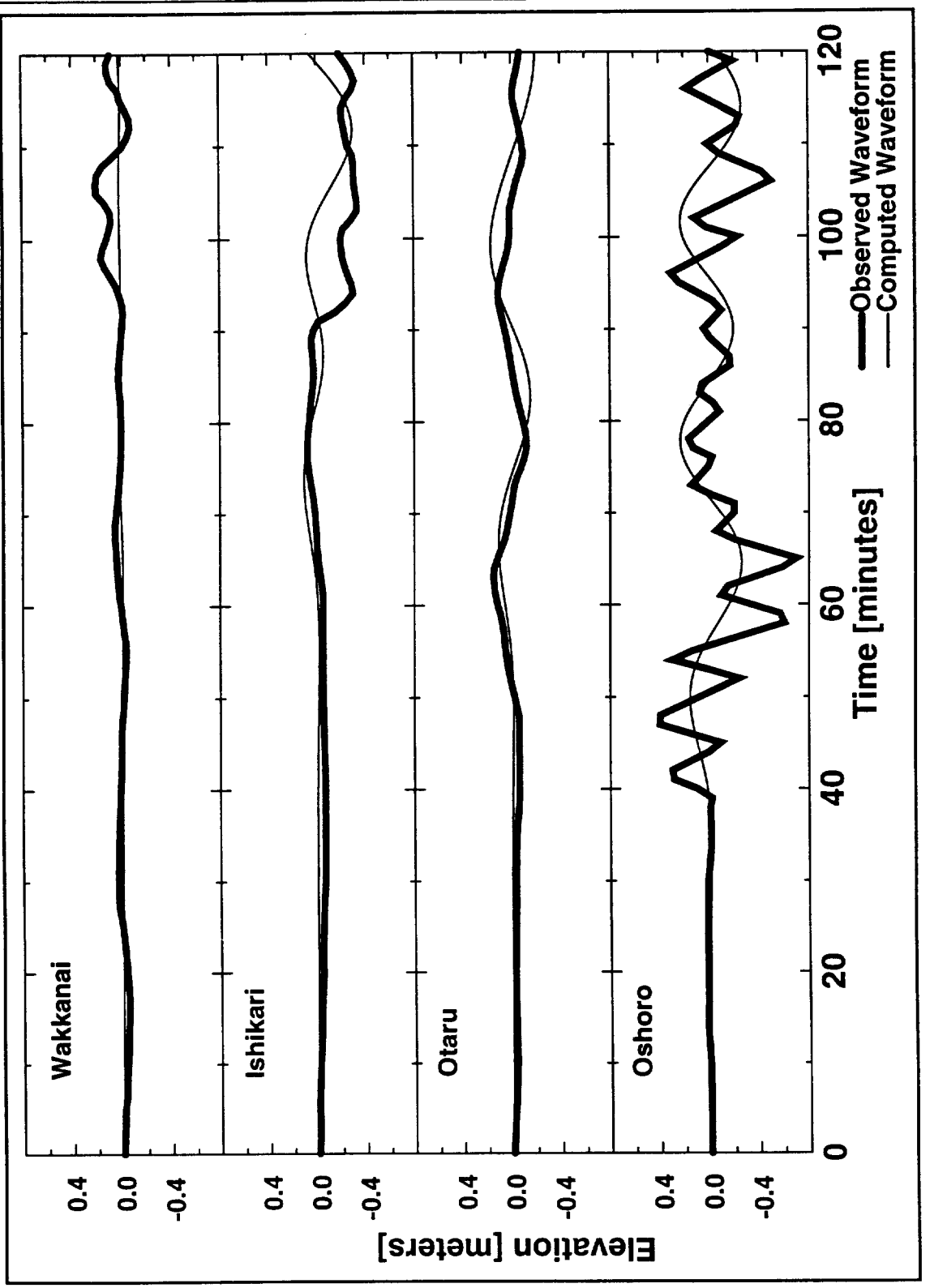

FIGURE 3.49 Comparisons of Source WW Results with Observed Waveforms

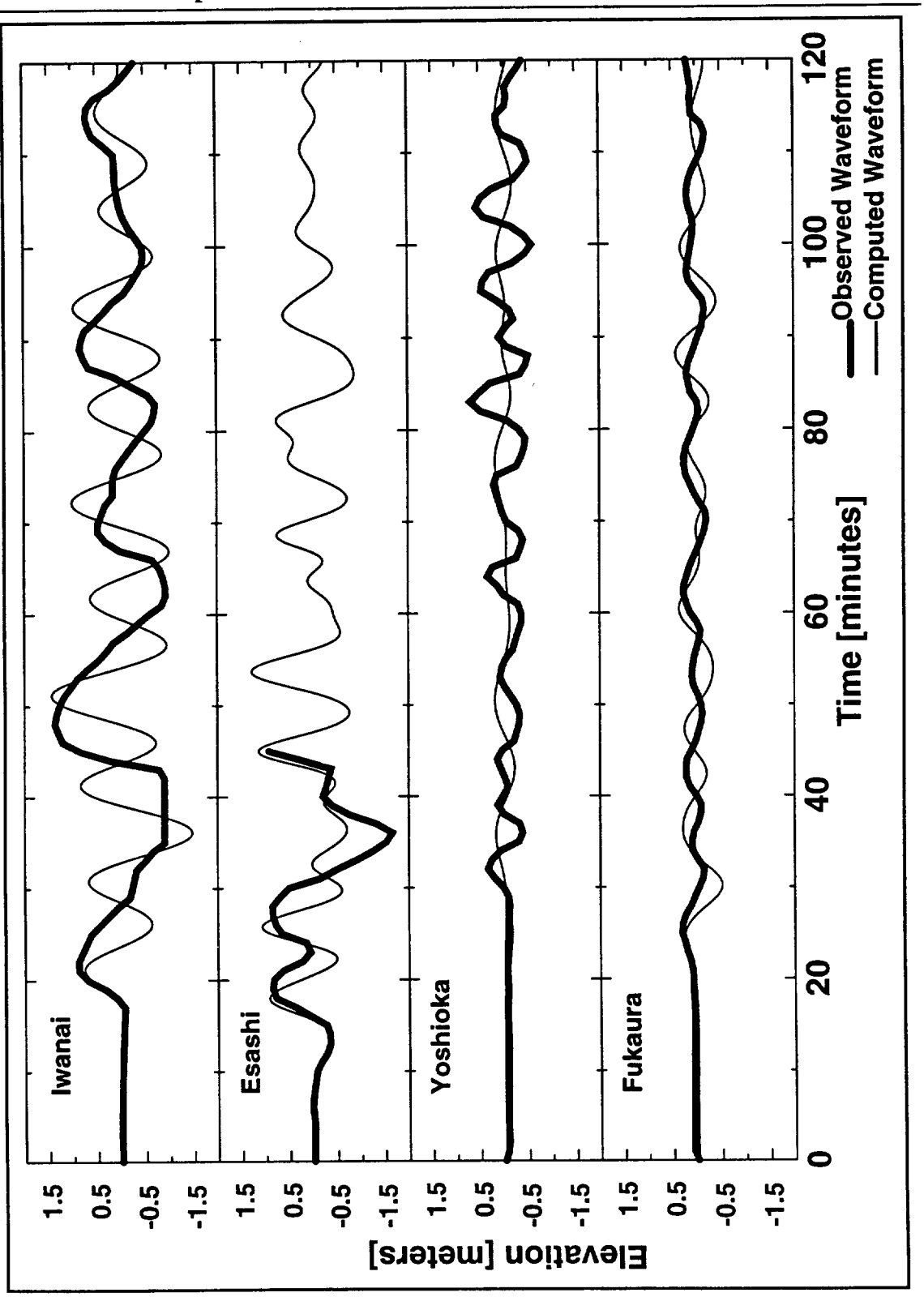

FIGURE 3.50 Comparisons of Source WW Results with Observed Waveforms

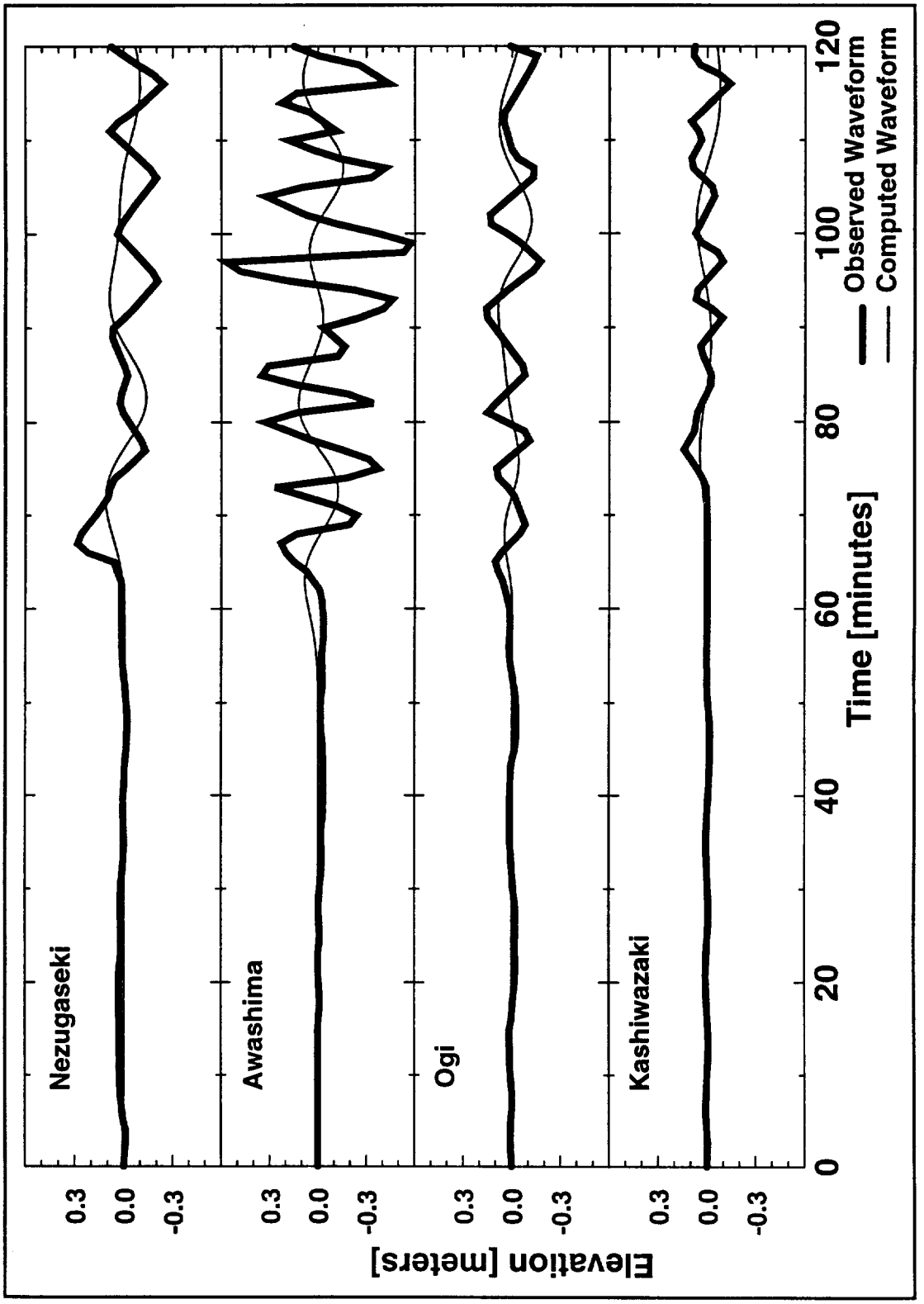

FIGURE 3.51 Comparisons of Source WW Results with Observed Waveforms

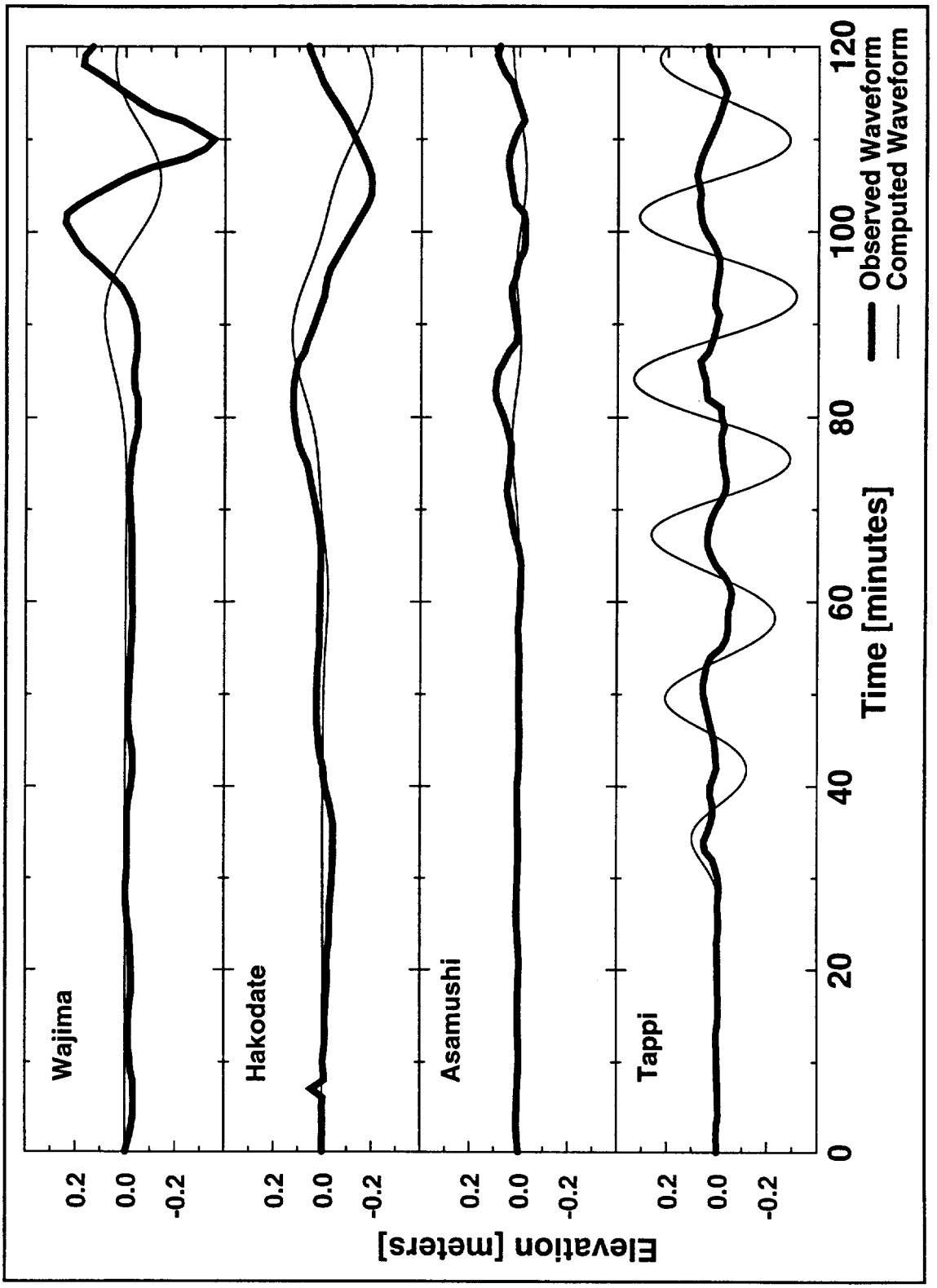

FIGURE 3.52 Propagation of Energy Over Time for WW Simulation

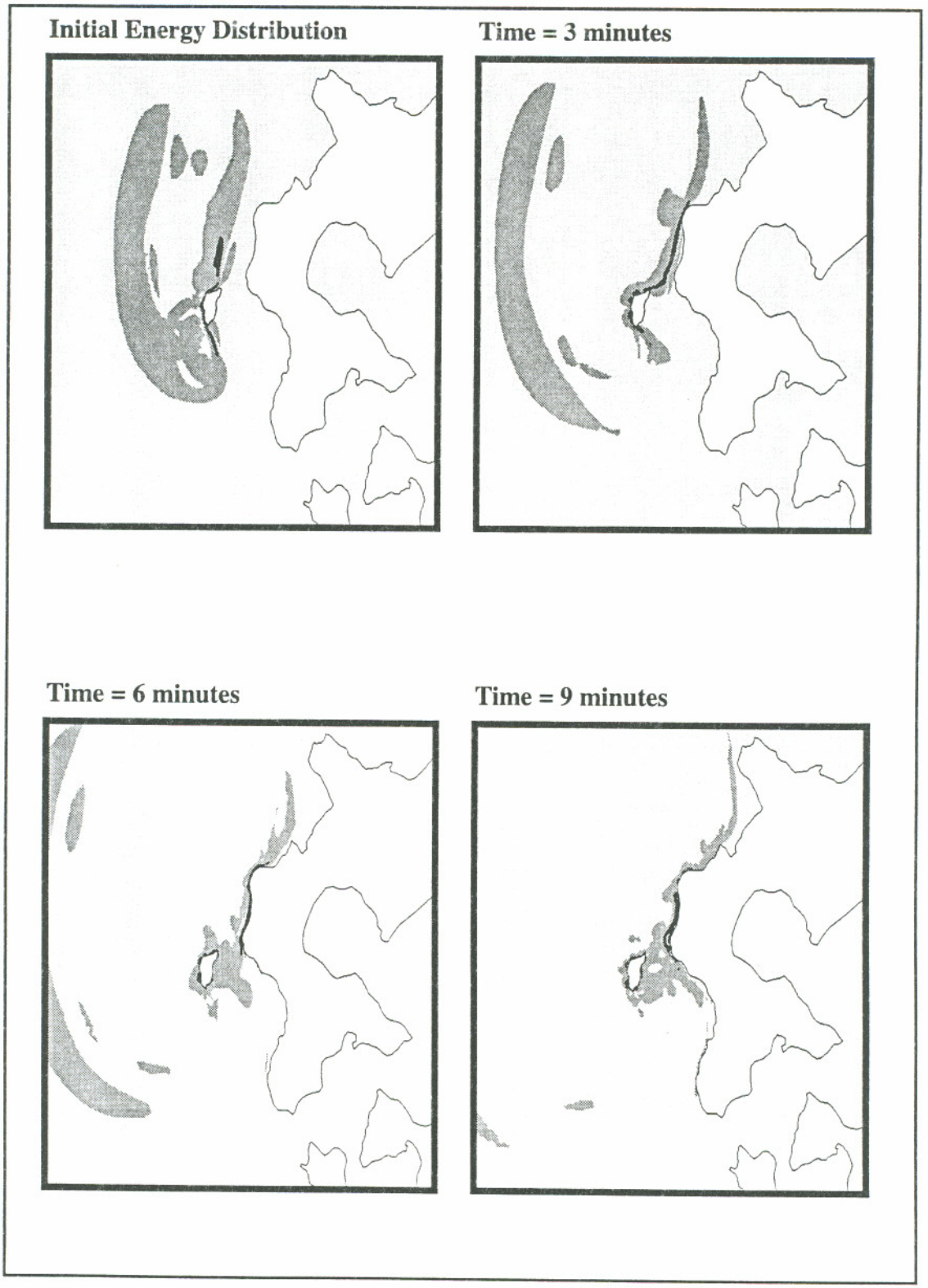

FIGURE 3.53 Propagation of Energy Over Time for WW Simulation

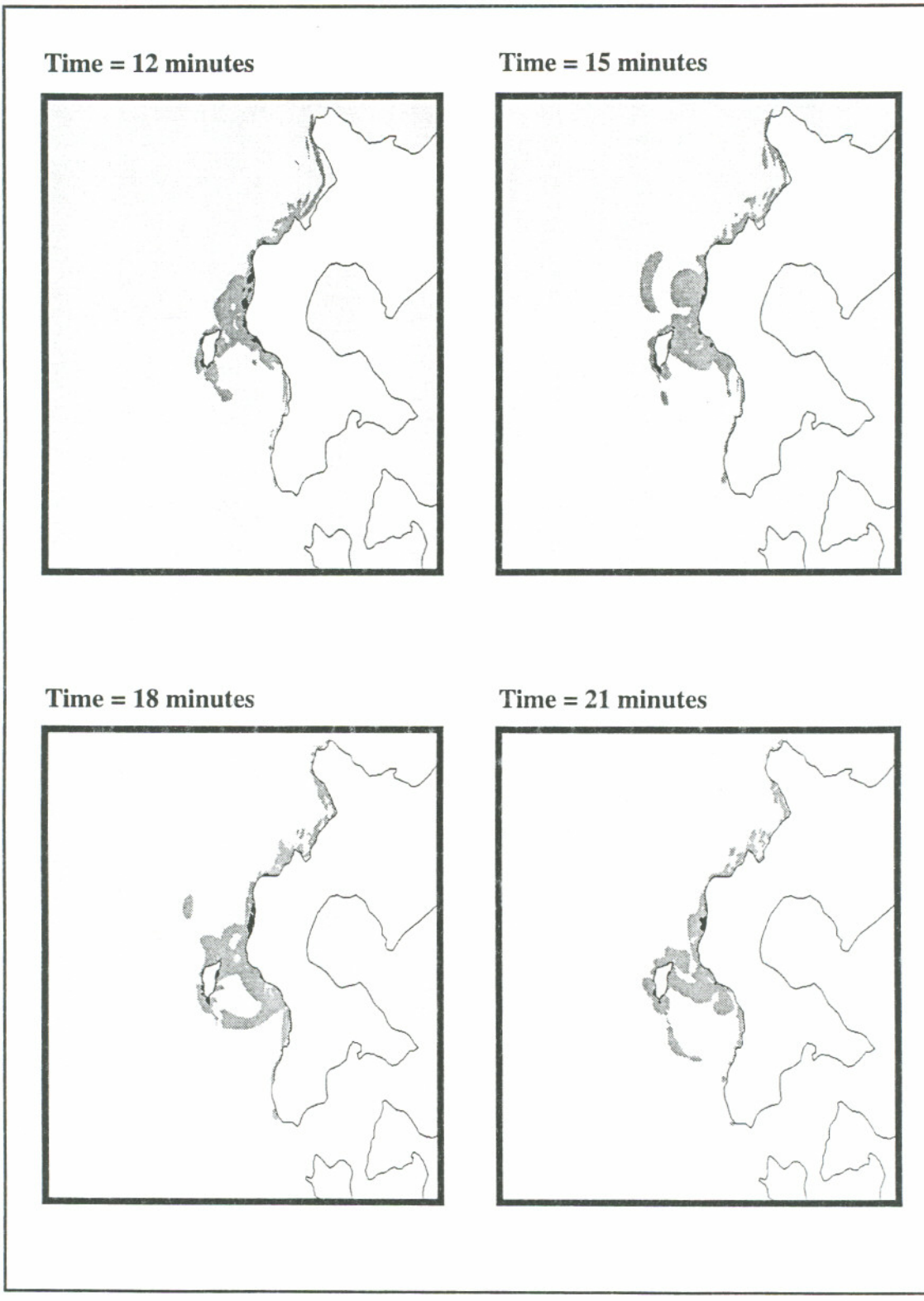

FIGURE 3.54 Isolines of Maximum Energy and Run-up Measurements

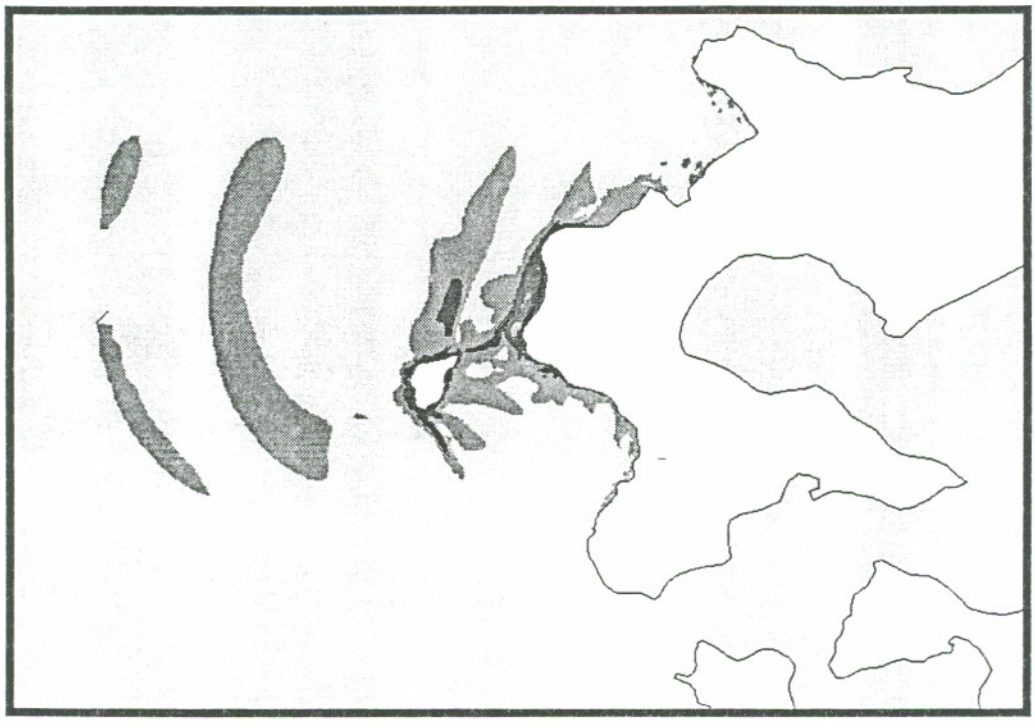

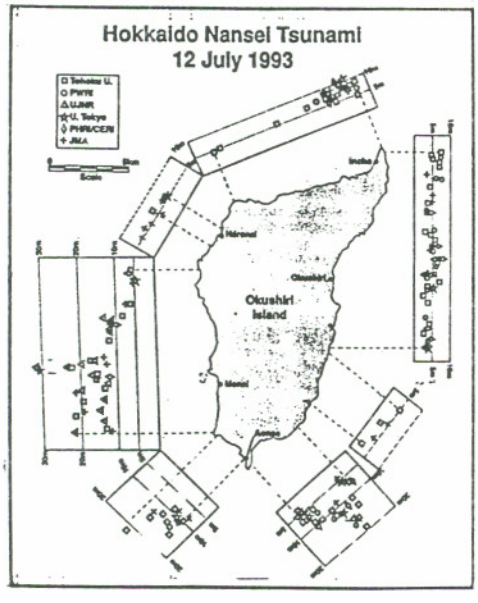

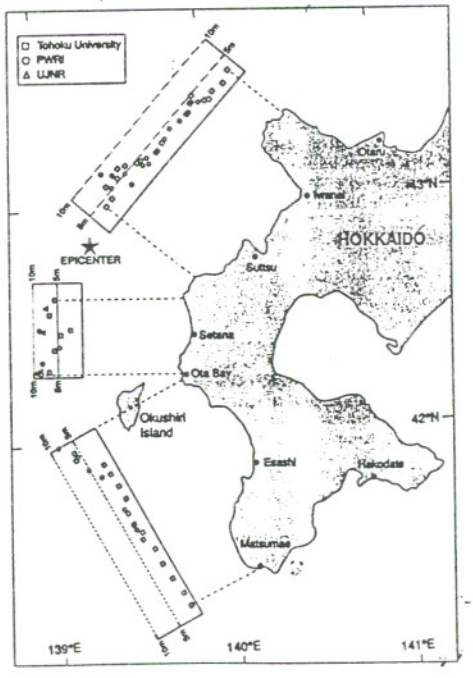

FIGURE 3.55 Computed Maximum Wave Elevations Along Okushiri

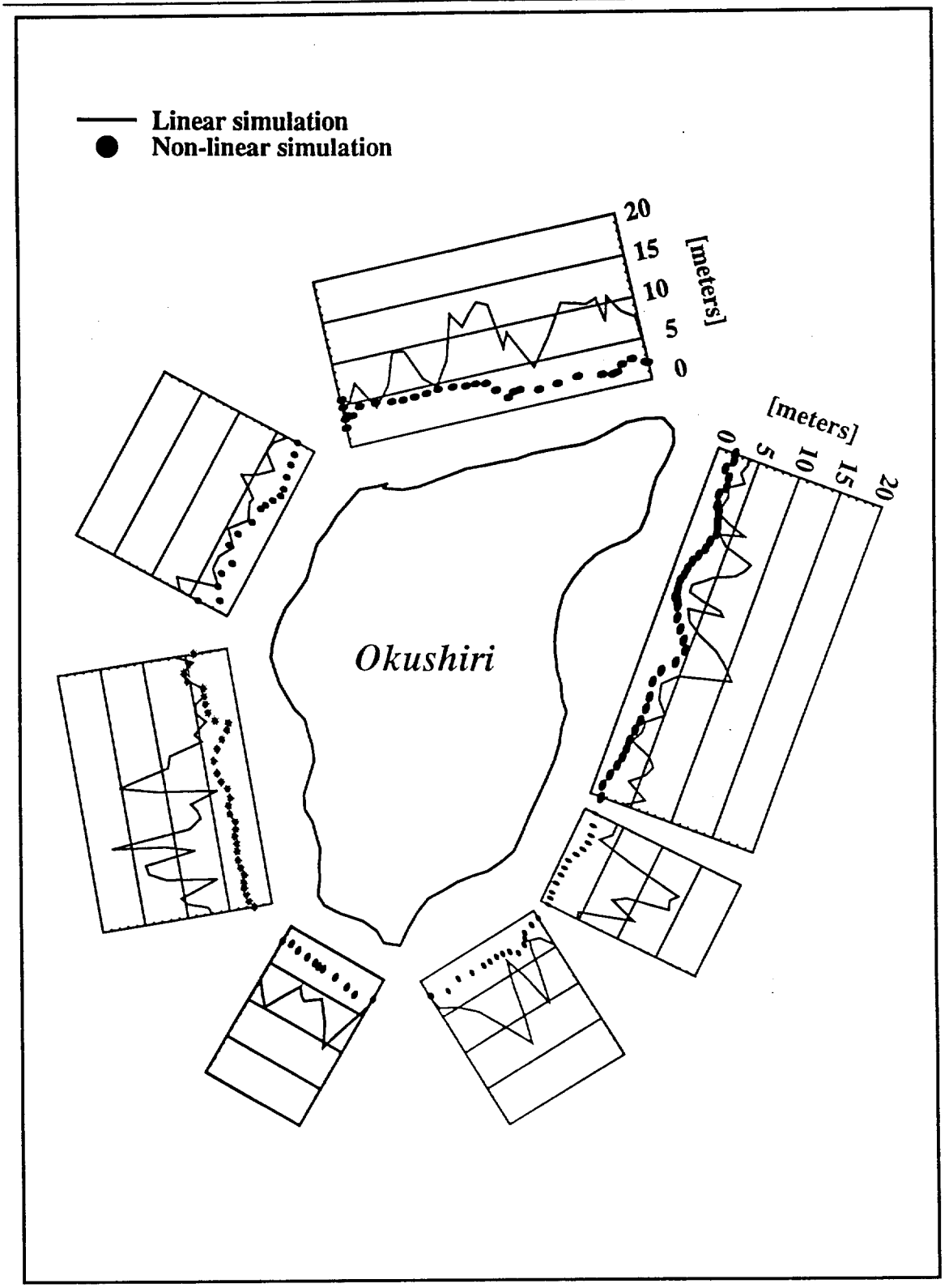

FIGURE 3.56 Computed Maximum Wave Elevations Along Hokkaido

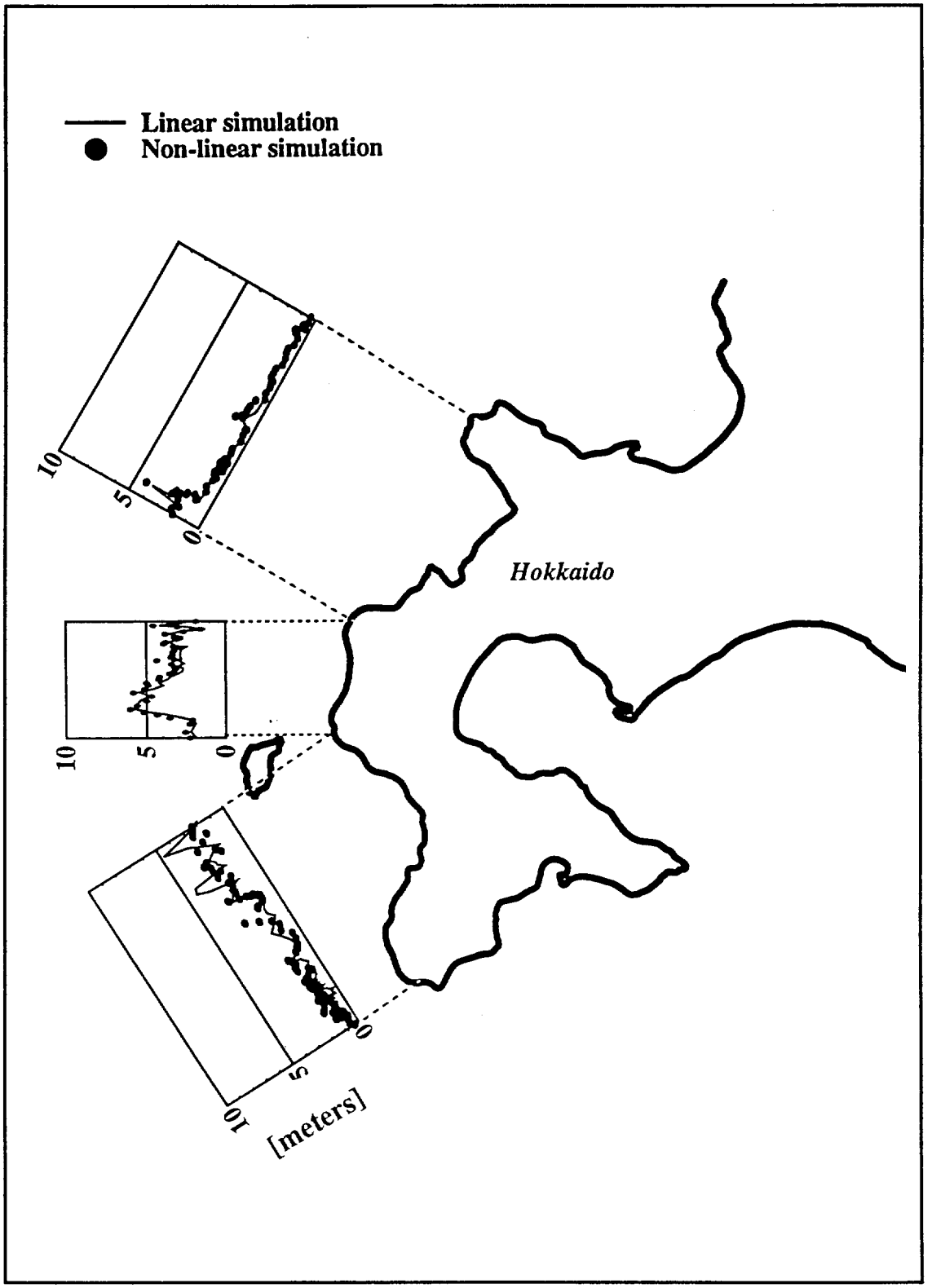

CHAPTER 4

Modeling Potential Pacific Northwest Tsunamis

Seismic Source Scenarios

Two seismic source scenarios were considered for potential subduction events in the Pacific Northwest. The first is a moment magnitude 8.8 earthquake with a source area of 650 km x 80 km. The sea floor deformation which extends from the middle of the Washington coast to northern California is displayed in Figure 4.1. The deformation for this event ranges from -2.0 meters to 4.13 meters. The second seismic source scenario was recommended for an Oregon tsunami preparedness exercise called Quakex. The scenario was recommended by Oregon geologists as a likely event for the Cascadia Subduction Zone. The deformation for this event is displayed in Figure 4.2, with a maximum deformation ranging between -1.39 meters and 3.71 meters. The various parameters used to generate the sea floor deformations for these two events are listed in Table 4.1.

The computed deformations can be compared with actual data pertaining to prehistoric tsunamis. Such data includes the analysis of what types of ecosystems appeared to have existed at various places at the time of subduction. For example, certain species of trees and plants will only grow at certain levels with respect to mean sea level. By taking core samples at various points and analyzing which types of species existed in those core layers, an estimate of the coastal coseismic subsidence may be made. Table 4.4 displays some of these estimated values of subsidence for parts of the Oregon and Washington coastal regions [*Peterson*, 1994]. Also shown in Table 4.4 are the computed subsidence for the two seismic source scenarios considered here.

TABLE 4.1 Source Parameters Used for Seismic Source Scenarios

M_W	Length (km)	Width (km)	Strike	Dip	Rake	Depth (km)	Slip (m)
8.8	650.0	80.0	358.0	13.0	90.0	20.0	9.61
8.5	375.0	70.0	360.5	13.0	90.0	0.00	6.74

The comparisons between computed subsidence and estimated subsidence clearly indicates differences in the magnitudes. A couple of factors may be responsible for such discrepancies. First, the location of the computed seismic sources may be too far to the west. For example, if the location of the sources is moved a little to the east, the magnitudes of the deformation will increase significantly. Also, the magnitude of the prehistoric earthquakes may be much larger than what is used in the computations.

Calibration

Calibration of a numerical model for Pacific Northwest tsunamis is limited by the fact that available data consist of prehistoric evidence of past subduction events. Therefore it is not possible to determine appropriate friction and diffusion factors for the numerical model as applied to tsunamis. However, it was shown in Chapter 3 that the differences in the error measure used to compare the effect of different values of these parameters are relatively small for the numerical simulations considered. Thus, it is reasonable to select characteristic values for the friction factor and the diffusion coefficient. For the simulations considered here in this chapter, a Manning coefficient of 0.03 and a diffusion coefficient of 1.0 m^2/sec were selected. Calibration can be performed for the GWCE weighting factor by checking mass conservation. The finite element grid used for the Pacific Northwest is displayed in Figure 4.3. Results from the calibration are shown in Figures 4.4-4.6, which indicate that a weighting factor of 0.08 appears to do the best with regards to conserving mass while remaining numerically stable. This value for the weighting factor is smaller than that which was selected for the Sea of Japan simulations which was 0.3.

Numerical Results

The raytracing program used for the Sea of Japan was likewise applied to the Pacific Northwest to look at wave channeling effects due to regional bathymetry. Bathymetry used for the program consists of the ETOPO-5 database, NOAA/NOS hydrographic data, and digitized NOAA bathymetric maps from 1968. Figure 4.7 shows the raytracing results from two initial point sources located off the coast of Oregon. The two points correspond roughly with the northern and southern portions of the Cascadia Subduction Zone. Although this certainly does not indicate the wave propagation resulting from a seismic source, it serves to indicate possible wave propagation patterns which may result from local bathymetric effects. An interesting aspect of the raytracing results is the manner in which the rays are "pulled" toward the northern California coast due to the bathymetry in the final time steps. Crescent City, CA has been known to focus energy due to local bathymetry and the orientation of the coastline.

Using the initial conditions for the two seismic sources, computer simulations using ADCIRC-2DDI were performed using the grid in Figure 4.3. Figures 4.8 and 4.9 show computed energy and mass errors for these two cases. The results show the same general trend as those from the Sea of Japan simulations. The energy peak which is achieved over the time steps of deformation is less than the theoretical tsunami energy for both of the seismic scenarios. Using the expressions for theoretical tsunami energy provided in Chapter 2, Table 4.2 shows this comparison between computed and theoretical tsunami energy:

TABLE 4.2 Comparison of Theoretical and Computed Tsunami Energy

Event	Theoretical Tsunami Energy	Computed Tsunami Energy
8.5	3.459 e+14	0.700 e+14
8.8	1.377 e+15	3.219 e+14

There is a significant decrease in total energy during the first ten minutes or so which tapers off into a slight decrease after that point. Mass error for the $M_W = 8.5$ scenario appears to be reasonable for the first two hours. However after that point, mass is progressively introduced so much that after six hours there is approximately 45% (of the initial volume of deformation) additional mass in the system. This is unreasonable for numerical simulations, and therefore only the results from the first two hours should be focused upon. The mass error for the $M_W = 8.8$ scenario likewise is fairly reasonable for the first two hours, after which point too much mass begins to accumulate in the system (up to 18% of the initial volume of deformation).

The energy diagrams in Figures 4.8 and 4.9 show two sharp declines in energy throughout the simulation. The first one occurs just after the initial conditions are imposed, and the second occurs about 30 minutes into the simulation. The first is interpreted to occur due to the fact that the shallow water equations are neglecting pressure due to vertical accelerations. The second sharp decrease is believed to result from the wave exiting the transmissive boundary, since the wave reaches this boundary at about the same time. The gradual decreases in energy which occur at other times are thought to be related to the interaction of the waves with land boundaries, where again vertical accelerations will be important. A more detailed discussion of these energy considerations is provided in Chapter 5.

The effect of the transmissive boundaries on mass and energy variation is examined by simulating the M_W=8.8 scenario using a grid in which all boundaries are land boundaries. The results for this test are displayed in Figure 4.10. As can be seen, the mass variation which had occurred before was due to the use of transmissive boundaries. This was also observed for the Sea of Japan, thus offering more reason to believe that it is the transmissive boundary formulation which is not conserving mass. As was mentioned in Chapter 3, this may be due to the fact that the continuity equation is not strictly obeyed in the enforcement of transmissive or amplitude/phase specified boundaries. Some energy leaves the domain as the waves interact with the transmissive boundaries, as expected. In

particular, the second sharp decline in energy which had been observed before is seen to be a result of energy leaving through the transmissive boundary.

Figures 4.11 and 4.12 show the isolines of energy for the two cases. As in the figures in Chapter 3, the darker regions reflect higher energy levels. The important aspect of these figures is the distribution of energy over the domain, and therefore numbers were not placed alongside the isolines. As may be seen, the energy is fairly well distributed off (mainly) the Oregon coastline through the first 20 minutes of the simulation for both cases. The image at 20 minutes is revealing in the fact that the isolines seem to show which parts of the coastline appeared to gather the most energy. For the $M_W = 8.5$ event, these areas include the Oregon coastline (except in the south) and the southern coastline of Washington. For the $M_W = 8.8$ event, they include the southern portion of Washington, northern California (particularly near Crescent City, CA), and the Oregon coastline except between North Bend and Port Orford. Interestingly, Crescent City is an area which was affected by the 1964 Alaska tsunami due to the geometry of the region and local bathymetry. As can be seen from Figures 4.11 and 4.12, the energy distribution at 40 and 50 minutes is quite 'patchy', and appears to have been significantly dissipated due to the interaction with the coastline for both cases. Local energy effects may further be seen in Figure 4.13, which shows the isolines of maximum energy throughout the entire simulation for both cases.

Looking back to Figures 4.1 and 4.2, it may be seen that the deformation to the sea floor is oriented almost directly to the north. However, the deformation in general occurs in deeper water to the north and shallower water to the south. Initial waveforms which are located in deeper water will result in higher coastal waveforms than the same waveforms which commence in shallower water. Therefore, coastal wave heights should be larger in the northern part of Oregon and the southern part of Washington. Although coastal wave heights will in general be smaller in southern Oregon, they will arrive in a shorter amount of time (most likely on the order of 5 to 10 minutes). In northern Oregon and southern Washington, arrival times will most likely be on the order of 15 to 20 minutes. The maximum coastal wave heights have been plotted in Figures 4.14 and 4.15 and show this trend

of larger wave heights in northern Oregon and southern Washington tapering off as one heads south. These plots also show some local effects mentioned before with regards to localization of energy. For example, the M_W=8.8 case shows the large wave heights in the Crescent City, CA region.

Figures 4.16-4.30 show some waveforms at various coastal locations generated by the numerical simulations. The amplitudes and arrival times are similar to those generated by Whitmore [1992] for the M_W=8.8 case. A comparison among results for a few locations between Whitmore's results and those presented here is shown in Table 4.3.

TABLE 4.3 Comparison of Results with Whitmore's Simulations

	Maximum Wave Height [feet]		Time of First Crest [minutes]	
Location	Whitmore	M_W=8.8*	Whitmore	M_W=8.8*
Cannon Beach, OR	18	22	38	37
Long Beach, WA	21	20	33	25
Astoria, OR	2	4	60	50

* M_W=8.8 results from this thesis

As can be seen, the arrival times of the first crest are approximately ten minutes different for Long Beach, WA and Astoria, OR. This may be a result of different coastal discretizations or different bathymetry representations.

The upper right image in each of Figures 4.16-4.30 is a focus on the first two hours of the simulation, whereas the lower figure shows the continuation of wave action through six hours. As was mentioned, significant mass error occurs after approximately two hours, and therefore the waveforms for these first two hours should be evaluated. A few important conclusions may be drawn from these figures. First, the wave activity at coastal locations will last many hours. Second, it is the trough of the wave which will arrive first in virtually all instances. Finally, the largest wave may be any of these waves and thus may arrive much later in time than the first wave. Many fatalities in tsunami events occur due to these three reasons. People may become curious as to why the water has receded and

will try to go out on the exposed seabed, try to retrieve boats, etc. At that point, the crest of the wave will soon be arriving, thus leaving no chance for escape. Those that do run inland and avoid the first wave may think it is safe to go back to their coastal communities when in reality more waves (and quite possibly larger) will be arriving for hours. The best way to prevent such disasters is to raise public awareness with regards to the three safety concerns mentioned above. It is particularly important that emergency teams are aware of them, for if they fall victim to the tsunami, the people will have no emergency help.

References

Peterson, C.D., *personal communication, 1994.*

Whitmore, P.M., Hypothetical Cascadia Tsunamis, *Alaska Tsunami Warning Center,* August 1992.

FIGURE 4.1 Sea Floor Deformation for Mw = 8.8 Seismic Source

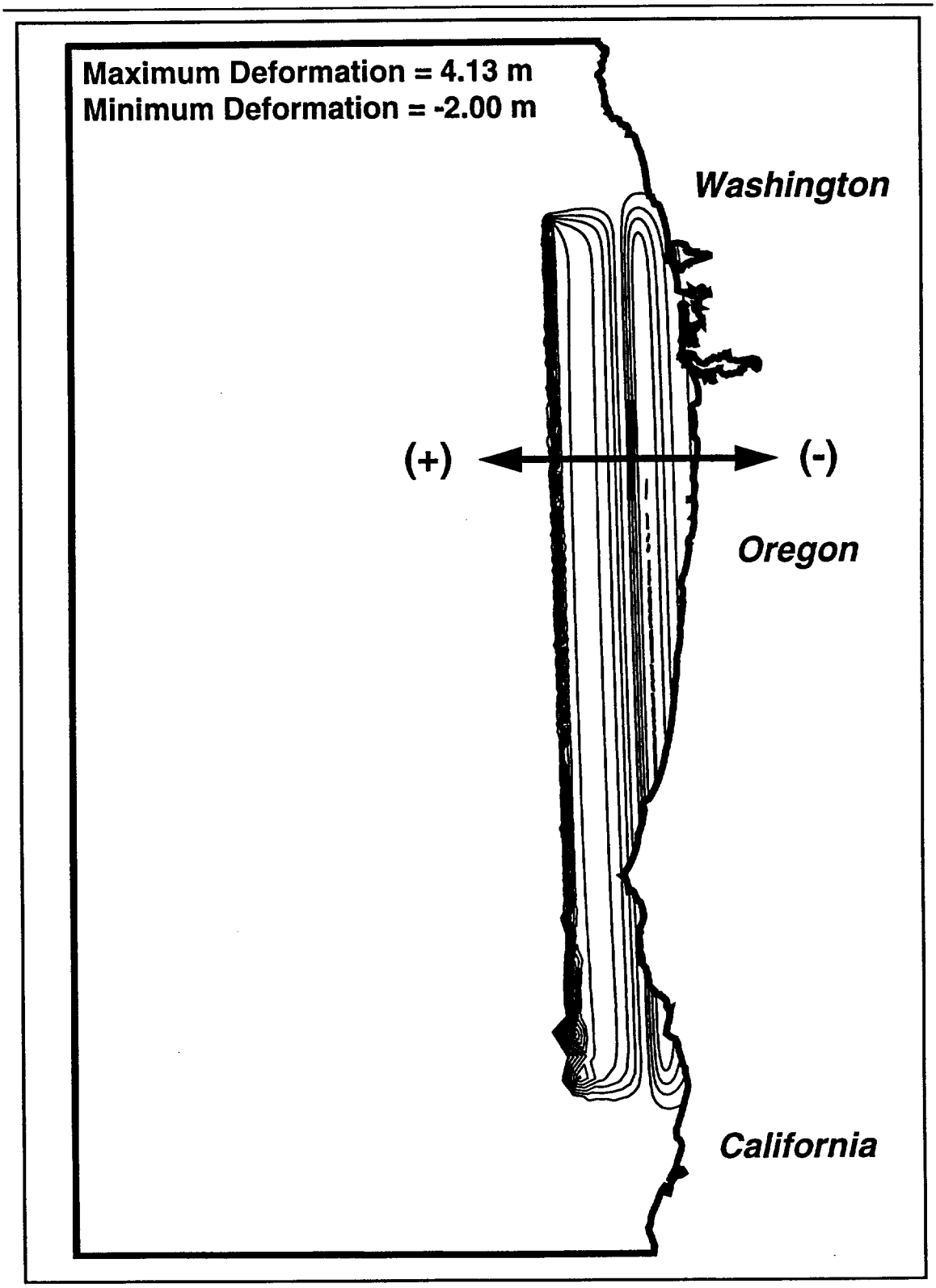

FIGURE 4.2 Sea Floor Deformation for M_W = 8.5 Seismic Source

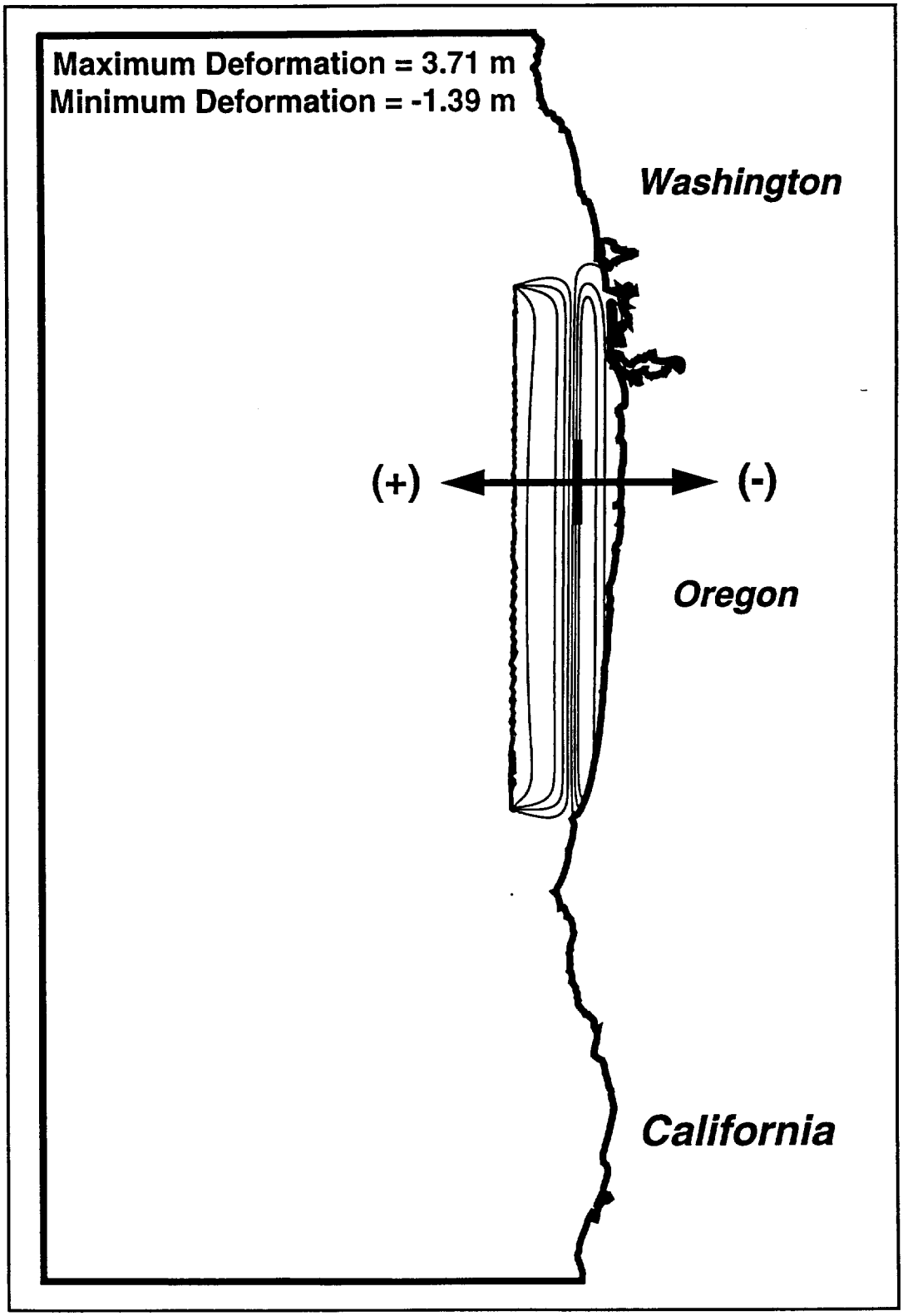

TABLE 4.4 Computed Deformation Compared with Estimated Subsidence

Site of Evidence	Computed Subsidence (meters) Mw=8.8	Mw=8.5	Estimated Subsidence (meters)
Copalis, WA	0.48	0.06	1) 0.5-1.5 2) >1.5
Grays Harbor, WA			
1) Aberdeen	0.11	0.04	>1.5
2) Chenois Creek	0.29	0.07	>1.5
3) Chelahis River	0.09	0.03	>1.5
4) Blue Slough	0.09	0.03	>1.5
5) Johns River	0.26	0.09	0.5-1.5
	0.29	0.10	0.5-1.5
	0.27	0.10	0.5-1.5
Willapa Bay, WA			
1) South Bend	0.11	0.05	0.5-1.5
2) Bear River	0.29	0.22	>1.5
3) Bay Center	0.27	0.18	>1.5
4) Niawiakum	0.22	0.13	>1.5
5) Oysterville	0.37	0.29	>1.5
Young's Bay, OR	0.21	0.14	0.5-1.5
Columbia River			
1) Blind Slough	0.08	0.04	>1.5
2) Skamokawa	0.05	0.02	<0.5
3) Cathlamet	0.04	0.01	0.0
Necanicum, OR	0.27	0.19	0.5-1.5
Netarts, OR	0.37	0.25	0.5-1.5
Nestucca, OR	0.35	0.23	0.5-1.5
Siletz, OR	0.54	0.36	0.5-1.5
Yaquina, OR	0.34	0.18	0.5-1.5
Alsea, OR	0.46	0.25	<0.5

FIGURE 4.3 Finite Element Grid Used in Numerical Simulations

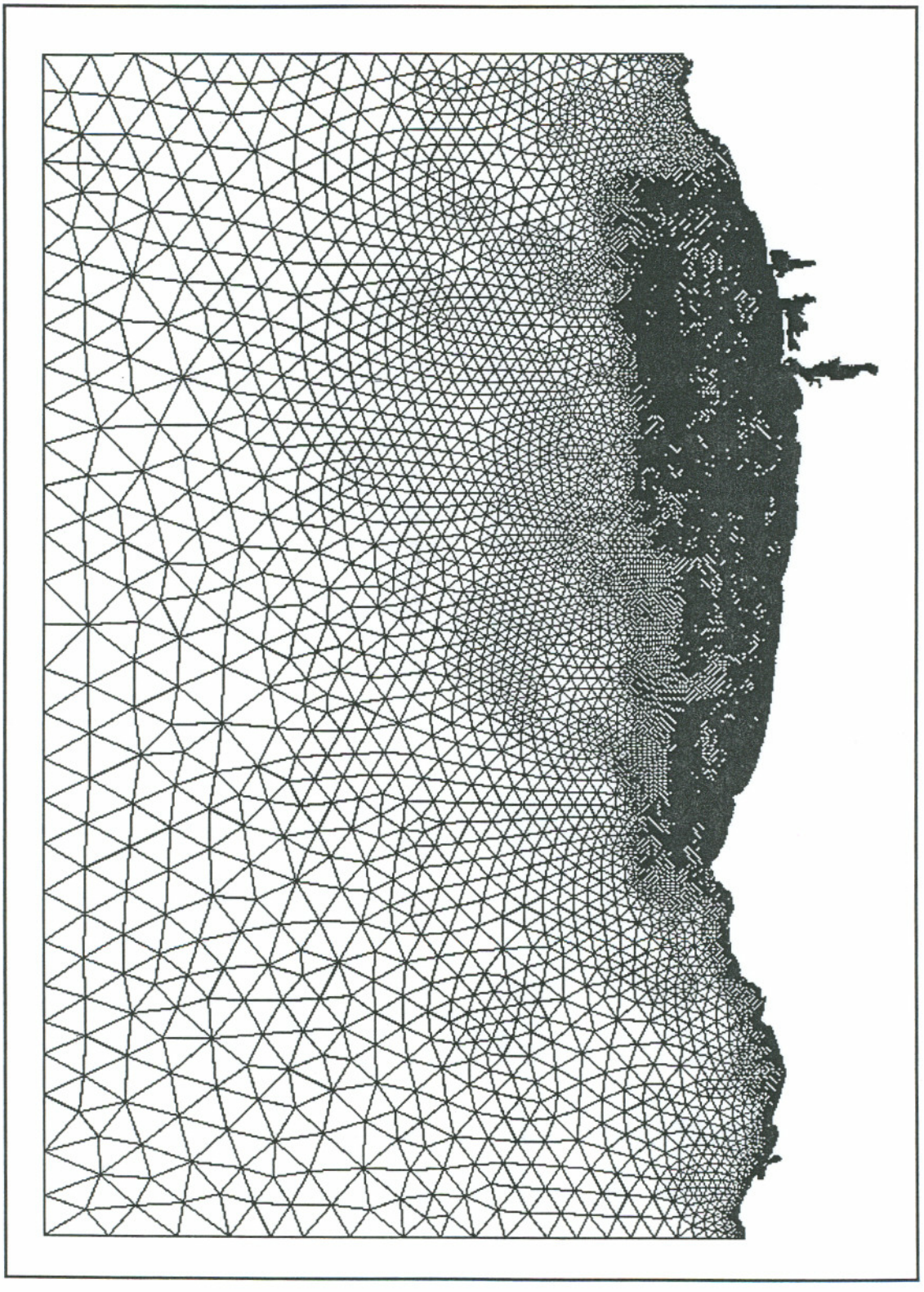

FIGURE 4.4 Mass (Scaled by Volume of Deformation) Conservation Over Time

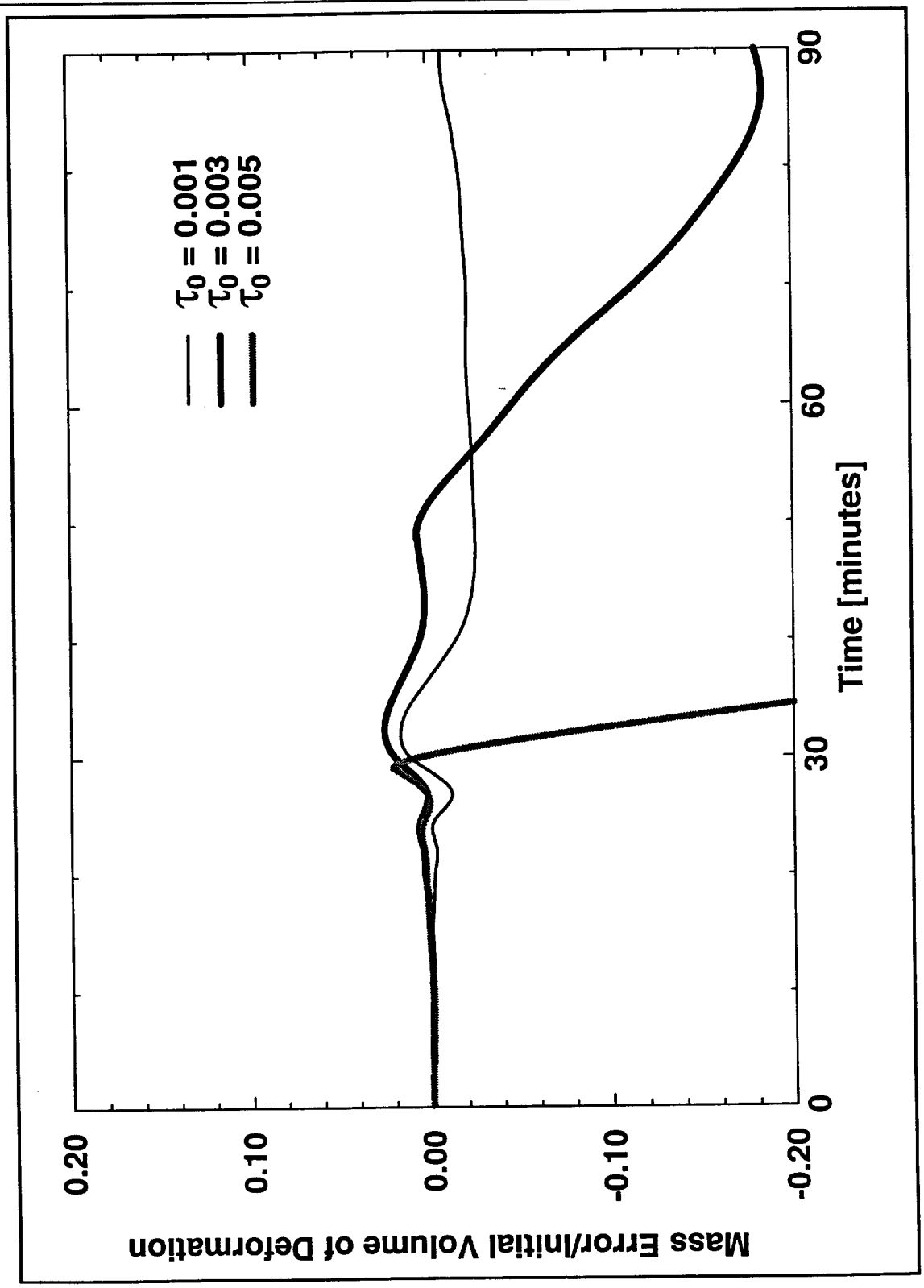

FIGURE 4.5 Mass (Scaled by Volume of Deformation) Conservation Over Time

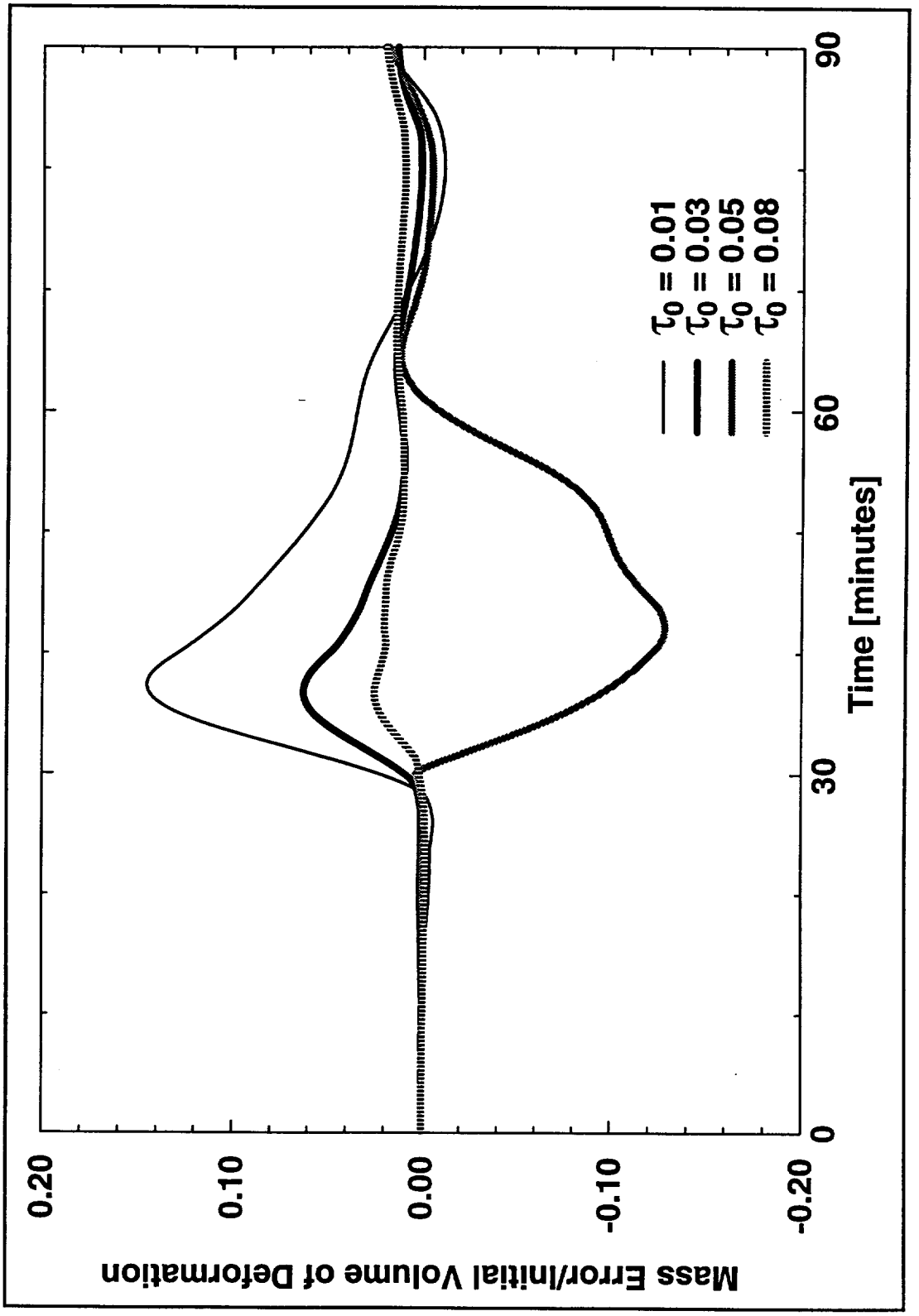

FIGURE 4.6 Mass (Scaled by Volume of Deformation) Conservation Over Time

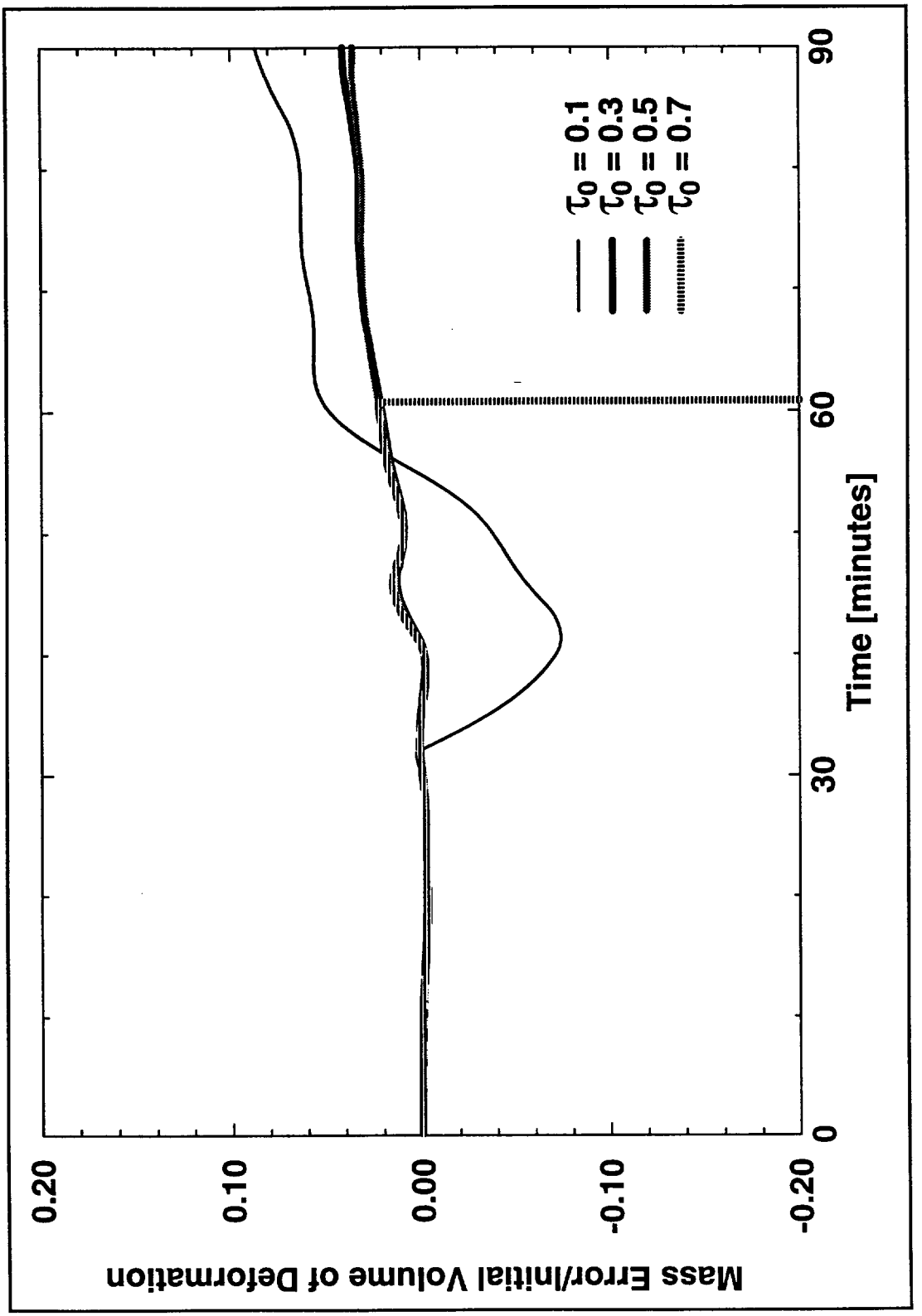

FIGURE 4.7 Raytracing Using Two Initial Point Sources

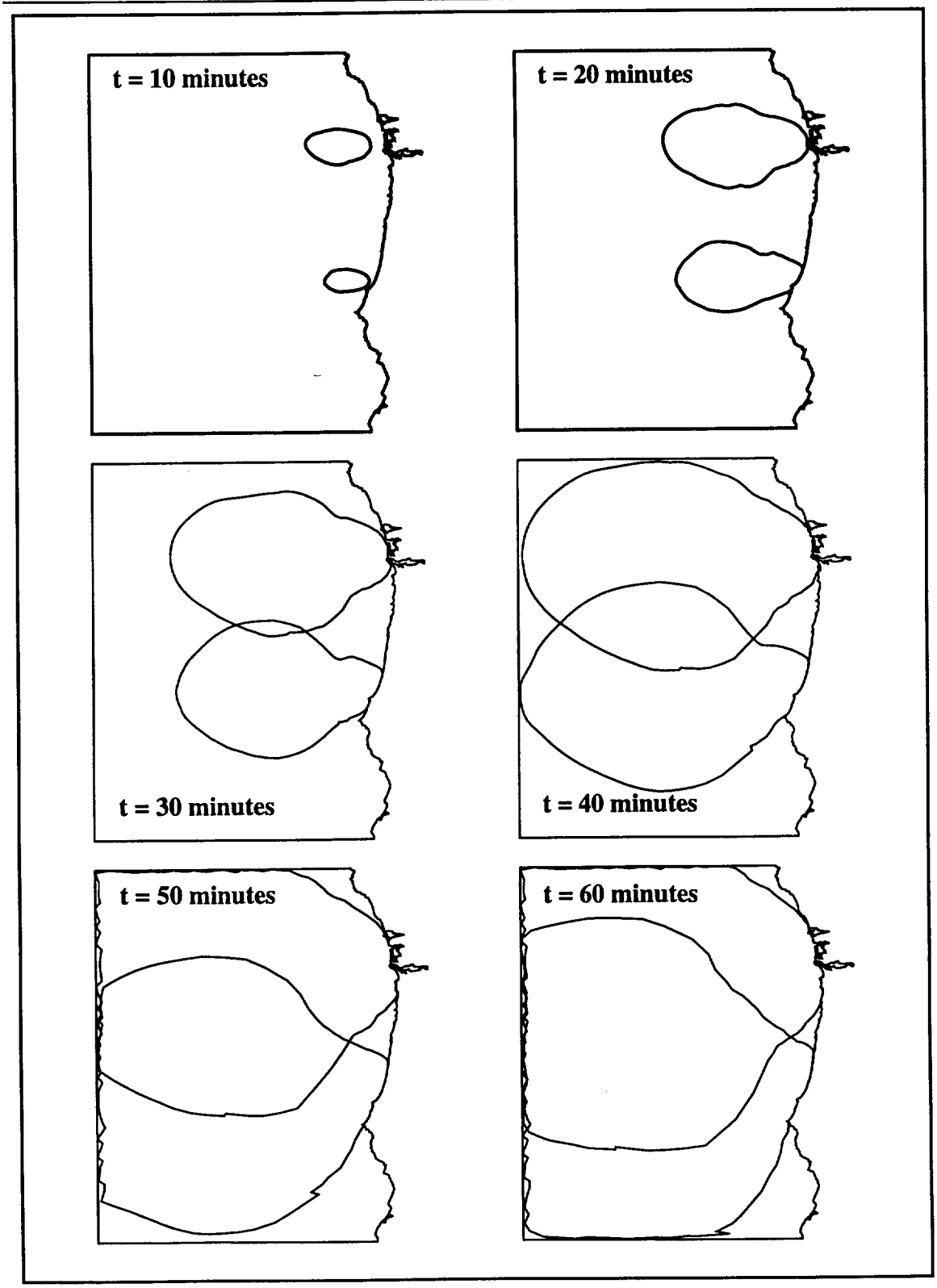

FIGURE 4.8 Conservation of Mass and Energy for M_W = 8.5 Scenario

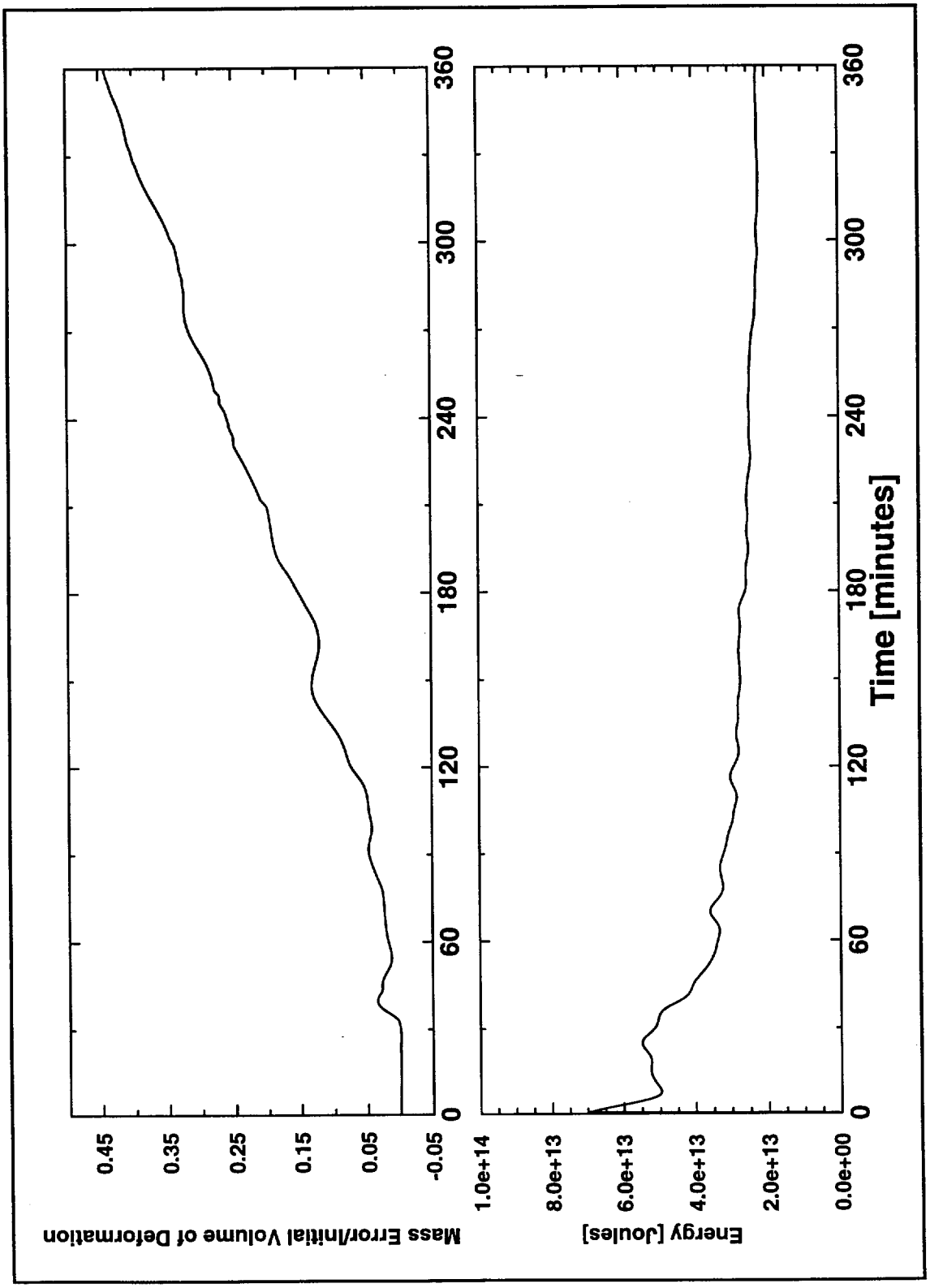

FIGURE 4.9 Conservation of Mass and Energy for M_W = 8.8 Scenario

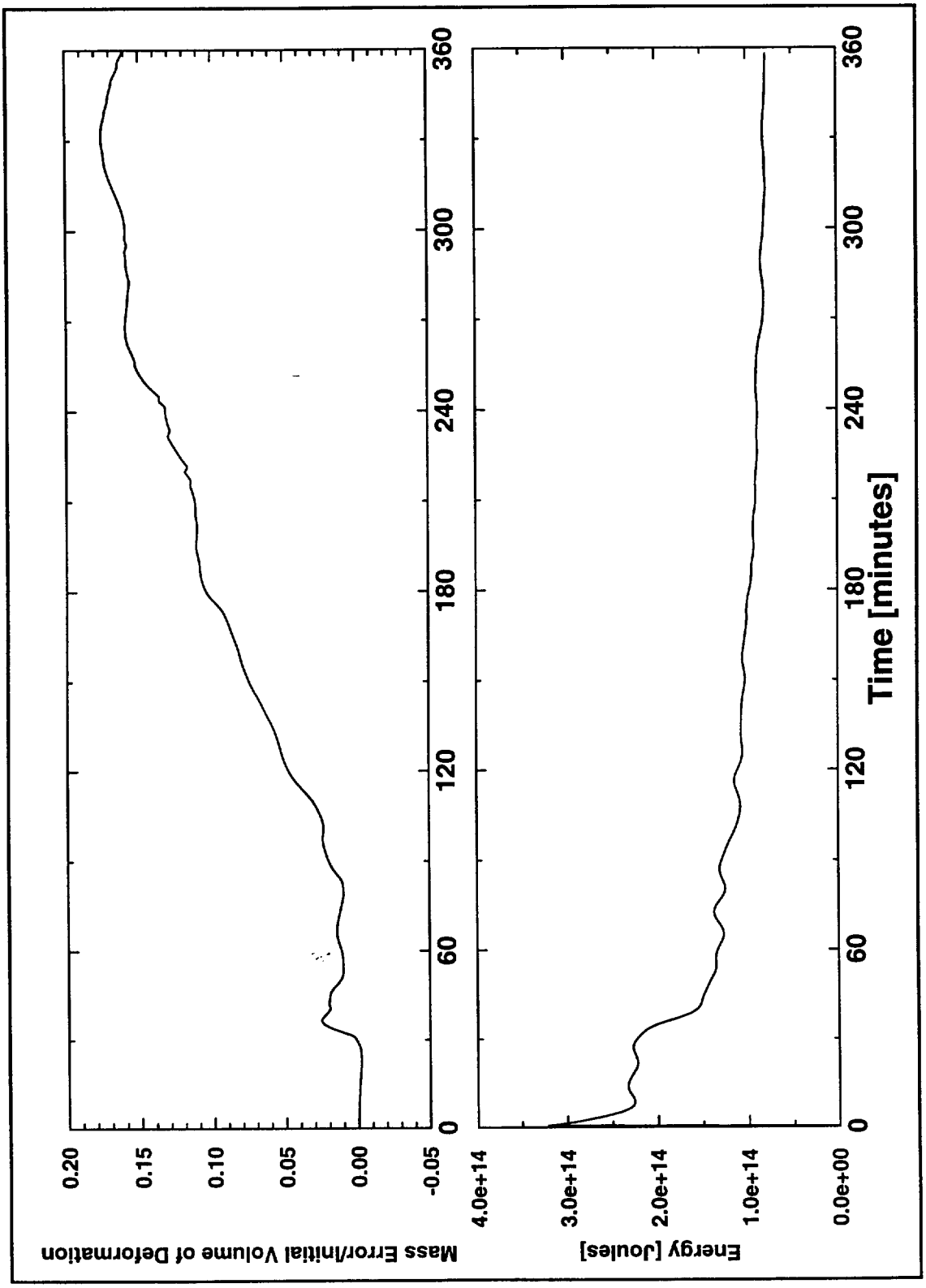

FIGURE 4.10 Effect of Transmissive Boundaries on Mass and Energy Variation

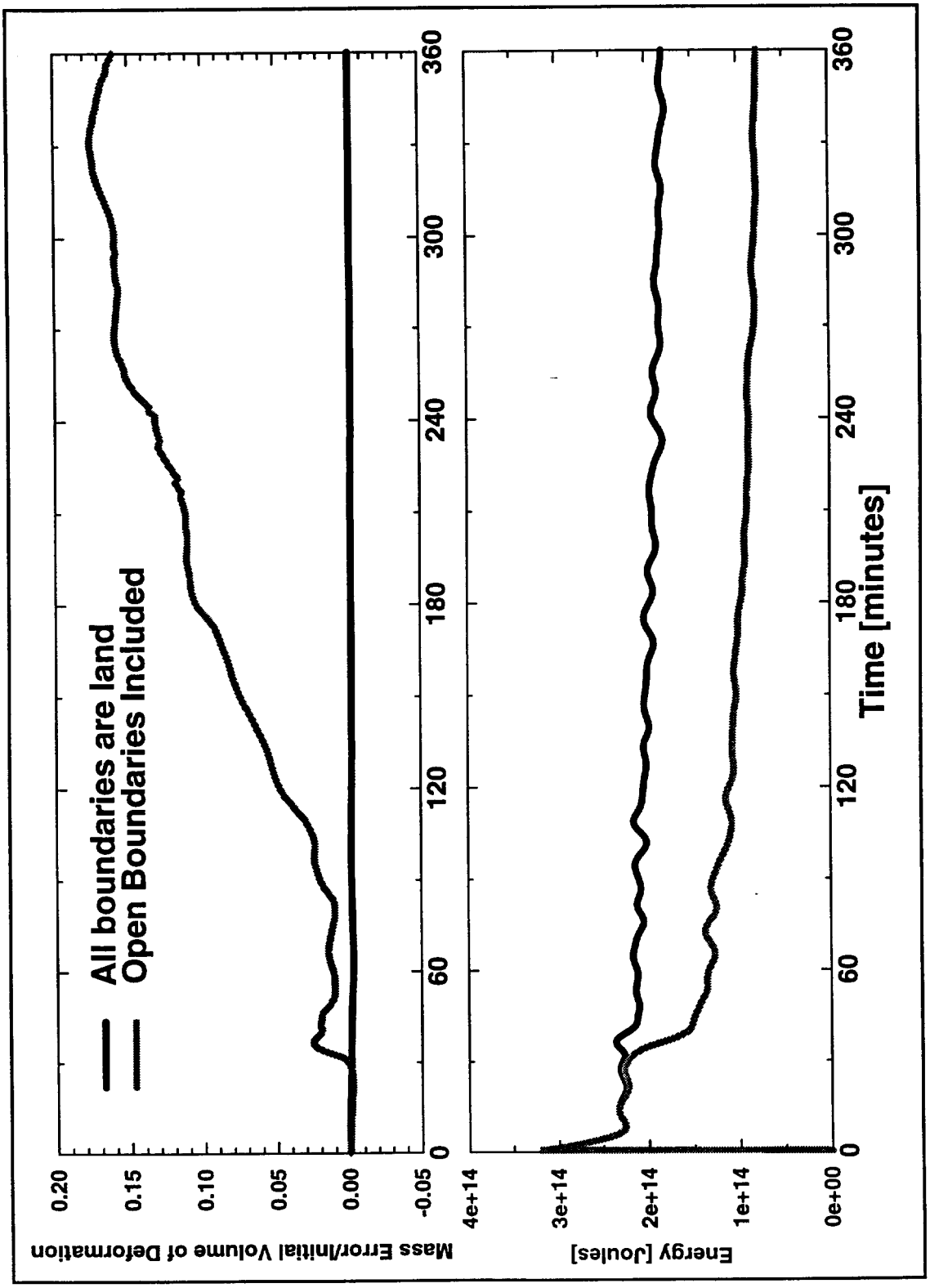

FIGURE 4.11 Propagation of Energy for M_W = 8.5 Scenario

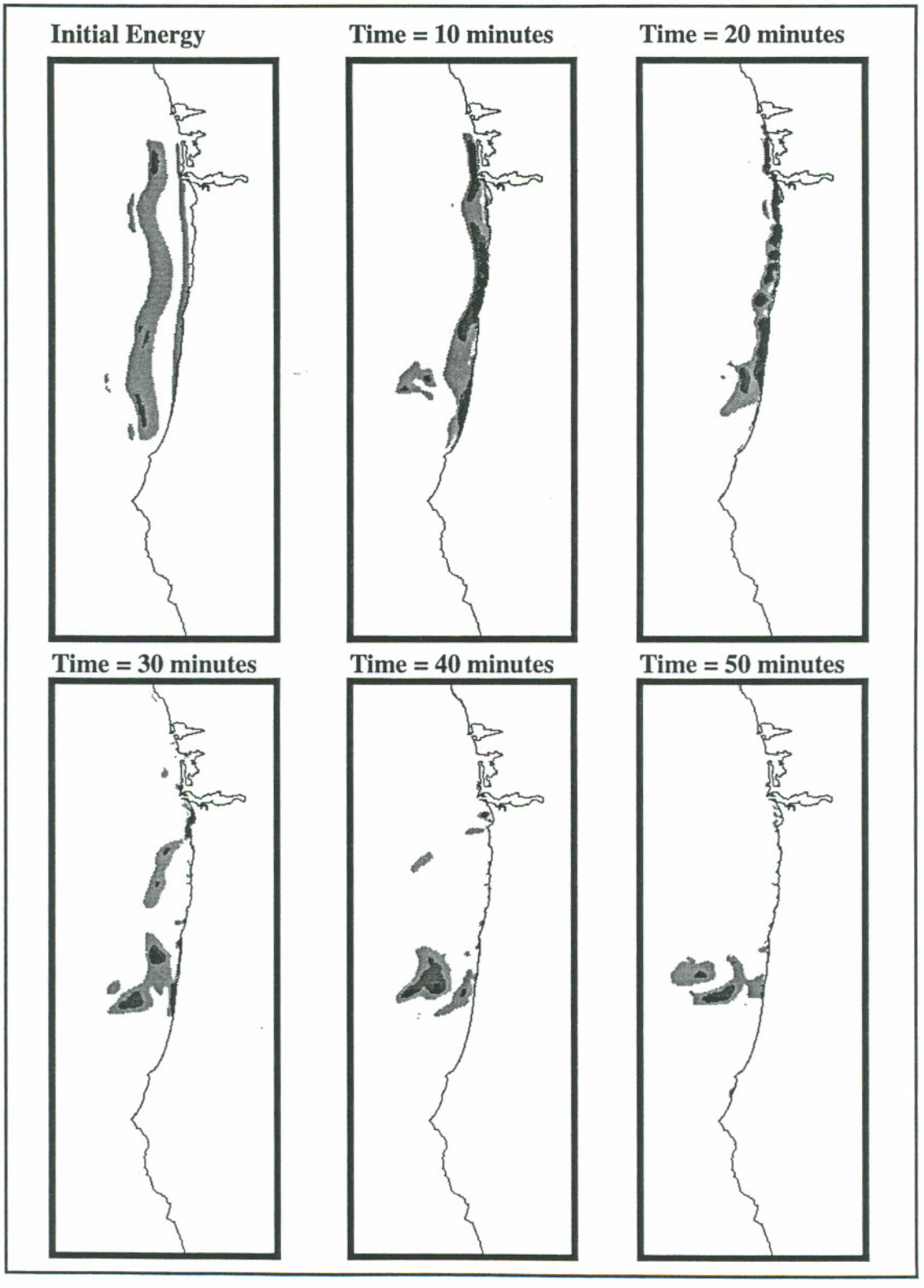

FIGURE 4.12 Propagation of Energy for M_W = 8.8 Scenario

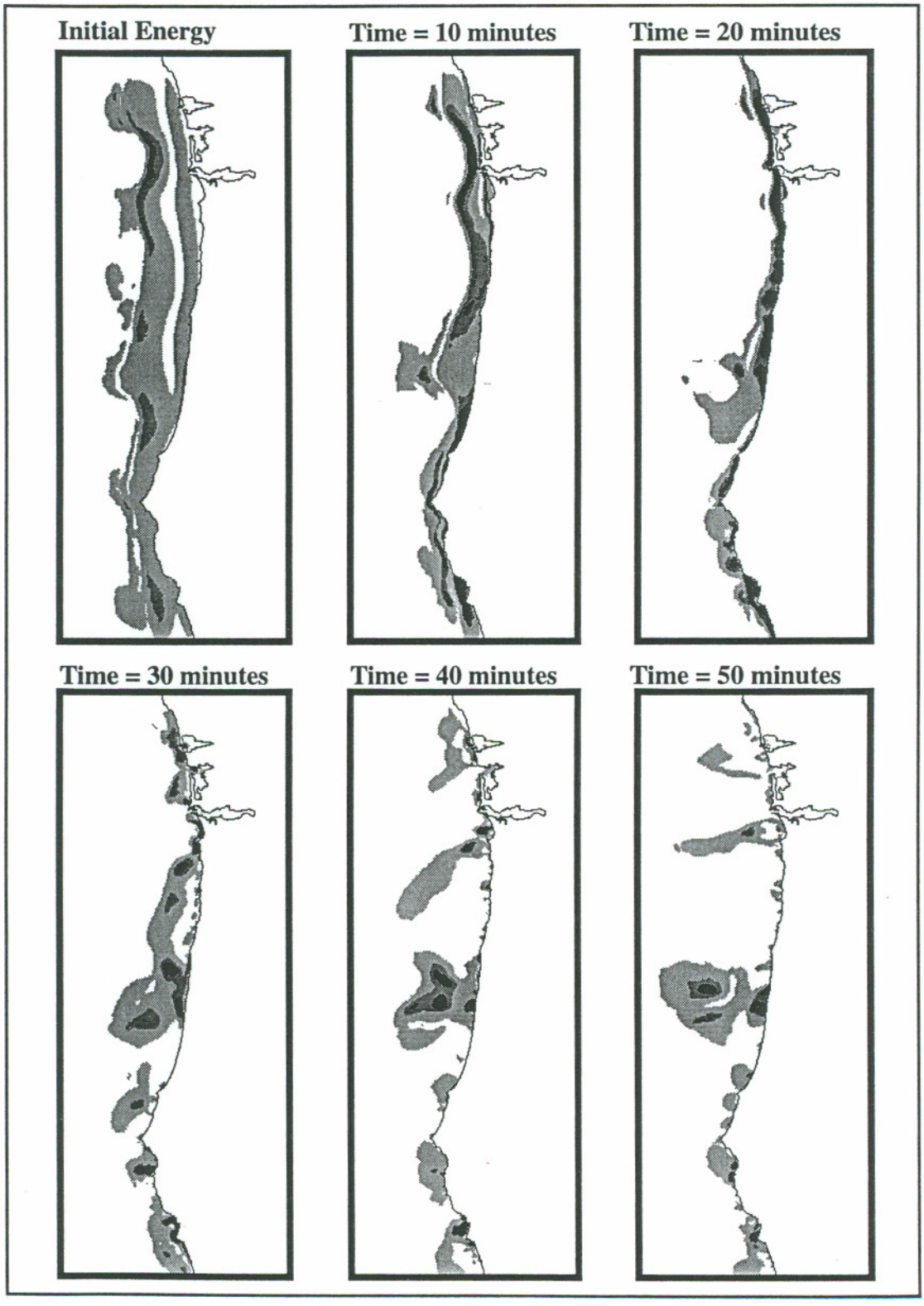

FIGURE 4.13 Isolines of Maximum Energy

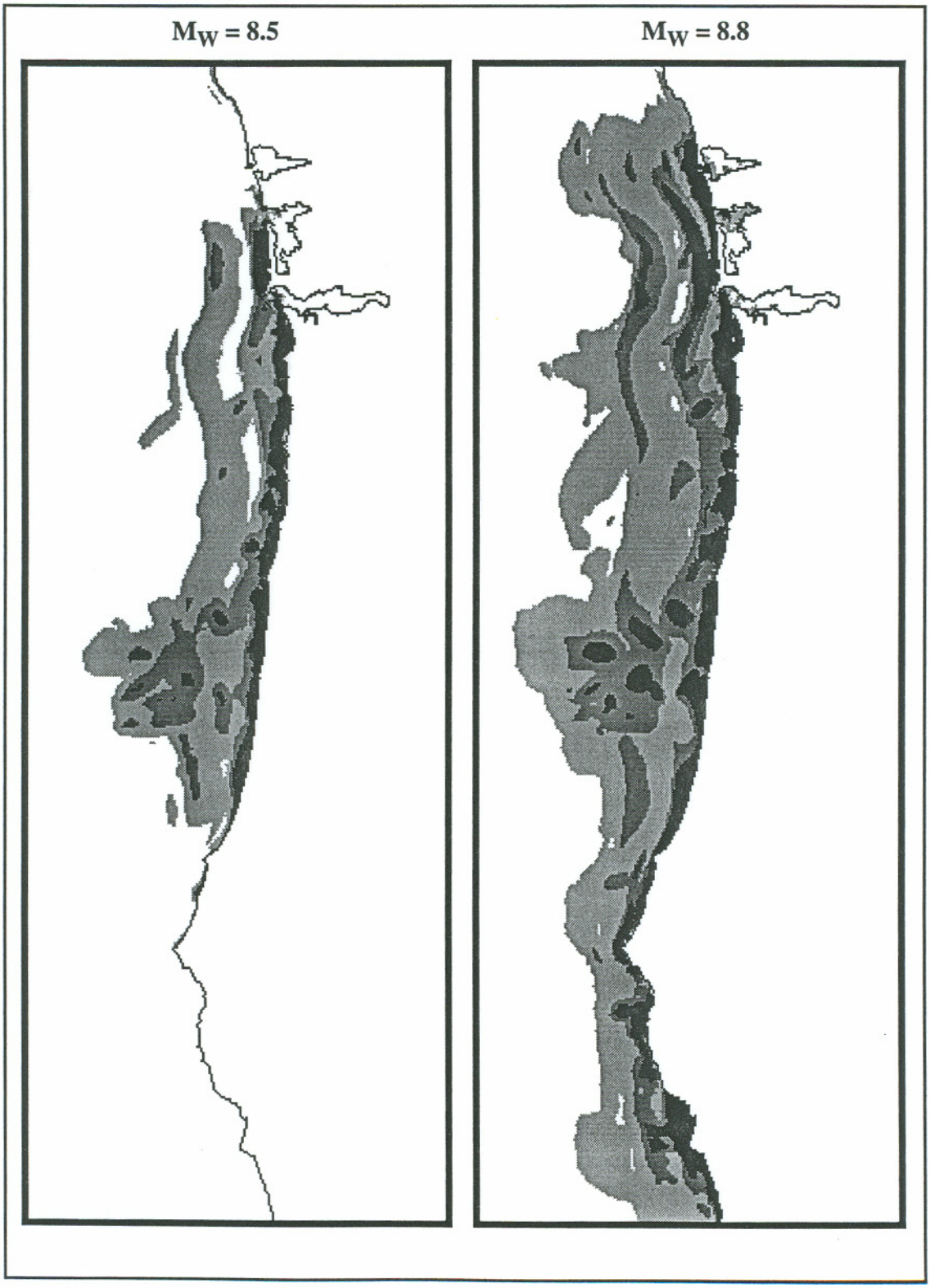

FIGURE 4.14 Maximum Coastal Wave Elevations for M_W = 8.5 Scenario

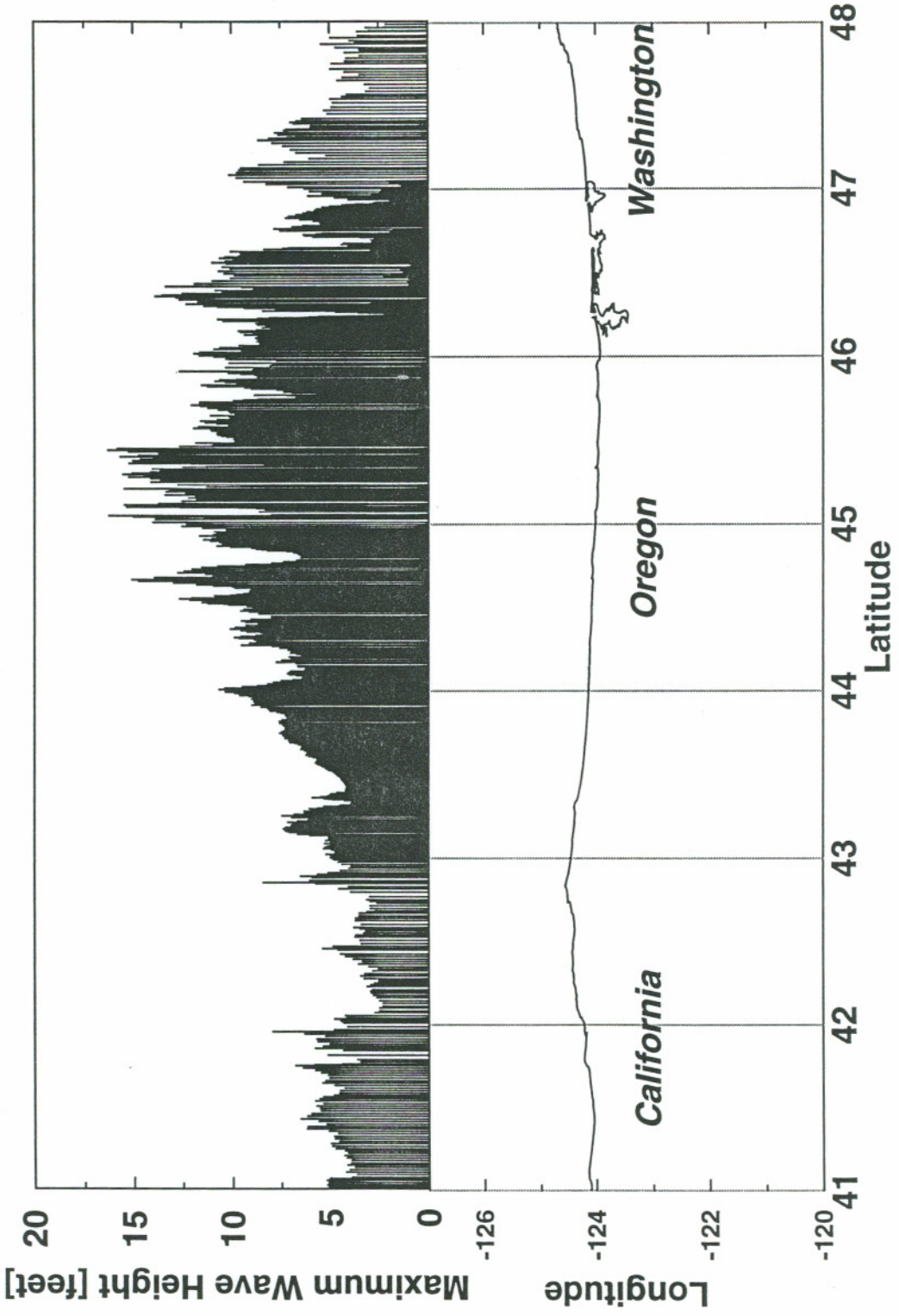

FIGURE 4.15 Maximum Coastal Wave Elevations for M_W = 8.8 Scenario

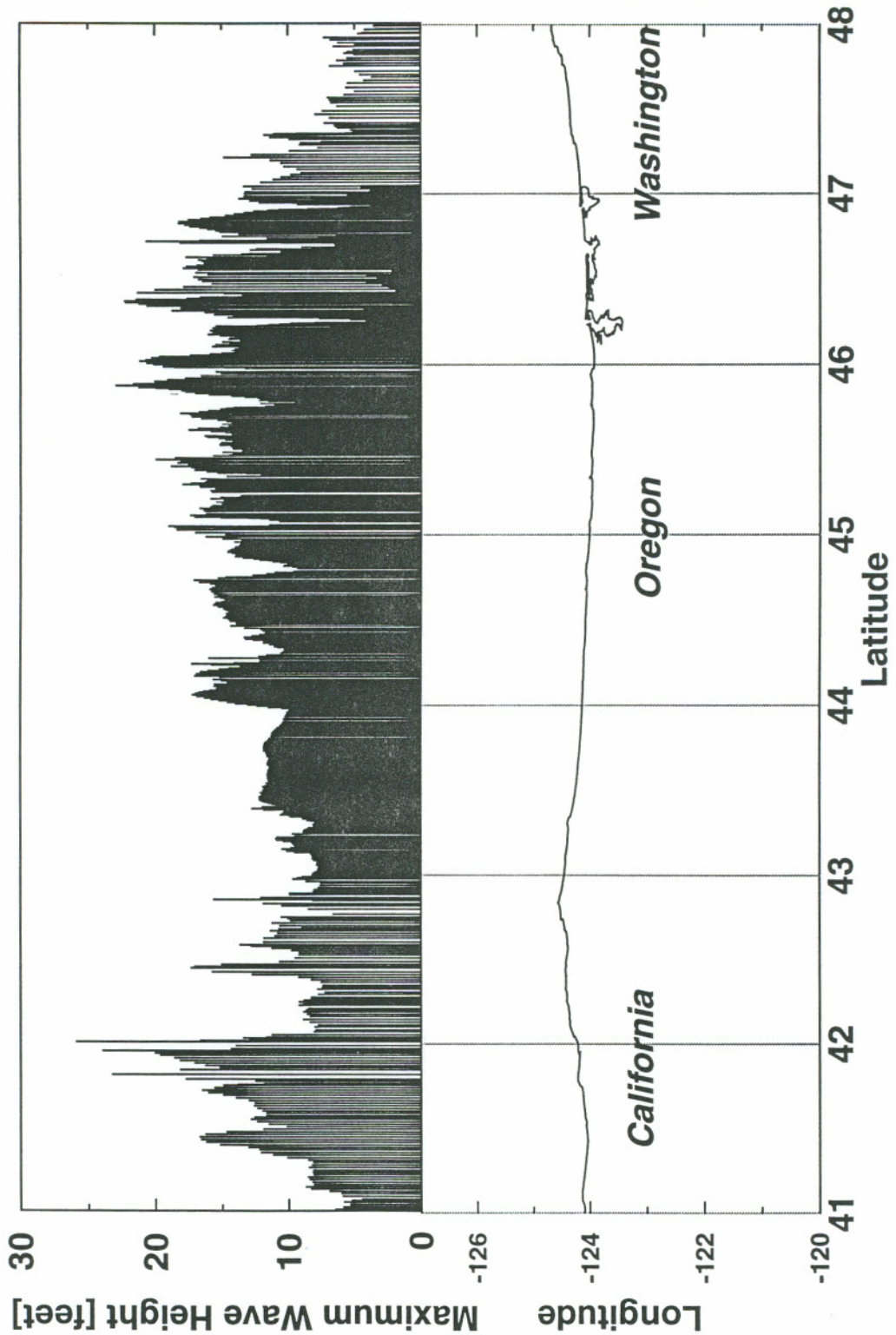

FIGURE 4.16 Computed Waveforms for Aberdeen

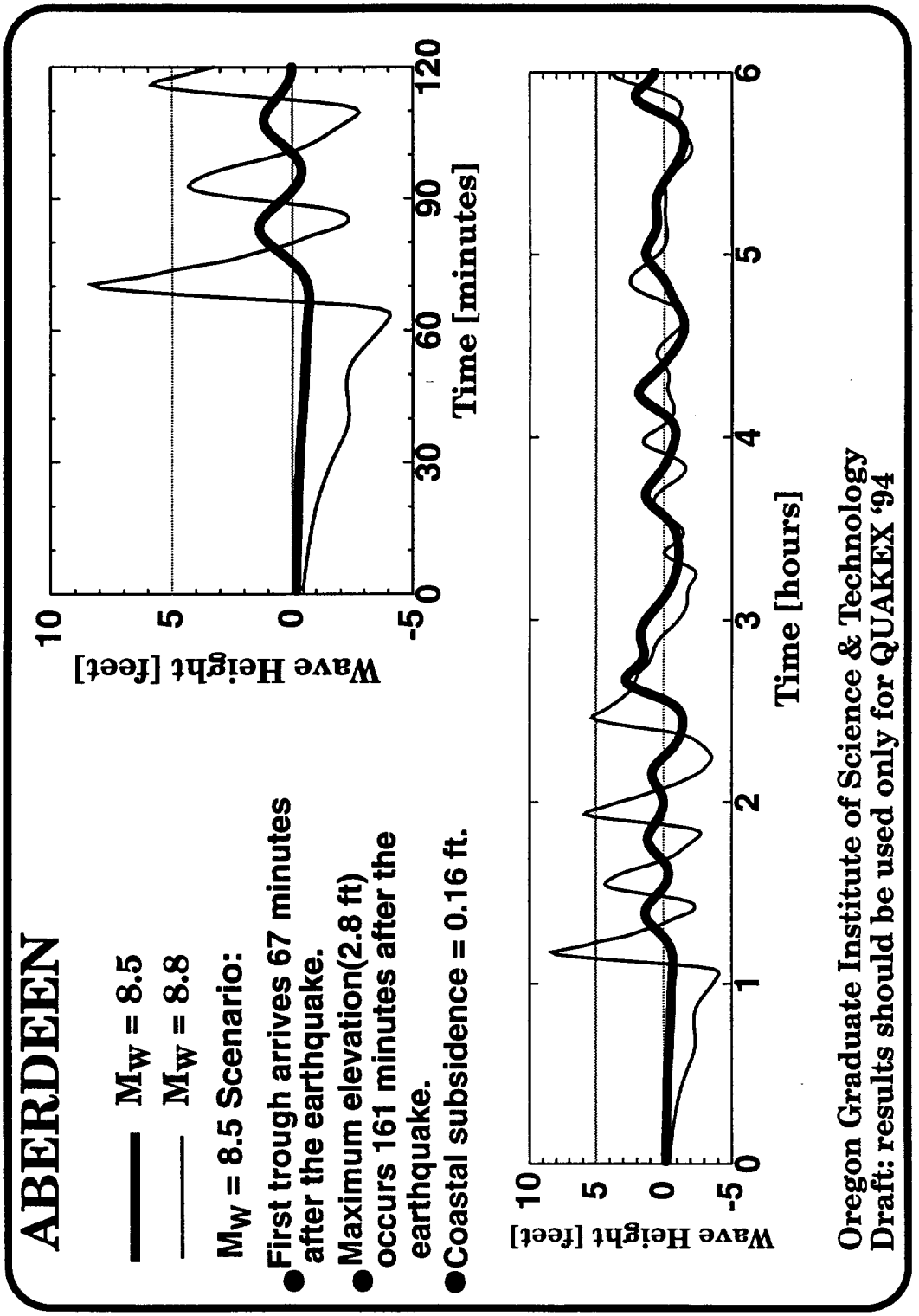

FIGURE 4.17 Computed Waveforms for Astoria

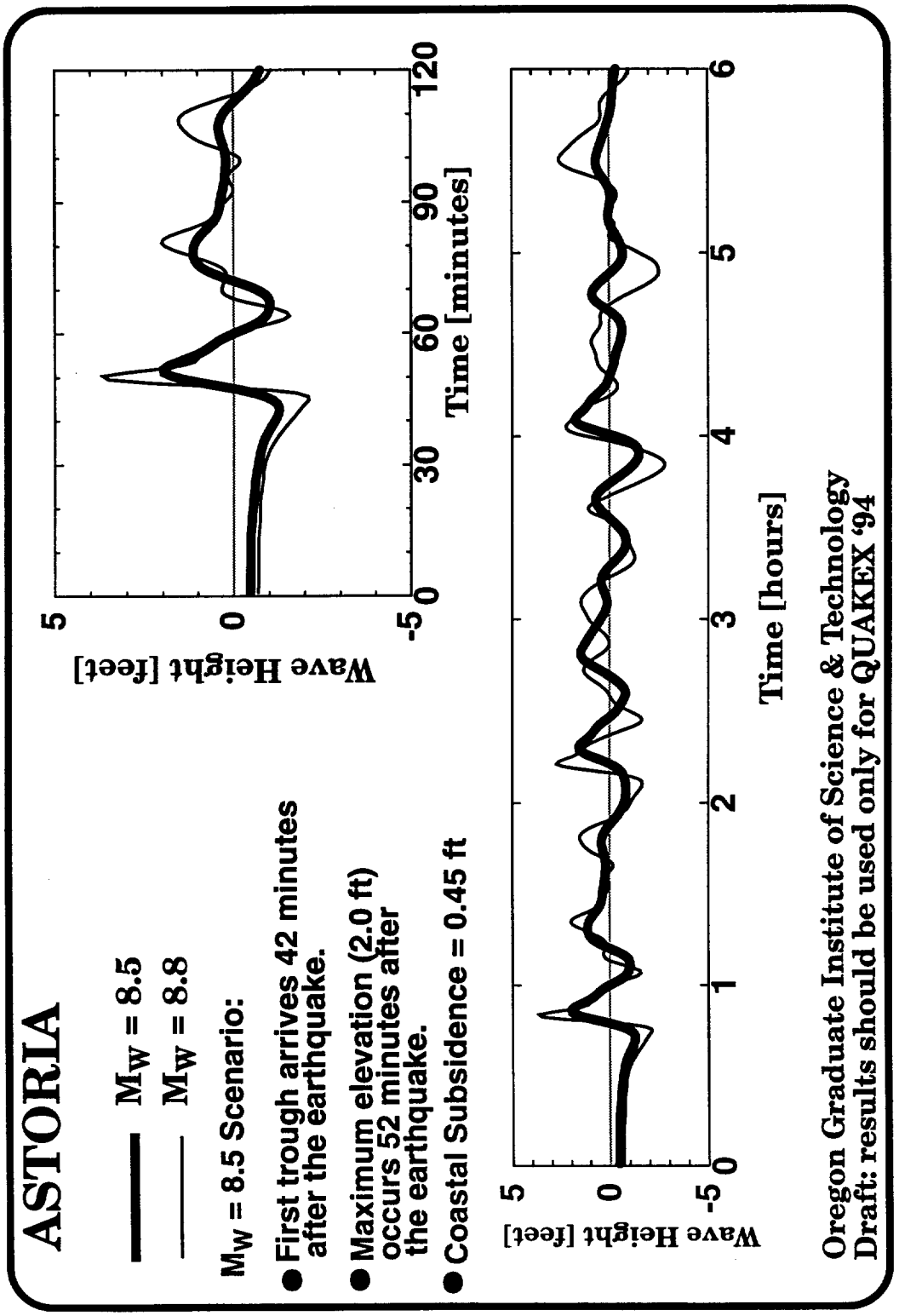

FIGURE 4.18 Computed Waveforms for Bandon

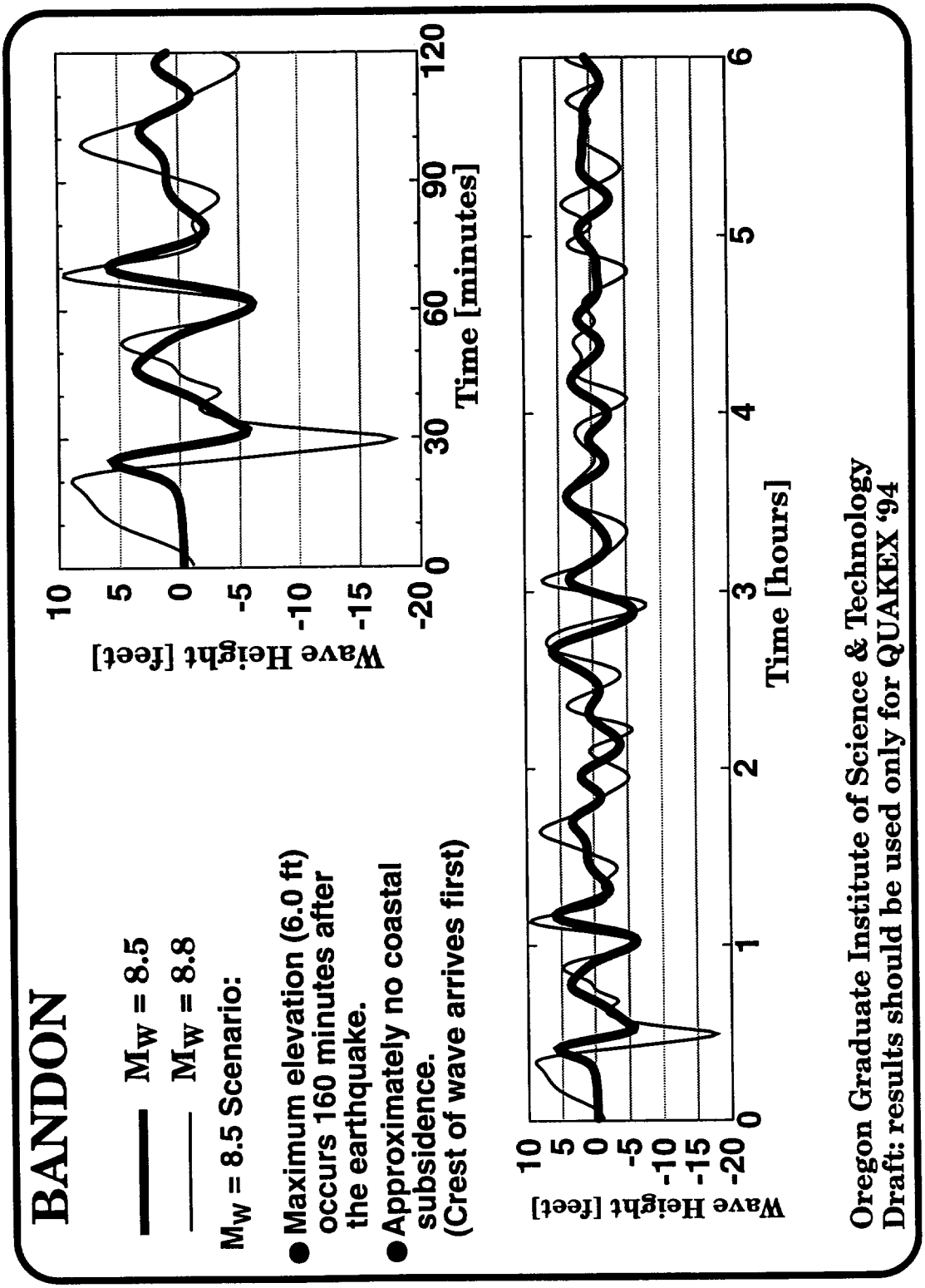

FIGURE 4.19 Computed Waveforms for Brookings

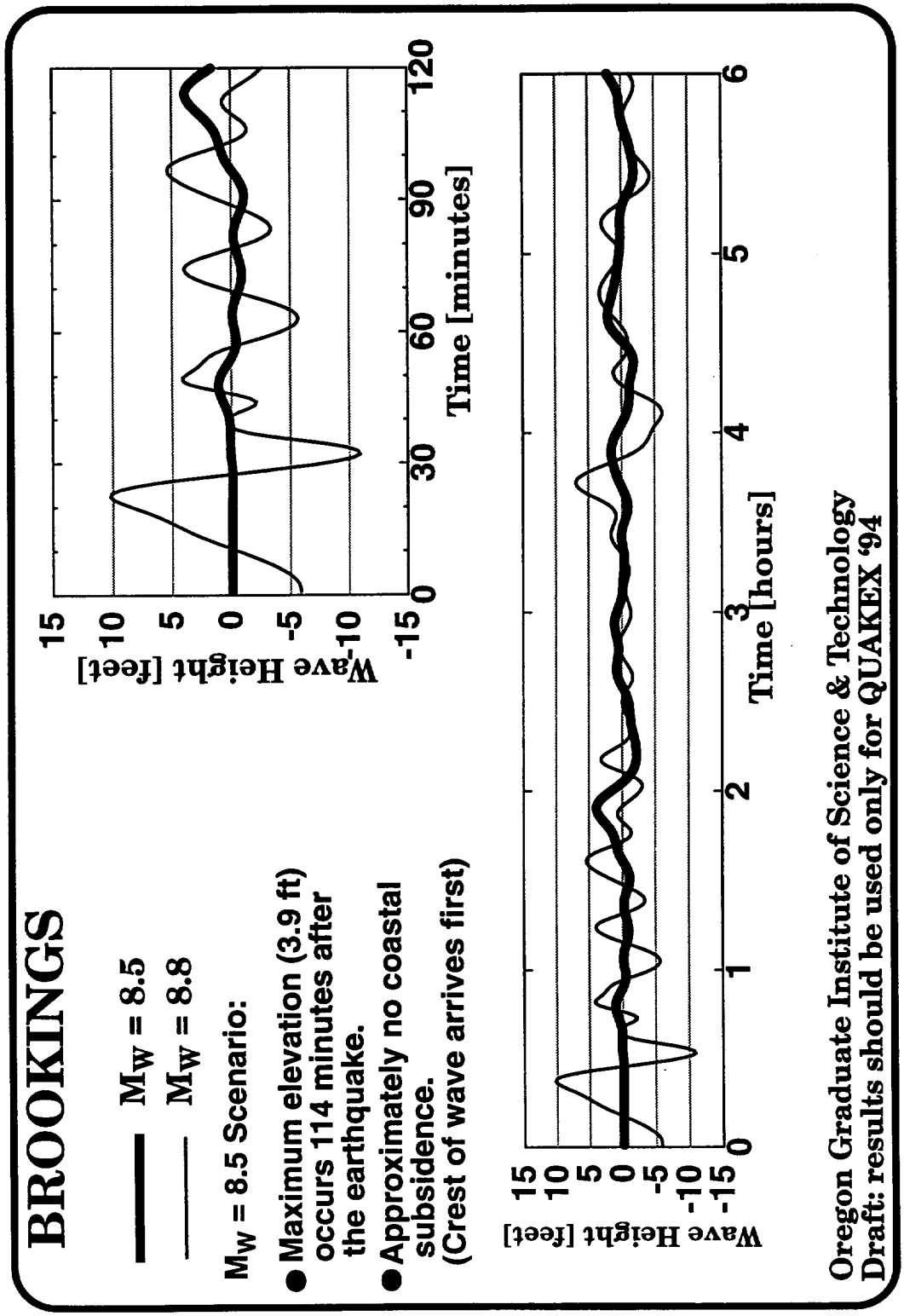

FIGURE 4.20 Computed Waveforms for Cannon Beach

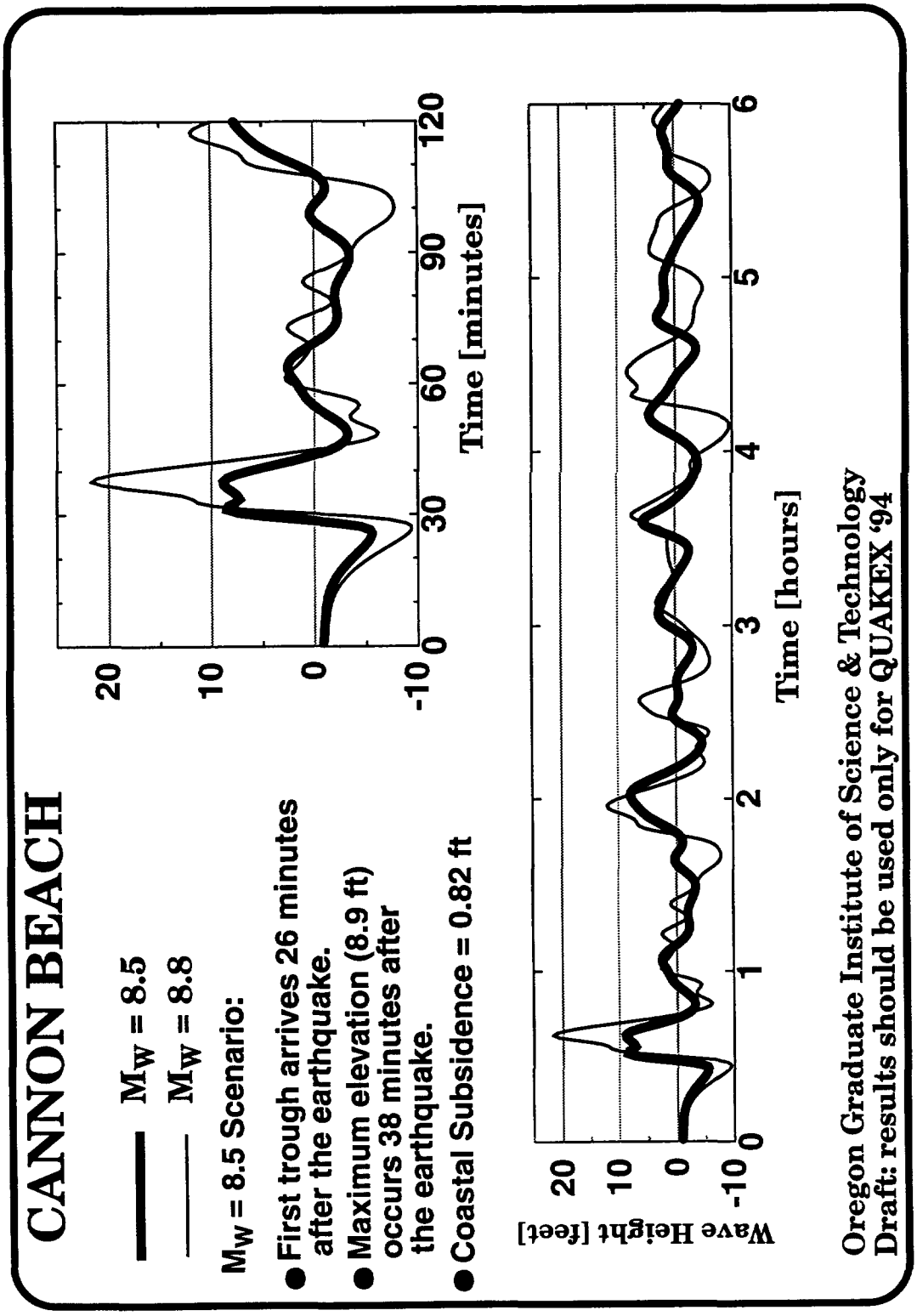

FIGURE 4.21 Computed Waveforms for Coos Bay

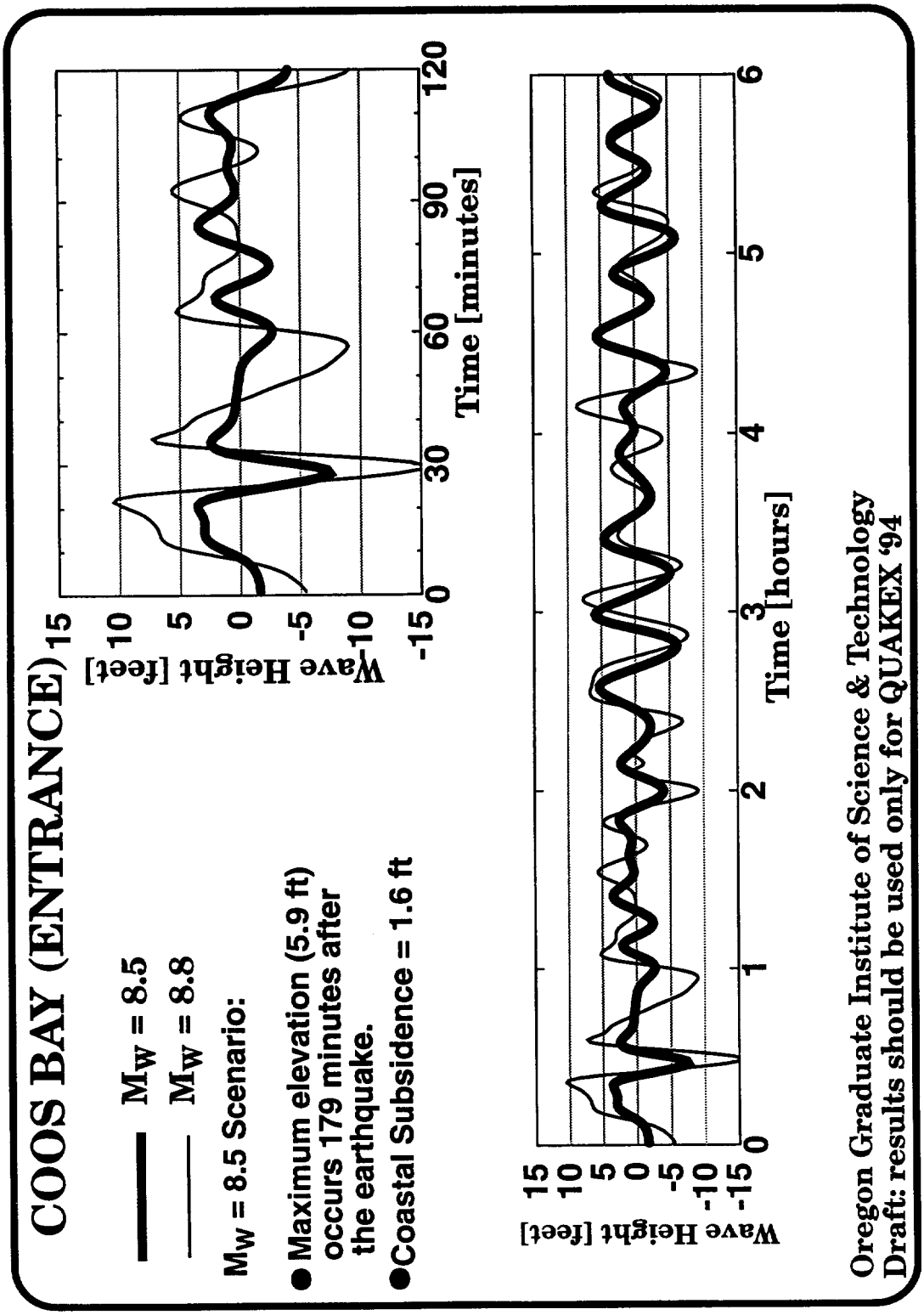

FIGURE 4.22 Computed Waveforms for Florence

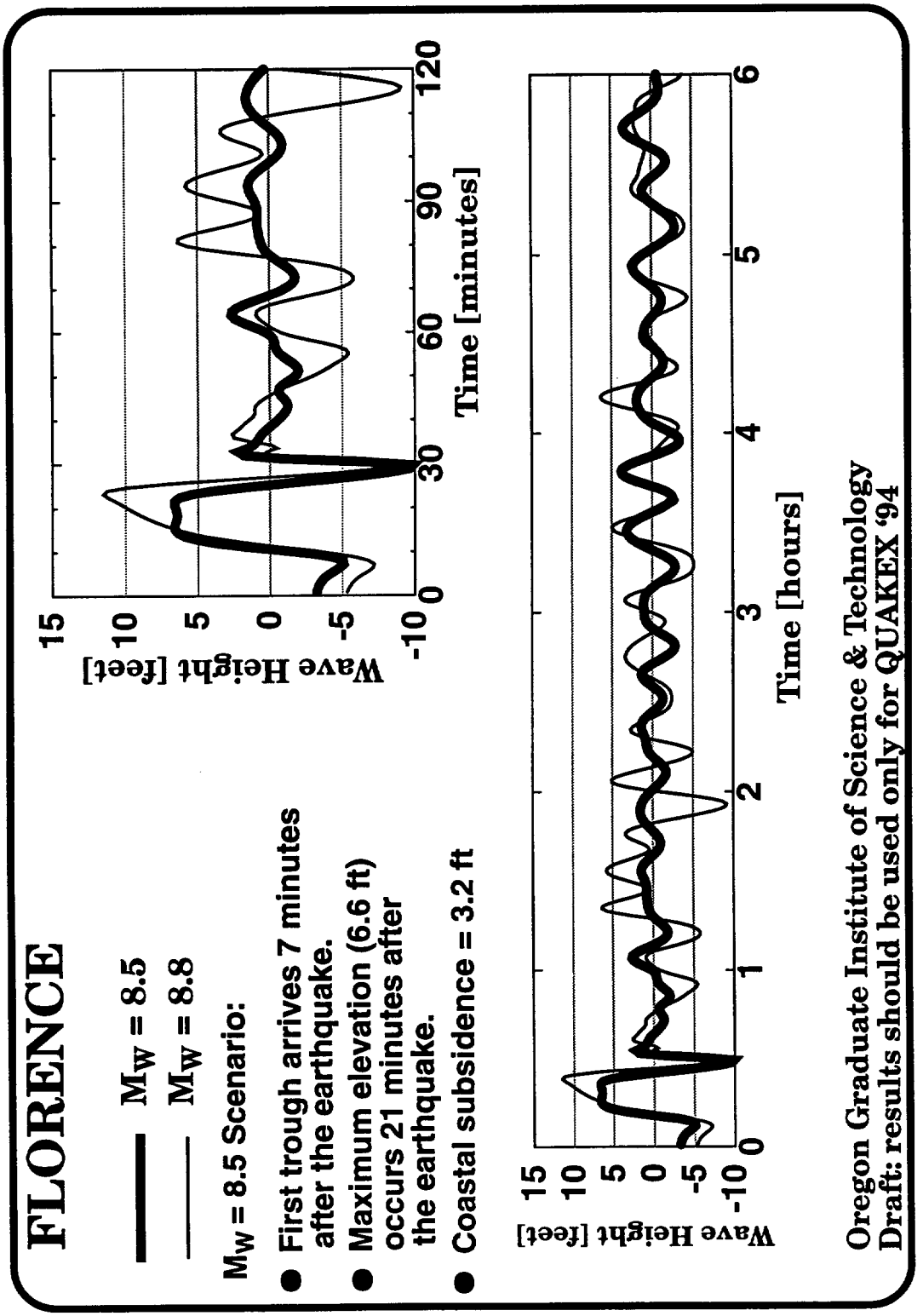

FIGURE 4.23 Computed Waveforms for Lincoln City

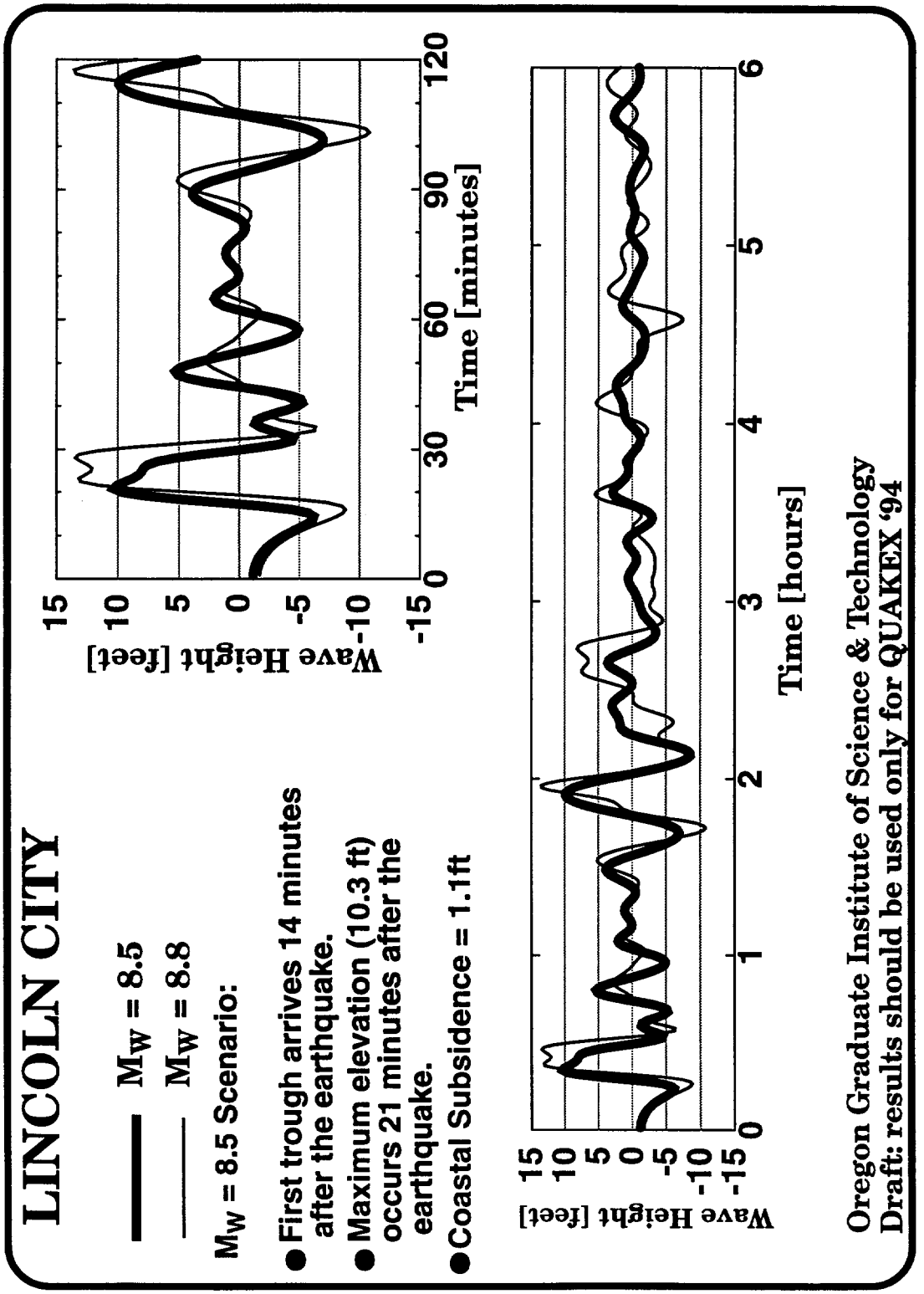

FIGURE 4.24 Computed Waveforms for Long Beach

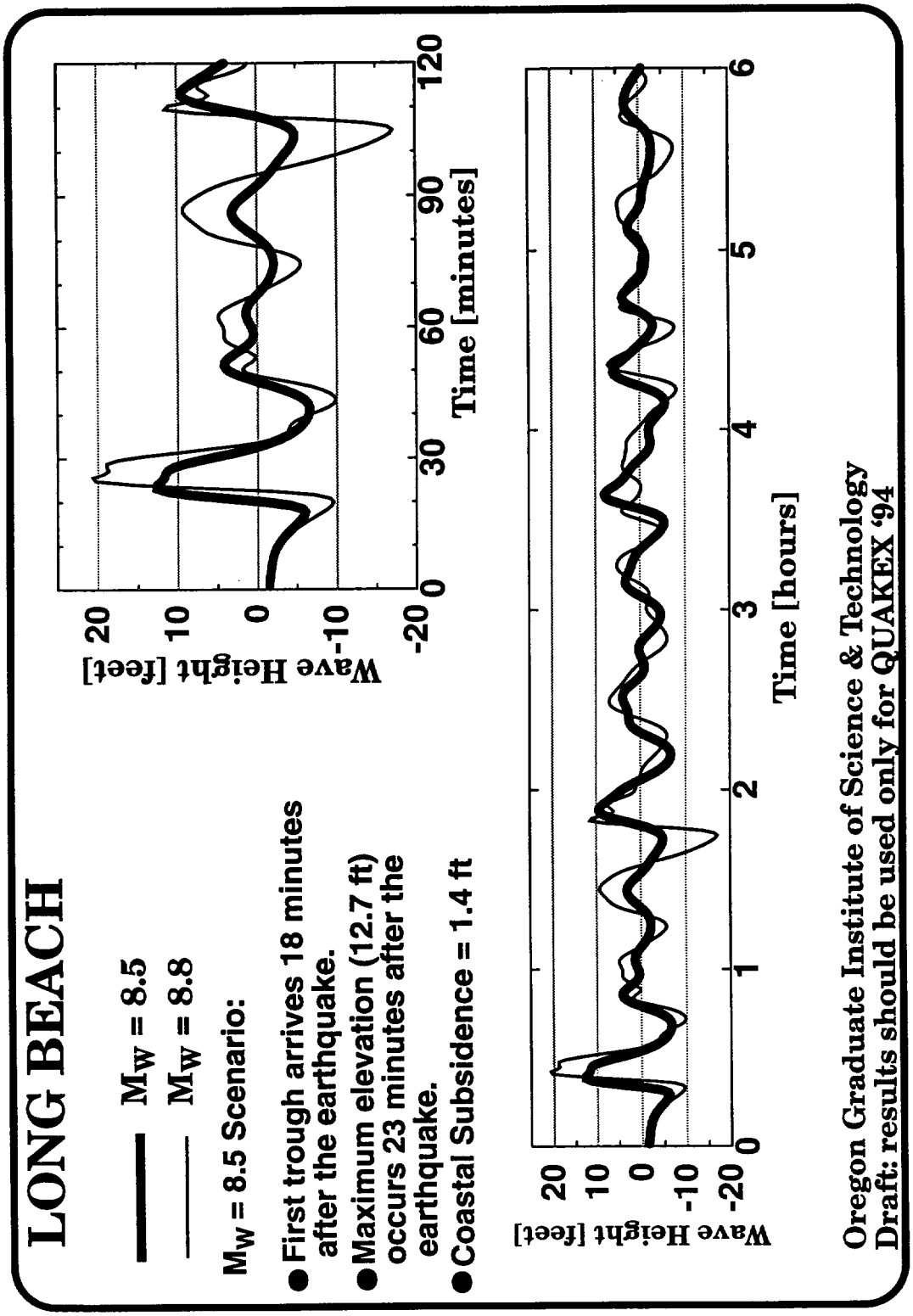

FIGURE 4.25 Computed Waveforms for Nehalem

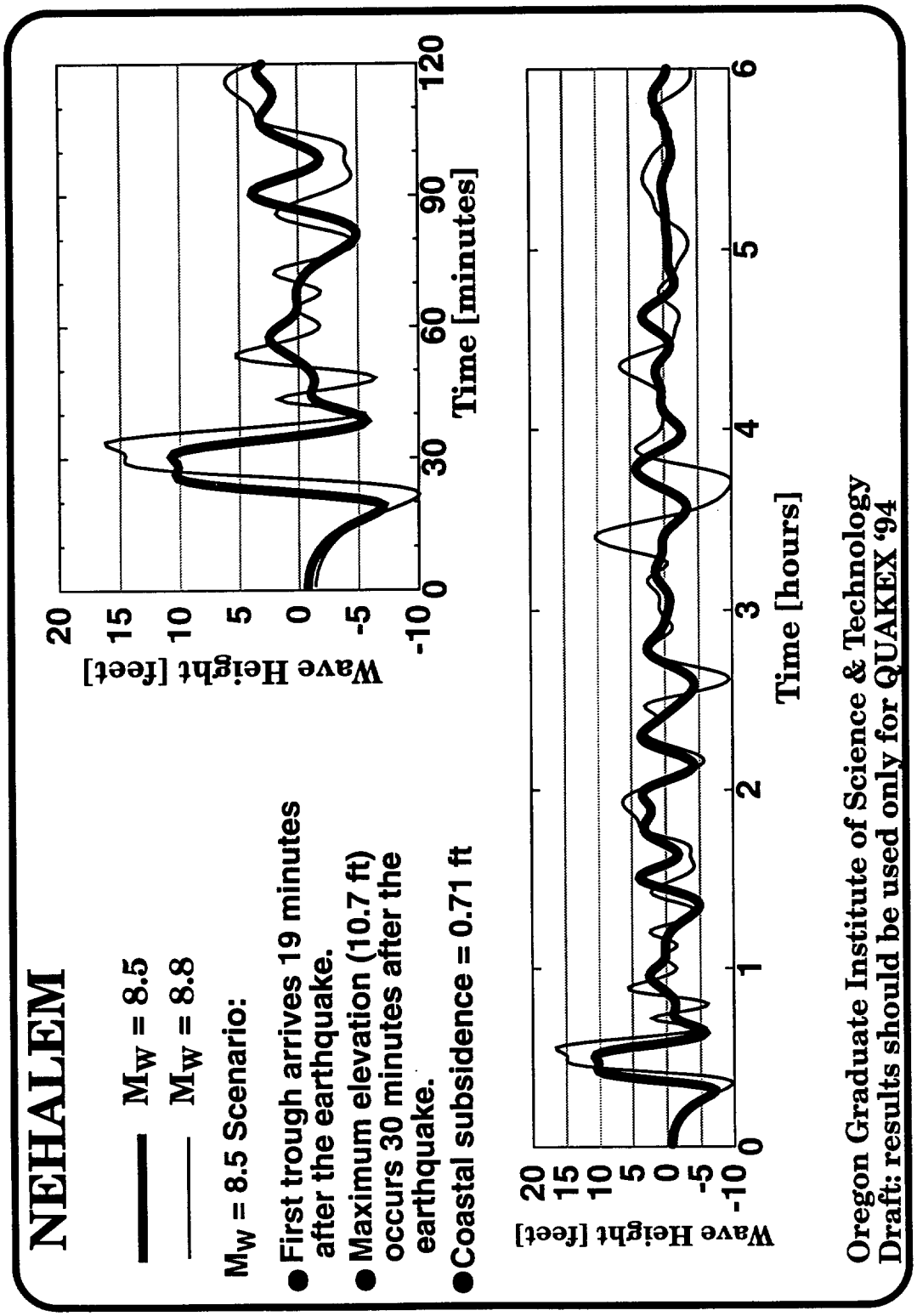

FIGURE 4.26 Computed Waveforms for Newport

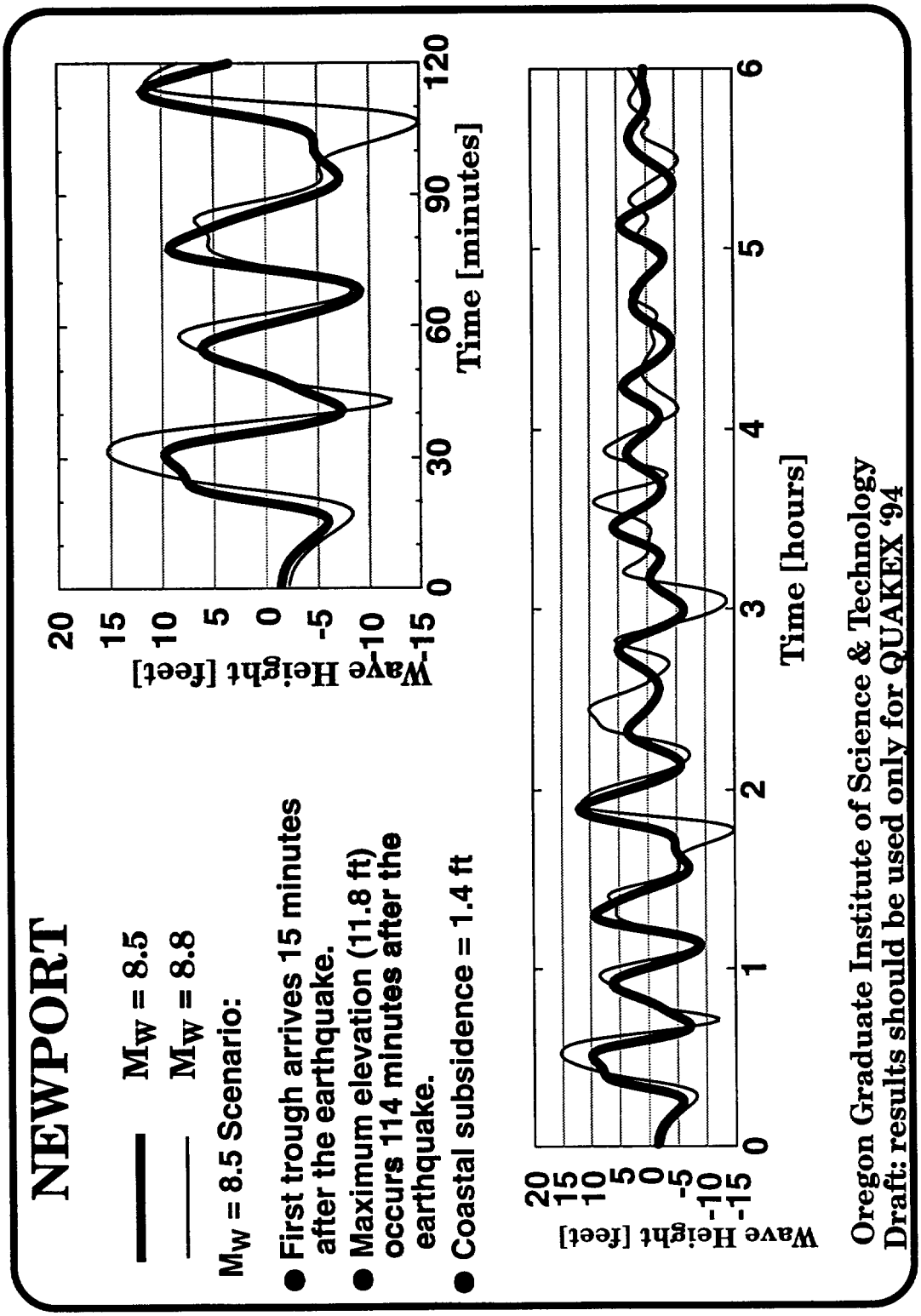

FIGURE 4.27 Computed Waveforms for Oretown

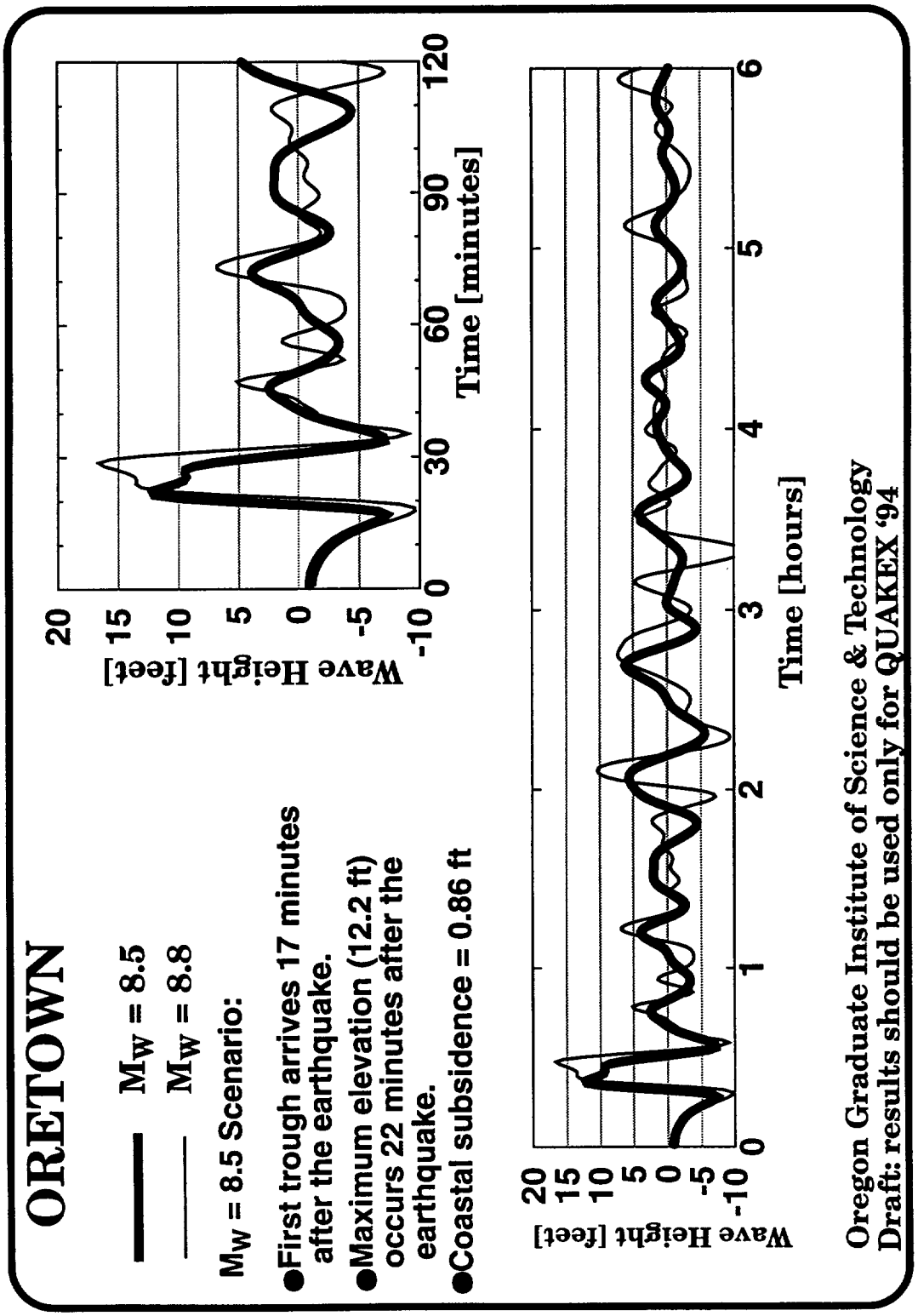

FIGURE 4.28 Computed Waveforms for Port Orford

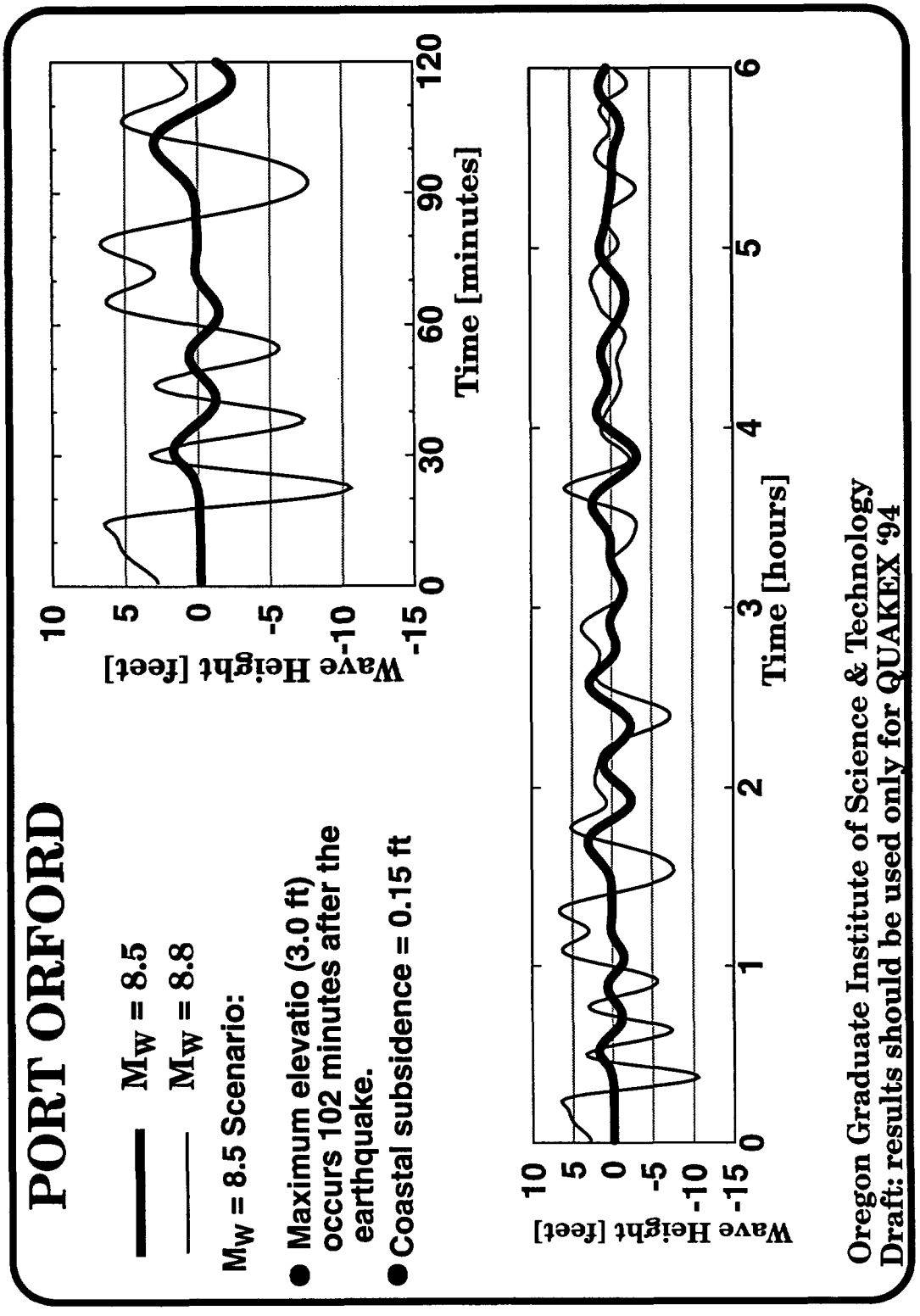

FIGURE 4.29 Computed Waveforms for Siletz Bay

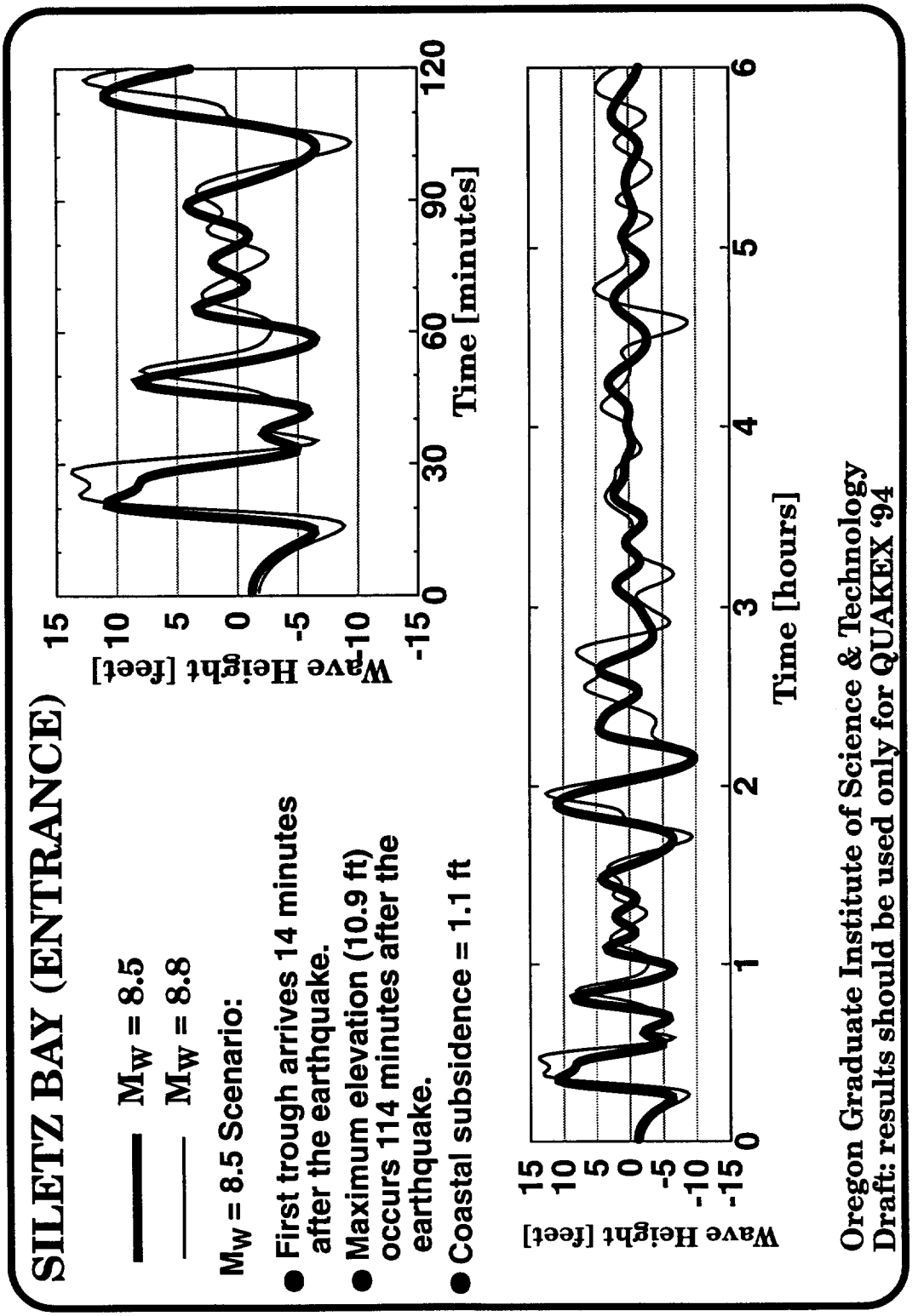

FIGURE 4.30 Computed Waveforms for Tillamook

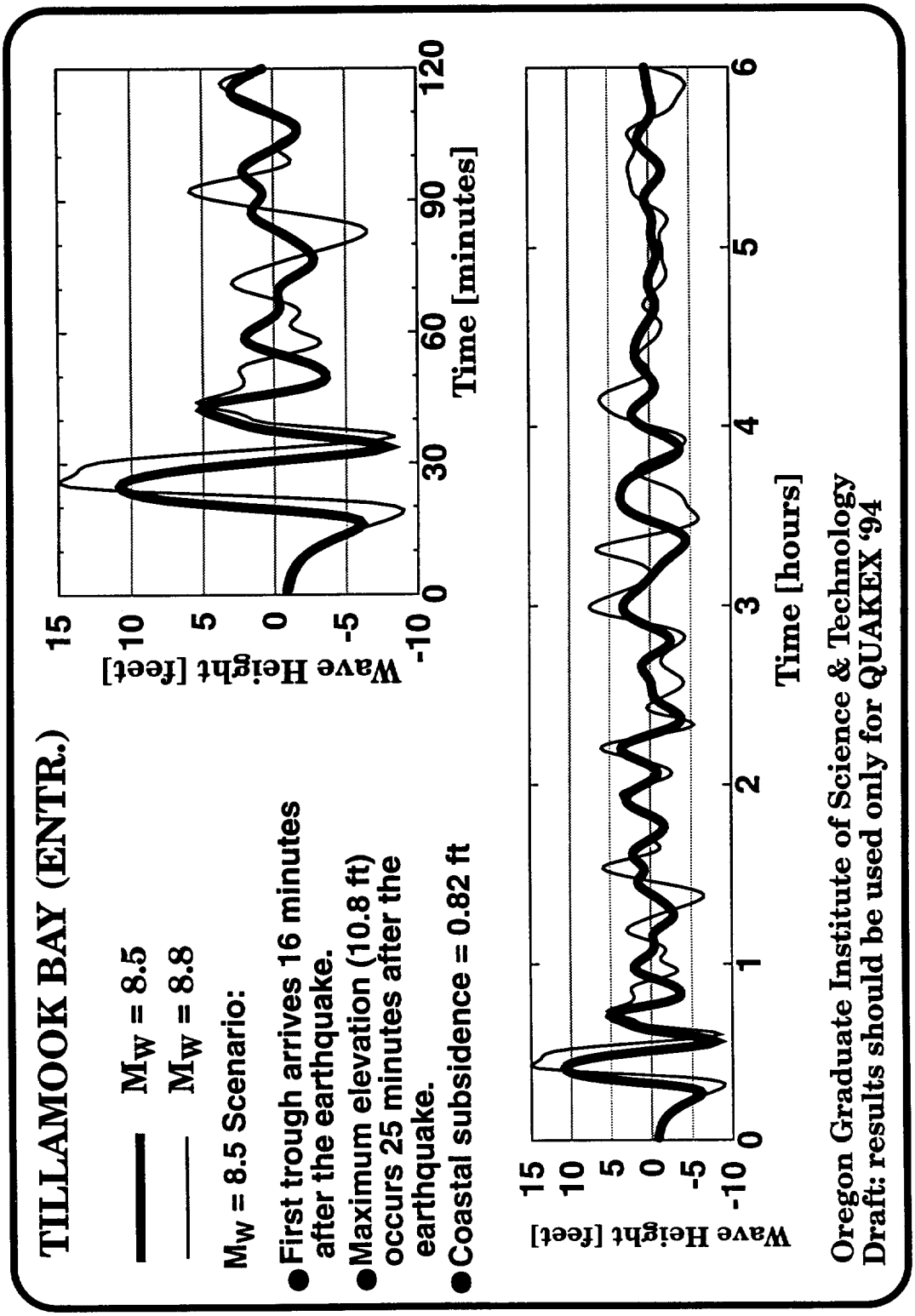

CHAPTER 5
Final Considerations

Contributions

Computer simulations of tsunamis provide useful information as to the propagation and form of the generated waves. It is crucial that results from such simulations be kept in perspective of the gravity of the topic. The events being modeled are ones which can destroy lives and communities easily. It is therefore important to point out not only the power of the generated results, but also the assumptions involved and the limiting factors within a model. This concept is the focus of this chapter, which will also allow a discussion of future research needed to improve the power of results from numerical modeling.

The results from this thesis contain significant implications. Previous applications of numerical modeling have focused on the use of finite difference schemes. One exception to this is a finite element model based on the shallow water equations developed by Liu and Yoon [1991] in which a leap frog scheme is used. This thesis has shown that finite element methods can be used to model tsunamis effectively. The modeler can thus take advantage of the ability to represent coastlines better, to define boundary conditions more systematically, and to discretize regions differently based upon criteria such as bathymetry and proximity to the source. The work presented here is the first to use the generalized wave continuity equation in tsunami simulations. Without such a wave continuity formulation, finite element solutions of coastal flow problems had previously been limited by $2\Delta x$ oscillations.

Waveforms are provided for stations throughout both the Japan and Pacific Northwest coastlines. Such figures portray the arrival times, the magnitudes, and the amount of

wave activity which can occur at individual locations. For the Hokkaido Nansei-oki tsunami, the magnitudes shown in the waveforms suggest that the fault plane model which was used can reasonably reproduce the correct magnitude of the bottom deformation.

Ideas such as conservation of mass and conservation of energy are ones which have not been addressed in other numerical modeling studies of tsunamis. This thesis has paid particular attention to such conservation principles. This allows a more detailed interpretation of not only the numerical results, but also of the model itself. Chapters 3 and 4 showed that mass was reasonably conserved throughout the time frame of interest. The mass variation which did exist for the two test cases was shown to be a result of the transmissive boundaries. The two previous chapters also demonstrated the trends in energy conservation seen throughout the simulations and offered some suggestions as to possible reasons for the energy variation which occurred. A more detailed analysis of these suggestions now ensues.

Energy Considerations

Three of the suggestions for why energy appeared not to be conserved are tested in more detail here. These include the effect of land boundaries, the effect of transmissive boundaries, and the influence of grid refinement near the seismic source. In order to check the influence of each, a test case was set up where the grid was a channel extracted from the Pacific Northwest (Figure 5.1). The same bathymetry was used as well as the same bottom deformation for the M_W=8.8 earthquake. A reference case was designed using this grid whereby all boundaries were made land boundaries, thus not allowing energy to exit the domain on account of transmissive boundaries. Three test cases were then considered, as described next.

The first test was to examine the effect of the open ocean transmissive boundary on energy. Using the same grid as the reference case, the left side boundary was changed to a transmissive boundary rather than a land boundary. All other conditions and parameters

were kept the same, and no friction was introduced for any of the cases. The comparison of the results from this first test case and the reference case is displayed in Figure 5.2. The initial drop in energy over the first 10 minutes or so is still existent and looks very similar to what was seen in previous chapters. Approximately 30 minutes into the simulation, the test case shows a sharp energy decrease which evolves into a gradual decrease for the remainder of the simulation. Upon examination of the wave patterns, it can be seen that the crest of the wave exits the boundary at about 30 minutes. It is believed that the sharp decrease in energy seen in this test case at about 30 minutes is caused by the departure of the main part of the wave from the boundary. This same drop in energy may be seen in the figures in Chapter 4. For the Sea of Japan, this second sharp decline in energy (the first being during the first ten minutes) is not significant, most likely due to the fact that not much energy is carried by the far-field wave which leaves the transmissive boundary (at about 35 minutes).

The second test case was designed to look at the effect of losing energy due to improper spatial discretization in the source region. A new grid for this test was generated with approximately four times the resolution as the reference case. All boundaries were considered as land boundaries, just as in the reference case. This test case was then performed using the same bathymetry and deformation as the reference grid. Figure 5.3 shows that refinement of the grid recovers some of the energy throughout the simulation, yet the trend of energy fluctuation still remains the same as that for the reference case. These results tell us that although grids should be refined as much as possible near the source, the sharp energy declines and overall fluctuation are due to other factors.

The reference case appears to show that significant energy variation occurs as the waves reach the land boundaries. To verify that the energy fluctuations which begin around 30 minutes into the simulation for the reference case are indeed caused by land boundary interaction, a third test case was created in which both the left and right side land boundaries were extended west and east, respectively. The reason for this grid extension was to see whether the energy variation would shift to a later time, since the waves would

take longer to reach these land boundaries. As shown in Figure 5.4, the energy fluctuations do indeed shift in time. The differences in magnitudes are due to the fact that a constant bathymetry was assumed for the extended portions of the grid. Thus, it seems that energy is improperly conserved when the waves reach land boundaries.

The above test cases show that transmissive boundaries are leading to energy loss during that part of the simulation for which the waves have been allowed to exit the domain. This is to be expected and shows that the transmissive boundaries are effectively allowing for departure of the waves and their energy from the system. If these waves contain a large amount of energy such as for the Pacific Northwest, a sharp decline will be noticed (Figures 4.8 and 4.9). On the other hand, if they contain smaller amounts of energy, the decrease will be seen as more gradual such as for the Sea of Japan (Figure 3.38). Fluctuations which are seen in the energy time histories appear to result from land boundary interaction. One reason for this may be the specification of land boundary conditions in the model. However, another very plausible reason may be found by examining the one piece of the puzzle that cannot be explained by the test cases. This missing piece is the sharp decline which occurs during the time steps immediately following the energy peak when the deformation to the sea floor is imposed. The physical link between the waves "climbing" the land boundaries (picture these as walls) and the wave pattern which results as the initial conditions are imposed is that both are situations where vertical accelerations are important. These accelerations will be more important during the initial conditions since the bottom deformation is assumed to move completely vertical, thus lifting the wave over a short period of time and letting it "fall" downward into its waveform.

With such vertical accelerations occurring, it should be pointed out that the shallow water equations (which are used with this model) assume a hydrostatic approximation:

$$p = p_{atm} + \rho g h \qquad \text{(EQ 5.1)}$$

where p is the pressure, p_{atm} is the atmospheric pressure, ρ is the density, g is gravity, and h is the depth. This approximation neglects pressure gradients resulting from vertical accelerations. It is thus questionable whether the shallow water equation inherently conserve energy. It is important that this question be resolved, and will therefore be examined more closely in future research.

Sea of Japan Simulations

The simulated wave patterns reproduce observations only to some extent. In particular, if we consider the reference numerical simulation:

- areas of observed energy concentration along Okushiri and Hokkaido are generally well identified;
- observed maximum amplitudes and arrival times at near-field tidal gauges (specifically, Iwanai and Esashi) are satisfactorily represented;
- significant wave activity persists for several days after the earthquake.

However:

- observed "run-ups" along the coasts of Okushiri and Hokkaido are systematically underpredicted, to a degree that can not be explained only by the model's inability to represent inundation;
- observed periods at the near-field tidal gauges are under-estimated;
- observed amplitudes, periods, and arrival times at far-field tidal gauges are reproduced unevenly;

- observed periods at several far-field gauges (Oshoro, in northern Hokkaido, and Nezugaseki, Awashima, Ogi, and Kashiwazaki, all on or in the vicinity of Honshu) are significantly over-estimated, suggesting that the model may not be representing correctly local dispersion or resonance effects.

The above differences between observations and simulations may result from a variety of factors. The following interpretation, although at times subjective, puts several of these factors into perspective:

- Fault plane model

  The adopted fault plane model (scenario WW) appears to represent some aspects of the source mechanism in a reasonable manner. In support of this argument, we note that (a) there is a rather satisfactory agreement between observed and simulated amplitudes and arrival times at Iwanai and Esashi, and (b) the disagreement between observed and simulated run-ups at Okushiri and Hokkaido appears to be primarily due to limitations of the hydrodynamic model (see discussion of formulation, below), rather than to the source mechanism. However, the fault plane model (e.g., through a combination of the adopted width and dip angle) may be largely responsible for the disagreement between observed and simulated periods; this argument is suggested by the fact that observed uplift/subsidence at Okushiri are poorly matched by the fault-plane model, and is arguably reinforced by the lack of a satisfactory alternative explanation.

- Hydrodynamic model / formulation

  The adopted finite element model has two major limitations: an intrinsic inability to describe inundation, a process that is not included in the model formulation; and a practical inability to remain stable for small water depths (i.e., large η/H) when non-linearities are accounted for. The latter limitation forced the artificial "deepening" of several coastal regions, which is arguably the leading reason why

the non-linear model systematically and very significantly underpredicts "run-ups" at Okushiri (where minimum depth was fixed at 15m); this argument is well supported by the comparison of linear and non-linear simulations (Figures 3.55 and 3.56).

- Hydrodynamic model / discretization

  The model benefited from the ability, inherent to finite elements, to flexibly place added refinement where needed (e.g., fault area and coast of Okushiri). Furthermore, the use of a versatile grid generator enabled effective grid adjustments throughout the modeling process. While the need to artificially "deepen" certain coastal regions arguably prevented a more full utilization of the available grid flexibility, sensitivity tests conducted with grids finer than the one shown in Figure 2 suggest that the adopted discretization was not a primary source of error.

- Tidal gauge data

  The tidal gauge data available for this study have potential inaccuracies, associated with at least three factors: measurement errors (gauges have built-in inertia relative to signals (including tsunamis) with smaller-than-tidal periods; digitization errors, both due to the mechanical reproduction of the original records and to operator inaccuracy; and processing errors, associated with the removal of tides. None of these factors explains satisfactorily the differences between observations and simulations, though. Indeed, earlier research on the response of Japanese tidal gauges to tsunamis [Satake, 1988] indicates that Iwanai and Esashi have lag-times of the order of only 1-3 minutes, which appear insufficient to explain why observed periods at these key gauges are so much larger than simulated periods. Digitization errors can be roughly estimated by visual examination of paper copies of the tidal gauge records released by JMA, and are relatively small. And while we know little about the filtering process, tides are too modest to have a significant impact.

Pacific Northwest Simulations

For a system such as the Pacific Northwest, the majority of the coastal sites along the Oregon and Washington coast can be considered near-field locations due to the location and orientation of the seismic source. Although there are errors associated with estimating the seismic source parameters, many of them have been determined to a reasonable extent. Therefore the initial conditions specified are certainly possible scenarios for subduction events in the Cascadia Subduction Zone. The numerically generated waveforms shown in Chapter 4 are thus also possible waveforms which may be seen arriving at the coastline. The wave heights which were shown for the Pacific Northwest coastline represent the maximum wave elevations as determined from the waveforms. As these waveforms inundate the land in a real system, they will in most instances "climb" to a land elevation which is higher than the maximum wave height in the waveform.

The discrepancies between the computed subsidence and estimated subsidence from field evidence are significant. It is important that this issue be resolved before meaningful results can be used extensively for coastal community planning. If the amount of subsidence is underestimated, the amplitudes of the waveforms will also be underestimated. The amplitudes and periods of the computed waves for the M_W=8.8 scenario are fairly similar to those computed by Whitmore [1992].

These Pacific Northwest waveforms are important pieces of information for coastal communities. Although it does not tell these communities which areas of land will be inundated, it provides them with images of what the waves will most likely look like as they arrive at their beaches. Correlating such waveforms with prehistoric evidence can prove to be quite valuable in preparing people for possible scenarios and in urban planning with regards to placement of critical facilities (schools, hospitals, fire stations, etc.). Such results have been made available through the earthquake/tsunami preparedness exercise (Quakex) and also to various Washington and Oregon coastal communities.

Limiting Factors to Tsunami Models

One of the primary limiting factors to hydrodynamic numerical models are the initial conditions obtained from seismological data. It has been shown that many different combinations of the pertinent seismological parameters can be derived for events which have occurred in the past. Determining which combination is most correct is evaluated based upon geodetic data, tidal gauge data, and possibly run-up measurements. The choice of the parameters involved can influence the generated waves with regards to amplitude, wavelength, time lag (phase), and directivity. Not only are there many possible combinations of the parameters, but each of the parameters are themselves limited by the ability to resolve them. For example, the spatial location of the subduction region is determined only from the distribution of earthquake aftershock data. There can be significant error in such an assumption which can be noticed in the amplitude, phase, and wavelength of the generated waves.

Once a set of parameters is decided upon, the conversion to a spatial deformation in the sea floor faces new assumptions. Current bottom deformation models assume a simple rectangular source in isotropic, homogeneous half-spaces. More elaborate models are limited by the fact that they can not be verified due to the lack of data from actual subduction events. At this time, however, simpler fault models appear to perform reasonably in computing sea floor deformations. This is exemplified in the Sea of Japan simulations where near-field stations showed that computed waveforms were similar to actual observations. Thus the initial conditions specified by the fault plane model (assuming that the length and width were correctly depicted) were able to generate waveforms close to what they appeared to be in reality.

The use of spatial sea floor deformations as input to hydrodynamic models can in some instances be limited by the rise time of a particular earthquake. One example of this is the "tsunami earthquake", which is a slow thrust event in which the magnitude of the earthquake is small compared to the magnitude of the generated tsunami. The September 1, 1992 tsunami in Nicaragua is an example of such an earthquake tsunami. These events

are generally difficult to model numerically unless some type of multiplication factor is employed. Therefore, either the depiction of the initial conditions based upon available seismological information needs to be evaluated in more detail or the determination of the seismological parameters for such events is facing many errors. It is also possible that the inability to model tsunami earthquakes properly may be a result of the energy factors considered earlier.

The hydrodynamic results shown in Chapters 3 and 4 exemplify the limiting factors in modeling tsunamis once the initial conditions have been defined. First of all, numerical stability must be maintained for a particular simulation. This can be ensured by checking that the finite element grid maintains reasonable dimensionless wavelengths, obeys the Courant number restriction for a particular time step of interest, and has a minimum depth sufficient to avoid wetting and drying of elements. The selection of the GWCE weighting factor also needs to be made such that the wave equation does not become so primitive that spurious $2\Delta x$ oscillations become evident.

Considerations for Future Research

Principles such as conservation of mass and conservation of energy have not been reported for most numerical modeling applications to tsunamis. The mass variation needs to be evaluated by investigating the mass conservation properties of the transmissive boundaries. It would be insightful to evaluate how well other models are able to maintain conservation of energy. If different models based upon the same sets of equations show similar patterns of energy variation, it would provide more support for the hypothesis that the equations do not inherently exhibit energy conservation qualities.

A promising area of improvement in tsunami modeling appears to be in the definition of initial conditions. The error, ambiguity, and assumptions in the seismological parameters and bottom deformation models constrain the hydrodynamic results and lead to significant computational costs. It would therefore be advantageous to determine initial

conditions without the use of either seismological information or a bottom deformation model. It may be possible to do so through the use of inverse methods [*Satake*, 1989, *Satake*, 1993, *Myers et. al.*, 1993].

The concept behind inversion methods is that available data from a particular event contains clues as to what types of sources could have been responsible for the observations. By looking at what happens in a system when a unit forcing is applied to each possible source, a least squares approach can be used to determine how much each source is responsible for the available observations. As applied to tsunamis, the sources would be seismic sources and the unit forcings at these sources may be unit amounts of slip, Gauss hills one unit in amplitude, etc. The observations may include tidal gauge waveforms, run-up measurements, or geodetic data. If we consider an observed tidal gauge waveform $b_i(\vec{x}, t)$ and let $A_{ij}(\vec{x}, t)$ represent the waveform at tidal gauge station i resulting from a unit forcing at source j, then the inverse problem can be solved as:

$$A_{ij}(\vec{x}, t) \cdot \omega_j = b_i(\vec{x}, t) \qquad \text{(EQ 5.2)}$$

This set of equations for a combination of stations and sources may be solved from a least squares perspective for the weighting factors ω_j. Since the least squares problem is a linear procedure, the equations involved must be linear. However, the hydrodynamic equations we are solving contain nonlinearities from friction, advection, and finite amplitude. Therefore, a generalized inversion method [*Myers et. al.*, 1993] should be used whereby corrections for the differences between nonlinear responses and the observations are solved for linearly in an iterative manner. The combinations of the unit forcings weighted by the solved weighting factors, should then provide information as to what the spatial deformation in the sea floor looks like. This may then be used as the initial condition for a forward simulation of the tsunami.

Inundation is a key component of what occurs in reality. Bringing this component into numerical modeling has proven to not be a trivial task. Difficulties have arisen in such attempts with regards to conserving momentum and continuity at the same time. There-

fore, new methods are currently in preparation which do obey such conservation laws. The results in this thesis thus provide information as to what the waves may look like as they arrive at the coastline. They do not deal with how far the waves will flood various regions of land. Inundation models are currently in development which will use the regional results provided from a numerical model such as ADCIRC-2DDI to compute the flooding of local regions.

Coupling the generation, propagation, and inundation components of a tsunami through numerical means will allow a comprehensive evaluation of the impact tsunamis can have at the coastlines and in coastal communities. Such an analysis can be verified using both tidal gauge data and run-up measurements from past events. If proven to be accurate, these methods could be applied more rigorously to theoretical events such as those which are believed to occur regularly along the Cascadia Subduction Zone.

References

Liu, P. and Yoon, S.B., Estimation of Tsunami Wave Heights along South Eastern Korean Shoreline, *Cornell University*, 1991.

Myers, E.P., Baptista, A.M., and Wang, Y., Non-linear Inversion of Tsunami Waveforms, *AGU 1993 Fall Meeting Abstract*, 1993.

Satake, K., Tide Gauge Response to Tsunamis: Measurement at 40 Tide Gauge Stations in Japan, *Journal of Marine Research*, 46, pp. 557-571, 1988.

Satake, K., Inversion of Tsunami Waveforms for the Estimation of Heterogeneous Fault Motion of Large Submarine Earthquakes: The 1968 Takachi-oki and 1983 Japan Sea Earthquakes, Journal of Geophysical Research, 94(B5), pp. 5627-5636, 1989.

Satake, K., Depth Distribution of Coseismic Slip Along the Nankai Trough, Japan, From Joint Inversion of Geodetic and Tsunami Data, Journal of Geophysical Research, 98(B3), pp. 4553-4565, 1993.

Whitmore, P.M., Hypothetical Cascadia Tsunamis, *Alaska Tsunami Warning Center*, August 1992.

FIGURE 5.1 Test Case Grid

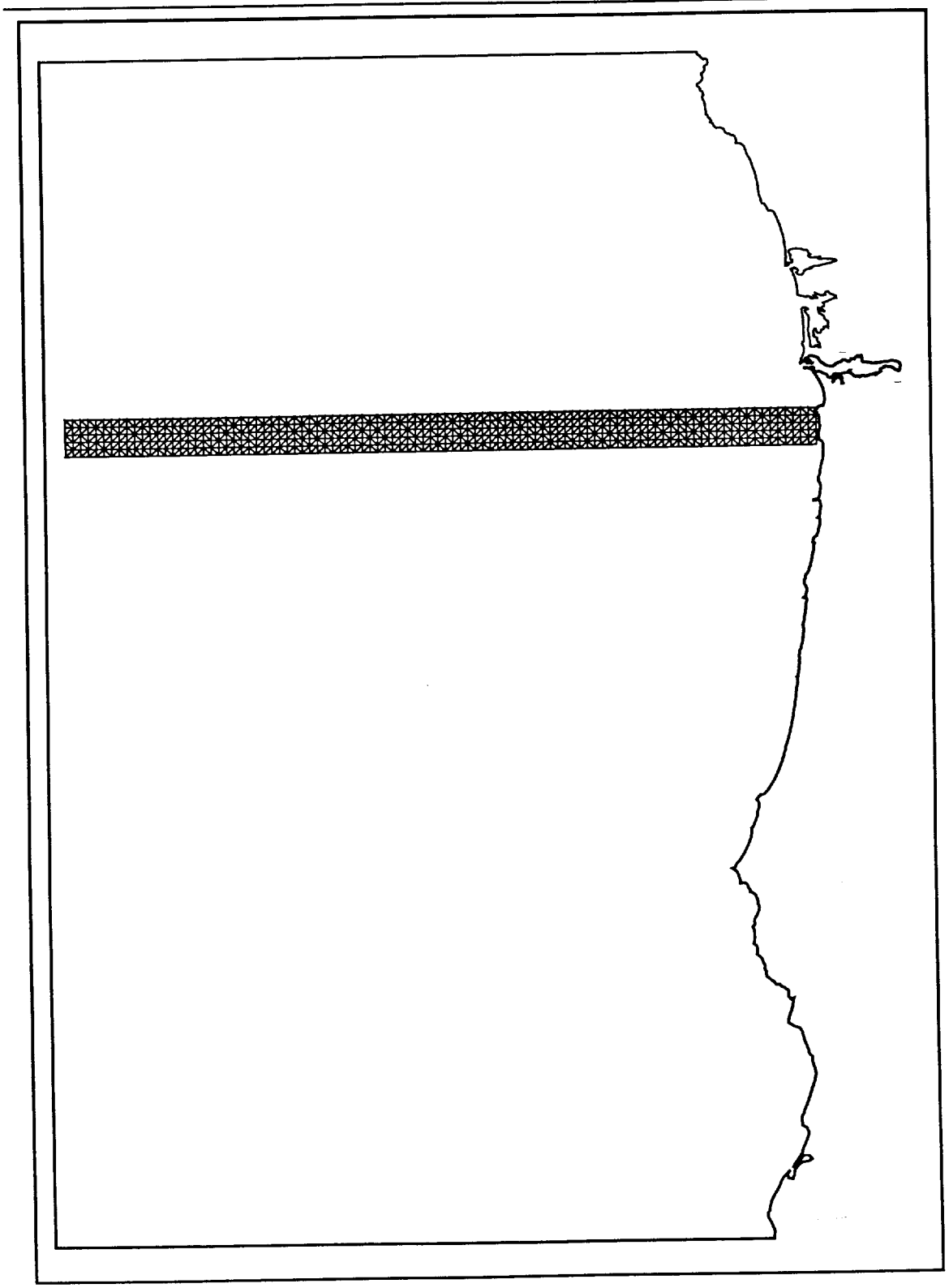

FIGURE 5.2 Energy Comparison for Reference and Open Boundary Cases

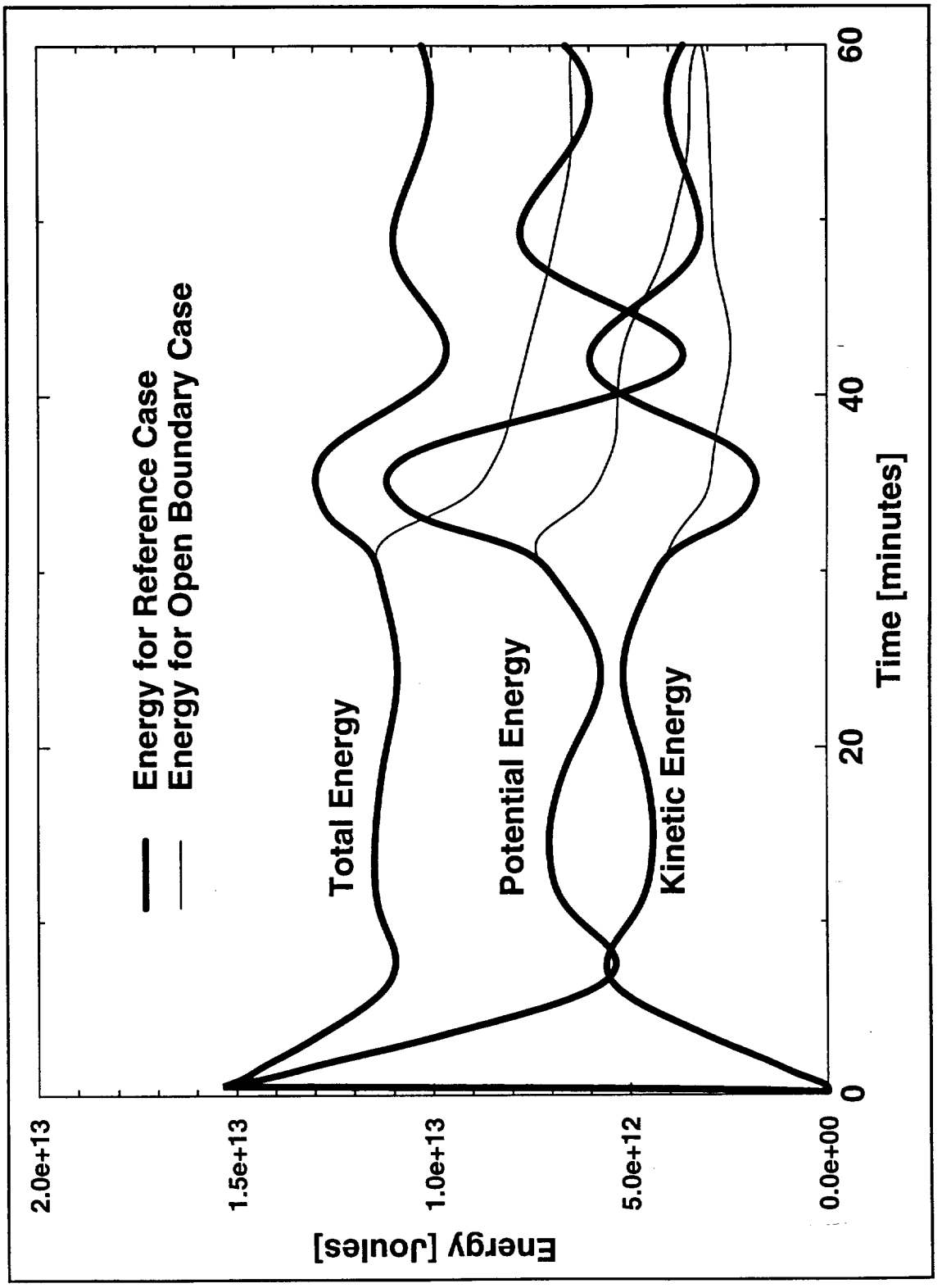

FIGURE 5.3 Energy Comparison for Reference and Refined Grid Cases

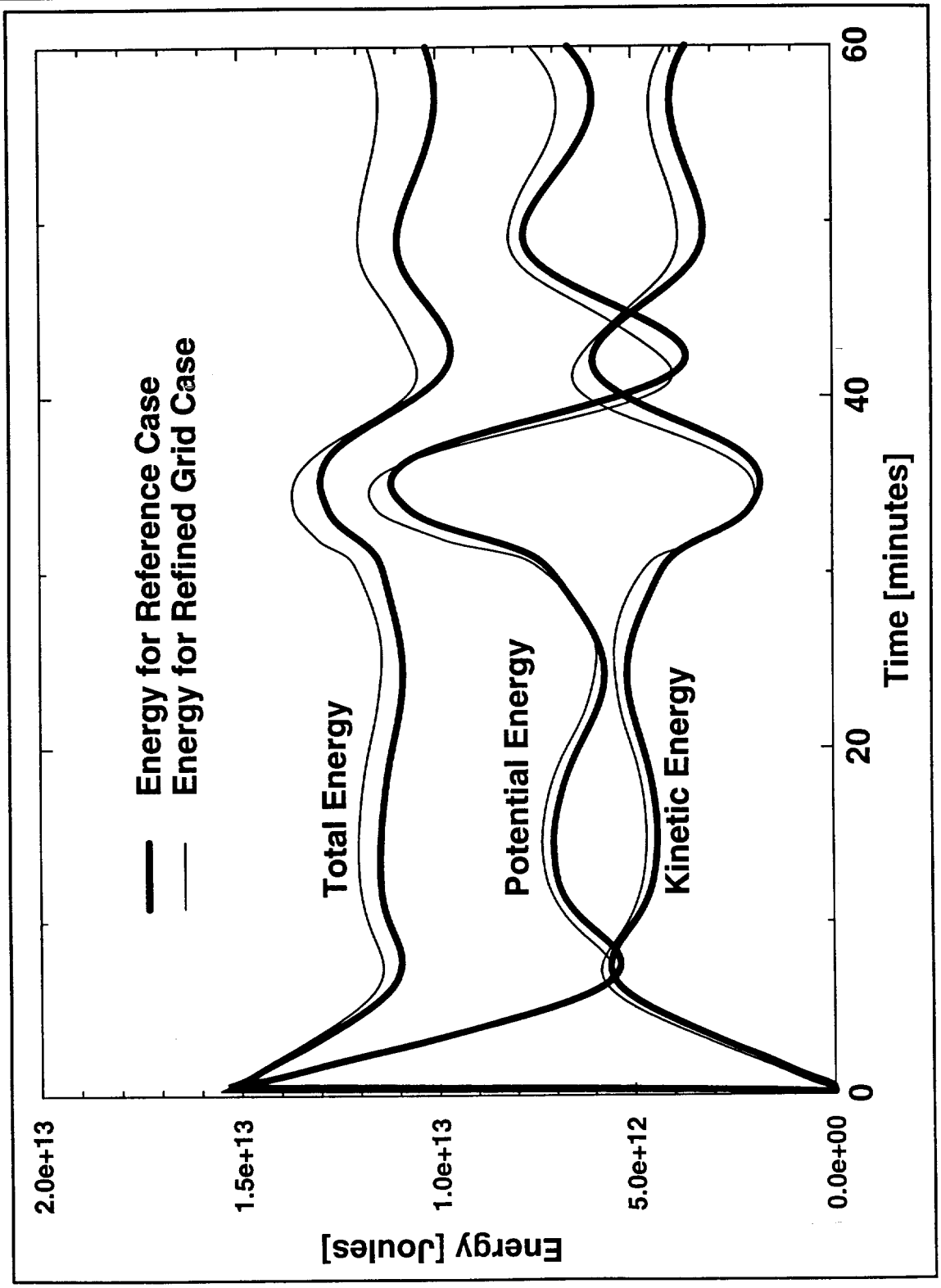

FIGURE 5.4 Energy Comparison for Reference and Extended Grid Cases

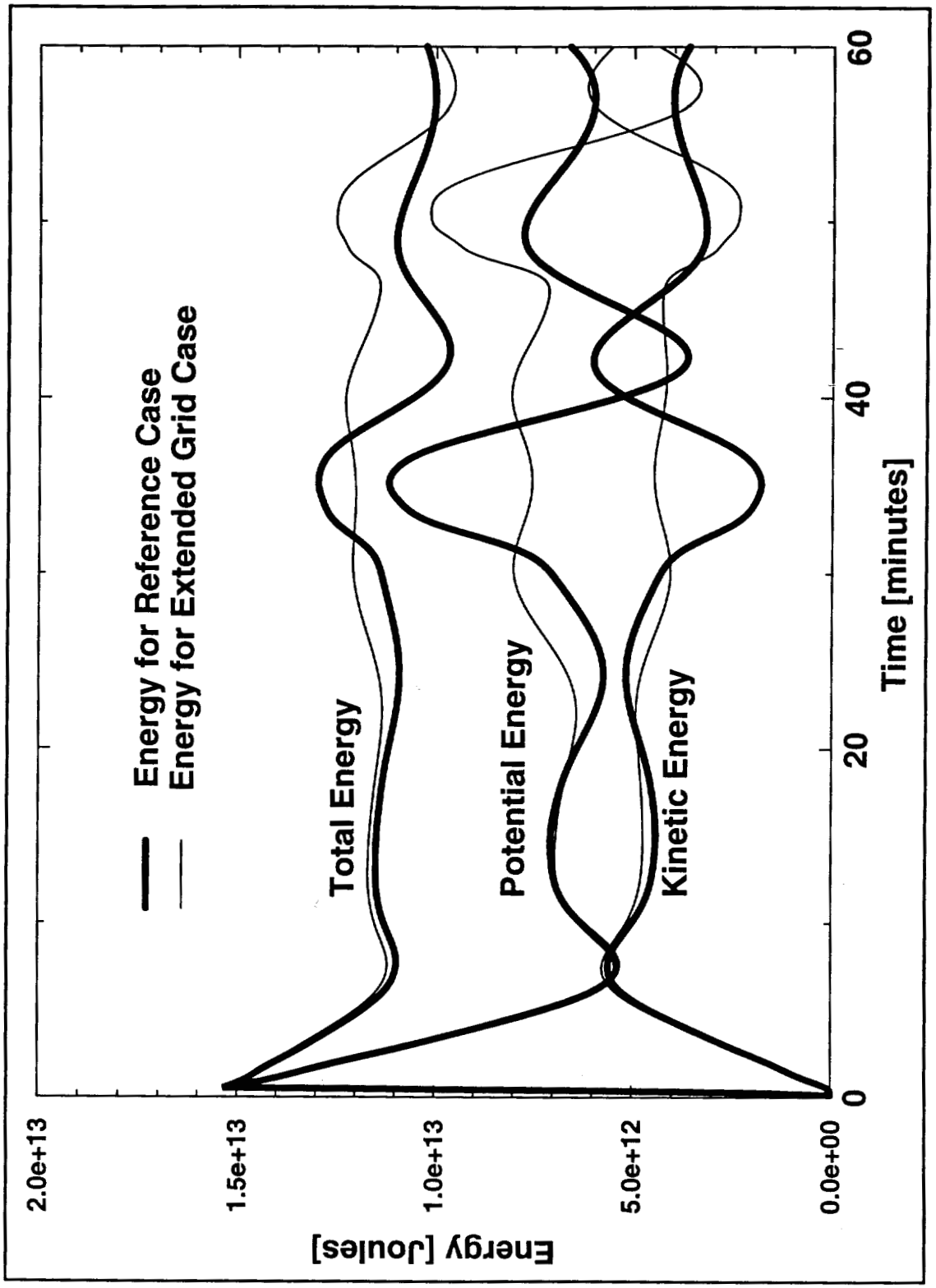

BIOGRAPHICAL SKETCH

The author was born on August 17th, 1970, in Pasadena, California. He entered Washington University in St. Louis, Missouri in September, 1988 and received his Bachelor of Science degree in Civil Engineering in May, 1992.

In September 1992, the author entered Oregon Graduate Institute of Science & Tecnology, under the supervision of Dr. António Melo Baptista. He was awarded his Master of Science in Environmental Science and Engineering in October, 1994.